Numerical and Analytical Methods in Low-Dimensional Strongly Correlated Quantum Systems

by

Changnan Peng

B.S., California Institute of Technology, 2019

Submitted to the Department of Physics
in partial fulfillment of the requirements for the degree of

DOCTOR OF PHILOSOPHY IN PHYSICS, STATISTICS, AND DATA SCIENCE

at the

MASSACHUSETTS INSTITUTE OF TECHNOLOGY

September 2024

Authored by:	Changnan Peng Department of Physics August 12, 2024
Certified by:	Maxim A. Metlitski Associate Professor of Physics, Thesis Supervisor
Accepted by:	Lindley Winslow Associate Department Head of Physics

Numerical and Analytical Methods in Low-Dimensional Strongly Correlated Quantum Systems

by

Changnan Peng

Submitted to the Department of Physics
on August 12, 2024 in partial fulfillment of the requirements for the degree of

DOCTOR OF PHILOSOPHY IN PHYSICS, STATISTICS, AND DATA SCIENCE

ABSTRACT

The study of low-dimensional strongly correlated quantum systems lies at the intersection of intricate theoretical models and practical numerical methods, offering deep insights into condensed matter physics. This thesis explores the application of various numerical and analytical methods to these systems. It addresses universal behaviors and phase transitions, exemplified by the phenomenon of multiversality. Specifically, the transition from a 1D Luttinger liquid to a charge density wave insulator, characterized by partly Kosterlitz-Thouless transition and partly Ising transition, is analyzed using both analytical renormalization group calculations and numerical density matrix renormalization group simulations. Additionally, the thesis introduces a statistical smoothing spline method to pinpoint transition points systematically. The work extends to quantum dynamics, presenting a generic theoretical framework for analyzing quantum-classical adiabatic dynamics with learning algorithms. A provably efficient adiabatic learning (PEAL) algorithm with favorable scaling properties is developed. The algorithm is numerically validated on the 1D Holstein model, demonstrating its precision in predicting dynamics. Furthermore, the thesis derives a Hamiltonian lattice formulation for the 2+1D compact Maxwell-Chern-Simons theory, providing an analytical solution that aligns with continuum theories and facilitating future numerical applications. Through these explorations, the thesis underscores the complementary roles of numerical and analytical methods in advancing the understanding of complex quantum systems.

Thesis supervisor: Maxim A. Metlitski
Title: Associate Professor of Physics

Acknowledgments

First and foremost, I would like to express my deepest gratitude to my advisor, Max Metlitski, for his unwavering guidance and support during my PhD. Max is among the most brilliant minds I have ever encountered, and each discussion with him has been enlightening. His kindness, patience, and integrity have made him a true role model for me. It has been an immense honor to be his student. Completing my PhD within five years and looking forward to a promising future would not have been possible without Max's assistance. Thank you, Max!

I am grateful to Liang Fu and Michael Williams for their time and effort as members of my thesis committee. Special thanks to Michael for supporting my participation in the Interdisciplinary Doctoral Program in Statistics (IDPS) and my summer internship. I also thank Liang Fu, Leonid Levitov, and Senthil Todadri for their time spent on my oral exam, and Xiao-Gang Wen for serving as my Academic Advisor.

I would like to acknowledge my research collaborators during my PhD studies. I am especially grateful to Di Luo, who introduced me to the field of Data Science and assisted in completing two major projects. His passion for research was truly inspiring. Additionally, I thank my collaborators Zhen Bi, Ruben Verresen, Gia-Wei Chern, Jin-Peng Liu, Cristina Diamantini, Lena Funcke, Syed Muhammad Ali Hassan, Karl Jansen, Stefan Kühn, and Pranay Naredi for their contributions to my thesis. Thanks to the MIT Supercloud Team, as most of my numerical computations were performed on the MIT Supercloud Cluster.

My sincere thanks go to the professors and teachers whose guidance and instruction

have been invaluable during my PhD: Leonid Levitov, Xiao-Gang Wen, Ashvin Vishwanath, Phiala Shanahan, Tracy Slatyer, Aram Harrow, Subir Sachdev, Senthil Todadri, Alex Shvonski, Jeff Gore, Marin Soljačić, Joshua Wolfe, Michelle Tomasik, Betty Lou McClanahan, Matthew LaVita, Tommi Jaakkola, Peter Kempthorne, Mehran Kardar, David Gamarnik, Gabriele Farina, Soonwon Choi, Nike Sun, Martin Wainwright, and Sasha Rakhlin. Your teaching and mentorship have greatly contributed to my growth and learning.

I am also grateful for the administrative support from Catherine Modica, Shannon Larkin, Sydney Miller, Lesley Keaney, Denise Wahkor, Elizabeth Milnes, and Kim Strampel. Special thanks to Cathy for her proactive support before and during my summer internship.

I would like to thank Dr. Michael Di Bianca from MIT Health for his psychological counseling, which helped me maintain a healthy state during the most stressful periods of my PhD and allowed me to face future challenges with confidence and resilience.

My friends have made my PhD journey enjoyable and memorable. Special thanks to my roommate of five years, Zhi Ren, for the countless meals, conversations, academic discussions, and fun activities we shared, and for his support during the COVID lockdown. Zhi also provided invaluable advice for my future career. I thank my office mates, Robert Jones and Zhiyu Dong, for our insightful discussions on physics. I am also grateful to my friends: Zhihuan Dong, Ali Ghorashi, Shankar Balasubramanian, Margarita Davydova, Arkya Chatterjee, Ethan Lake, Seth Musser, Olumakinde Ogunnaike, Abijith Krishnan, Xueyang Song, Zhengyan Darius Shi, Anjie Gao, Wenxuan Jia, Tianyu Yang, Jixiang Yang, Yuanjie Ren, Beili Hu, Ho Tat Lam, Yifan Su, Honglie Ning, Xirui Wang, Guoqing Wang, Yukun Lu, Zhaoyi Li, Daniel Mark, Samuel Alipour-fard, Saranesh Prembabu, Patrick Ledwith, Haoyu Guo, Hao Zhang, Taige Wang, Zihao Qi, Xiaotian Zhang, Yanke Song, Jing Ding, Shangzhou Xia, Zhen Huang, Yunkun Zhou, Fanying Chen, Sheng Feng, Pu Yu, Shengwen Gan, Weixiao Lu, Haoshuo Fu, Tiancheng Yu, Yuqiu Fu, Hang Du, Mingyang Deng, Ziqian Zhong, Rui Sun, Baiyu Zhu, and Yuxuan Zheng. Your presence made these five years truly wonderful. Thanks also to the Sidney-Pacific Community for providing a comfortable and resourceful

living environment, and to the Donghaiyuan food delivery during the challenging COVID period.

I would like to thank all the mentors who have encouraged me since childhood and guided me throughout my journey: Yuchao Sun, Xuelin Yao, Feng Song, Yousheng Shu, Heng Fan, Liangzhu Mu, Zhi Li, Gil Refael, Anton Kapustin, Frank Rice, and Shaojie Chen. I also thank my former research partners: Jiayu Li, Samuel Savitz, Arbel Haim, Torsten Karzig, and Yang Peng. Your support has been crucial to my achievements and optimism for the future.

Finally, no words can adequately express my gratitude to my family. Thank you to my parents for raising me with unconditional love, support, and patience. Your continued support has been a pillar of strength for me. I am also grateful to my grandparents for their love, care, and companionship. Special thanks to my beloved fiancée, Ke Shi, who fills my heart with immense joy. I love you all dearly.

Cambridge, Massachusetts

July 22, 2024

Contents

List of Figures

List of Tables

Chapter 1

Introduction

1.1 Overview

The study of low-dimensional strongly correlated quantum systems is a fascinating and complex field within condensed matter physics. Physicists in this domain often begin by conceptualizing intricate lattice models that reflect the realistic behaviors of materials observed in nature. These models serve as a foundation for understanding the universal behaviors and phase transitions of such materials. The next step typically involves developing a low-energy effective field theory from the complex lattice model to capture these universal aspects. Finally, researchers design minimal lattice models that can demonstrate the effective field theories in a more simplified and controlled manner.

An intriguing example of the complex phase transition phenomena in nature is multiversality [1]. This concept suggests that the universality classes of a continuous transition between two phases of matter may not be unique; different regions of the phase boundary may exhibit distinct universality classes. This phenomenon was first discovered in 3+1D gauge theory [2]. In Chapter 2 of this thesis, we describe an example of the multiversality phenomenon using a simpler model. We explore a 1+1D field theory and its realization in a 1D spin chain. We apply both analytical and numerical methods to study various aspects

of our model, and find consistent results.

Numerical algorithms have proven to be powerful tools when analytical methods alone are insufficient. For instance, in Chapter 2, we employ the Density Matrix Renormalization Group (DMRG) algorithm to demonstrate the absence of a first-order phase transition in the strongly coupling regime of our model, where the analytical Renormalization Group (RG) method is not able to predict this property. In Chapter 3 of this thesis, we continue the exploration of universality by introducing statistical tools to numerically identify critical points. With the statistical tools, we can systematically apply the data collapsing and scaling method, and the results agree with the ones from conventional methods.

As the complexity of the system increases, especially with many degrees of freedom and complicated couplings, numerical simulations become indispensable. Non-equilibrium dynamical processes present an even greater challenge. In Chapter 4 of this thesis, we develop a general numerical framework for simulating quantum-classical hybrid dynamics [3]. This framework is supported by rigorous analytical methods, such as statistical bound analysis, to prove the efficiency of our numerical algorithms. This synergy between numerical and analytical methods underscores their complementary nature.

In the pursuit of more advanced numerical algorithms, modern techniques such as machine learning, neural networks, and quantum simulations have become more noticeable. However, the challenge often starts with the first step: formulating the theory into a form that can be handled numerically. For example, designing a minimal lattice model to demonstrate the Chern-Simons effect has been a significant endeavor [4]–[10]. In Chapter 5 of this thesis, we present a Hamiltonian lattice formulation of compact Maxwell-Chern-Simons theory [11]. This lattice Hamiltonian retains all the physical properties of the Maxwell-Chern-Simons theory, including level quantization, states degeneracy, scaling law of Wilson loops, and their topological behavior. Our lattice Hamiltonian paves the way for future applications of numerical methods to this problem.

Each chapter of this thesis demonstrates the interplay between numerical and analytical

methods. In Chapter 2 and Chapter 3, numerical methods aid in analytical understanding, while in Chapter 4 and Chapter 5, analytical insights enhance numerical approaches.

1.2 Thesis outline

In the following chapters of this thesis, we will present how various numerical and analytical methods are applied in three quantum systems.

In Chapter 2 we will describe a 1+1D quantum field theory in which multiversality can be realized in a phase transition from a Luttinger liquid to a charge density wave (CDW) insulator. This multiversality includes a part of the phase transition described by the Kosterlitz-Thouless (KT) transition and another part by the Ising conformal field theory (CFT). We will construct a concrete microscopic lattice model that corresponds to this low-energy effective field theory. This correspondence is supported by analytical RG calculations. Additionally, we will perform DMRG simulations on the 1D lattice model with various parameters, system sizes, and boundary conditions. We will probe different aspects of the model by measuring physical observables such as energy levels, correlation functions, and entanglement entropy profiles, and by applying numerical data analysis methods like level spectroscopy, data collapsing, and operator scaling. The phase diagram constructed from these numerical results is consistent with the analytical predictions.

In Chapter 3 we will apply smoothing splines to the numerical data collected in Chapter 2. This data includes measurements of the entanglement entropy under different system sizes and parameters. Based on RG analysis around the Ising criticality, a universal scaling relation between the entanglement entropy and the system size is expected. We will use two different approaches with the smoothing spline to find the critical point. The first method involves performing smoothing spline regression on each curve and comparing the mean square differences between pairs of curves. The second method performs smoothing spline regression on all transformed data together and uses the Bayesian Information Criterion

(BIC) to determine the critical point. We will present and discuss the numerical results, highlighting the pros and cons of each method.

In Chapter 4 we will establish a generic theoretical framework for analyzing quantum-classical adiabatic dynamics using learning algorithms. Starting with the approximately constant linear model, we will derive the general error bounded condition for nonlinear models and the general relaxation method, providing a solid foundation for the reliability of learning algorithms in quantum-classical adiabatic dynamics. We will develop a provably efficient adiabatic learning (PEAL) algorithm for quantum-classical adiabatic dynamics. This algorithm offers a sample complexity scaling logarithmically with the system size and favorable scaling of evolution time. We will benchmark our algorithm on the 1D Holstein model, demonstrating accurate predictions of single path dynamics, ensemble dynamics observables, and transfer learning across different coupling constants. This framework opens new possibilities for efficient learning of quantum-classical dynamics. The content in this chapter is based on [3].

In Chapter 5 we will derive the Hamiltonian lattice formulation of compact 2+1D Maxwell-Chern-Simons theory. The Hamiltonian is quadratic in the gauge field, and is made a compact theory by the Villain approximation and two 1-form constraints. These constraints ensure invariance under large gauge transformations in two spatial dimensions. The compatibility of these constraints requires the quantization of the Chern-Simons level k, generating a k-fold degeneracy of the spectrum. We will solve the spectrum analytically, showing a gapped theory with massive photons. The Wilson loop operators show a perimeter law, and linked Wilson loops exhibit nontrivial topological phases. Moreover, anyons as the excitations at the ends of open Wilson lines display fractional mutual statistics and self statistics. These features align with the continuum Maxwell-Chern-Simons theory, confirming the validity of our lattice Hamiltonian formulation. The content in this chapter is based on [11].

Chapter 2

Multiversatily of Charge Density Wave Onset in a Luttinger Liquid

2.1 Introduction

It has recently been realized that the universality class of a continuous transition between two phases of matter may not be unique: different regions of the phase boundary may realize distinct universality classes. This special phenomenon of criticality is called “multiversality classes,” first introduced by Bi and Senthil in 2019 [1].

In a later paper by Bi, Lake, and Senthil, the authors further described such phase transitions in the "Landau beyond Landau" paradigm [2]. The RG flow of the paradigm is shown on the right in Fig. 2.1. One of the fixed points (e.g. the green dot) is in the standard universality class described by the Landau-Ginzburg theory based on the order parameters in the two phases on either side of the transition. There could be new fixed points (e.g. the purple and red dots) where the physics cannot be described in terms of order parameter fluctuations alone. This is a situation where a Landau-allowed phase transition is not necessarily described within the Landau paradigm, and is thus called "Landau beyond Landau" paradigm.

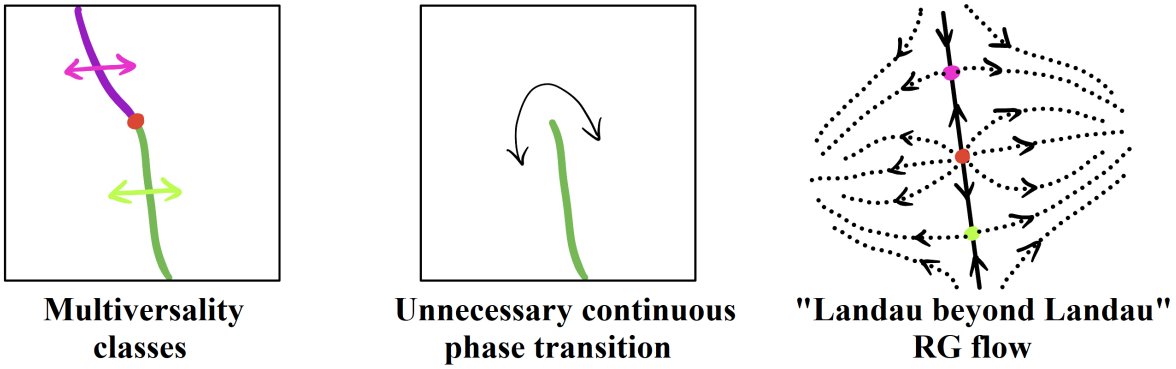

Figure 2.1: Schematic phase diagrams for multiversality classes (left) and unnecessary continuous phase transitions (middle). Multiversality classes can be described by the "Landau beyond Landau" paradigm (right).

Multiversality classes are often discussed together with the concept of "unnecessary continuous phase transitions," which describes continuous transitions that happen within the same phase [1]. Schematic phase diagrams for multiversality classes and unnecessary continuous phase transitions are shown in Fig. 2.1.

These special phenomena of criticality are quite unexpected: When talking about quantum critical points in condensed matter physics, the most fundamental question is often to understand what the distinction is between the phases on either side of the transition, and how that distinction is related to the universality class of the transition. The unnecessary continuous phase transitions show that quantum critical points may occur in a case that does not separate two distinct phases, while the multiversality classes we are interested in here show that the same phase transition admits multiple universality classes depending on where the phase boundary is crossed.

In the original paper by Bi, Lake, and Senthil, multiversality classes were constructed with gauge theories in 3+1D space-time dimensions [2]. Here we describe an example of such multiversality: a transition from a 1D Luttinger liquid (LL) to a charge density wave (CDW) insulator. We show that one part of the boundary between these two phases realizes the Kosterlitz-Thouless (KT) transition. The KT transition has a central charge $c = 1$ and

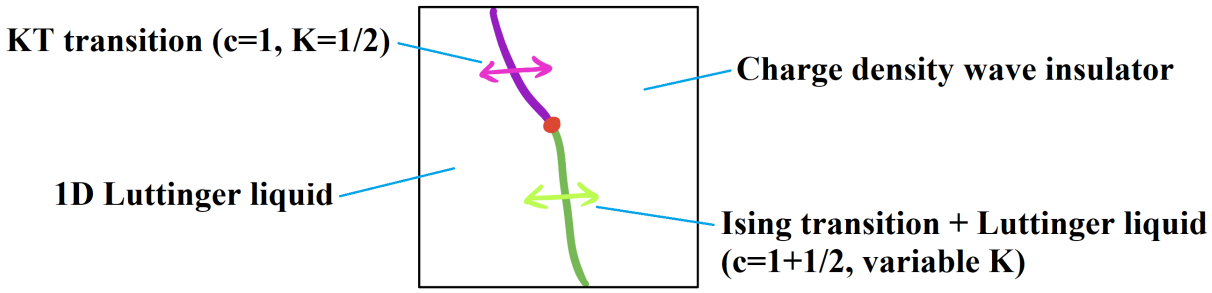

Figure 2.2: A schematic phase diagram of the multiversality classes we describe in this chapter.

a Luttinger parameter $K = 1/2$. The other part of the boundary is described by an Ising transition coexisting with the Luttinger liquid. This coexisting part has a central charge $c = 1/2 + 1$ and a variable Luttinger parameter. The schematic phase diagram is shown in Fig. 2.2.

Normally people would think that the phase transition between a 1D Luttinger liquid and a CDW insulator is a KT transition. Therefore, the appearance of multiversality with the Ising conformal field theory (CFT) on the boundary is unexpected. In Section 2.2, we will explain the physical intuition of the appearance of multiversality from the field theory idea.

In Section 2.3, we will present a more rigorous analysis starting from a microscopic lattice model. We will demonstrate these conclusions using analytical renormalization group (RG) calculations.

In Section 2.4, we will show the results from numerical density martrix renormalization group (DMRG) simulations of the concrete microscopic model. Various numerical methods will be applied: The level spectroscopy method is used to find the precise location of the KT transition point [12], [13]. The data collapsing method is used to find the Ising critical point. The scaling laws of the operators are used to identify different phases. Finally, we will present a phase diagram showing the best numerical results we could achieve.

Unfortunately, we are not able to directly see the multiversality classes from the numerical results. Because of limited precision, we have difficulty nailing down the Ising segment in

the phase boundary. Nevertheless, our numerical results are consistent with the analysis. Discussions and a summary of this chapter are presented in Sec. 2.5.

2.2 Field theory intuition

We start by considering the following field theory model:

$$L = L_{\mathrm{LL}} + L_{\mathrm{Ising}} + s \cdot \sigma \cdot \sin\theta, \tag{2.1}$$

where $L_{\mathrm{LL}} = \frac{1}{8\pi K}(\partial_\mu \theta)^2$ is the Lagrangian of the 1D Luttinger liquid (LL) with Luttinger parameter K and variable θ [14]. L_{Ising} is the Lagrangian of the Ising conformal field theory (CFT) with order parameter σ. s is a coupling constant between LL and Ising CFT.

This Lagrangian is designed based on the following intuition. The original idea that we couple the Ising CFT to LL comes from the fact that, in the normal charge density wave (CDW) onset of the Luttinger liquid, there are relevant double-period operators. The Ising CFT can naturally include double-period operators in the ordered phase. Therefore, when the Ising CFT and LL couple with each other, interesting phenomena can appear from this combination.

We now try to analyze the effect of this coupling term ($s \cdot \sigma \cdot \sin\theta$) on the phase diagram. In Figure 2.3, we show a slice in the parameter space. The horizontal ais represents the parameter that drives the Ising phase transition. On the left hand side it is an Ising disorder phase, with the order parameter expectation value $\langle\sigma\rangle = 0$. On the right hand side it is the ordered phase, where the order parameter has non-zero expectation value, $\langle\sigma\rangle \neq 0$. The vertical axis represents the Luttinger parameter K.

At the Ising transition, which is shown by the vertical axis in Fig. 2.3, we have a CFT

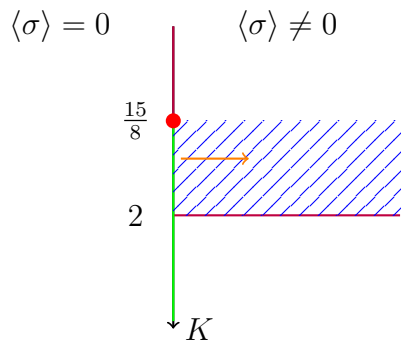

Figure 2.3: A schematic diagram showing the physical intuition of the multiversality.

and can calculate the scaling dimensions of the operators [15], [16]:

$$[\sin\theta] = K, \tag{2.2}$$

$$[\sigma] = 1/8. \tag{2.3}$$

Therefore, the coupling term $(s \cdot \sigma \cdot \sin\theta)$ is irrelevant when

$$[\sin\theta] + [\sigma] = K + 1/8 > 2, \tag{2.4}$$

i.e. when $K > 15/8$.

This special K value is marked as the red dot in Fig. 2.3. We draw a green vertical line for the K value that is greater than 15/8. This green line shows a criticality of decoupled Ising CFT and Luttinger liquid with variable $K > 15/8$. The central charge of the phase transition on the green line is $c = 1/2 + 1$.

Now we leave this green critical line, and move into the Ising ordered phase, as shown by the orange arrow in Fig. 2.3. The situation is now different from what is on the critical line: The Ising order parameter gets a non-zero expectation value $\langle\sigma\rangle \neq 0$. Now the scaling dimension of the coupling term $(s \cdot \sigma \cdot \sin\theta)$ only depends on $\sin\theta$, which has dimension K. Therefore, when we move to the right hand side of the diagram, the coupling is irrelevant when $K > 2$.

Something interesting happens between $15/8 < K < 2$. In this range of K, the region on the right hand side of the diagram is dangerously irrelevant, shown as the shaded area in Fig. 2.3. Dangerous irrelevancy means that the coupling term seems irrelevant on the critical line, but one step away from the critical line the coupling turns relevant. When the coupling is relevant, the double-period CDW onset gaps out the Luttinger liquid: It is a trivial gapped phase in the shaded area.

When K is strictly greater than 2, the Ising sector and the LL sector fully decouple. It is shown as the area in the bottom right corner, below the horizontal purple line in Fig. 2.3. In this area, there is a coexistence of the gapless Luttinger liquid and a charge density wave in the Ising sector.

To go from this gapless region back to the gapped dangerously irrelevant region (shaded area), we have a transition from a gapless (LL + CDW) to a gapped CDW insulator. This is an onset of the $\sin\theta$ operator, and can be described by a phase transition given by a standard KT transition with parameter $K = 2$, which is labeled by the horizontal purple line in Fig. 2.3.

For $K < 15/8$, the coupling term $(s \cdot \sigma \cdot \sin\theta)$ is relevant. We enter the strong coupling region. Although we are not analytically able to predict the fate of the RG flow when $s \to \infty$, one possibility is that in this regime the CDW onset is described by a conventional KT transition:

$$L = \frac{1}{8\pi\tilde{K}}(\partial_\mu\theta)^2 + u\cos 2\theta, \tag{2.5}$$

where $\tilde{K}$ is a renormalized Luttinger parameter, and u is a renormalized effective coupling constant. This conjectured strongly coupled KT transition is shown as the vertical purple line segment in Fig. 2.3. On this segment of phase transition, $\tilde{K} = 1/2$.

It is also possible that it flows to a first order phase transition. However, we will show later with our numerical simulation that there is no evidence of a first order phase transition

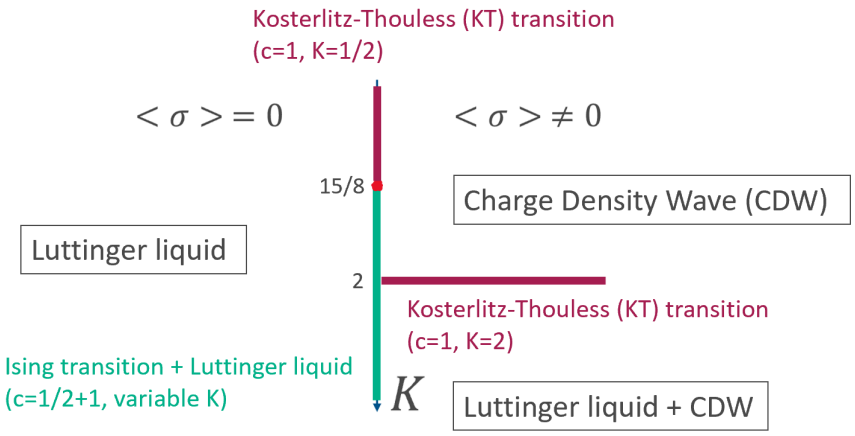

Figure 2.4: A schematic conjectured phase diagram for the field theory model in Eq. 2.1 for small s. Universality classes of the transition are noted and the value of K indicated is the true infra-red K of the Luttinger liquid.

up to the precision we could get.

We expect the following phase diagram of this field theory, as shown in Fig. 2.4. We have a gapless Luttinger liquid on the left, a gapped CDW insulator on the upper right, and a coexisting of decoupled gapless LL and CDW on the bottom right. Between the LL (left) and the LL+CDW (bottom right) the phase transition is described by an Ising CFT (vertical green line). Between the CDW (upper right) and the LL+CDW (bottom right) the phase transition is a $K = 2$ KT transition (horizontal purple line). The most interesting part in the phase diagram is that there are two possible ways to have the CDW onset, between the LL (left) and the CDW (upper right). For a small K value in the strong coupling region, we have the KT transition with a central charge $c = 1$ and $K = 1/2$ (vertical purple segment). For a larger K value, weaker coupling, we have coexisting Ising CFT and LL with variable K, central charge $c = 1/2 + 1$ (vertical green segment).

The region around the red dot at $K = 15/8$ on the critical line in Fig. 2.4 is exactly what we showed earlier in Fig. 2.2, the multiversality classes. Therefore, we expect to see multiversality of charge density wave onset in a Luttinger liquid.

2.3 Lattice model and renormalization group

2.3.1 Microscopic lattice model

Now it's time for us to realize the field theory with a microscopic lattice model, and to see whether we could find evidence for the multiversality classes. We begin with the microscopic lattice Hamiltonian:

$$H = \sum_n (X_n X_{n+1} + Y_n Y_{n+1} + \Delta Z_n Z_{n+1}) + \sum_n (J\sigma_n^z \sigma_{n+1}^z + \sigma_n^x) + \lambda \sum_n Z_n \sigma_n^z, \qquad (2.6)$$

where X, Y, Z are Pauli-matrices corresponding to the spins in an XXZ chain. σ^x and σ^z are Pauli-matrices for a transverse-field Ising model (TFIM). λ is the coupling between the spins in the XXZ chain and in the TFIM, which is related to the coupling constant s in the field theory, as will be shown later.

The model has the following symmetries:

- $U(1)$ rotations generated by $Z_{tot} = \frac{1}{2}\sum_n Z_n$.
- π-rotation (particle-hole): $U_{ph} = \prod X_n \sigma_n^x$. This symmetry, in particular, guarantees half-filling $Z_{tot} = 0$.
- Translation T_x.
- Site reflection R_x.
- Time-reversal $\mathcal{T}$ (non-Kramers) - complex conjugation in the Z,σ^z basis.

Here the time-reversal symmetry does not create doubly degenerate states by the Kramers' theorem, because the total spin is not a half-integer.

We now pass to a low-energy description at small λ and for J close to 1 (the Ising

transition point in the TFIM).

$$L = L_{LL} + L_I + s a^{K-15/8} v_L \sin\theta\, \sigma, \tag{2.7}$$

$$L_{LL} = \frac{i}{2\pi}\partial_x\varphi\partial_\tau\theta + \frac{v_L}{2\pi}\left(K(\partial_x\varphi)^2 + \frac{1}{4K}(\partial_x\theta)^2\right). \tag{2.8}$$

Here L_I is the Ising CFT with velocity v_I, whose action we won't write explicitly. $\sigma(x)$ is the order parameter of the Ising CFT. s is a coupling constant, and a is the lattice spacing introduced to make s dimensionless. This is a more complete version of Eq. 2.1.

The correspondence between microscopic operators and effective fields is the following:

$$X_n + iY_n \propto (-1)^n e^{i\varphi}, \tag{2.9}$$

$$Z_n \sim -\frac{1}{2\pi}\partial_x\theta + (-1)^n A_Z a^K \sin\theta, \tag{2.10}$$

$$\sigma^z_n \sim (-1)^n A_\sigma a^{1/8}\sigma, \tag{2.11}$$

where A_Z and A_σ are constant parameters.

We will set the lattice spacing $a = 1$ in the following analysis. We normalize $e^{i\theta}$ and σ so that at $\lambda = 0$, when the XXZ chain and the TFIM are decoupled, there are

$$\langle e^{i\theta(x)} e^{-i\theta(0)}\rangle = \frac{1}{(\mathrm{x}^2 + v_L^2\tau^2)^K}, \tag{2.12}$$

$$\langle \sigma(x)\sigma(0)\rangle = \frac{1}{(\mathrm{x}^2 + v_I^2\tau^2)^{1/8}}. \tag{2.13}$$

For $\lambda = 0$, the various parameters in the microscopic model in Eq. 2.6 are [17], [18]:

$$-\Delta = \cos \pi\eta, \tag{2.14}$$

$$K = \frac{1}{2\eta}, \tag{2.15}$$

$$v_I = 2, \tag{2.16}$$

$$v_L = \frac{2 \sin \pi\eta}{1-\eta} \approx 2.02676, \tag{2.17}$$

$$A_\sigma \approx 0.80312, \tag{2.18}$$

$$A_z = \frac{4}{\pi} \left[\frac{\Gamma\left(\frac{\eta}{2-2\eta}\right)}{2\sqrt{\pi}\Gamma\left(\frac{1}{2-2\eta}\right)} \right]^{\frac{1}{2\eta}} \exp\left[\frac{1}{2} \int_0^\infty \frac{dt}{t} \left(\frac{\sinh((2\eta-1)t)}{\sinh \eta t \cosh((1-\eta)t)} - \frac{2\eta-1}{\eta} e^{-2t} \right) \right]$$

$$\approx 0.285118. \tag{2.19}$$

Here v_L and A_z are computed at the value of $\Delta = \Delta_c^0 \approx -0.669131$ corresponding to $K = 15/8$ (this value of K plays an important role as we discussed earlier in Sec. 2.2). Note that accidentally the two velocities v_I and v_L are very close to each other at this value of Δ. With this conventions we have the following relation between the coupling s in Eq. 2.8 and λ in the microscopic model in Eq. 2.6:

$$s = \frac{A_z A_\sigma}{v_L} \lambda \approx 0.11298\, \lambda, \tag{2.20}$$

where the constant of proportionality has been again evaluated in the last step at $K = 15/8$.

Symmetry	Field Theory	Lattice Model
$U(1)$	$\varphi \to \varphi + \alpha$	$(X_n, Y_n)^T \to U_\alpha (X_n, Y_n)^T$
U_{ph}	$\varphi \to -\varphi, \quad \theta \to -\theta, \quad \sigma \to -\sigma$	$Z_n \to -Z_n, \quad \sigma_n^z \to -\sigma_n^z, \quad S_n^+ \to S_n^-$
T_x	$\varphi \to \varphi + \pi, \quad \theta \to \theta + \pi, \quad \sigma \to -\sigma$	$n \to n+1$
R_x	$\theta \to -\theta + \pi, \quad x \to -x$	$n \to -n$
$\mathcal{T}$	$\varphi \to -\varphi, \quad i \to -i, \quad t \to -t$	$i \to -i, \quad t \to -t$

Table 2.1: The mapping between symmetries in the field theory and in the lattice model.

The symmetries act in the low energy theory as:

$$\begin{aligned} U(1): &\qquad \varphi \to \varphi + \alpha, \\ U_{ph}: &\qquad \varphi \to -\varphi, \quad \theta \to -\theta, \quad \sigma \to -\sigma, \\ T_x: &\qquad \varphi \to \varphi + \pi, \quad \theta \to \theta + \pi, \quad \sigma \to -\sigma, \\ R_x: &\qquad \varphi \to \varphi, \quad \theta \to -\theta + \pi, \quad \sigma \to \sigma, \quad \mathrm{x} \to -\mathrm{x}, \\ \mathcal{T}: &\qquad \varphi \to -\varphi, \quad \theta \to \theta, \quad \sigma \to \sigma, \quad t \to -t, \quad i \to -i. \end{aligned} \tag{2.21}$$

Here we gave the action of time-reversal symmetry in real time, where it is anti-unitary.

The mapping between the symmetries in the field theory and the ones in the lattice model is summarized in Table 2.1.

2.3.2 Renormalization group

For $K > 15/8$ ($\Delta < \Delta_c^0$) the interaction s in Eq. 2.8 is irrelevant and we expect the Ising and Luttinger liquid (LL) sectors to decouple at the Ising transition. However, on the ordered side of the Ising transition we expect the coupling s to generate a term:

$$L_{coupl} \approx s a^{K-15/8} v_L \langle \sigma \rangle \sin\theta \tag{2.22}$$

This term is relevant for $K < 2$, where we expect it to lead to gapping out of the Luttinger liquid. Thus, in the narrow range $15/8 < K < 2$ we expect a transition between a Luttinger

liquid and a fully gapped charge-density-wave (CDW) state to be governed by the decoupled LL+Ising theory, where the exponents of the LL sector are varying. We can say that the coupling s is dangerously irrelevant at this transition. Note that in terms of the bare parameter Δ this window corresponds to $-0.669131 < \Delta < -0.707107$ as $\lambda \to 0$, although the critical values of Δ defining the boundaries of this window will be renormalized at finite λ.

For $K > 2$ the perturbation in Eq. 2.22 is irrelevant even in the Ising ordered phase, so we expect that in that parameter regime the onset of CDW order does not immediately gap out the Luttinger liquid.

For $K < 15/8$ the coupling s in Eq. 2.8 is relevant. Although we are not analytically able to predict the fate of the flow $s \to \infty$, one possibility is that in this regime the CDW onset is described by a conventional KT transition.

$$L = \frac{i}{2\pi}\partial_x\varphi\partial_\tau\theta + \frac{v_L}{2\pi}\left(\tilde{K}(\partial_x\varphi)^2 + \frac{1}{4\tilde{K}}(\partial_x\theta)^2\right) + u\cos 2\theta \tag{2.23}$$

where $\tilde{K}$ is a renormalized Luttinger parameter. As is well-known the true infra-red value of the Luttinger parameter at the transition in this case is $\tilde{K} = 1/2$. The CDW onset here is again accompanied by gapping out of the Luttinger liquid.

Putting all of the above observations together, we obtain a schematic phase diagram in Fig. 2.4. We have not discussed the horizontal purple transition line yet, which separates the gapped CDW region from the CDW coexisting with the Luttinger liquid. Since translational symmetry is already broken in this region, the transition is expected to be of KT nature with physical $K' = 2$:

$$L = \frac{i}{2\pi}\partial_x\varphi\partial_\tau\theta + \frac{v_L}{2\pi}\left(K'(\partial_x\varphi)^2 + \frac{1}{4K'}(\partial_x\theta)^2\right) + v\sin\theta \tag{2.24}$$

All these analyses agree with the physics intuition described earlier in Sec. 2.2, where we had used the field theory as the starting point.

We now discuss the physics in the neighbourhood of the red point ($K = 15/8$) in Fig. 2.4 in more detail. In this region s becomes nearly marginal and we can perform an RG calculation. We will see that this RG is quite similar with to conventional KT RG, with the red point described by a decoupled LL + Ising theory ($c = 1 + 1/2$) with infra-red $K = 15/8$ up to logarithmically suppressed corrections. In the $\Delta > \Delta_c$ region where the transition (vertical purple segment line) is conjectured to be described by a $c = 1$ KT theory with Eq. 2.23, the cross-over length scale between $c = 1 + 1/2$ and $c = 1$ theories diverges as $\xi \sim \exp(C/\sqrt{\Delta - \Delta_c})$.

We note that this divergence of the cross-over length scale is exponentially fast. For a lattice system of size L, the smallest Δ difference it can resolve is $(\Delta - \Delta_c) \sim 1/(\log L)^2$. Within this Δ difference, everything probed by the finite-size lattice system is dominated by the red point ($K = 15/8$). If we want to see the existence of a dangerously irrelevant window, $-0.669131 < \Delta < -0.707107$, we might have to go to a very large system size.

Moreover, after renormalized by finite λ, the range of the dangerously irrelevant window shrinks. We need even a larger system size for a large λ value because we want to probe into a smaller window. On the other hand, if λ is small, s is even smaller by Eq. 2.20. The scaling dimension of s tells us that we need a system size L such that $(s \cdot L^{15/8-K} \sim 1)$ in order to truly have a strong coupling. Therefore, it is unavoidable to simulate a large system in order to see numerical evidence of the muliversality classes in this model.

Here we show a more solid analysis from RG. We will ignore the velocity anisotropy between the LL and Ising sectors, setting $v_L = v_I$. This velocity anisotropy does not qualitatively alter the physics (even though the two velocities do not sync in the infra-red). We thus set $v_L = v_I = 1$ for now. One RG equation is

$$\frac{ds}{d\ell} = \left(\frac{15}{8} - K\right) s. \tag{2.25}$$

Here ℓ is the RG scale: $x \sim e^{\ell}$. The other RG equation can be obtained by doing perturbation

theory in s to second order, using the OPE:

$$\sigma(x)\sigma(0) \sim \frac{1}{x^{1/4}} + \dots \tag{2.26}$$

$$e^{i\theta(x)}e^{-i\theta(0)} \sim \frac{1}{x^{2K}}\left(1 - \frac{1}{4}x^2(\partial_\mu\theta)^2 + \dots\right) \tag{2.27}$$

Here, we've kept only Lorentz singlet operators in the OPE. We've also dropped the ϵ term in the $\sigma \times \sigma$ OPE: this term is assumed to have been fine-tuned to zero in the action by tuning J to its critical value J_c in the microscopic model. Performing second order perturbation theory in s:

$$\delta S = -\frac{s^2}{2}a^{2(K-15/8)}\int d^2x_1 d^2x_2 \sin\theta(x_1)\sigma(x_1)\sin\theta(x_2)\sigma(x_2) \tag{2.28}$$

$$\to \frac{s^2}{2}a^{2(K-15/8)}\frac{1}{2}\cdot\frac{1}{4}\int d^2x_1 d^2x_2 (x_1 - x_2)^{7/4-2K}(\partial_\mu\theta(x_2))^2, \tag{2.29}$$

where we've used the OPE in the last step. From this, near $K = 15/8$,

$$\frac{dK}{d\ell} = -\pi^2 K^2 s^2 \approx -\left(\frac{15\pi}{8}\right)^2 s^2. \tag{2.30}$$

We can define re-scaled variables

$$u = K - \frac{15}{8}, \quad v = \frac{15\pi}{8}s, \tag{2.31}$$

so that

$$\frac{dv}{d\ell} = -uv, \quad \frac{du}{d\ell} = -v^2, \tag{2.32}$$

which are the standard KT-like RG equations. Without loss of generality, we take $v > 0$. The transition corresponds to the line $u = v$, along which $u(\ell) = v(\ell) = \frac{u}{1+u\ell}$. Thus, at the transition K flows logarithmically to $15/8$ — this is the red point in Fig. 2.4. Note that the value of bare K at which the red point sits is not precisely $15/8$, but rather $K_c^0 \approx \frac{15}{8}(1 + \pi s)$

for $s \to 0$. If we substitute $\lambda = 0.3$, i.e. $s \approx 0.0339$, we obtain $K^0 \approx 2.07$, which is already larger than $K^0 = 2$ corresponding to the start of the horizontal purple line in Fig. 2.4 in the limit $\lambda = 0$. Thus, it is not clear if perturbation theory in λ is applicable at $\lambda = 0.3$.

For $K^0 < K^0_c$, we can estimate the cross-over length $\xi = e^\ell$ between the $c = 1 + 1/2$ regime in the UV and the $c = 1$ regime in the IR. Integrating our RG equations, we find that u and v diverge at

$$\begin{aligned} \ell &= \frac{1}{\sqrt{v^2 - u^2}} \left(\frac{\pi}{2} + \tan^{-1} \left(\frac{u}{\sqrt{v^2 - u^2}} \right) \right), \quad |u| < v \\ \ell &= \frac{1}{2\sqrt{u^2 - v^2}} \log \frac{|u| + \sqrt{u^2 - v^2}}{|u| - \sqrt{u^2 - v^2}}, \quad u < -v \end{aligned} \tag{2.33}$$

For instance, at $\lambda = 0.3$, plugging in $\Delta = -0.65$ gives $u = -0.055$ and $v = 0.200$, so that $\ell = 6.73$, i.e. $\xi \sim 830$. For $\Delta = -0.5$ we similarly estimate $\ell = 3.92$ and $\xi \sim 50$. Thus, one might need to go to fairly large system sizes in order to see the true infra-red behavior even for Δ some distance from the true critical value. This agrees with the earlier discussion.

2.4 Numerical simulation and data analysis

We simulate a 1D spin chain with the following Hamiltonian using the density matrix renormalization group (DMRG) algorithm [19]:

$$H = \sum_n (X_n X_{n+1} + Y_n Y_{n+1} + \Delta Z_n Z_{n+1}) + \sum_n (J \sigma^z_n \sigma^z_{n+1} + \sigma^x_n) + \lambda \sum_n Z_n \sigma^z_n. \tag{2.34}$$

We set the Hamiltonian on a finite-size lattice. A series of lattices sizes, as well as different boundary conditions, are simulated in order to study the level spectroscopy and the scaling law of operators. We use the TeNPy Python library to perform DMRG calculations to get various physics properties of the system [20]. For review of DMRG algorithm, see Ref. [21], [22].

In Section 2.4.1, we focus on the level spectroscopy close to the KT transition lines in

order to locate the purple critical lines in Fig. 2.4. We collect the data of the ground state energy E_0, the excitation energy E_{exct} in the $Z_{tot} = \frac{1}{2}\sum_n Z_n = 0$ sector, and the excitation energy E_{s1} and E_{s2} in the $Z_{tot} = 1$ and 2 sectors, respectively.

In Section 2.4.2, we focus on the data collapsing method on observables close to the Ising transition in order to locate the green critical line in Fig. 2.4. We collect the data of the entanglement entropy profile. There we perform the data collapsing method by eye-viewing the best overlapping of curves. Explorations on performing data collapsing with statistical methods are discussed in Chapter 3.

In Section 2.4.3, we focus on the scaling laws of different correlation functions. We can use their scaling dimensions to extract the Luttinger parameter K for different points on the phase diagram. We can also extract the information for the Ising order parameter.

In Section 2.4.4, we summarize all the numerical results in the earlier sections on a numerical phase diagram.

The data we collect come from two experiments. In both experiments, we set the parameter in the Hamiltonian Eq. 2.34, $\lambda = 1$. The DMRG is performed with gradually increasing bond dimensions $\chi \in \{100, 200, 400, 800, 1200\}$ until convergence within $\epsilon = 10^{-5}$ energy error. In the first experiment, we study an open-boundary chain with length $L \in \{24, 32, 64, 128, 256, 384\}$. The other parameters are grid sampled from ranges $\Delta \in [-0.81, -1.0]$ and $J \in [0.91, 1.1]$. In the second experiment, we study a twisted-periodic-boundary chain with length $L \in \{10, 20, 30, 40, 50, 60\}$. The other parameters are grid sampled from ranges $\Delta \in [-0.86, -0.95]$ and $J \in [0.98, 1.1]$.

2.4.1 Level spectroscopy

The KT transition has exponentially diverging cross-over length when we are close to the critical line. Therefore, it is difficult to precisely locate the KT transition line by studying the scaling law of operators. However, we can seek help from the level spectroscopy method. Due to the emergent SU(2) symmetry at the KT transition point, E_{exct} and E_{s1} will be

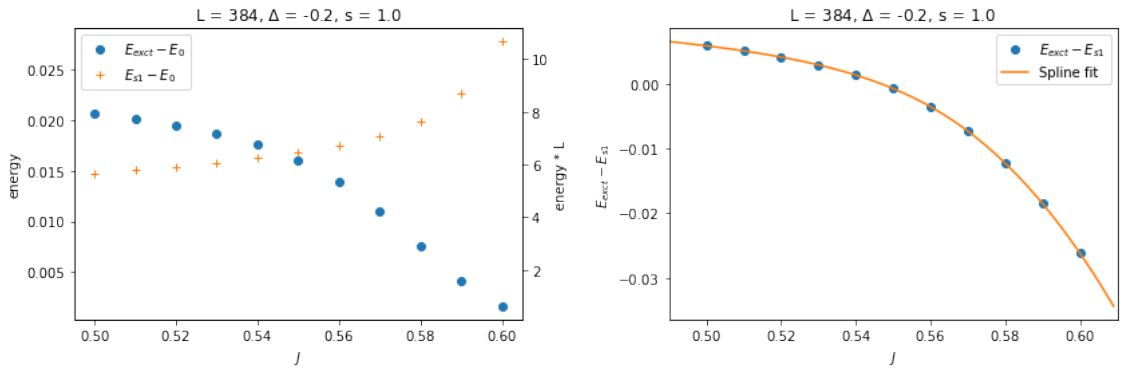

Figure 2.5: (Left) Level spectroscopy for $K = 1/2$ KT transition. Blue dots are the first excited states in the $Z_{tot} = 0$ sector, and orange crosses are the lowest-energy states in the $Z_{tot} = 1$ sector. A level crossing is observed at $J \approx 0.55$. (Right) Using cubic spline interpolation to find the crossing point, which is $J_{cross} = 0.5468$.

degenerate at the transition [23], [24]. Therefore, the KT transition point can be precisely located by the level crossing between the first excited states in the $Z_{tot} = 0$ and 1 sectors [12].

To locate the conjectured $K = 1/2$ KT transition line shown as the vertical purple segment in Fig. 2.4, we perform the level spectroscopy for a scan on the J parameter direction. We first fix the parameter λ, Δ, and the system size L. We sample some values of J and do DMRG to get the corresponding energy levels E_0, E_{exct}, and E_{s1}. For each energy level, the DMRG algorithm uses increasing bond dimensions until the final energy is stable within a threshold. We extract the level crossing position J_{cross} between the levels of E_{exct} and of E_{s1} by calculating the root of a cubic spline interpolation on $E_{exct} - E_{s1}$. An example with $\Delta = -0.2, \lambda = 1.0, L = 384$ is shown in Fig. 2.5.

We then change the system size L and calculate the corresponding J_{cross} for each L. We do an extrapolation to estimate the level crossing point when $L \to \infty$. This extrapolated level crossing point is the KT transition point for an infinite system. Reference [12] suggests $J_{cross}(L) \sim J^{\infty}_{cross} + const.\frac{1}{L^2}$. A recent paper [13] suggests $J_{cross}(L) \sim J^{\infty}_{cross} + const.\frac{1}{\alpha(L)L^2}$, where $\alpha(L)$ is the slope of the energy difference $E_{exct} - E_{s1}$ vs. J at the spline root. The authors in [13] derives $\alpha(L) \sim \log L$ from RG analysis. In our experiment, we directly measure the numerical value of $\alpha(L)$ based on the slope of the $E_{exct} - E_{s1}$ vs. J curve.

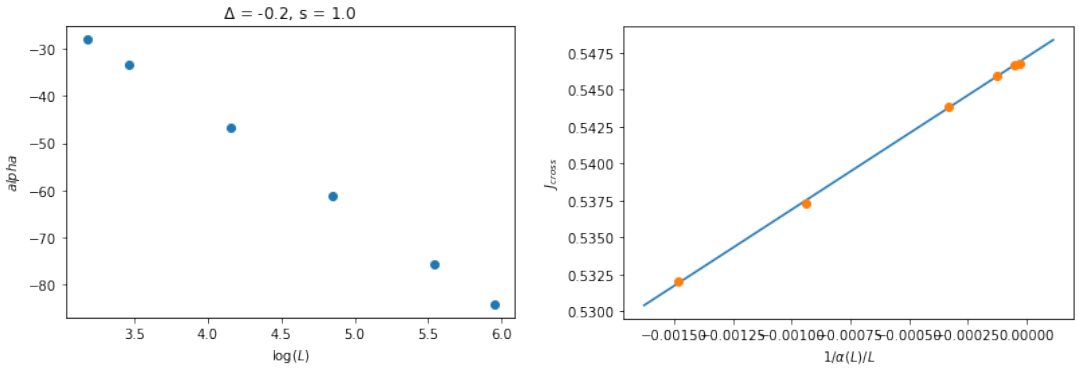

Figure 2.6: Scaling of the crossing point J_{cross} with the system size L for $K = 1/2$ KT transition. (Left) $\alpha(L)$ vs. $\log L$, which agrees nicely with the RG analysis result $\alpha(L) \sim \log L$. (Right) J_{cross} vs. $\frac{1}{\alpha(L)L}$, which fits nicely to a straight line and implies the existence of a scaling dimension 3 operator in the theory. The fitted straight line extrapolates to $J^{\infty}_{cross} = 0.5472$.

However, in our experiment we find strong numerical evidence which instead suggests the scaling $J_{cross}(L) \sim J^{\infty}_{cross} + const.\frac{1}{\alpha(L)L}$ (see Fig. 2.6), implying the existence of a scaling dimension 3 operator in the theory. We are not sure what is the origin of this operator. We use this modified scaling relation to extrapolate the $K = 1/2$ KT critical point J^{∞}_{cross} for $L \to \infty$.

To locate the $K = 2$ KT transition (horizontal purple line in Fig. 2.4), we need to change the direction of scanning in the parameter space. This time we fix J, and measure the change of level spectrum with Δ. Note that for the $K = 2$ KT transition, the emergent SU(2) symmetry does not imply the level crossing between E_{exct} and E_{s1}. Instead, the lowest-energy state in the boundary-twisted $Z_{tot} = 0$ sector, E_{twist}, and the lowest-energy state in the $Z_{tot} = 2$ sector, E_{s2}, degenerate at the $K = 2$ KT transition point. Therefore, we have to perform DMRG on a periodic boundary condition, which limits the system size we could achieve. Nevertheless, we find the scaling between the crossing point Δ_{cross} with the system size L as $\Delta_{cross}(L) \sim \Delta^{\infty}_{cross} + const.\frac{1}{\alpha(L)L}$, also implying the existence of an unknown scaling dimension 3 operator. We use this modified scaling relation to extrapolate the $K = 2$ KT critical point Δ^{∞}_{cross} for $L \to \infty$.

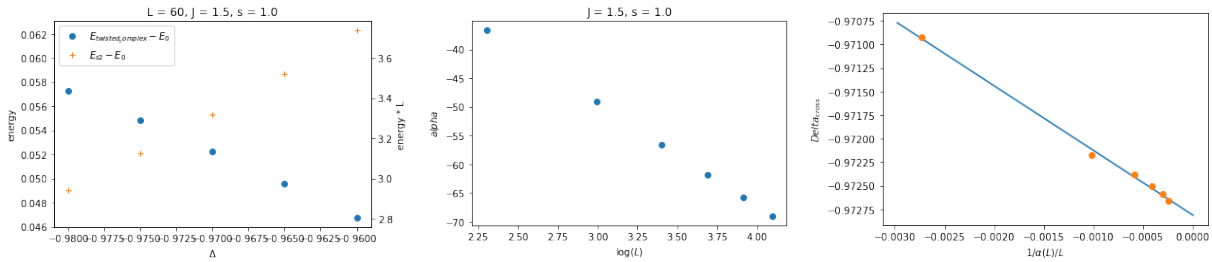

Figure 2.7: (Left) Level spectroscopy for $K = 2$ KT transition. Blue dots are the lowest-energy states in the boundary-twisted $Z_{tot} = 0$ sector, and orange crosses are the lowest-energy states in the $Z_{tot} = 2$ sector. A level crossing is observed at $\Delta \approx -0.972$. (Mid) $\alpha(L)$ vs. $\log L$, which agrees nicely with the RG analysis result $\alpha(L) \sim \log L$. (Right) Scaling of the crossing point Δ_{cross} with the system size L for $K = 2$ KT transition. Δ_{cross} vs. $\frac{1}{\alpha(L)L}$ fits nicely to a straight line and implies the existence of a scaling dimension 3 operator in the theory. The fitted straight line extrapolates to $\Delta^{\infty}_{cross} = -0.9728$.

2.4.2 Data collapsing

In the KT transition, the length scale diverges exponentially when getting closer to the critical line, which makes it difficult to apply scaling methods. In the Ising transition, however, the length scale acts as a power law. Therefore, we can apply data collapsing and scaling methods to locate the Ising transition line, which is shown as the vertical green segment in Fig. 2.4.

At the 2D Ising critical point, the critical exponent of the correlation length $\nu = 1$ [15]. This exponent tells us that close to the critical point, physical observables have a universal behavior after the rescaling $(J - J_{crit}) \to (J - J_{crit}) \cdot L$, where J is the parameter tuning the Ising transition, J_{crit} is the critical parameter, L is the system size.

Here we look at the entanglement entropy between the left half and the right half of an open chain, i.e. the value of the entanglement entropy profile $S(L/2)$ at the middle point of the chain. After subtracting the finite-size effect $\frac{c}{6} \log L$ from the entanglement entropy, the remaining observable $S(L/2) - \frac{c}{6} \log L$ should have a scaling behavior around the critical point [25]. Here $c = 1/2 + 1 = 3/2$ is the central charge of the coexisting Ising CFT and Luttinger liquid.

In Figure 2.8, we show an example of the data collapsing for the Ising transition at

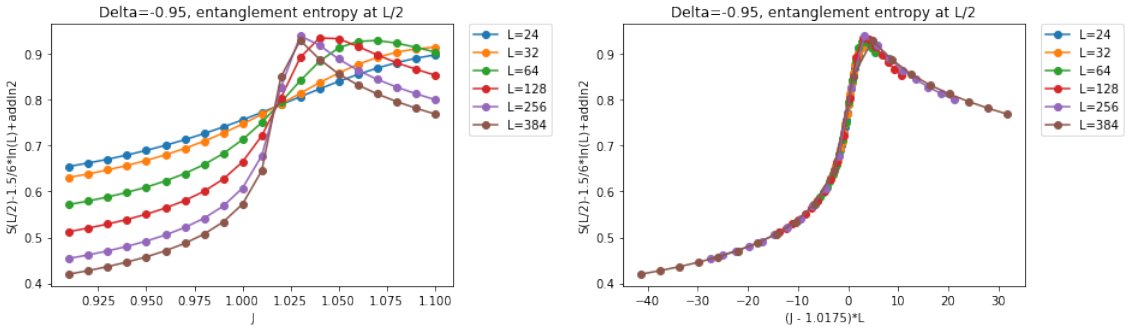

Figure 2.8: Scaling law of entanglement entropy at Ising critical point. (Left) We plot $S(L/2) - \frac{c}{6}\log L$ vs. J for different system size L. We can see that curves for different L intersect at the critical J value. (Right) We extract $J_{crit} = 1.0175$ from the left figure. We plot $S(L/2) - \frac{c}{6}\log L$ vs. $(J - J_{crit}) \cdot L$. We can see that the curves for different L collapse onto a universal function.

$\Delta = -0.95$. We fix the value of Δ parameter, scan a line in the parameter space by changing J parameter, collect the entanglement entropy $S(L/2)$ from the DMRG output, and repeat this process for various system size L. On the left figure, we can see that the curves for different L values intersect at one point. This point with the parameter value J_{crit} is the critical point we would like to locate, and use as the center of the scaling method.

Here we read the the parameter value J_{crit} at the intersection point by eye. We can also perform a more systematic analysis to extract the most likely value of J_{crit}. In Chapter 3, we will apply statistical methods and criteria to determine the best value of the critical point using scaling and data collapsing.

On the right in Fig. 2.8, we rescale the x-axis to $(J - J_{crit}) \cdot L$. We can see that the data points on different L curves collapse onto one universal function. This universal function agrees with the entanglement entropy of an Ising CFT [25].

We repeat this scanning on lines in the parameter space specified by different Δ values, until we reach the point where the entanglement entropy data points cannot be collapsed well enough. For each Δ value we are able to perform the data collapsing, we locate the corresponding J_{crit}. This is how we locate the Ising transition line (vertical green segment in Fig. 2.4) in the real Δ-J parameter space.

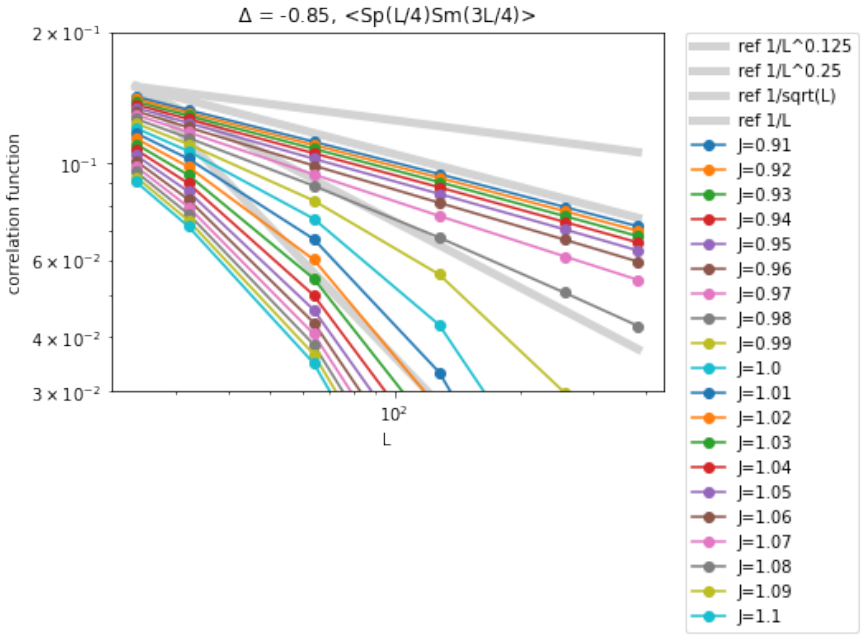

Figure 2.9: We use the operator scaling law in Eq. 2.35 to measure the Luttinger parameter K.

2.4.3 Operator scaling

As we see from the analysis in Sec. 2.2, the Luttinger parameter K plays an important role in the relevancy of the coupling, and thus leads to different phases. Therefore, we would like to measure the value of K for different points in the real Δ-J parameter space, in order to help us visualize the phases and the phase transition lines. In particular, we would like to confirm that on the horizontal purple line in Fig. 2.4, we indeed have $K = 2$; on the vertical purple segment in Fig. 2.4, we indeed have $\tilde{K} = 1/2$; hopefully, we could resolve the multiversality between $15/8 < K < 2$.

The way we measures the K value is as follows. We know that the scaling dimension of the operator $[e^{\pm i\varphi}] = 1/(4K)$ [16], where φ is the Luttinger variable in Eq. 2.8. From correspondence between the lattice operator and the field variable in Eq. 2.9, we know the correlation function

$$\langle S^+(L/4)S^-(3L/4)\rangle \sim \frac{1}{L^{1/(2K)}}, \tag{2.35}$$

where $S^{\pm} = X \pm iY \propto e^{\pm i\varphi}$. The location $L/4$ and $3L/4$ are chosen to avoid the boundary effect on an open chain.

In Figure 2.9, we show the scaling between the correlation function $\langle S^{+}(L/4)S^{-}(3L/4)\rangle$ and the system size L, for a fixed $\Delta = -0.85$ and various J values. For a small J value, e.g. $J = 0.91$ (topmost blue line), the system is deep in the Ising disorder phase, coexisting with Luttinger liquid. The Luttinger parameter can be read out from the slope of the line in the log-log plot. For example, for $J = 0.91$ the slope is $-1/(2K) \approx -0.25$, and thus $K \approx 2$.

As J increases, the slope of the lines slightly increases, corresponding to a slight decrease in K. However, we can see in Fig. 2.9 that going from $J = 0.98$ (grey) to $J = 0.99$ (yellow), the correlation function suddenly drops. For $J \geq 0.99$ (yellow line and lines below), the correlation functions decrease faster than any power law. Actually, the correlation functions decrease exponentially, which shows that the system is gapped. Therefore, we see a transition from a gapless (Ising disorder + LL) phase to a gapped Ising-order CDW insulator phase.

We can also apply the operator scaling law to direcly measure the Ising order. We know that the Ising spins σ^z have a long-range order in the ordered phase, and have decaying correlation function in the disordered phase [15]. Therefore, we can determine the Ising phases by seeing the behavior of the correlation function $\langle \sigma^z(L/4)\sigma^z(3L/4)\rangle$ when $L \to \infty$. Again, we choose $L/4$ and $3L/4$ to avoid the boundary effect.

In Figure 2.10, we show the relation between the correlation function $\langle \sigma^z(L/4)\sigma^z(3L/4)\rangle$ and the system size L, for a fixed $\Delta = -0.95$ and various J values. For a large J value, e.g. $J = 1.1$ (topmost light blue line), the system is deep in the Ising ordered phase. We can see that the correlation function converges to a constant value when $L \to \infty$, i.e. showing a long-range order in σ^z.

When J decreases, the constant value decreases, and when going from $J = 1.02$ (orange) to $J = 1.01$ (deep blue), the correlation function suddenly converges to zero. Therefore, we see a transition from an Ising ordered phase to an Ising disordered phase. At the value $\Delta = -0.95$, the Luttinger sector decouples with the Ising sector, so it is a coexistence with

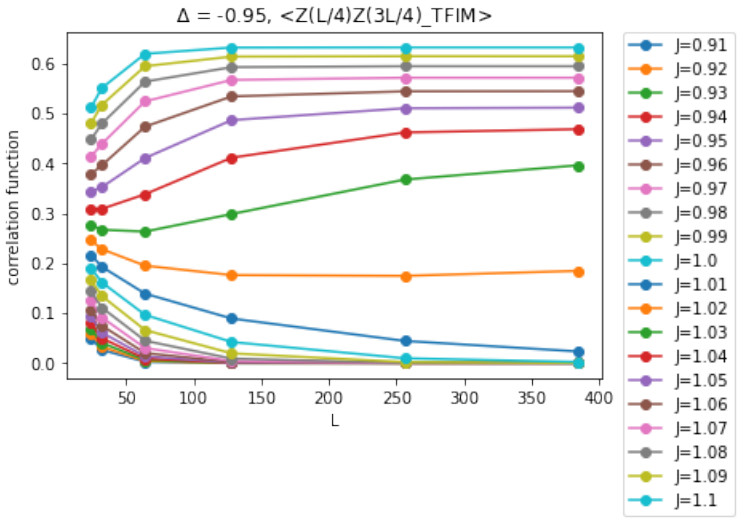

Figure 2.10: We use the operator correlation function to measure the Ising order.

Luttinger liquid in both phases.

2.4.4 Phase diagram

Here we summarize all the numerical results in the earlier sections into one phase diagram. In Figure 2.11, we show a plane in the parameter space specified by $\lambda = 1$, $\Delta \in [-0.81, -1.0]$, and $J \in [0.91, 1.1]$. This plane contains data points where we do our numerical experiments.

For each point of (J, Δ), we measure the Luttinger parameter K using the operator scaling method mentioned in Sec. 2.4.3, shown as the colored circles. The colors of the circles represent the value of K, and the sizes of the circles represent the quality of a power-law fit in the correlation function. The small circles on the upper right corner of the diagram mean the system is gapped and has exponentially decaying correlation functions. In the region where the correlation functions show a reasonable power law (i.e. large-sized circles), we observe K values ranging from 0.5 to 3.

We also measure the Ising order using the method mentioned in Sec. 2.4.3. Shaded areas in the diagram have a long-range order in the Ising spins, and thus marks out the (Ising order+LL) phase in the bottom right and the Ising-order CDW insulator phase in the upper right. The unshaded areas on the left shows the (Ising disorder+LL) phase.

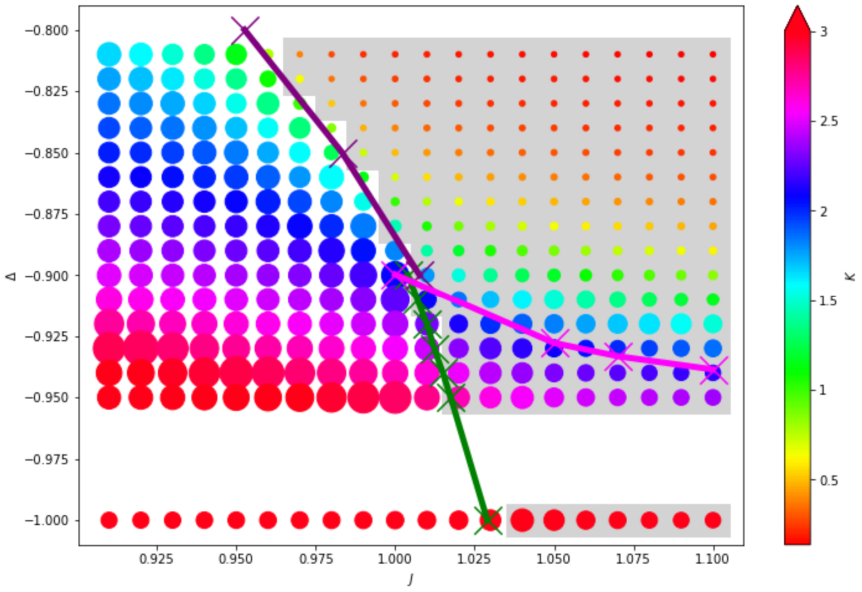

Figure 2.11: Numerical measured phase diagram for the model in Eq. 2.6. The $-1.0 < \Delta < -0.95$ region has several broken data points due to the instability of the DMRG, so we remove the points in the range.

We observed three boundaries in our phase diagram. The green line between the the left (Ising disorder+LL) and bottom right (Ising order+LL) is an Ising CFT, located by the data collapsing method mentioned in Sec. 2.4.2. the dark purple line between the the left (Ising disorder+LL) and upper right (CDW insulator) is a $\tilde{K} = 1/2$ KT transition, located by the level spectroscopy method on an open chain mentioned in Sec. 2.4.1. The light purple line between the upper right (CDW insulator) and bottom right (Ising order+LL) is a $K = 2$ KT transition, located by the level spectroscopy method on a twisted-boundary chain mentioned in Sec. 2.4.1. These three lines correspond to the same lines in our conjectured phase diagram Fig. 2.4 from the theory. We note that the green line and the dark purple line match well with the boundary of the shaded area showing the onset of Ising order. The dark purple line from its bottom to top goes from $K \approx 2$ to $1/2$. The light purple line matches the boundary between small circles (exponentially decaying correlation function, i.e. gapped) and large circles (power-law correlation function, i.e. gapless). Moreover, the light purple line sits nicely on $K \approx 2$.

We note that the interesting $15/8 < K < 2$ region is difficult for us to resolve in this

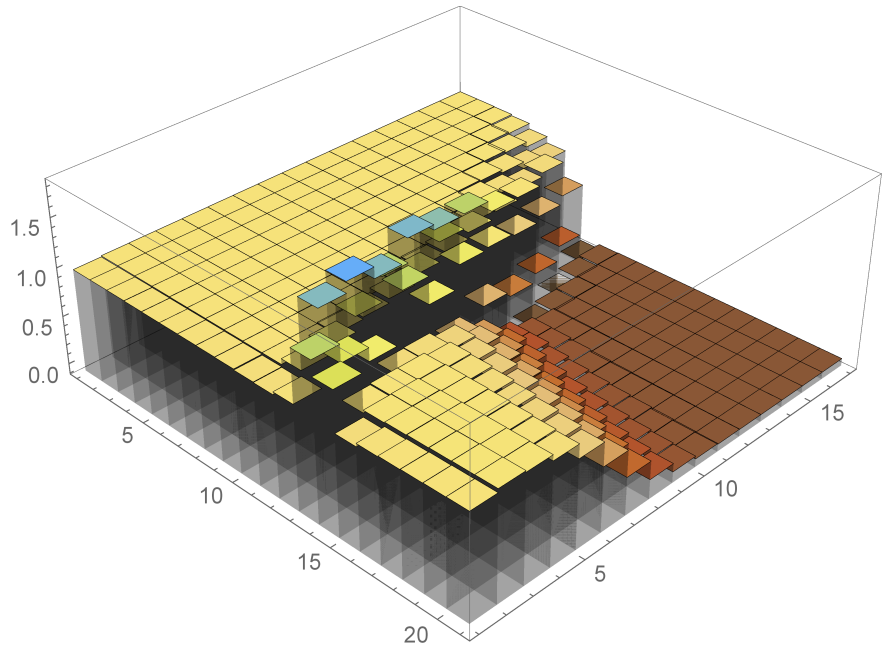

Figure 2.12: Numerical measured central charge in the parameter plane. The grids one-to-one map to the circles in Fig. 2.11.

numerical phase diagram. Although we have difficulty to nail down the small Ising segment marking multiversality in the phase diagram in this model, nevertheless we did not see a first order transition, and we did see a $\tilde{K} = 1/2$ KT transition. Also, we do not recognize a field theory which supports a multicritical point that splits the phase diagram into the these three classes of phase transitions: $\tilde{K} = 1/2$ KT, $K = 2$ KT, and (Ising CFT+LL). Therefore, our numerical results are consistent with the field theory described in Sec. 2.2 which shows the multiversality classes.

In Figure 2.12, we show the central charge measured numerically from the entanglement entropy profile along an open chain. Each grid in the figure corresponds to a (J, Δ) data point, and maps to a circle in Fig. 2.11. The height and color represent the value of the measured central charge c. We can clearly see a gapped phase with $c = 0$ (brown platform) in the right corner in Fig. 2.12, which maps to the upper right corner in Fig. 2.11. The yellow platform with $c = 1$ in Fig. 2.12 shows the Luttinger liquid. The drop from the yellow $c = 1$ platform to the $c = 0$ brown platform displays the KT transition from LL to CDW insulator. The ridge of $c > 1$ on the yellow platform shows the Ising CFT, which contributes additional

1/2 central charge. It is difficult for us to tell convincingly that the ridge extends into the brown platform: we need to perform scaling analysis with larger system sizes in order to see the clear evidence for the multiversality classes.

2.5 Summary and discussion

We described a 1D quantum field theory in which multiversality could be realized in a phase transition from a Luttinger liquid to a charge density wave insulator. The multiversality included a part of phase transition described by KT, and another part by Ising CFT. We constructed a concrete microscopic lattice model which had the corresponding low-energy effective field theory. We performed DMRG simulations on the 1D lattice model with a variety of parameters, system sizes, and boundary conditions. We measureed physical observables such as energy levels, correlation functions, and entanglement entropy profiles. We applied various numerical data analysis methods, including level spectroscopy, data collapsing, and operator scaling, to probe different aspects of the model. We summarized the information into a numerical phase diagram, and displayed consistent results. We saw no evidence of a first order phase transition, and we indeed saw the conjectured $\tilde{K} = 1/2$ KT transition in the strong coupling region.

We recently realized that multiversality was also observed in generalized 2D classical XY models [26]. Their 2D classical theory and our 1+1D quantum theory are orbifolds of each other. The authors in [26] also reported no evidence of a first order transition in the model.

The data collapsing method we applied in Sec. 2.4.2 was performed in a traditional way, where we plotted the curves and observed the center of the scaling transformation by eye. We could make the data collapsing method more systematic by introducing statistical data analysis tools, such as the smoothing spline method and the maximum likelihood estimation (MLE). This will be the main topic of our next chapter.

Chapter 3

Find Critical Points with Smoothing Spline Method

3.1 Introduction

The concept of universality has been an essential aspect of physics for many decades, particularly in the field of statistical mechanics and condensed matter physics. Universality refers to the notion that certain physical systems exhibit similar behavior, despite differences in their microscopic details. With powerful theoretical frameworks, such as the renormalization group, people can study such systems and understand their universal properties. These theoretical frameworks are used to describe the behavior of a system as one changes the length or energy scale at which it is probed. This idea leads to one of the most widely used applications of universality – the finite size scaling method.

In particular, in the vicinity of a critical point, systems of different sizes behave the same way up to a scaling factor. Moreover, experimental data collected under different system sizes exhibit similar curves. By applying finite size scaling, one can make all the curves coincide onto a universal functional form. This method is called data collapsing, and can be used to extract important physical quantities such as the critical points and critical exponents.

For example, consider the Ising model

$$H(\sigma) = -J \sum_{<ij>} \sigma_i \sigma_j$$

where i, j are sites on a 2-dimensional square lattice, and on each site i there is an assigned integer $\sigma_i = \pm 1$, usually called a "spin". $< ij >$ denotes all nearest-neighbor pairs of sites in the lattice. In a configuration of spins σ, for each nearest-neighbor pair (σ_i, σ_j), if there is $\sigma_i = \sigma_j$, this parallel pair of spins contributes $-J$ energy to the Hamiltonian $H(\sigma)$; on the other hand if $\sigma_i = -\sigma_j$, this opposite pair contributes $+J$. The probability of a configuration σ occurring is proportional to $e^{-H(\sigma)}$, where lower-energy configurations have larger probability of occurrence. In particular, a parallel pair is e^{2J} more likely of occurring than an opposite pair.

One might naturally think that the most probable configuration would be all the spins being in parallel. However, this is not the most "typical" configuration. For example, if only one spin is flipped, then there will be four opposite pairs generated. The probability of a single-spin-flipped configuration is e^{-8J} comparing to the probability of an all-spin-parallel configuration. There are only two all-spin-parallel configurations, e.g. all $+1$ or all -1. However, there are $\sim 2L^2$ number of single-spin-flipped configurations, where L is the size of the square lattice. For a significantly large system size L, the single-spin-flipped configurations dominate the all-spin-parallel configurations in the samples.

Therefore, for the most typical configuration, there is a balance between the probability of occurrence and the possible number of configurations. This is also called energy versus entropy in the language of physics.

Interestingly, there is a phase transition in the Ising model. When J is large, the spins still prefer more ordered configurations, and the sum of spins in the most typical configuration is non-zero. When J is small, however, disordered configurations dominate in the samples, and thus the sum of spins in the most typical configuration is zero. There is a critical point J_0

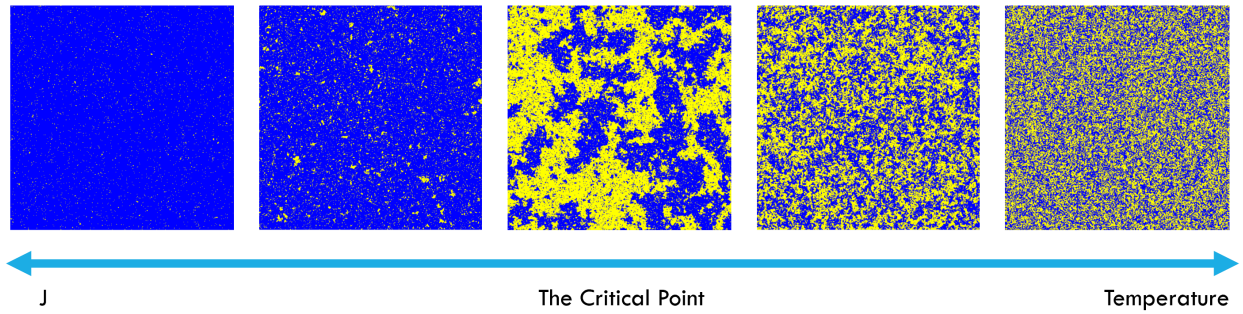

Figure 3.1: Simulation of the Ising model using the simulator in [27]. Here blue and yellow represent ± 1. To the left of the critical point, $J > J_0$, the most typical configuration has a non-zero sum of spins. This sum decreases as J approaches the critical point J_0. When $J \leq J_0$, the sum of spins in the most typical configuration becomes zero. In physics, $1/J$ is proportional to the temperature of the system. A "cold" (large J) system is more ordered, and a "hot" (small J) system is more disordered.

between these two phases. Figure 3.1 demonstrates how the parameter J affects the typical configurations in the Ising model. In physics, $1/J$ is proportional to the temperature of the system.

Using a more statistical language, we consider the distribution of the sum of spins of the configurations. In an ordered phase, this distribution is double peaked at two opposite values. In a disordered phase, this distribution is single peaked at zero. The critical point J_0 is the parameter when the single peak at zero starts to split. This phase transition is one example of spontaneous symmetry breaking in physics.

In the middle panel of Fig. 3.1, we see that at the critical point J_0, the most typical configuration shows a fractal behavior: The figure is self-similar to a crop of itself. There is also such similarity close to the critical point. In Fig. 3.2, we show configurations at the critical point, at a mid-high temperature, and at a very high temperature. We also show the configurations at two scales. We see that the large-size critical-point configuration is similar to the small-size critical-point configuration, and the large-size mid-temperature configuration is similar to the small-size high-temperature configuration. Therefore, we have the finite size scaling relation that a change of the temperature in terms of $(J - J_0)$ is equivalent to a change of the system size L.

In the Ising universality class, systems with the same value of $(J-J_0)\cdot L$ behave similarly. Therefore, physical observable y in an experiment can be described by a uni-variate function $y = f((J - J_0) \cdot L)$. In Fig. 3.3, we show data in a real numerical experiment, where the observable y is the entanglement entropy S. Regarding the $y \sim J$ plot, for each L value there is a curve, and all curves cross at the critical point J_0. After transforming the horizontal axis into $(J - J_0) \cdot L$ with the correct J_0 value, all curves coincide and exhibit a universal functional form. More generally, we would like to solve the following problem. Given data (x, y, L), we want to find the best x_0 value such that $y = f((x - x_0) \cdot L)$ with a smooth function $f(\cdot)$.

In the literature, researchers often perform this process manually: deriving a theory which predicts the existence of a crossing point, fine sampling data points around the crossing point, tuning parameters for best collapsing data onto a single curve. If this process can be automated with the help of statistical methods, researchers can produce results faster, requiring fewer data, and having a quantitative goodness-of-fit test.

However, the universal function at criticality, i.e. the functional form of the curve onto which data collapse, is often hard to be calculated analytically. Therefore, non-parametric fitting methods have to be applied. Common non-parametric fitting methods include splines [28], [29], the Gaussian process [30], [31], the kernel ridge regression [32], and neural networks [33].

In this chapter, we apply the smoothing spline method [28] and the corresponding R package [29] on the numerical data collected in Sec. 2.4. The data includes measurements of the entanglement entropy S under different system sizes L and parameters J. With the renormalization group analysis, one expects a universal relation $S = f((J - J_0) \cdot L)$, where $f(\cdot)$ is a uni-variate function on which different curves of $S \sim J$ will collapse, and J_0 is the critical point that we can tune to make the best data collapsing. An example of the data is shown in Figure 3.3.

We use two different approaches with the smoothing spline on finding the critical points.

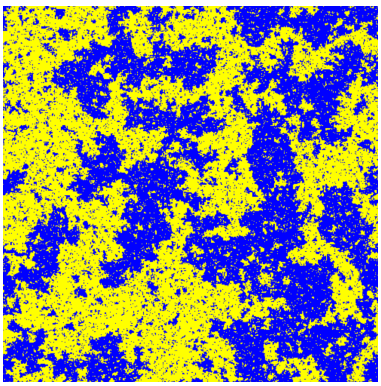

(a) 500×500. Critical point.

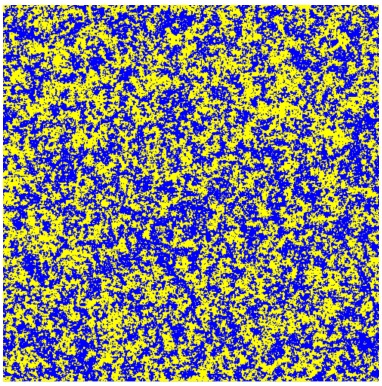

(b) 500×500. Mid temp.

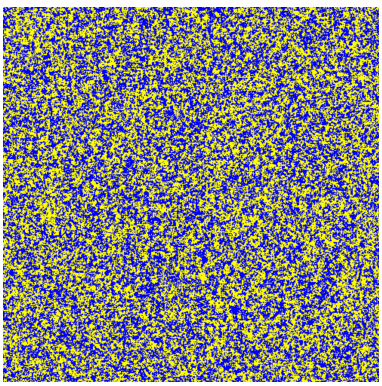

(c) 500×500. High temp.

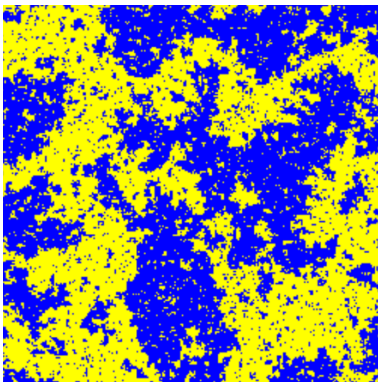

(d) 250×250. Critical point.

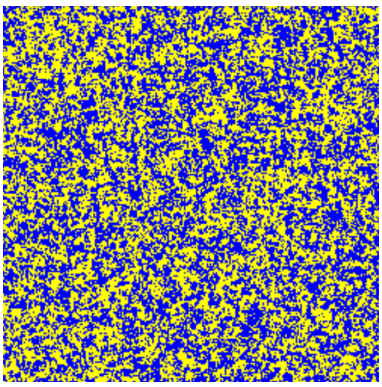

(e) 250×250. High temp.

Figure 3.2: Simulation of the Ising model using [27]. (a-c) are sampled with a system size 500×500. (a) is sampled at the critical point J_0. (b) is sampled at a medium distance $(J - J_0)$ to the critical point, while (c) is sampled at a further distance. (d) is the upper-right crop of (a), and (e) is the upper-left crop of (c). Note the similarity between (a) and (d), as well as the similarity between (b) and (e). These similarities demonstrate the finite size scaling in the vicinity of a critical point.

In our first method, we perform smoothing spline regression on each curve and compare the mean square differences between pairs of curves. In the second method, we perform smoothing spline regression on all transformed data together, and use the Bayesian Information Criterion (BIC) to determine the value and the uncertainty of the critical point J_0. In Section 3.2, we will introduce these two methods in details. In Section 3.3, we will show our data and results. We will discuss the pros and cons of the two methods in Section 3.4.

3.2 Methods

We follow the tutorial of using the smoothing spline method with the ss function in the npreg package in R [29]. Suppose we have an independent sample of n observations $(x_i, y_i) \sim F_{X,Y}$ from some continuous bivariate distribution $F_{X,Y}$. Consider the non-parametric regression model

$$y_i = f(x_i) + \epsilon_i$$

where $f(\cdot)$ is an unknown smooth function (i.e. the universal function we would like to collapse the data on). $\epsilon_i \sim (0, \sigma^2)$ are iid error terms with mean zero and variance σ^2. To estimate $f(\cdot)$, a smoothing spline minimizes the penalized lease squares functional

$$f_\lambda = \text{argmin}_{f \in H} \frac{1}{n} \sum_{i=1}^{n} (y_i - f(x_i))^2 + \lambda J_m(f)$$

where $J_m(f) = \int |f^{(m)}(z)|^2 dz$ is a penalty term that prefers a smoother function, and $\lambda > 0$ is the smoothing parameter that controls the influence of the penalty. Note that $f^{(m)}(\cdot)$ denotes the m-th derivative of $f(\cdot)$, and $H = \{f : J_m(f) < \infty\}$ is the space of functions with square integrable m-th derivative. The parameters λ and m affect the smoothness of the fitted function.

The Kimeldorf-Wahba representer theorem tells us that a piece-wise polynomial function minimizes the penalized lease squares functional. We can quantify the quality of the regression using the Mean Squared Error (MSE).

As an alternative method, if we assume the errors are iid Gaussian, we could use information criteria to select the parameter: Given an independent sample of n observations, the log-likelihood function has the form

$$l(\lambda, \sigma^2) = -\frac{1}{2\sigma^2} \sum_{i=1}^{n} (y_i - f_\lambda(x_i))^2 - \frac{n}{2} \log(\sigma^2) - \frac{n}{2} \log(2\pi).$$

Because the true variance in an experiment is usually unknown. The maximum likelihood estimate (MLE) variance

$$\sigma_\lambda^2 = \frac{1}{n}\sum_{i=1}^{n}(y_i - f_\lambda(x_i))^2$$

can be used in the error variance.

Substituting the MLE variance gives the log-likelihood

$$\tilde{l}(\lambda) = l(\lambda, \sigma_\lambda^2) = -\frac{n}{2} - \frac{n}{2}\log(\sigma_\lambda^2) - \frac{n}{2}\log(2\pi)$$

The Bayesian Information Criterion (BIC) select the parameter by adding a penalty of complexity to the log-likelihood

$$BIC(\lambda) = -2\tilde{l}(\lambda) + \log(n)\nu_\lambda$$

where ν_λ is the effective degrees of freedom (EDF) in a nonparametric regression model.

In the following part, we apply the default parameter setting of the ss function in the npreg package.

3.2.1 Method 1: pair-wise mean squared difference

In our first method, we perform the smoothing spline regression on each transformed $S \sim (J - J_0) \cdot L$ curve (examples shown in Figure 3.3b and 3.3c). For each pair of the curves, we calculate the mean squared difference between their spline functions. We estimate the best critical point J_0 by minimize this mean squared difference. Note that we will generate a table of estimations, each corresponds to a pair of curves we have chosen.

Another subtle issue in calculating the mean squared difference is that each curve spans a different domain of definition because of their scaling with L (see Figure 3.3b and 3.3c). Furthermore, there is an obvious deviation from the universal function when the data is too far from the critical point J_0. Therefore, the window we used to calculate the mean squared

difference is chosen to be half of the smaller domain of the two curves.

An example of applying this method to a pair of curves corresponding to $L = 24$ and $L = 32$ is shown in Figure 3.4.

3.2.2 Method 2: one smoothing spline on all data

In our second method, we ignore the L label and treat all the data points as generated from a single function. We perform one smoothing spline regression on these unlabeled data points, and calculate the BIC of the regression. We know that the posterior model probabilities satisfy

$$\pi(J_0|x, y, L) \propto e^{-\frac{1}{2}BIC}$$

Therefore, we can do a quadratic regression at the bottom of the BIC curve to extract the MLE and the uncertainty of J_0. If the bottom of the BIC curve can be fit by

$$BIC(J_0) = aJ_0^2 + bJ_0 + c$$

then the posterior model probabilities are proportional to

$$e^{-\frac{1}{2}BIC} = e^{-\frac{1}{2}(aJ_0^2+bJ_0+c)} = e^{-\frac{a}{2}(J_0+\frac{b}{2a})^2+\frac{b^2}{8a}-\frac{c}{2}}$$

from which we can read out the MLE $J_0 = -\frac{b}{2a}$ and uncertainty $\sigma_{J_0} = \frac{1}{\sqrt{a}}$. The 95% confidence interval will be $[-\frac{b}{2a} - 1.96\frac{1}{\sqrt{a}}, -\frac{b}{2a} + 1.96\frac{1}{\sqrt{a}}]$.

In comparison with the first method, we also apply the second method to each pair of the curves. Note that we now have a measure of uncertainty in the result. We will see that most of the time the minima we get using Method 1 agree with the confidence interval.

An example of applying this method to a pair of curves corresponding to $L = 24$ and $L = 32$ is shown in Figure 3.5.

L	32	64	128	256	384
24	1.0338	1.0334	1.0318	1.0306	1.0302
32		1.0334	1.0318	1.0306	1.03
64			1.0312	1.0304	1.0302
128				1.0302	1.0302
256					1.03

Table 3.1: The optimal critical points are obtained by Method 1.

L	32	64	128	256	384
24	1.035±0.002	1.0343±0.0008	1.0325±0.0004	1.0311±0.0003	1.0304±0.0002
32		1.0346±0.0009	1.0325±0.0004	1.0311±0.0003	1.0305±0.0002
64			1.0319±0.0007	1.0307±0.0003	1.0300±0.0002
128				1.0302±0.0005	1.0298±0.0003
256					1.0300±0.0009

Table 3.2: The MLE critical points and the corresponding standard deviation are obtained by Method 2.

3.3 Results

Now we are ready to display the results. First, our baseline results of optimal critical points came from viewing the best data collapsing by human eyes, which is $J_0 = 1.0302$.

We apply a grid search to find the optimal critical points using Method 1 in Section 3.2.1. We do a coarse grid search followed by a fine search. The optimal critical points are summarized in Table 3.1.

In order to compare with the results using Method 1, We perform the analysis using Method 2 in Section 3.2.2 for each pair of L. The MLE critical points and the corresponding standard deviations are summarized in Table 3.2.

We also perform Method 2 on all the data together to get an overall estimation. The MLE critical point is $J_0 = 1.0309 \pm 0.0002$. We present the corresponding smoothing spline regression in Fig 3.6.

All the results are summarized in Fig 3.7. We see that for large system sizes, the critical point agrees more with the baseline value. For smaller system sizes, although the estimations are systematically biased to a larger value, the uncertainties are also larger, which still

makes the baseline value close to the edge of the confidence intervals. The reason for larger system sizes being more accurate may be that in an eye-viewing data collapsing, the curves corresponding to larger system sizes have wider domains: They are more significant in the data collapsing.

It is also interesting to see that within the same color group (i.e. same larger L), the uncertainty is smaller when the second L is smaller. This is counter intuitive at first glance, but actually makes sense because the location of the crossing point should be more accurate when the difference between the two L's are larger.

We also notice that for a certain pair of L, the optimal critical point by Method 1 is often smaller than the MLE critical point by Method 2. (Red circles in Fig. 3.7 are often lower than the dots.) However, this is not always true, as counterexamples appear for (384, 64) and (384,128). We are not sure whether this law is true or just a random effect.

3.4 Summary and discussion

In this chapter, we applied the smoothing spline method to an actual data set in a numerical physics project. We proposed two methods to estimate the critical point. Based on the performance of the two methods in the previous section, we can see their advantages and disadvantages:

- Method 1:
  - Advantage: Stable in the effective degree of freedoms. Very sensitive at the minimum (see the sharp tip at the minimum in Figure 3.4c.
  - Disadvantage: Requires an artificially defined window to calculate the mean squared difference. Only works for a pair of L.
- Method 2:

- Advantage: Works for any number of L's in general. Difference in function domains does not affect its applicability.
- Disadvantage: The absolute value of BIC is not as intuitive as the MSE.

When the two methods are both applicable, their estimation of the critical points are consistent. In particular, when the system sizes are large, their estimations are very close to the baseline estimation by human eyes.

There are several future steps we can take from this project. First, we have estimations of the critical point from each pair of system sizes. One question is how to combine all the estimations coherently. Based on the similarity between the large-system-size results and the human baseline, it seems reasonable to weight more on the results with larger system sizes.

Second, we would like to design an automatic process to help us find the critical points. So far our methods were only tested on one data set. We can improve the reliability by testing on more data sets.

Finally, the data we used in this project were known to have the critical point and coincidence feature. In theory, the two methods we proposed here could be applied even when the data do not coincide. We need to check the reliability of the data collapsing by actually doing the transformation and plotting the curves. It will be interesting to think about how to design a criterion to distinguish whether or not there will be coincidence on the data.

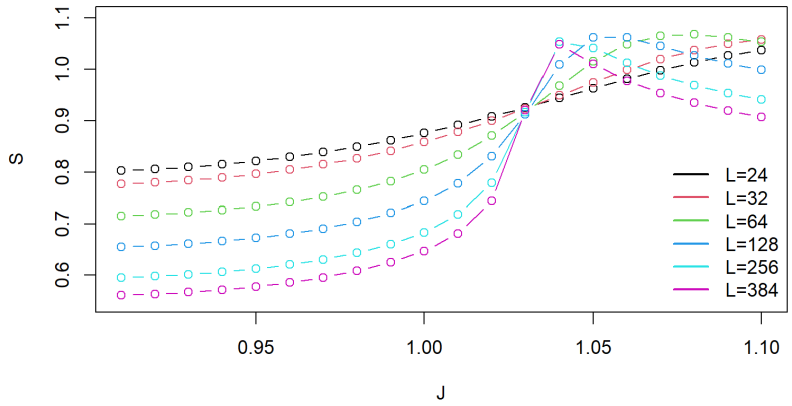

(a) Original data without transformation.

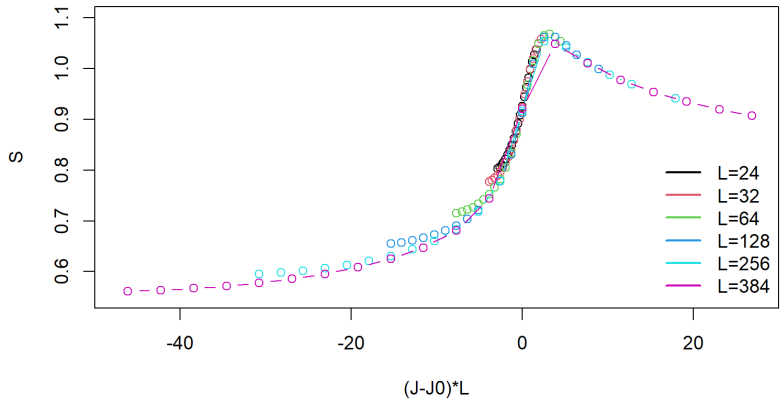

(b) Scaled data with $J_0 = 1.03$.

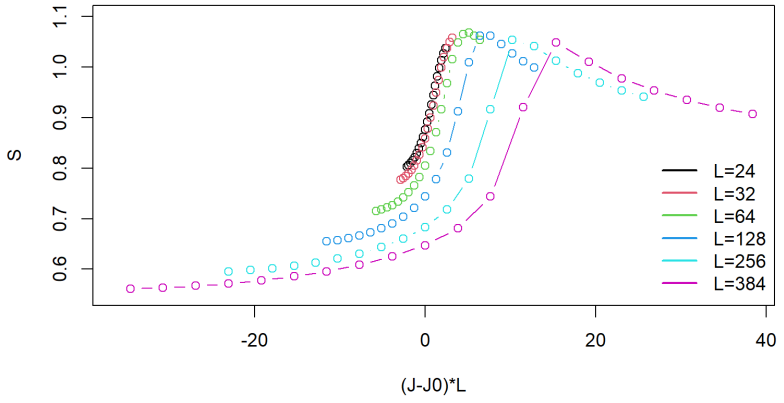

(c) Scaled data with $J_0 = 1.0$.

Figure 3.3: Example of data in a real numerical experiment. Here the observable is the entanglement entropy S. The best data collapsing appears around $J_0 \approx 1.03$.

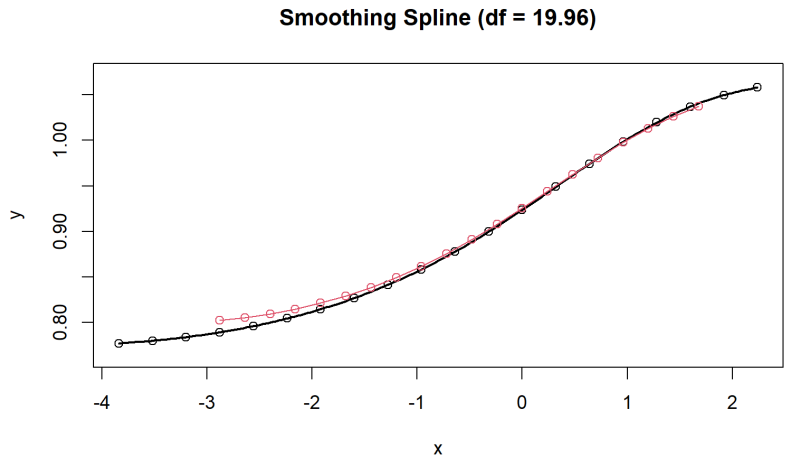

(a) (red) $L = 24$. (black) $L = 32$. $J_0 = 1.03$. MSD $= 0.00276$.

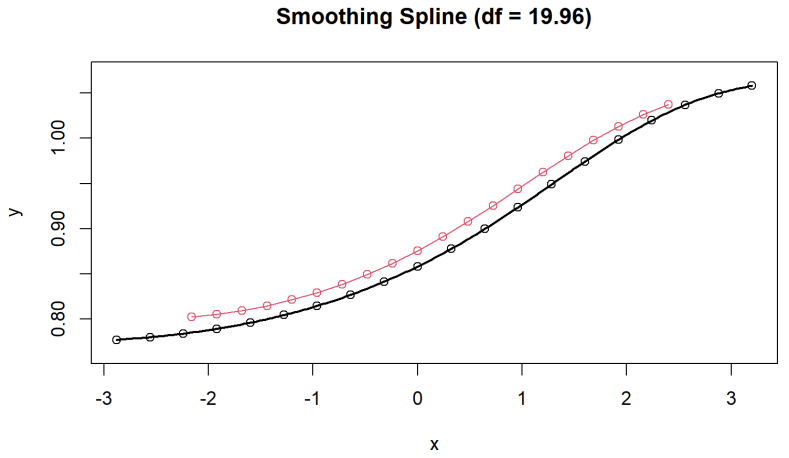

(b) (red) $L = 24$. (black) $L = 32$. $J_0 = 1.0$. MSD $= 0.01771$.

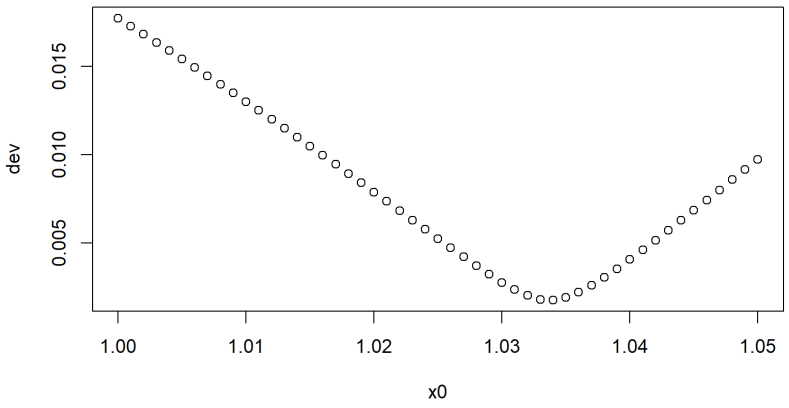

(c) Minimize the mean squared difference. Optimal $J_0 = 1.034$.

Figure 3.4: Example of applying Method 1 in Section 3.2.1 to the data.

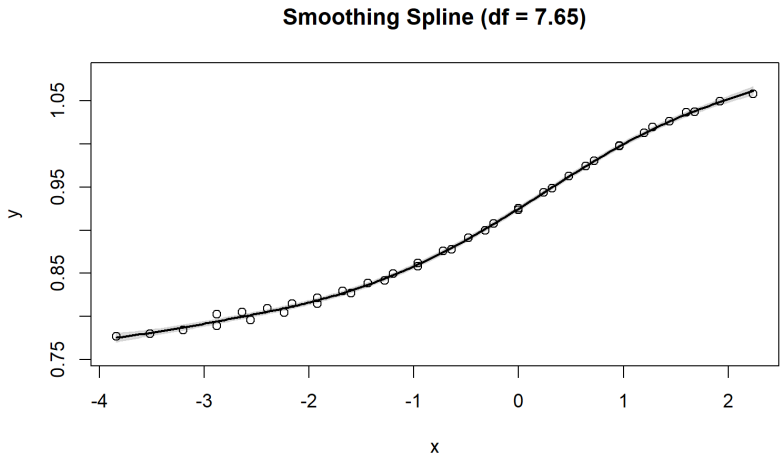

(a) $L = 24$ and $L = 32$. $J_0 = 1.03$. BIC $= -329.1987$.

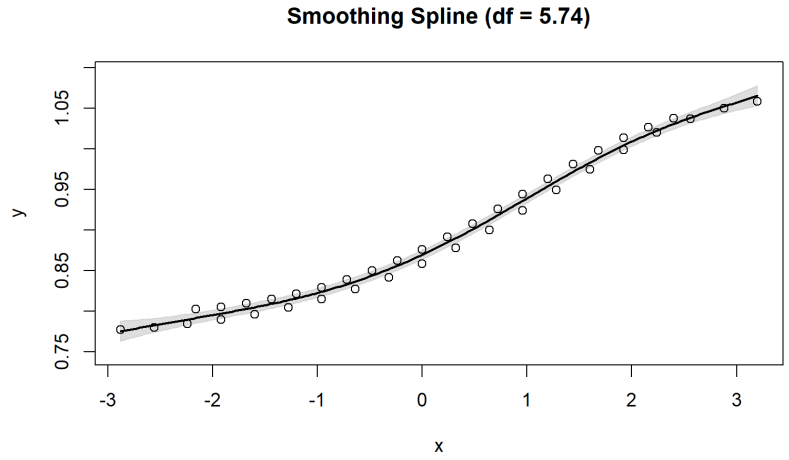

(b) $L = 24$ and $L = 32$. $J_0 = 1.0$. BIC $= -252.5144$.

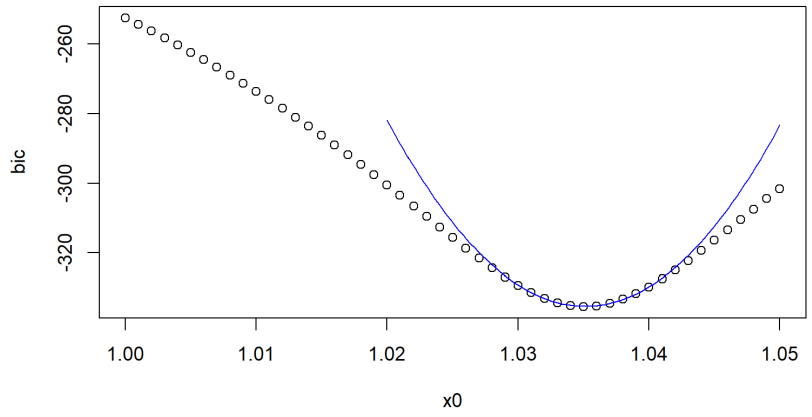

(c) Quadratic regression of the BIC. $J_0 = 1.035 \pm 0.002$.

Figure 3.5: Example of applying Method 2 in Section 3.2.2 to the data.

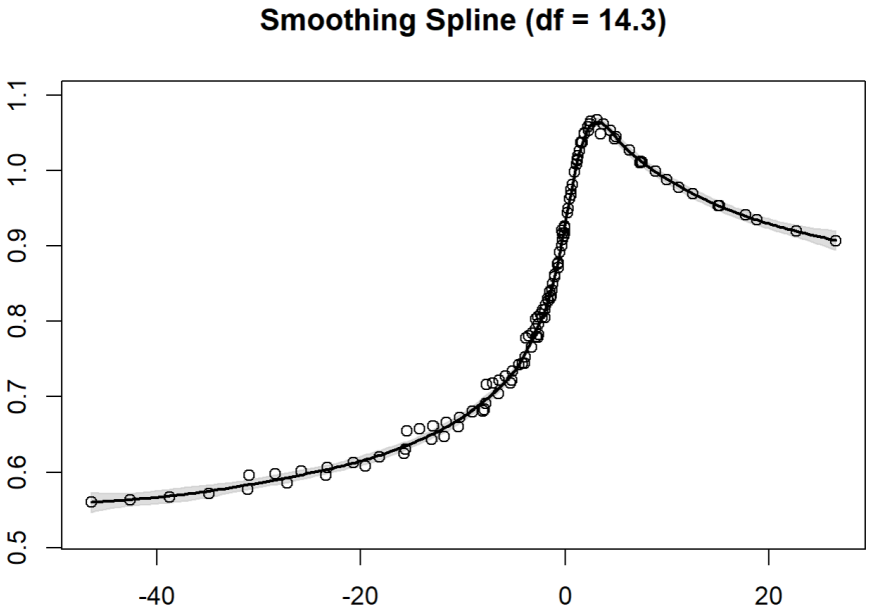

Figure 3.6: Best smoothing spline regression of all data with Method 2. $J_0 = 1.0309 \pm 0.0002$.

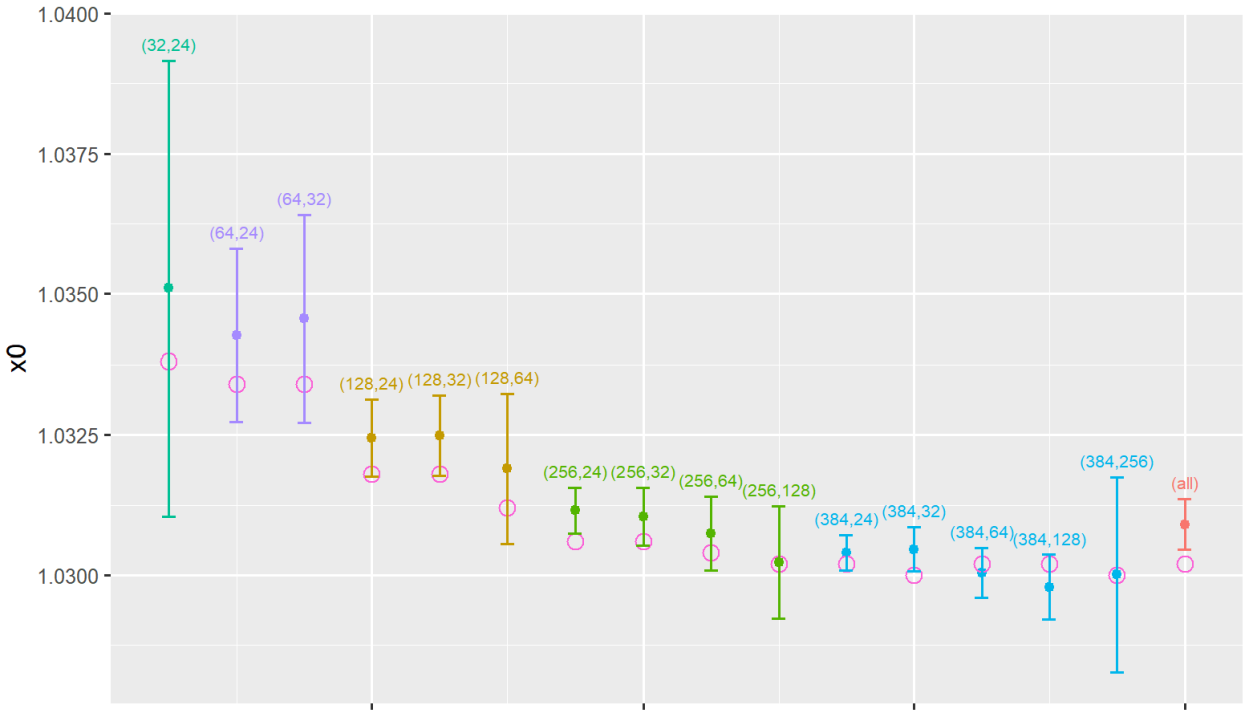

Figure 3.7: Summary of results from both methods. The red circles represent the optimal critical points estimated by Method 1, except for the right-most one showing the human-eye estimation. The dots and error bars show the MLE critical points and the corresponding 95% confidence intervals by Method 2. The right-most one shows the result for all data, and the others for a pair of L. The colors are grouped by the larger L in the pairs.

Chapter 4

Provably Efficient Adiabatic Learning for Quantum-Classical Dynamics

4.1 Introduction

The material of this Chapter is largely based on Ref. [3]. In the earlier chapters in this thesis, we saw that numerical algorithms were powerful when analytical methods could not fully solve the problem. For example, we used the DMRG algorithm to see there was no first order phase transition in the model in Sec. 2.4. In general, we have to rely more on the numerical simulations when there are many degrees of freedoms with complicated couplings between them, not to mention non-equilibrium dynamical processes. In this chapter, we will develop a general numerical framework for simulating quantum-classical hybrid dynamics. Interestingly, rigorous analytical methods such as the statistical bound analysis will be involved to help prove the efficiency of our numerical algorithm. Numerical methods and analytical methods are really good friends!

Efficient simulation of quantum-classical hybrid dynamics is crucial to multi-scale modelings of a wide range of physical systems, opening new avenues for advancements in material science, chemistry, and drug discovery by providing a more comprehensive understanding

of molecular interactions [34]–[40]. A common hybrid dynamics approach relies on the adiabatic approximation, where two well-separated timescales of a system allow one to treat the slow dynamics classically while quantum calculations are used to solve the fast, often electronic, degrees of freedom that adiabatically follow the classical dynamics. A well-known example is the Born-Oppenheimer approximation which is widely used in *ab initio* molecular dynamics [41]. The significance of quantum-classical hybrid dynamics lies in its potential to revolutionize how we model and predict the behavior of complex systems, ultimately pushing the frontiers of both fundamental research and practical applications.

The simulations of quantum-classical dynamics, however, is computationally challenging due to not only an exponentially large Hilbert space of quantum sub-systems and repeated time-consuming quantum calculations at every time step, but also the nonlinear differential equation coupled both the quantum and the classical variables. In the past two decades, machine learning (ML) has emerged as a powerful tool in developing force fields and interatomic potentials for *ab initio* molecular dynamics [42]–[53]. ML force-field approaches have recently been generalized to enable large-scale dynamical simulations of condensed-matter lattice systems [54]–[58]. This approach leverages massive datasets of quantum mechanical results to train models that can predict the potential energy surfaces with high precision. ML-enhanced force fields facilitate the simulation of large intricate systems by accurately capturing the essential quantum mechanical effects while maintaining computational efficiency. Despite intensive studies and wide applications of ML force field models over past decades, critical questions on the error bound, sample complexity and generalizability of the ML methods have remained unresolved.

In this work, we establish a generic theoretical framework for analyzing quantum-classical adiabatic dynamics with learning algorithms. We start with the analysis of the approximately constant linear model, derive the error bounded condition for the non-linear model, and introduce the relaxation method to check the error bounded property for a generic model, which lays down a solid foundation for the reliability of learning algorithms in quantum-classical

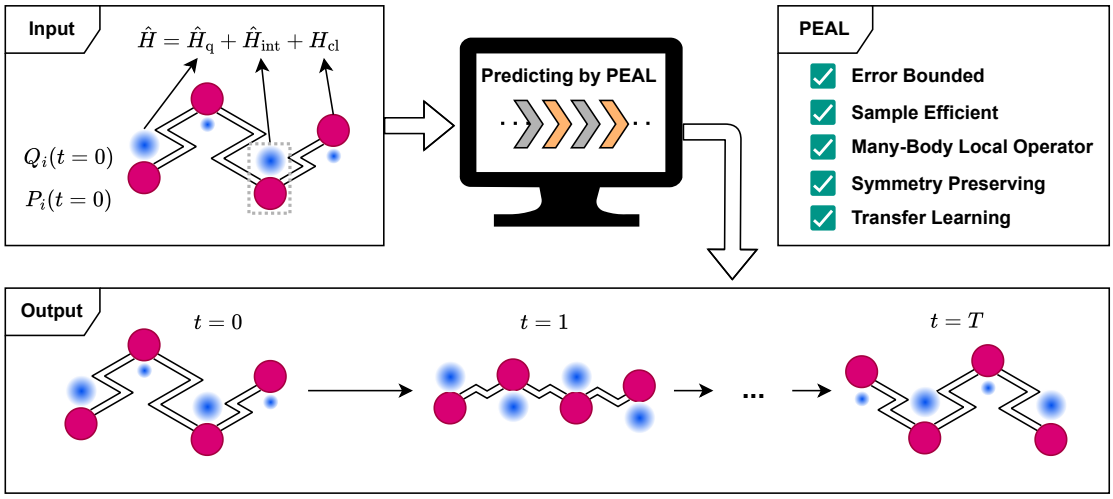

Figure 4.1: Schematic diagram for PEAL.

adiabatic dynamics. Inspired by the recent development of quantum information theoretic learning theory for quantum many-body systems [59]–[72], we develop a provably efficient adiabatic learning (PEAL) algorithm for quantum-classical dynamics, which offers a sample complexity scaling logarithmically with the system size and favorable scaling of evolution time. We benchmark our algorithm on the Holstein model and demonstrate accurate prediction of the single path dynamics and ensemble dynamics observables, as well as transfer learning across different couplings between quantum and classical degrees of freedom.

4.2 Adiabatic quantum-classical dynamics learning

We consider a general quantum-classical Hamiltonian:

$$\hat{H} = \hat{H}_q + \sum_{\alpha,i} g_\alpha \hat{O}_{\alpha,i} G_{\alpha,i}(\vec{P},\vec{Q}) + H_{cl}(\vec{P},\vec{Q}), \tag{4.1}$$

where $\hat{H}_q$ is the Hamiltonian operator for the quantum degrees of freedom, g_α is the quantum-classical coupling coefficient, α is the index of different types of couplings, $i \in \{1,\ldots,L\}$ is the label of local regions (e.g. lattice sites), $\hat{O}_{\alpha,i}$ is the quantum operator that enters the

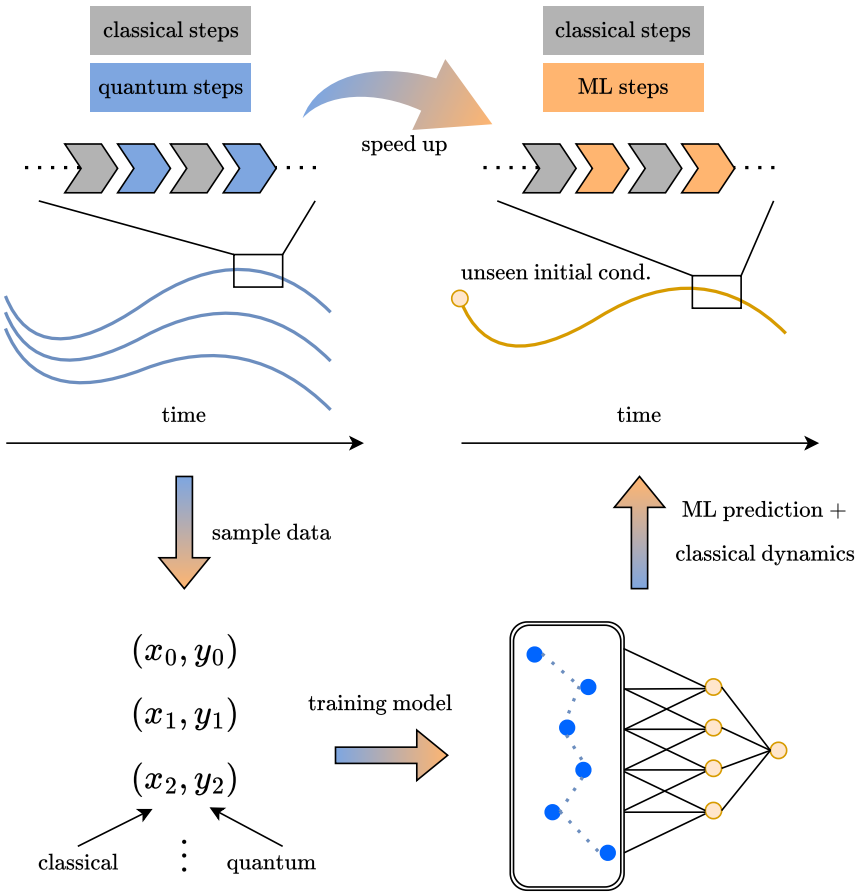

Figure 4.2: Schematic diagram for the steps of PEAL.

coupling, $G_{\alpha,i}(\vec{P},\vec{Q})$ is a general function of the classical degree of freedom $\vec{Q} = (Q_1, \ldots, Q_L)$ and its canonical momentum $\vec{P} = (P_1, \ldots, P_L)$, and $H_{cl}(\vec{P},\vec{Q})$ is the classical Hamiltonian.

We study the adiabatic evolution dynamics driven by the quantum-classical Hamiltonian in Eq. (4.1). In this adiabatic limit, similar to the Born-Oppenheimer approximation in quantum molecular dynamics, the quantum subsystem is assumed to quickly relax to the ground state of the total Hamiltonian $\hat{H}$, while the classical degrees of freedom follow the Hamilton's equations of motion (EOM):

$$\frac{d}{dt}Q_j = \sum_{\alpha,i} g_\alpha \langle \hat{O}_{\alpha,i} \rangle \frac{\partial}{\partial P_j} G_{\alpha,i} + \frac{\partial}{\partial P_j} H_{cl}, \tag{4.2}$$

$$\frac{d}{dt}P_j = -\sum_{\alpha,i} g_\alpha \langle \hat{O}_{\alpha,i} \rangle \frac{\partial}{\partial Q_j} G_{\alpha,i} - \frac{\partial}{\partial Q_j} H_{cl} - \gamma P_j, \tag{4.3}$$

where $j \in \{1, \ldots, L\}$, $\langle \cdot \rangle$ is the ground state expectation, and $\gamma > 0$ is the damping coefficient due to dissipation.

The conventional way to solve the above equations is through an iterative scheme, where one first updates $\{Q_j(t), P_j(t)\}$ based on the classical EOM, and then solve the ground state from $\hat{H}$. The updated ground state is used to compute expectation values $\langle \hat{O}_{\alpha,i} \rangle$ which determine the driving terms of the EOM for the next step. However, repeated ground-state calculations of $\hat{H}$ at every time step could be computationally costly using quantum state solvers (QSS), such as exact diagonalization (ED) [73], density functional theory [74], DMRG [75], neural network [76]–[80], and quantum computers [81]–[84].

We consider a general quantum-classical ML model for learning such dynamics, which we call *Adiabatic Dynamics Model Learning* (ADML). ADML consists of two components, which uses machine learning to predict the quantum observables and evolves the classical observables using classical numerical schemes. The ML force-field models widely used in quantum molecular dynamics can be viewed as special classes of ADML [42]–[53]. Our goal here is to predict the adiabatic dynamics of Eq. (4.1) with a learning-based approach. Given access to a dataset $\bigcup_{s=1}^{N_s} \{(g_\alpha, \vec{P}(t), \vec{Q}(t), \langle \hat{O} \rangle(t))_s : t \in \mathcal{T}_s\}$, where $\mathcal{T}_s$ is the set of sampled time steps, N_s is the number of initial conditions $\{(g_\alpha, \vec{P}(t_{\text{init}}), \vec{Q}(t_{\text{init}}))_s\}_{s=1}^{N_s}$ sampled from a distribution $\mathcal{D}_{\text{init}}$, and $\hat{O}$ stands for $\hat{O}_{\alpha,i}$ in Eq. (4.1) or other operators of insterest but not in the Hamiltonian, the task is to design ADML for predicting the dynamics starting with other $\{(g_\alpha, \vec{P}(t_{\text{init}}), \vec{Q}(t_{\text{init}}))\}$ from $\mathcal{D}_{\text{init}}$. In the following, we analyze and derive the error bounded conditions for ADML.

4.2.1 Approximately constant linear model

To serve as a starting point, we consider a simple example of Eq. (4.1), $\hat{H} = \hat{H}_q + \sum_i g \hat{O}_i Q_i + \sum_i \left(\frac{1}{2M} P_i^2 + \frac{1}{2} k Q_i^2 \right)$, where we only consider one type of quantum-classical coupling with $G_{\alpha,i}(\vec{P}, \vec{Q}) = Q_i$, and the classical Hamiltonian $H_{cl}(\vec{P}, \vec{Q})$ is for simple harmonic oscillators with mass M and spring constant k. Further assuming that during the dynamical process

we are interested in, the response $\frac{\partial\langle\hat{O}_i\rangle}{\partial Q_i}$ is approximately a constant, and the off-diagonal response $\frac{\partial\langle\hat{O}_i\rangle}{\partial Q_j}$ $(i \neq j)$ is approximately zero, the EOM of the system is then reduced to that of independent simple harmonic oscillators.

Focusing on the classical degree of freedom Q_i, we can view the quantum-classical coupling $g\hat{O}_i Q_i$ as a driving force on the oscillator. Since the EOM in Eq. (4.2) and (4.3) are approximately linear in this case, the accumulated momentum and position errors between ML and the exact simulation using QSS, $p(t) = P_{i,\mathrm{ML}}(t) - P_{i,\mathrm{Exact}}(t)$, $q(t) = Q_{i,\mathrm{ML}}(t) - Q_{i,\mathrm{Exact}}(t)$ (i index suppressed), also satisfy a similar EOM:

$$\frac{d}{dt}q(t) = \frac{1}{M}p(t), \tag{4.4}$$

$$\frac{d}{dt}p(t) = F(t) - Kq(t) - \gamma p(t) + o(q(t)), \tag{4.5}$$

where we define the error force $F(t) = -g\delta\langle\hat{O}_i\rangle(t)$ and the error stiffness $K = g\frac{\partial\langle\hat{O}_i\rangle}{\partial Q_i} + k$. $\delta\langle\hat{O}_i\rangle(t) = \langle\hat{O}_i\rangle_{\mathrm{ML}}(\vec{Q}_{\mathrm{ML}}(t)) - \langle\hat{O}_i\rangle_{\mathrm{Exact}}(\vec{Q}_{\mathrm{ML}}(t))$ is the ML prediction error at the t-th time step. $o(q(t))$ means higher order terms in $q(t)$ (See Appendix 4.6.3 for the derivation). Given a bounded $F(t)$, even if it is tuned to drive the oscillator optimally, as long as $K, \gamma > 0$, the oscillator cannot be driven to infinite amplitude, i.e. the accumulated momentum and position errors are bounded. For $F(t)$ to be bounded, it suffices to have $\delta\langle\hat{O}_i\rangle(t)$ bounded, which motivates us to define an Error Bounded Property such that when $\delta\langle\hat{O}_i\rangle(t)$ is bounded, $p(t)$ and $q(t)$ are also bounded. More precisely, we define the following

Definition 1 (Error Bounded Property)**.** *A model satisfies the Error Bounded Property with respect to $\delta\langle\hat{O}_i\rangle(t)$ for $t \in [t_{init}, t_{end}]$, if and only if the following claim is true: $\exists\, C_q, C_p > 0$ such that $\forall\epsilon > 0$, if $\forall t \in [t_{init}, t_{end}]$, $|\delta\langle\hat{O}_i\rangle(t)|^2 \leq \epsilon$, then there are $|q(t)| \leq C_q\sqrt{\epsilon}$ and $|p(t)| \leq C_p\sqrt{\epsilon}$, $\forall t \in [t_{init}, t_{end}]$.*

Proposition 1. *The approximately constant linear model satisfies the Error Bounded Property if $K > 0$.*

The proof of Prop. 1 is in Appendix 4.6.6.

4.2.2 Non-linear model

We can generalize the approximately constant linear model to allow non-linearity. We drop the assumption that the response $\frac{\partial\langle\hat{O}_i\rangle}{\partial Q_i}$ is approximately a constant, allow $G_{\alpha,i}(\vec{P},\vec{Q})$ to be a non-linear function of Q_i, and allow the potential $\frac{1}{2}kQ_i^2$ to include non-quadratic component in Q_i, as long as we can Taylor expand the potential at its minimum. These generalizations can be absorbed by a redefined $F(t)$ and a time-dependent error stiffness $K(t)$. Unlike the approximately constant linear model, the oscillator could have infinite amplitude even if $K(t) > 0$ for all the time. We present a condition in Appendix 4.6.7 which guarantees a bounded bounded in the worst case scenario. Summarized as an informal theorem, we have:

Theorem 1 (Error Bounded Condition for non-linear model (Informal))**.** *If $K(t) > M(\gamma/2)^2 + C$ with a positive constant C for all t, and the error stiffness $K(t)$'s fluctuation, as well as $G_{\alpha,i}(\vec{P},\vec{Q})$ and its first derivatives are bounded, then the non-linear model satisfies the Error Bounded Property in Def. 1.*

The proof for Thm. 1 is provided in Appendix 4.6.7. We can further apply it to the Hamiltonian in normal mode with the quadratic momentum under Fourier transform, which could appear in a more general setup.

4.2.3 General relaxation method

We now come back to the most general ADML. We allow arbitrary $G_{\alpha,i}(\vec{P},\vec{Q})$ and $H_{cl}(\vec{P},\vec{Q})$ in Eq. (4.1), and we make no assumption on the response $\frac{\partial\langle\hat{O}_i\rangle}{\partial Q_j}$. Because in the most general case the classical degrees of freedom are no longer decoupled, we restore the i index of the accumulated momentum and position errors, $p_i(t) = P_{i,\mathrm{ML}}(t) - P_{i,\mathrm{Exact}}(t)$, $q_i(t) = Q_{i,\mathrm{ML}}(t) - Q_{i,\mathrm{Exact}}(t)$.

For a general ADML, the EOM for the errors $q_i(t)$, $p_i(t)$ can in general be derived from

Eq. (4.2) and (4.3):

$$\frac{d}{dt}q_i = \sum_j \left(\mathcal{K}_{q_j,q_i}q_j + \mathcal{K}_{p_j,q_i}p_j\right) + \mathcal{F}_{q_i} + o(q,p), \tag{4.6}$$

$$\frac{d}{dt}p_i = \sum_j \left(\mathcal{K}_{q_j,p_i}q_j + \mathcal{K}_{p_j,p_i}p_j\right) + \mathcal{F}_{p_i} - \gamma p_i + o(q,p), \tag{4.7}$$

where the error stiffness matrix $\mathcal{K}_{q(p)_j,q(p)_i}$ and the error force vector $\mathcal{F}_{q(p)_i}$ depend on $(\vec{P},\vec{Q})$, and $\mathcal{F}_{q(p)_i}$ is linear in $\delta\langle\hat{O}_{\alpha,i}\rangle(t)$ (see Appendix 4.6.5 for details).

While it is difficult to write down an error bounded condition for a general ADML, we propose a relaxation method to provide a sufficient (but not necessary) condition to check the Error Bounded Property in Def. 1. The idea is to consider the worst case scenario. If in the worst case scenario the error still converges, then it is safe to use ADML to accelerate our dynamical simulation. The relaxation method is as follows. First, we require $\mathcal{K}$ elements, as well as $G_{\alpha,i}(\vec{P},\vec{Q})$ and its first derivatives, are bounded. Second, assuming $|\delta\langle\hat{O}_{\alpha,i}\rangle(t)|^2 \leq \epsilon$, we identify possible upper and lower bounds for the elements in $\mathcal{K}$ and $\mathcal{F}$. The bounds just only need to be effective during the time range of the simulation. Third, to achieve the worst case scenario, we want to maximize dq_i/dt when q_i is positive, and minimize when negative (the same for p_i). Therefore, we insert the upper bound of $\mathcal{K}_{q(p)_j,q(p)_i}$ when $q(p)_i$ and $q(p)_j$ have the same sign, and the lower bound if the opposite sign. $\mathcal{F}_{q(p)_i}$ are adjusted to their upper or lower bounds accordingly. Fourth, we perform a classical simulation of the EOM in Eq. (4.6) and (4.7), with the worst case scenario stated above. Finally, if the simulation shows there exist constants C_{q_i} and C_{p_i} such that for any $\epsilon > 0$, there are $|q_i(t)| \leq C_{q_i}\sqrt{\epsilon}$ and $|p_i(t)| \leq C_{p_i}\sqrt{\epsilon}$ during the time range of interest, then the Error Bounded Property is verified with the relaxation method.

4.3 Provably efficient learning algorithm

Next, we present a provably efficient learning algorithm for the above ADML models based on quantum information theory, which we call *Provable Efficient Adiabatic Learning* (PEAL). The PEAL algorithm, equipped with a learning model $\mathcal{M}$ and a classical ordinary differential equation (ODE) solver, consists of the following steps.

(i) Data collection for training. We sample a set of N_s number of initial conditions $\{(g_\alpha, \vec{P}(t_{\text{init}}), \vec{Q}(t_{\text{init}}))_s\}_{s=1}^{N_s}$ from a distribution $\mathcal{D}_{\text{init}}$. We evolve the system with QSS and ODE solver to get $(\vec{P}(t), \vec{Q}(t), \langle\hat{O}\rangle(t))_s$. For each s, we sample a set of time steps $\mathcal{T}_s$ uniformly from $[t_{\text{init}}, t_{\text{end}}]$.

(ii) Model training. We use the dataset $\bigcup_{s=1}^{N_s}\{(g_\alpha, \vec{P}(t), \vec{Q}(t), \langle\hat{O}\rangle(t))_s : t \in \mathcal{T}_s\}$ to train a model $\mathcal{M} : (g_\alpha, \vec{P}, \vec{Q}) \mapsto \langle\hat{O}\rangle$ with the learning algorithm developed in [60].

(iii) Prediction. For any unseen new initial condition $(g_\alpha, \vec{P}(t_{\text{init}}), \vec{Q}(t_{\text{init}}))_{\text{new}} \sim \mathcal{D}_{\text{init}}$, PEAL outputs the dynamical trajectory $(\vec{P}(t), \vec{Q}(t), \langle\hat{O}\rangle(t))_{\text{new}}$ for $t \in [t_{\text{init}}, t_{\text{end}}]$, by alternatively updating $\langle\hat{O}\rangle(t)$ with $\mathcal{M}$ and $\vec{P}(t), \vec{Q}(t)$ with ODE solver, integrated with our symmetry-preserving techniques shown later.

The sample complexity and error bounds are summarized in the following theorem.

Theorem 2 (Provably Efficient Adiabatic Learning Theorem (Informal))**.** *When the Error Bounded Property in Def. 1 is satisfied, for T time steps quantum-classical adiabatic dynamics of an n-qubit gapped system, with sample complexity $O(\log(n))$, PEAL gives rise to controllable accumulated errors of classical variables and all k-local, bounded quantum observables scaling as (i) $O(\sqrt{T})$ for generic model $\mathcal{M}$ (ii) $O(\sqrt{\log T})$ for sub-Gaussian $\mathcal{M}$'s prediction error (iii) independent on T for bounded $\mathcal{M}$'s prediction error.*

We leave the proofs for the above theorem in Appendix 4.6.8. We note that the computational time for PEAL's prediction under a fixed g_α is $O(\min\{nN_s, c(n)\}T)$, where $c(n)$ is the ODE solver per time step complexity and the nN_s factor comes from the model $\mathcal{M}$ [60]. For

Theorem 2, it can also be applied to an n-qubit system with ground states of exponential-decay correlation functions using recent results [62]. We highlight that PEAL works for unseen couplings $g_{\alpha,\text{new}} \notin \{g_{\alpha,s}\}_{s=1}^{N_s}$, demonstrating transfer learning over a family of Hamiltonian. Furthermore, PEAL can predict any k-local observable $\hat{O}$ even if it does not appear in the Hamiltonian.

4.4 Numerical experiments

We consider the Holstein model [85]–[87] which describes the electron phonon interaction as follows:

$$H = -\sum_{i,j} c_i^\dagger c_j - g\sum_i \left(c_i^\dagger c_i - \frac{1}{2}\right) Q_i + \sum_i \left(\frac{P_i^2}{2M} + \frac{kQ_i^2}{2}\right), \tag{4.8}$$

where c_i is related to the fermionic degree of freedom, while Q_i and P_i are the position and momentum of the phonon as classical degrees of freedom.

In the numerical experiment, we study such model on a 1D periodic chain with $L = 50$ sites. We set $M = k = 1$ and the damping coefficient $\gamma = 0.1$. The electronic degree of freedom at time t will be the ground state of $H_e(\{Q_i(t)\})$ due to the fast relaxation, showing a 1D strong Anderson localization [88]. Therefore, PEAL's requirement of a ground state with exponential-decay correlation functions is satisfied. Analytically, the 1D adiabatic Holstein model always cools down to a charge density wave (CDW) in zero temperature. In Appendix 4.6.2, we derive the relation between phonon amplitude and CDW response function, showing the error stiffness K is always positive when it's close to a checkerboard configuration. We also numerically measure the error stiffness $K(t)$ during the time range of interest, confirming the Error Bounded Property (see Appendix 4.6.7). Therefore, we can apply PEAL to the 1D adiabatic Holstein model with a bounded error guarantee during the dynamics.

Since Eq. (4.8) has the $U(1)$ and translation symmetry, we develop a symmetry-preserving PEAL. The $U(1)$ global symmetry is respected by conserving the total electron density, and

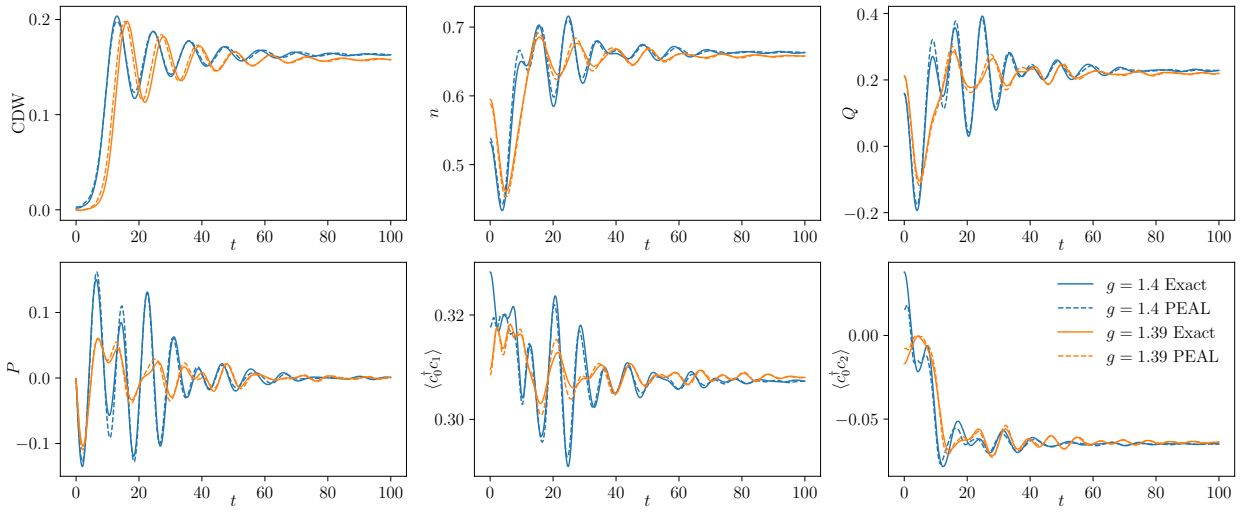

Figure 4.3: PEAL (dashed) vs. exact simulation (solid) in single-path prediction. Blue curves correspond to standard learning with $g = 1.4$, and orange curves correspond to transfer learning with $g = 1.39$.

the translation symmetry by applying the same model on all sites. The $U(1)$ symmetry preserving is a new feature in our PEAL that does not exist in previous literature and we have shown that the symmetry-preserving PEAL maintains provably efficient error bound in Appendix 4.6.10.

We begin with the single-path prediction task by training a model using some initial conditions and certain g values. The goal is to predict observable dynamics from different initial conditions under both the training g values (standard learning) and unseen g values (transfer learning). Here, we choose $g \in G_{\text{SL}} = \{1.3, 1.32, 1.34, 1.36, 1.38, 1.4\}$ for training. In Figure 4.3, we demonstrate the single-path prediction by PEAL. The solid curves are the exact simulation using exact diagonalization (ED) for QSS and RK4 for classical ODE solver [89], and the dashed curves are with PEAL. Blue curves are for $g = 1.4$ (standard learning), and orange curves for $g = 1.39$ (transfer learning). We present the time evolution of six different observables during the dynamics, which are the total charge density wave (CDW) $\sum_i (-1)^i n_i$, the electron density at the first site n, the phonon amplitude at the first site Q, the phonon momentum at the first site P, the hopping term $\langle c_0^\dagger c_1 \rangle$, and the next-nearest-neighbor correlation $\langle c_0^\dagger c_2 \rangle$. We note that CDW is a sum of local observables,

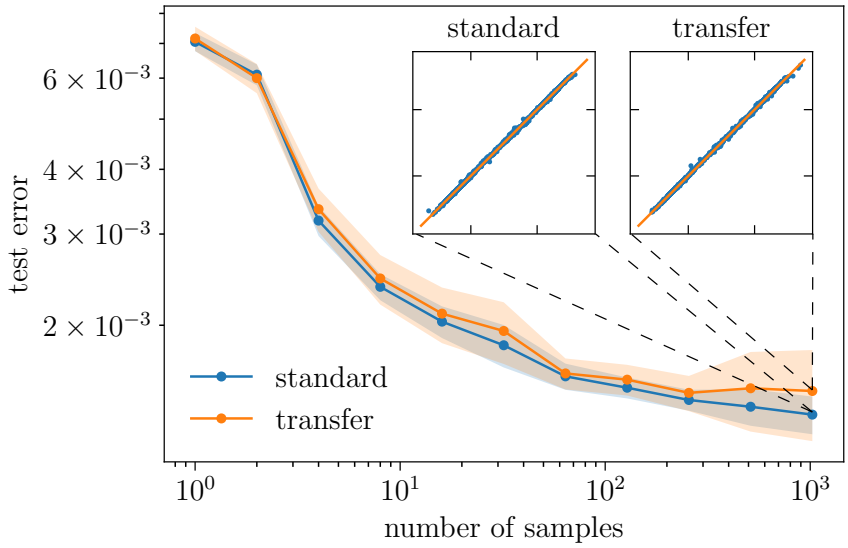

Figure 4.4: Test errors for standard learning (blue) and transfer learning (orange). Inner pannels: n_{PEAL} vs. n_{Exact} for standard learning with $g \in G_{\mathrm{SL}}$ (Left) and transfer learning with $g \in G_{\mathrm{TL}}$ (Right).

$\langle c_0^\dagger c_1 \rangle$ does not enter classical EOM, and $\langle c_0^\dagger c_2 \rangle$ does not even appear in the Hamiltonian. Nevertheless, all observables in the PEAL curves agree well with their corresponding exact simulations, demonstrating that PEAL guarantees a controllable error for k-local observable and well performs in transfer learning.

In Figure 4.4, we present the sample complexity of PEAL. We use the same training data in the single-path prediction, build the test set with $g \in G_{\mathrm{SL}}$ but with different initial conditions, and demonstrate transfer learning with $g \in G_{\mathrm{TL}} = \{1.31, 1.33, 1.35, 1.37, 1.39\}$. For illustration, we consider the root mean square of $|n_{\mathrm{PEAL}} - n_{\mathrm{Exact}}|$ as the test error. The test errors for both standard learning and transfer learning show a logarithmic scaling law with the number of samples. The inner panels also demonstrate that n_{PEAL} in standard learning and transfer learning match well with n_{Exact}.

Generically, the ensemble dynamics (i.e. the dynamics average over an ensemble of paths from different initial conditions) can provide more information of the underlying physics. In Figure 4.5, we compare the ensemble averages of the correlation function $Q_i(t)Q_j(t)$ at time $t = 100$ for $g = 1.4$ and $g = 1.7$. Here, $g = 1.4$ prediction is based on PEAL training

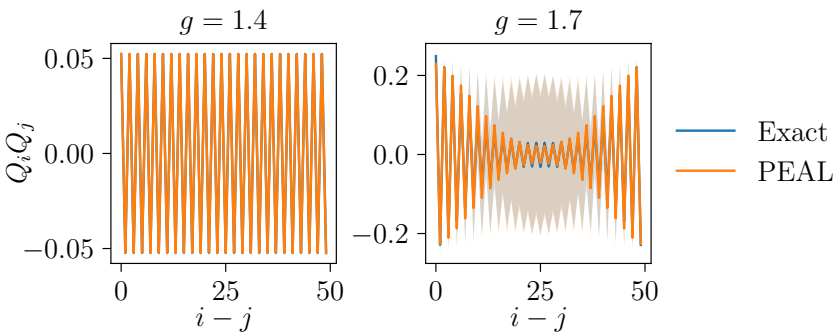

Figure 4.5: Consistent agreement between PEAL and the exact simulation for the ensemble $Q_i(t)Q_j(t)$ correlation at $t = 100$ of $g = 1.4$ (Left) and $g = 1.7$ (Right).

in $g \in G_{SL}$, and $g = 1.7$ prediction is based on another model from PEAL training in $g \in \{1.6, 1.62, 1.64, 1.66, 1.68, 1.7\}$ where long-lasting domain walls exist. For $g = 1.4$, the system has cooled down to a pure checkerboard configuration, and shows an oscillating correlation function. For $g = 1.7$, since the system has domain walls, it shows a decaying correlation function and a large variance. PEAL provides a good agreement with the exact simulations for both the mean and the variance over different g values.

4.5 Summary and discussion

In this chapter, we establish a comprehensive theoretical framework for analyzing quantum-classical adiabatic dynamics using learning algorithms. We provide a systematic analysis for the error bounded properties of the approximately constant linear model, the non-linear model, and generic models, ensuring the reliability of ADML. We develop a provably efficient adiabatic learning algorithm PEAL, demonstrating logarithmic scaling of sample complexity with system size and favorable evolution time scaling. Benchmarking PEAL on the Holstein model, we achieve accurate predictions of single-path dynamics and ensemble dynamics observables, with effective transfer learning across various quantum-classical coupling strengths.

Our framework and algorithm pave the way for provably efficient learning in quantum-

classical dynamics. Future research directions include exploring the application of PEAL to a wider range of quantum-classical systems beyond the Holstein model. Investigating the integration of advanced machine learning techniques, such as deep learning and reinforcement learning, could further enhance the accuracy and efficiency of the dynamics predictions. Additionally, extending our approach to real-time quantum-classical dynamics and non-adiabatic processes could significantly broaden its applicability. Further integration with experiments could solidify the practical utility of our methods in material science, chemistry, and other related fields.

4.6 Appendix

4.6.1 Dimensionless model

Consider the standard spinless Holstein model:

$$H = -t_{nn} \sum_{\langle ij \rangle} c_i^\dagger c_j - g \sum_i \left(c_i^\dagger c_i - \frac{1}{2} \right) Q_i + \sum_i \left(\frac{P_i^2}{2M} + \frac{k Q_i^2}{2} \right). \tag{4.9}$$

And the equation of motion for the phonons is

$$\frac{dQ_i}{dt} = \frac{P_i}{M}, \quad \frac{dP_i}{dt} = g n_i - k Q_i, \tag{4.10}$$

where $n_i = \langle c_i^\dagger c_i \rangle$ is the on-site fermion number. The mass m and elastic constant k are related by the familiar formula,

$$\omega = \sqrt{\frac{k}{M}}, \tag{4.11}$$

The inverse ω^{-1} gives a characteristic time scale for the dynamical problem. Next, one can introduce a "length scale" Q_0 for the displacement of the simple harmonic oscillator. The

energy related to Q at a given site is

$$E(Q) = -gn_iQ_i + \frac{kQ^2}{2}. \tag{4.12}$$

Assuming electron number $n \sim 1$, minimization with respect to Q gives $\partial E/\partial Q|_{Q_0} = 0$:

$$Q_0 \sim \frac{g}{k}. \tag{4.13}$$

From this one can then introduce a scale for the momentum via the relation $dQ/dt = P/M$

$$\omega Q_0 \sim \frac{P_0}{M} \implies P_0 = M\omega Q_0 = \frac{M\omega g}{k}. \tag{4.14}$$

We can now define the dimensionless time, displacement and momentum as

$$\tilde{t} = \omega t, \quad \tilde{Q}_i = \frac{Q_i}{Q_0}, \quad \tilde{P}_i = \frac{P_i}{P_0}. \tag{4.15}$$

In terms of dimensionless quantities, the equation of motion is then simplified to

$$\frac{d\tilde{Q}_i}{d\tilde{t}} = \tilde{P}_i, \quad \frac{d\tilde{P}_i}{d\tilde{t}} = n_i - \tilde{Q}_i. \tag{4.16}$$

Next, we consider the tight-binding Hamiltonian for the fermions for a given $\{Q_i\}$ configuration. We factor out the nearest-neighbor hopping constant t_{nn} and use it as the unit for energy. Also, we use the dimensionless $\tilde{Q}_i$:

$$H_{TB} = t_{nn}\left[-\sum_{\langle ij\rangle} c_i^\dagger c_j + \frac{gQ_0}{t_{nn}}\sum_i \tilde{Q}_i c_i^\dagger c_i\right]. \tag{4.17}$$

The coefficient of the second term above gives an important dimensionless parameter for Holstein model. Instead of t_{nn}, we can introduce the bandwidth of the tight-binding model:

$W = 4t_{nn}$ for the 1D model. We then define a dimensionless electron-phonon coupling

$$\lambda = \frac{gQ_0}{W} = \frac{g^2}{kW}. \tag{4.18}$$

The dimensionless tight-binding Hamiltonian then becomes

$$\tilde{H}_{TB} = -\sum_{\langle ij \rangle} c_i^\dagger c_j + 4\lambda \sum_i \tilde{Q}_i c_i^\dagger c_i. \tag{4.19}$$

One can see that, using these dimensionless quantities, the only adjustable parameter of the adiabatic dynamics of the Holstein model is this dimensionless λ. In general, for real materials $\lambda \lesssim 1$. For example, we can set it to $\lambda = 0.5$ or 0.25 in the simulations.

4.6.2 Holstein model charge density wave response analysis

Consider a tight binding model on a 1D lattice:

$$H = -t \sum_i (c_i^\dagger c_{i+1} + h.c.) - g \sum_i (-1)^i Q c_i^\dagger c_i, \tag{4.20}$$

where $i \in \{0, 1, \ldots, L-1\}$, L is the lattice size and is even. The lattice has periodic boundary condition. The effective potential on the lattice is staggered: $[-gQ, +gQ, -gQ, +gQ, \ldots]$. The unit cell consists of 2 lattice sites.

We can solve the single-particle wavefunctions using the ansatz

$$|\psi_k\rangle = (a, be^{ik}, ae^{2ik}, be^{3ik}, \ldots)^{\mathrm{T}}, \quad k \in \{0, \frac{2\pi}{L}, \ldots, \frac{2\pi}{L}(\frac{L}{2} - 1)\}. \tag{4.21}$$

Note that the range of k is halved because the unit cell is doubled.

The eigenvalue equation $H|\psi_k\rangle = E|\psi_k\rangle$ becomes

$$-gQa - 2(\cos k)b = Ea, \tag{4.22}$$

$$-(2\cos k)a + gQb = Eb, \tag{4.23}$$

which requires $E = \pm\sqrt{(gQ)^2 + (2\cos k)^2}$ to have nontrivial solutions.

The solutions form two bands. At half filling, all the states in the lower band, which has negative E, are filled with a particle. The charge density wave amplitude for $|\psi_k\rangle$ is $n_k = (a^2 - b^2)/2$. From the eigenvalue equation and the normalization $(L/2)(a^2 + b^2) = 1$, we can solve the CDW amplitude for $|\psi_k\rangle$:

$$n_k = \frac{\mathrm{sgn}(gQ)}{L\sqrt{(\frac{2\cos k}{gQ})^2 + 1}}, \tag{4.24}$$

where $\mathrm{sgn}(gQ)$ is the sign of gQ.

The total charge density wave at half filling is

$$n = \sum_k n_k = \sum_k \frac{\mathrm{sgn}(gQ)}{L\sqrt{(\frac{2\cos k}{gQ})^2 + 1}}. \tag{4.25}$$

The range of k has been described above.

In the infinite lattice limit, $L \to \infty$, the sum over k turns into an integral

$$n \to \int_0^\pi \frac{dk}{2\pi} \frac{\mathrm{sgn}(gQ)}{\sqrt{(\frac{2\cos k}{gQ})^2 + 1}} = \mathrm{sgn}(gQ)\frac{\mathrm{EllipticK}[-(\frac{2}{gQ})^2]}{\pi}, \tag{4.26}$$

where $\mathrm{EllipticK}[m] \equiv \frac{\pi}{2}{}_2F_1(\frac{1}{2}, \frac{1}{2}; 1; m)$ is the complete elliptic integral of the first kind, ${}_2F_1(a, b; c; x)$ is the hypergeometric function [90].

When $gQ \to 0$, the result says $n \to 0$. However, the derivative $\frac{\partial n}{\partial(gQ)}$ diverges at zero as $\log(\frac{1}{gQ})$. More precisely, $n \sim -gQ\log(gQ)$ for small gQ.

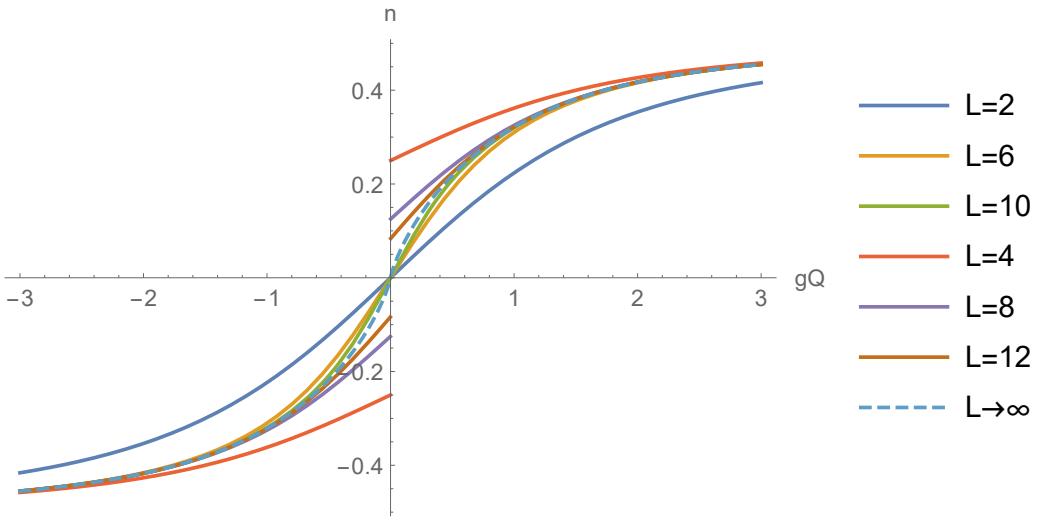

Figure 4.6: The charge density wave amplitude n as a function of the staggering potential gQ. For $L = 4N$, the function has a discontinuity at zero: There is a constant CDW $= \frac{1}{L}$ even when $g \to 0$. For $L = 4N + 2$, the function is continuous and has a finite slope at zero: There is a critical slope for which a straight line cross the origin could have other crossing points with the function. i.e. There exists a critical g value, below which the system does not have a stable CDW configuration. For $L \to \infty$ (dashed curve), the function is continuous and has a logarithmically diverging slope at zero: There is always CDW, but the amplitude is exponentially small for small g.

The property of n as a function of gQ is important, especially for gQ close to zero. This is because when the system stabilizes, the equation of motion tells us $k_{\text{spring}}Q = gn$, i.e. the forces are balanced. This means a straight line $n = (k_{\text{spring}}/g^2)gQ$ that crosses the origin. The number of crossing points between this straight line and the n vs. gQ function determines whether the system have a stable CDW in the long time. Figure 4.6 shows the function curves for different lattice size.

For example, in the infinite lattice limit, the derivative diverges at zero. Therefore, any straight line crossing the origin with a finite slope will cross the function at some other points. This means that there always exists a stable CDW for the infinite lattice. However, we can estimate how large the CDW amplitude should be for a small g. Combine the straight line $n = (k_{\text{spring}}/g^2)gQ$ and the asymptotic behavior $n \sim -gQ\log(gQ)$, we can solve a non-trivial crossing point at the phonon amplitude $Q \sim e^{-k_{\text{spring}}/g^2}/g$. We see that the amplitude decays exponentially when $g \to 0$.

L	2	6	10	22	50	102	1002	$L \to \infty$
slope	0.25	0.4167	0.4972	0.6224	0.7529	0.8664	1.2300	$\sim \log(L)$
g_{crit}	2	1.5492	1.4182	1.2676	1.1524	1.0743	0.9017	$\sim \frac{1}{\sqrt{\log L}}$

Table 4.1: Table of slope (Eq. 4.27) and g_{crit} values (Eq. 4.28) for different L. We choose $k_{\text{spring}} = 1$.

However, for a finite system size L, the situation is different. For $L = 4N$, the function n has a finite limit $\pm\frac{1}{L}$ when $gQ \to 0$, and has a discontinuity at 0. Therefore, a straight line crossing the origin always has non-trivial intersections with the function curve. i.e. There exists CDW with amplitude at least $\frac{1}{L}$ for all values of g. For $L = 4N + 2$, the function n goes to zero when $gQ \to 0$, and has a finite slope at 0. When g is small, (k_{spring}/g^2) exceeds this slope, the straight line only has intersection with the function curve at zero. When g is large, (k_{spring}/g^2) smaller than this slope, there are non-trivial intersections. Therefore, there is a phase transition due to the finite system size: When $g < g_{crit}$, no CDW; when $g > g_{crit}$, there is CDW. The system size we study, $L = 50$, is in this situation.

We can analytically solve g_{crit}. We can take the derivative of Eq. 4.26 at the limit to zero:

$$\left.\frac{\partial n}{\partial(gQ)}\right|_{gQ\to 0^+} = \sum_k \frac{1}{2L|\cos k|}. \tag{4.27}$$

By identifying $(k_{\text{spring}}/g_{crit}^2)$ with this slope, we get

$$g_{crit} = \sqrt{\frac{2k_{\text{spring}}L}{\sum_k \frac{1}{|\cos k|}}}. \tag{4.28}$$

Some numerical values for $k_{\text{spring}} = 1$ are listed in Table. 4.1

For our choice $L = 50$, $g_{crit} = 1.1524$. The domain wall formation g value for $L = 50$ is around 1.6. Therefore, we pick $g \in [1.3, 1.4]$ in our numerical experiment, to avoid the finite size effect and the domain walls.

In the main text, we see the bounded error requires $k_{\text{spring}} - g\frac{\partial n}{\partial Q} > 0$. We can prove

this is true when the system is close to the stable CDW configuration. We apply the self-consistency equation $k_{\text{spring}} = gn/Q$. From the concavity of the n vs. gQ function when $gQ > 0$, and the convexity when $gQ < 0$, we see $\frac{n}{gQ} > \frac{\partial n}{\partial(gQ)}$ as long as $gQ \neq 0$. Therefore, $k_{\text{spring}} - g\frac{\partial n}{\partial Q} = g^2(\frac{n}{gQ} - \frac{\partial n}{\partial(gQ)}) > 0$ almost surely, because the $gQ = 0$ case has measure 0. This completes our proof.

4.6.3 EOM of (p,q) — Approximately constant linear model

In the main text, we introduced the "approximately constant linear model", which has the Hamiltonian:

$$\hat{H} = \hat{H}_q + \sum_i g\hat{O}_i Q_i + \sum_i \left(\frac{1}{2M}P_i^2 + \frac{1}{2}kQ_i^2\right). \tag{4.29}$$

It has the EOM for Q_i and P_i:

$$\frac{d}{dt}Q_i(t) = \frac{1}{M}P_i(t), \tag{4.30}$$

$$\frac{d}{dt}P_i(t) = -g\langle\hat{O}_i\rangle - kQ_i(t) - \gamma P_i(t), \tag{4.31}$$

where the quantum observable $\langle\hat{O}_i\rangle$ is computed based on the configuration $\vec{Q}(t)$.

The EOM above is equally valid for both the exact dynamical path and the ML dynamical path:

$$\frac{d}{dt}Q_{i,\text{Exact}}(t) = \frac{1}{M}P_{i,\text{Exact}}(t), \tag{4.32}$$

$$\frac{d}{dt}P_{i,\text{Exact}}(t) = -g\langle\hat{O}_i\rangle_{\text{Exact}} - kQ_{i,\text{Exact}}(t) - \gamma P_{i,\text{Exact}}(t), \tag{4.33}$$

and

$$\frac{d}{dt}Q_{i,\mathrm{ML}}(t) = \frac{1}{M}P_{i,\mathrm{ML}}(t), \tag{4.34}$$

$$\frac{d}{dt}P_{i,\mathrm{ML}}(t) = -g\langle\hat{O}_i\rangle_{\mathrm{ML}} - kQ_{i,\mathrm{ML}}(t) - \gamma P_{i,\mathrm{ML}}(t). \tag{4.35}$$

Take the difference between the ML EOM and the exact EOM, define the accumulated position and momentum errors $q(t) = Q_{i,\mathrm{ML}}(t) - Q_{i,\mathrm{Exact}}(t)$, $p(t) = P_{i,\mathrm{ML}}(t) - P_{i,\mathrm{Exact}}(t)$, we get

$$\frac{d}{dt}q(t) = \frac{1}{M}p(t), \tag{4.36}$$

$$\frac{d}{dt}p(t) = -g(\langle\hat{O}_i\rangle_{\mathrm{ML}} - \langle\hat{O}_i\rangle_{\mathrm{Exact}}) - kq(t) - \gamma p(t). \tag{4.37}$$

However, here the observables depend on different configurations, $\langle\hat{O}_i\rangle_{\mathrm{ML}} = \langle\hat{O}_i\rangle_{\mathrm{ML}}(\vec{Q}_{\mathrm{ML}}(t))$, and $\langle\hat{O}_i\rangle_{\mathrm{Exact}} = \langle\hat{O}_i\rangle_{\mathrm{Exact}}(\vec{Q}_{\mathrm{Exact}}(t))$. When we take their difference, we not only need to take care about the difference between the prediction methods, we also need to take care about the difference between the configurations $\vec{Q}_{\mathrm{ML}}$ and $\vec{Q}_{\mathrm{Exact}}$.

We do a Taylor expansion and apply the assumption that the off-diagonal response $\frac{\partial\langle\hat{O}_i\rangle}{\partial Q_j}$ $(i \neq j)$ is approximately zero. We can make the difference between the observables into two terms:

$$\begin{aligned}
&\langle\hat{O}_i\rangle_{\mathrm{ML}}(\vec{Q}_{\mathrm{ML}}(t)) - \langle\hat{O}_i\rangle_{\mathrm{Exact}}(\vec{Q}_{\mathrm{Exact}}(t)) \\
&= \langle\hat{O}_i\rangle_{\mathrm{ML}}(\vec{Q}_{\mathrm{ML}}(t)) - \langle\hat{O}_i\rangle_{\mathrm{Exact}}(\vec{Q}_{\mathrm{ML}}(t)) + \frac{\partial\langle\hat{O}_i\rangle}{\partial Q_i}q(t) + o(q(t)) \\
&= \delta\langle\hat{O}_i\rangle(t) + \frac{\partial\langle\hat{O}_i\rangle}{\partial Q_i}q(t) + o(q(t)),
\end{aligned} \tag{4.38}$$

where $\delta\langle\hat{O}_i\rangle(t) = \langle\hat{O}_i\rangle_{\mathrm{ML}}(\vec{Q}_{\mathrm{ML}}(t)) - \langle\hat{O}_i\rangle_{\mathrm{Exact}}(\vec{Q}_{\mathrm{ML}}(t))$ is the single-step prediction error.

Insert the two terms back to the EOM, we get the same result as in the main text:

$$\frac{d}{dt}q(t) = \frac{1}{M}p(t), \tag{4.39}$$

$$\frac{d}{dt}p(t) = -g\delta\langle\hat{O}_i\rangle(t) - g\frac{\partial\langle\hat{O}_i\rangle}{\partial Q_i}q(t) - kq(t) - \gamma p(t) + o(q(t)). \tag{4.40}$$

4.6.4 EOM of (p,q) — Non-linear model

In the main text, we then generalized a bit to the non-linear model, which has the Hamiltonian:

$$\hat{H} = \hat{H}_q + \sum_i g\hat{O}_i G_i(Q_i) + \sum_i \left(\frac{1}{2M}P_i^2 + V_i(Q_i)\right). \tag{4.41}$$

It has the EOM for Q_i and P_i:

$$\frac{d}{dt}Q_i(t) = \frac{1}{M}P_i(t), \tag{4.42}$$

$$\frac{d}{dt}P_i(t) = -g\langle\hat{O}_i\rangle G_i^{'}(Q_i) - V_i^{'}(Q_i) - \gamma P_i(t), \tag{4.43}$$

where the quantum observable $\langle\hat{O}_i\rangle$ is still computed based on the configuration $\vec{Q}(t)$.

The EOM above is equally valid for both the exact dynamical path and the ML dynamical path:

$$\frac{d}{dt}Q_{i,\mathrm{Exact}}(t) = \frac{1}{M}P_{i,\mathrm{Exact}}(t), \tag{4.44}$$

$$\frac{d}{dt}P_{i,\mathrm{Exact}}(t) = -g\langle\hat{O}_i\rangle_{\mathrm{Exact}}G_i^{'}(Q_{i,\mathrm{Exact}}) - V_i^{'}(Q_{i,\mathrm{Exact}}) - \gamma P_{i,\mathrm{Exact}}(t), \tag{4.45}$$

and

$$\frac{d}{dt}Q_{i,\mathrm{ML}}(t) = \frac{1}{M}P_{i,\mathrm{ML}}(t), \tag{4.46}$$

$$\frac{d}{dt}P_{i,\mathrm{ML}}(t) = -g\langle\hat{O}_i\rangle_{\mathrm{ML}}G_i^{'}(Q_{i,\mathrm{ML}}) - V_i^{'}(Q_{i,\mathrm{ML}}) - \gamma P_{i,\mathrm{ML}}(t). \tag{4.47}$$

Take the difference between the ML EOM and the exact EOM, define the accumulated position and momentum errors $q(t) = Q_{i,\mathrm{ML}}(t) - Q_{i,\mathrm{Exact}}(t)$, $p(t) = P_{i,\mathrm{ML}}(t) - P_{i,\mathrm{Exact}}(t)$, expand to first order of $q(t)$, we get:

$$\frac{d}{dt}q(t) = \frac{1}{M}p(t), \tag{4.48}$$

$$\begin{aligned}\frac{d}{dt}p(t) = &-g(\langle\hat{O}_i\rangle_{\mathrm{ML}} - \langle\hat{O}_i\rangle_{\mathrm{Exact}})G_i^{'}(Q_{i,\mathrm{ML}}) - g\langle\hat{O}_i\rangle_{\mathrm{Exact}}G_i^{''}(Q_{i,\mathrm{Exact}})q(t) - V_i^{''}(Q_{i,\mathrm{Exact}})q(t) \\ &- \gamma p(t) + o(q(t)).\end{aligned} \tag{4.49}$$

We apply the same technique as in the approximately constant linear model. Insert

$$\langle\hat{O}_i\rangle_{\mathrm{ML}} - \langle\hat{O}_i\rangle_{\mathrm{Exact}} = \delta\langle\hat{O}_i\rangle(t) + \frac{\partial\langle\hat{O}_i\rangle}{\partial Q_i}q(t) + o(q(t)), \tag{4.50}$$

we get

$$\frac{d}{dt}q(t) = \frac{1}{M}p(t), \tag{4.51}$$

$$\begin{aligned}\frac{d}{dt}p(t) &= -g\delta\langle\hat{O}_i\rangle(t)G_i^{'}(Q_{i,\mathrm{ML}}) - g\frac{\partial\langle\hat{O}_i\rangle}{\partial Q_i}G_i^{'}(Q_{i,\mathrm{ML}})q(t) - g\langle\hat{O}_i\rangle_{\mathrm{Exact}}G_i^{''}(Q_{i,\mathrm{Exact}})q(t) \\ &\quad - V_i^{''}(Q_{i,\mathrm{Exact}})q(t) - \gamma p(t) + o(q(t)), \\ &= F(t) - K(t)q(t) - \gamma p(t) + o(q(t)),\end{aligned} \tag{4.52}$$

where we define the effective driving force and the effective spring constant as

$$F(t) = -g\delta\langle\hat{O}_i\rangle(t)G_i^{'}(Q_{i,\mathrm{ML}}(t)), \tag{4.53}$$

$$K(t) = g\frac{\partial\langle\hat{O}_i\rangle}{\partial Q_i}G_i^{'}(Q_{i,\mathrm{ML}}(t)) + g\langle\hat{O}_i\rangle_{\mathrm{Exact}}G_i^{''}(Q_{i,\mathrm{Exact}}(t)) + V_i^{''}(Q_{i,\mathrm{Exact}}(t)). \tag{4.54}$$

This EOM is equivalent to a damped spring with time dependent driving force and spring constant. We can prove the amplitude of the spring will not diverge if $F(t)$ is bounded and $K(t)$ does not fluctuate largely.

4.6.5 EOM of (p,q) — Generic model

The generic model has the Hamiltonian

$$\hat{H} = \hat{H}_q + \sum_{\alpha,i} g_\alpha \hat{O}_{\alpha,i} G_{\alpha,i}(\vec{P},\vec{Q}) + H_{cl}(\vec{P},\vec{Q}), \tag{4.55}$$

and the EOM

$$\frac{d}{dt}Q_j = \sum_{\alpha,i} g_\alpha \langle \hat{O}_{\alpha,i} \rangle \frac{\partial}{\partial P_j} G_{\alpha,i} + \frac{\partial}{\partial P_j} H_{cl}, \tag{4.56}$$

$$\frac{d}{dt}P_j = -\sum_{\alpha,i} g_\alpha \langle \hat{O}_{\alpha,i} \rangle \frac{\partial}{\partial Q_j} G_{\alpha,i} - \frac{\partial}{\partial Q_j} H_{cl} - \gamma P_j. \tag{4.57}$$

We can repeat the techniques above: writing down the EOM for ML and the exact simulation, making a difference of the EOM, defining q_i and p_i (here the index i cannot be suppressed), doing Taylor expansion, and combining terms up to the first order. After similar derivations, we can get the result

$$\frac{d}{dt}q_i = \sum_j \left[q_j \mathcal{K}_{q_j,q_i}(\vec{P},\vec{Q}) + p_j \mathcal{K}_{p_j,q_i}(\vec{P},\vec{Q}) \right] + \mathcal{F}_{q_i} + o(q,p), \tag{4.58}$$

$$\frac{d}{dt}p_i = \sum_j \left[q_j \mathcal{K}_{q_j,p_i}(\vec{P},\vec{Q}) + p_j \mathcal{K}_{p_j,p_i}(\vec{P},\vec{Q}) \right] + \mathcal{F}_{p_i} - \gamma p_i + o(q,p), \tag{4.59}$$

where

$$\mathcal{K}_{q_j,q_i} = \sum_{\alpha,k} g_\alpha \left(\frac{\partial \langle \hat{O}_{\alpha,k} \rangle}{\partial Q_j} \frac{\partial G_{\alpha,k}}{\partial P_i} + \langle \hat{O}_{\alpha,k} \rangle \frac{\partial^2 G_{\alpha,k}}{\partial Q_j \partial P_i} \right) + \frac{\partial^2 H_{cl}}{\partial Q_j \partial P_i}, \tag{4.60}$$

$$\mathcal{K}_{p_j,q_i} = \sum_{\alpha,k} g_\alpha \left(\frac{\partial \langle \hat{O}_{\alpha,k} \rangle}{\partial P_j} \frac{\partial G_{\alpha,k}}{\partial P_i} + \langle \hat{O}_{\alpha,k} \rangle \frac{\partial^2 G_{\alpha,k}}{\partial P_j \partial P_i} \right) + \frac{\partial^2 H_{cl}}{\partial P_j \partial P_i}, \tag{4.61}$$

$$\mathcal{K}_{q_j,p_i} = -\sum_{\alpha,k} g_\alpha \left(\frac{\partial \langle \hat{O}_{\alpha,k} \rangle}{\partial Q_j} \frac{\partial G_{\alpha,k}}{\partial Q_i} + \langle \hat{O}_{\alpha,k} \rangle \frac{\partial^2 G_{\alpha,k}}{\partial Q_j \partial Q_i} \right) - \frac{\partial^2 H_{cl}}{\partial Q_j \partial Q_i}, \tag{4.62}$$

$$\mathcal{K}_{p_j,p_i} = -\sum_{\alpha,k} g_\alpha \left(\frac{\partial \langle \hat{O}_{\alpha,k} \rangle}{\partial P_j} \frac{\partial G_{\alpha,k}}{\partial Q_i} + \langle \hat{O}_{\alpha,k} \rangle \frac{\partial^2 G_{\alpha,k}}{\partial P_j \partial Q_i} \right) - \frac{\partial^2 H_{cl}}{\partial P_j \partial Q_i}, \tag{4.63}$$

$$\mathcal{F}_{q_i} = \sum_{\alpha,j} g_\alpha \delta \langle \hat{O}_{\alpha,j} \rangle(t) \frac{\partial}{\partial P_i} G_{\alpha,j}(\vec{P}, \vec{Q}), \tag{4.64}$$

$$\mathcal{F}_{p_i} = -\sum_{\alpha,j} g_\alpha \delta \langle \hat{O}_{\alpha,j} \rangle(t) \frac{\partial}{\partial Q_i} G_{\alpha,j}(\vec{P}, \vec{Q}). \tag{4.65}$$

4.6.6 Proof of Proposition 1

Here we prove that the approximately constant linear model satisfies the Error Bounded Property in Def. 1 if $K > 0$. We use the analogy to a damped harmonic oscillating spring, phrasing the error force $F(t)$ in the main text as the "driving force" and the error stiffness K in the main text as the "spring constant". For a damped spring, given a bounded driving force, even if the force is tuned to drive the spring optimally, as long as $K, \gamma > 0$, the spring cannot be driven to infinite amplitude. This can be seen by the following worst-case analysis. In a worst case scenario, the driving force is set to be the maximal value in the direction of the spring movement. We know a constant driving force means a shift of the reference point of the spring. Therefore, by shifting the reference point back and forth, the driving force at most linearly increases the amplitude with the motion cycles of the spring. However, a finite damping decreases the amplitude of the spring by a constant factor in each cycle. Therefore, for a large enough initial amplitude, the decrement of the amplitude due to the damping must exceed the increment of the amplitude due to the driving force in the cycle, and thus

the amplitude in the next cycle must be smaller than the initial one, which tells us that the damped spring cannot be driven to infinite amplitude.

Now we analyze the relation between the maximal amplitude $\bar{q}$, the maximal momentum $\bar{p}$, and the maximal driving force $\bar{F}$, using the dimensional analysis. At t_{init}, there are no accumulated errors, i.e. $q(t_{\text{init}}) = p(t_{\text{init}}) = 0$. Therefore, the only physical quantity that carries the dimension of length is the maximal driving force $[\bar{F}] = [M][L][T]^{-2}$, where $[M]$, $[L]$, and $[T]$ are the dimension of mass, length, and time, respectively. Note that the maximal amplitude $[\bar{q}] = [L]$ and the maximal momentum $\bar{p} = [L][T]^{-1}$ both carries power one of the length dimension $[L]$. Therefore, by dimensional analysis, they are both proportional to the maximal driving force $\bar{F}$. i.e. $\exists\ \bar{C}_q, \bar{C}_p$ such that $\bar{q} = \bar{C}_q\bar{F}$, $\bar{p} = \bar{C}_p\bar{F}$.

For any $\epsilon > 0$, if $|\delta\langle\hat{O}_i\rangle(t)|^2 \leq \epsilon$, by the definition $F(t) = -g\delta\langle\hat{O}_i\rangle(t)$, we have $|F(t)| \leq |g|\sqrt{\epsilon}$. By the analogy above, it means that the maximal force $\bar{F} = |g|\sqrt{\epsilon}$. Therefore, by the meaning of the maximal amplitude and the maximal momentum, there are $|q(t)| \leq \bar{q} = \bar{C}_q\bar{F} = \bar{C}_q|g|\sqrt{\epsilon}$ and $|p(t)| \leq \bar{p} = \bar{C}_p\bar{F} = \bar{C}_p|g|\sqrt{\epsilon}$. Define two new constants $C_q = |g|\bar{C}_q$ and $C_p = |g|\bar{C}_p$, we get $|q(t)| \leq C_q\sqrt{\epsilon}$ and $|p(t)| \leq C_p\sqrt{\epsilon}$, which is what we want to show. This completes the proof of Prop. 1. □

4.6.7 Proof of Theorem 1 (Error bounded condition for non-linear model)

Here we present the formal version of Thm. 1 in the main text. We use the analogy to a damped harmonic oscillating spring, phrasing the error force $F(t)$ in the main text as the "driving force" and the error stiffness $K(t)$ in the main text as the "spring constant".

Theorem 3 (Error Bounded Condition for non-linear model)**.** *Consider a damped harmonic*

oscillator with the following EOM:

$$\frac{d}{dt}q(t) = \frac{1}{M}p(t), \tag{4.66}$$
$$\frac{d}{dt}p(t) = F(t) - K(t)q(t) - \gamma p(t) + o(q(t)), \tag{4.67}$$

where q is the classical coordinate, p is the classical momentum, t is time, M is the mass of the oscillator, $F(t)$ is a time-dependent driving force, $K(t)$ is a time-dependent spring constant, γ is the damping coefficient.The initial condition is $q(t_{init}) = p(t_{init}) = 0$.

Given $K_{\max} > K_{\min} > M(\gamma/2)^2$ satisfying the following inequality:

$$\frac{K_{\max}}{K_{\min}} < \exp\left[2\left(\frac{arctan\ \omega_{\min}}{\omega_{\min}} + \frac{\pi - arctan\ \omega_{\max}}{\omega_{\max}}\right)\right], \tag{4.68}$$

where $\omega_{\max} = \sqrt{\frac{K_{\max}}{M(\gamma/2)^2} - 1}$, $\omega_{\min} = \sqrt{\frac{K_{\min}}{M(\gamma/2)^2} - 1}$.

If $K(t) \in [K_{\min}, K_{\max}]$ for all t, and $G_{\alpha,i}(\vec{P}, \vec{Q})$ and its first derivatives are bounded, then the Error Bounded Property in Def. 1 is satisfied, i.e. $\exists\ C_q, C_p > 0$ such that $\forall \epsilon > 0$, if $|\delta\langle\hat{O}_i\rangle(t)|^2 \leq \epsilon$ for all t, then there are

$$|q(t)| \leq C_q\sqrt{\epsilon}, \quad |p(t)| \leq C_p\sqrt{\epsilon}, \quad \textit{for all } t. \tag{4.69}$$

Proof. Consider a damped harmonic oscillator with the following EOM:

$$\frac{d}{dt}q(t) = \frac{1}{M}p(t), \tag{4.70}$$
$$\frac{d}{dt}p(t) = F(t) - K(t)q(t) - \gamma p(t) + o(q(t)), \tag{4.71}$$

where q is the classical coordinate, p is the classical momentum, t is time, M is the mass of the oscillator, $F(t)$ is a time-dependent driving force, $K(t)$ is a time-dependent spring constant, $\gamma > 0$ is the damping coefficient. We assume $F(t) \in [-\bar{F}, \bar{F}]$, $K(t) \in [K_{\min}, K_{\max}]$, where $K_{\max} > K_{\min} > M(\gamma/2)^2$. Note that with Eq. 4.53, $F(t) = -g\delta\langle\hat{O}_i\rangle(t)G_i'(Q_{i,\mathrm{ML}}(t))$,

the assumption $|\delta\langle\hat{O}_i\rangle(t)|^2 \leq \epsilon$ implies $\bar{F} \leq O(\sqrt{\epsilon})$ given bounded G_i'.

We consider the worst case scenario. The mass on the spring starts from one side with a large amplitude. As the mass moving towards the other side, the driving force always keeps the maximal value towards the other side. Before the mass crosses the origin, the spring constant is set as $K_{\max}$ to maximize the drag towards the other side. After the mass crosses the origin, the spring constant is set as $K_{\min}$ to minimize the burden for its moving as far as possible. In this worst case scenario, the mass will stop at its largest amplitude on the other side. If this amplitude on the other side is smaller than the one it started with, than the spring cannot have diverging amplitude, and therefore the error converges.

We now analyze this worst case scenario. Assume the mass starts at $q(-t_0) = -q_0$, $\dot{q}(-t_0) = 0$. At time $t = 0$ it crosses the origin, $q(0) = 0$, with a velocity $\dot{q}(0) = v$. At time $t = t_1$ it stops on the other side at $q(t_1) = q_1$, $\dot{q}(t_1) = 0$.

Before the mass crosses the origin, the spring constant is $K_{\max}$. The EOM is

$$\ddot{q}(t) = -\gamma\dot{q}(t) - \frac{K_{\max}}{M}q(t) + \frac{\bar{F}}{M}, \quad t \in [-t_0, 0]. \tag{4.72}$$

The EOM has a general solution

$$q(t) = Ae^{-\frac{\gamma}{2}t}\sin\Omega_{\max}t + Be^{-\frac{\gamma}{2}t}\cos\Omega_{\max}t + \frac{\bar{F}}{K_{\max}}, \tag{4.73}$$

where $\Omega_{\max} = \sqrt{\frac{K_{\max}}{M} - (\frac{\gamma}{2})^2}$.

Inserting the boundary condition at $t = 0$, we get equations

$$q(0) = 0 = B + \frac{\bar{F}}{K_{\max}}, \tag{4.74}$$

$$\dot{q}(0) = v = \Omega_{\max}A - \frac{\gamma}{2}B, \tag{4.75}$$

from which we solve

$$A = \frac{1}{\Omega_{\max}}\left(v - \frac{\gamma}{2}\frac{\bar{F}}{K_{\max}}\right), \tag{4.76}$$

$$B = -\frac{\bar{F}}{K_{\max}}. \tag{4.77}$$

Inserting the boundary condition at $t = -t_0$, we get equations

$$q(-t_0) = -q_0 = -Ae^{\frac{\gamma}{2}t_0}\sin\Omega_{\max}t_0 + Be^{\frac{\gamma}{2}t_0}\cos\Omega_{\max}t_0 + \frac{\bar{F}}{K_{\max}}, \tag{4.78}$$

$$\begin{aligned}\dot{q}(-t_0) = 0 = A&\left(\frac{\gamma}{2}e^{\frac{\gamma}{2}t_0}\sin\Omega_{\max}t_0 + \Omega_{\max}e^{\frac{\gamma}{2}t_0}\cos\Omega_{\max}t_0\right)\\ &+ B\left(-\frac{\gamma}{2}e^{\frac{\gamma}{2}t_0}\cos\Omega_{\max}t_0 + \Omega_{\max}e^{\frac{\gamma}{2}t_0}\sin\Omega_{\max}t_0\right).\end{aligned} \tag{4.79}$$

We can solve t_0 from the second equation:

$$t_0 = \frac{1}{\Omega_{\max}}\text{arccot}\frac{(\gamma/2)A + \Omega_{\max}B}{-\Omega_{\max}A + (\gamma/2)B} = \frac{1}{\Omega_{\max}}\text{arccot}\left(-\frac{(\gamma/2)v - \bar{F}/M}{\Omega_{\max}v}\right), \tag{4.80}$$

where we have inserted the solution of A and B. We can then insert everything into the first equation to solve q_0, but we do not do it now.

Let's also take a look at the time after the mass crosses the origin. The spring constant changes to $K_{\min}$. The EOM is

$$\ddot{q}(t) = -\gamma\dot{q}(t) - \frac{K_{\min}}{M}q(t) + \frac{\bar{F}}{M}, \quad t \in [0, t_1]. \tag{4.81}$$

The EOM has a general solution

$$q(t) = Ce^{-\frac{\gamma}{2}t}\sin\Omega_{\min}t + De^{-\frac{\gamma}{2}t}\cos\Omega_{\min}t + \frac{\bar{F}}{K_{\min}}, \tag{4.82}$$

where $\Omega_{\min} = \sqrt{\frac{K_{\min}}{M} - (\frac{\gamma}{2})^2}$.

Inserting the boundary condition at $t = 0$, we get equations

$$q(0) = 0 = D + \frac{\bar{F}}{K_{\min}}, \tag{4.83}$$

$$\dot{q}(0) = v = \Omega_{\min} C - \frac{\gamma}{2} D, \tag{4.84}$$

from which we solve

$$C = \frac{1}{\Omega_{\min}} \left(v - \frac{\gamma}{2} \frac{\bar{F}}{K_{\min}} \right), \tag{4.85}$$

$$D = -\frac{\bar{F}}{K_{\min}}. \tag{4.86}$$

Inserting the boundary condition at $t = t_1$, we get equations

$$q(t_1) = q_1 = C e^{-\frac{\gamma}{2} t_1} \sin \Omega_{\min} t_1 + D e^{-\frac{\gamma}{2} t_1} \cos \Omega_{\min} t_1 + \frac{\bar{F}}{K_{\min}}, \tag{4.87}$$

$$\begin{aligned} \dot{q}(t_1) = 0 = C & \left(-\frac{\gamma}{2} e^{-\frac{\gamma}{2} t_1} \sin \Omega_{\min} t_1 + \Omega_{\min} e^{-\frac{\gamma}{2} t_1} \cos \Omega_{\min} t_1 \right) \\ & + D \left(-\frac{\gamma}{2} e^{-\frac{\gamma}{2} t_1} \cos \Omega_{\min} t_1 - \Omega_{\min} e^{-\frac{\gamma}{2} t_1} \sin \Omega_{\min} t_1 \right). \end{aligned} \tag{4.88}$$

We can solve t_1 from the second equation:

$$t_1 = \frac{1}{\Omega_{\min}} \text{arccot} \frac{(\gamma/2) C + \Omega_{\min} D}{\Omega_{\min} C - (\gamma/2) D} = \frac{1}{\Omega_{\min}} \text{arccot} \frac{(\gamma/2) v - \bar{F}/M}{\Omega_{\min} v}, \tag{4.89}$$

where we have inserted the solution of C and D. Note that comparing to the case before, there is no minus sign in the arccot function.

To have a bounded error, we want that for large enough q_0, there is $\frac{q_1}{q_0} < 1$, where q_0 is the starting amplitude and q_1 is the stopping amplitude, i.e. the amplitude never diverges. Iteratively we consider q_1 as the next starting amplitude, and we can see the sequence of amplitudes converges in the long time. Note that the amplitude has the dimension of length, and among all given parameters, only the maximal force $\bar{F}$ carries the dimension of length.

Using dimension analysis, we see that the maximal amplitude the system could reach will be proportional to the maximal force $\bar{F}$. The maximal momentum the system could reach will also be proportional to $\bar{F}$ from dimension analysis. i.e. $q(t) \leq O(\bar{F})$, $p(t) \leq O(\bar{F})$. Combining with the assumption $\bar{F} \leq O(\sqrt{\epsilon})$, it leads to $q(t) \leq O(\sqrt{\epsilon})$, $p(t) \leq O(\sqrt{\epsilon})$, which is what we want to show.

Now the final step is to simplify the condition $\frac{q_1}{q_0} < 1$. Note that for arbitrarily large q_0, the velocity v can also be arbitrarily large. Therefore, we can consider the limit $\bar{F}/v \to 0$. Under this limit,

$$A/v \to \frac{1}{\Omega_{\max}}, \tag{4.90}$$

$$B/v \to 0, \tag{4.91}$$

$$C/v \to \frac{1}{\Omega_{\min}}, \tag{4.92}$$

$$D/v \to 0, \tag{4.93}$$

$$t_0 \to \frac{1}{\Omega_{\max}} \operatorname{arccot}\left(-\frac{(\gamma/2)}{\Omega_{\max}}\right) = \frac{\pi - \arctan(2\Omega_{\max}/\gamma)}{\Omega_{\max}}, \tag{4.94}$$

$$t_1 \to \frac{1}{\Omega_{\min}} \operatorname{arccot}\frac{(\gamma/2)}{\Omega_{\min}} = \frac{\arctan(2\Omega_{\min}/\gamma)}{\Omega_{\min}}. \tag{4.95}$$

Finally,

$$\begin{aligned}
\frac{q_1}{q_0} &= \frac{Ce^{-\frac{\gamma}{2}t_1}\sin\Omega_{\min}t_1 + De^{-\frac{\gamma}{2}t_1}\cos\Omega_{\min}t_1 + \bar{F}/K_{\min}}{Ae^{\frac{\gamma}{2}t_0}\sin\Omega_{\max}t_0 - Be^{\frac{\gamma}{2}t_0}\cos\Omega_{\max}t_0 - \bar{F}/K_{\max}} \\
&\to \frac{(1/\Omega_{\min})e^{-\frac{\gamma}{2}t_1^*}(\Omega_{\min}/\sqrt{K_{\min}/M})}{(1/\Omega_{\max})e^{\frac{\gamma}{2}t_0^*}(\Omega_{\max}/\sqrt{K_{\max}/M})} \\
&= \sqrt{\frac{K_{\max}}{K_{\min}}}e^{-\frac{\gamma}{2}(t_0^*+t_1^*)},
\end{aligned} \tag{4.96}$$

where we have used the equality: $\sin\left[\operatorname{arccot}\left(-\frac{(\gamma/2)}{\Omega_{\max}}\right)\right] = \frac{\Omega_{\max}}{\sqrt{K_{\max}/M}}$, $\sin\left[\operatorname{arccot}\frac{(\gamma/2)}{\Omega_{\min}}\right] = \frac{\Omega_{\min}}{\sqrt{K_{\min}/M}}$. Here t_0^* and t_1^* are the limiting values in Eq. 4.94 and 4.95, respectively.

We define $\omega_{\max} = \frac{\Omega_{\max}}{(\gamma/2)} = \sqrt{\frac{K_{\max}}{M(\gamma/2)^2} - 1}$ and $\omega_{\min} = \frac{\Omega_{\min}}{(\gamma/2)} = \sqrt{\frac{K_{\min}}{M(\gamma/2)^2} - 1}$. After rear-

ranging the terms, we simplifies the condition $\frac{q_1}{q_0} < 1$ into

$$\frac{K_{\max}}{K_{\min}} < \exp\left[2\left(\frac{\arctan\,\omega_{\min}}{\omega_{\min}} + \frac{\pi - \arctan\,\omega_{\max}}{\omega_{\max}}\right)\right], \tag{4.97}$$

which is the inequality we see in Eq. 4.68 in Thm. 3. This completes the proof of Thm. 3. □

Note that the inequality in Eq. 4.68 in Thm. 3 is satisfied in the limit $\frac{K_{\max}-K_{\min}}{K_{\min}} \to 0$. We can see this by take a log on both sides of the inequality and get

$$\log\left(1 + \frac{K_{\max} - K_{\min}}{K_{\min}}\right) < 2\left(\frac{\arctan\,\omega_{\min}}{\omega_{\min}} + \frac{\pi - \arctan\,\omega_{\max}}{\omega_{\max}}\right), \tag{4.98}$$

whose left hand side is $O(\frac{K_{\max}-K_{\min}}{K_{\min}})$ and right hand side is $O(1)$ because $\omega_{\min} \approx \omega_{\max}$. Therefore, in the limit $\frac{K_{\max}-K_{\min}}{K_{\min}} \to 0$, the inequality always holds. This agrees with the Error Bounded Property of the approximately constant linear model stated in Prop. 1. (Actually the approximately constant linear model satisfies the Error Bounded Property under a more general condition: instead of $K > M(\gamma/2)^2$ we only need $K > 0$ for the approximately constant linear model.)

If we transform the coordinates of the system to their normal modes, because the normal modes are also described by damped harmonic oscillators, all the analysis works the same for normal modes. This addresses the comment under Thm. 1 in the main text.

In Figure 4.7, we show an example of the fluctuation of the error stiffness $K(t) = k - g\frac{\partial n}{\partial Q}$ during the Holstein model dynamics. We see that the error stiffness $K(t) > M(\gamma/2)^2 = 0.0025$, where $M = 1$ and $\gamma = 0.1$. The highest and lowest points in the plot are 0.7104 and 0.5011. We insert these numbers into Eq. 4.68. The left hand side of the condition results in 1.418, and the right hand side 1.501. Therefore, we confirm that the inequality in Eq. 4.68 in Thm. 3 is satisfied during the time range we are interested in, and thus the Error Bounded Property is satisfied in the Holstein model.

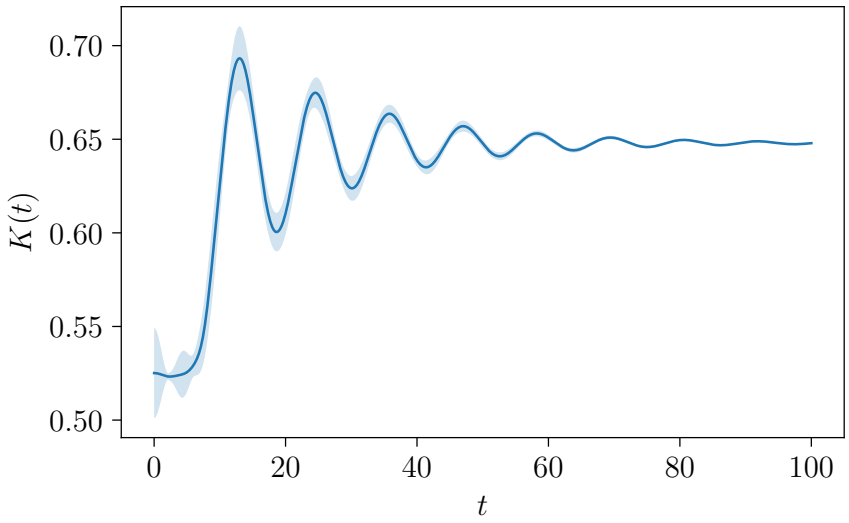

Figure 4.7: Numerical measurement of the error stiffness $K(t) = k - g\frac{\partial n}{\partial Q}$ during the time range of interest. $g = 1.4$ is used in the experiment. The highest point in the plot reaches 0.7104, and the lowest is 0.5011. Inserting these values into Eq. 4.68, we get $LHS = 1.418 < 1.501 = RHS$.

4.6.8 Provably efficient adiabatic learning

Here we provide more details about how the PEAL algorithm is performed.

Step I: Collecting data. To be able to train a learning model, we first need to collect data samples from the distribution we are interested in. For example, one can sample a few different initial conditions, and use either classical solver or quantum computer to obtain a few dynamical evolution paths. The "configuration"-"observable" pairs sampled from those paths can serve as the data set we need. If one wants to predict other k-local observable that is not involved in the dynamics, one can compute that observable along the paths and collect the data for the next training step as well.

Step II: ML training. A provable efficient ML algorithm for predicting ground state properties was presented recently [60]. Here we apply this algorithm to adiabatic dynamics. On the data set collected in Step I, a nonlinear feature map with geometrically local region information is performed. A model is trained with an l_1-regularized regression (LASSO) on the features. Hyperparameters in the model are properly chosen. One can train a single

model for one type of observable if the system has translation symmetry. The same training process can be applied to the data set of observable that is not involved in the dynamics. Moreover, the learning model can be transferred to unseen physical parameter g_α in the Hamiltonian. An example is shown in our numerical experiment, also illustrated in Fig. 4.3 in the main text.

Step III: ML prediction. For dynamical evolution paths with unseen initial conditions, we can use the PEAL prediction to speed up the simulation, instead of repeatedly using costly classical solver or quantum computer. The dynamical simulation is realized by iteratively updating the classical degree of freedom and the quantum degree of freedom. The classical updating step is done by classical ODE solver. The quantum updating step is done by ML prediction. In each iteration, we can add an extra correction step to achieve symmetry-preserving PEAL (see details in the following Appendix 4.6.10). The provably efficiency and controllable error of the PEAL algorithm will be presented later in Thm. 6.

Before we formally present Thm. 6, we would like to mention two other theorems introduced in other works. In Ref. [60], the authors prove two theorems:

Theorem 4. *Consider any family of n-qubit geometrically-local Hamiltonians* $\{H(x) : x \in [-1,1]^m\}$ *in a finite spatial dimension, such that each local term in* $H(x)$ *depends smoothly on* x*, and the smallest eigenvalue and the next smallest eigenvalues have a constant gap* $\geq \Omega(1)$ *between them. Then the ground state properties can be efficiently predicted.*

Theorem 5. *Given* $n, \delta > 0, \frac{1}{e} > \epsilon > 0$ *and a training data set* $\{x_t, y_t\}_{t=1}^N$ *of size*

$$N = \log(n/\delta)2^{polylog(1/\epsilon)},$$

where x_t *is sampled from an unknown distribution* D *and* $|y_t - Tr(O\rho(x_t))| \leq \epsilon$ *for any observable* O *with eigenvalues between* -1 *and* 1 *that can be written as a sum of geometrically local observables. With a proper choice of the efficiently computable hyperparameters* δ_1, δ_2*,*

and B, the learned function $h^*(x) = \mathbf{w}^* \cdot \phi(z)$ satisfies

$$\mathbb{E}_{x\sim D} \left| h^*(z) - Tr(O\rho(z)) \right|^2 \leq \epsilon$$

with probability at least $1-\delta$. The training and prediction time of the classical ML model are bounded by $\mathcal{O}(nN) = n\log(n/\delta)2^{polylog(1/\epsilon)}$.

The request in the first one, that the Hamiltonian has a constant gap, can be soften into that the correlation length has a finite upper bound.

Now we present the formal version of Thm. 2 in the main text.

Theorem 6 (Provably Efficient Adiabatic Learning (PEAL) Theorem)**.** *Given $n, \delta, \eta > 0$, $\frac{1}{e} > \epsilon > 0$ and a training data set $\{(g_\alpha, \vec{P}, \vec{Q})_l, \langle \hat{O}_{\alpha,i}\rangle_l\}_{l=1}^N$ of size*

$$N = \log(n/\delta)2^{polylog(1/\epsilon)}, \tag{4.99}$$

where $l \in \{1, 2, \ldots, N\}$ is the index of data points, $(g_\alpha)_l$ is the coupling constant used when collecting the data, $(\vec{P}, \vec{Q})_l$ is classical variables sampled from exact simulation data, $\hat{O}_{\alpha,i}$ is an observable with eigenvalues in $[-1, 1]$ that can be written as a sum of geometrically local observables, $\langle \hat{O}_{\alpha,i}\rangle_l$ is the ground state expectation value with an n-qubit gapped geometrically local Hamiltonian $\hat{H}((\vec{P}, \vec{Q})_l)$. Apply an ML predicted model $\mathcal{M}$ learned with a proper choice of the efficiently computable hyperparameters. When the Error Bounded Property in Def. 1 is satisfied, a T-step PEAL prediction $Q_{i,PEAL}(T)$ comparing to the exact dynamical process $Q_{i,Exact}(T)$, i.e. the accumulated error, has an error bound

$$|Q_{i,PEAL}(T) - Q_{i,Exact}(T)| \leq O(\sqrt{T\epsilon/\eta}) \tag{4.100}$$

with probability $\mathbb{P} \geq 1 - \eta - \delta$.

If further assume the learning error of model $\mathcal{M}$ is sub-Gaussian distributed, the error

bound can be improved into

$$|Q_{i,PEAL}(T) - Q_{i,Exact}(T)| \leq O(\sqrt{2\epsilon \log(2T/\eta)}) \tag{4.101}$$

with probability $\mathbb{P} \geq 1 - \eta - \delta$.

If further more assume the learning error of model $\mathcal{M}$ *is bounded by* $\sqrt{\epsilon}$ *almost surely, the error bound can be further improved into*

$$|Q_{i,PEAL}(T) - Q_{i,Exact}(T)| \leq O(\sqrt{\epsilon}) \tag{4.102}$$

with probability $\mathbb{P} \geq 1 - \delta$*, i.e. the error is bounded by a constant.*

The accumulated error of classical variables P_i *and all* k*-local, bounded quantum observables also have the same scaling as the accumulated error of* Q_i.

Proof. To be able to apply the Error Bounded Property in Def. 1, we request that the prediction errors $|\delta\langle\hat{O}\rangle| = |\langle\hat{O}\rangle_{\text{PEAL}}(\vec{P}_{\text{PEAL}}, \vec{Q}_{\text{PEAL}}) - \langle\hat{O}\rangle_{\text{Exact}}(\vec{P}_{\text{PEAL}}, \vec{Q}_{\text{PEAL}})|$ are upper bounded for all T number of time steps. From the Thm. 5 above, we learn

$$\mathbb{E}|\delta\langle\hat{O}\rangle|^2 \leq \epsilon, \tag{4.103}$$

from which we can estimate the probability of a single-shot prediction error going beyond a threshold:

$$\begin{aligned} \mathbb{P}\left[|\delta\langle\hat{O}\rangle| \geq A\sqrt{\epsilon}\right] &= \mathbb{P}\left[|\delta\langle\hat{O}\rangle|^2 \geq A^2\epsilon\right] \\ &\leq \frac{\mathbb{E}|\delta\langle\hat{O}\rangle|^2}{A^2\epsilon} \\ &\leq \frac{1}{A^2}, \end{aligned} \tag{4.104}$$

where $A \geq 0$ is a constant factor we choose to describe the threshold. In the second line, we apply the Markov's inequality because $|\delta\langle\hat{O}\rangle|^2$ is non-negative.

For a dynamical simulation process with T number of prediction stpes, the probability of any prediction error going beyond the threshold is controlled by the union bound:

$$\mathbb{P}\left[\bigcup_{i=1}^{T}\left\{|\delta\langle\hat{O}\rangle(t_i)| \geq A\sqrt{\epsilon}\right\}\right] \leq \sum_{i=1}^{T}\mathbb{P}\left[|\delta\langle\hat{O}\rangle(t_i)| \geq A\sqrt{\epsilon}\right] \leq \frac{T}{A^2}. \tag{4.105}$$

Taking into account that the trained model could have at most δ probability of failure, we get the probability of not being able to apply our PEAL method is at most $(\frac{T}{A^2}+\delta)$ by another union bound.

When we are able to control all the prediction errors under the threshold $A\sqrt{\epsilon}$, we have

$$|q(t)| = |Q_{i,\mathrm{PEAL}}(T) - Q_{i,\mathrm{Exact}}(T)| \leq O(A\sqrt{\epsilon}) \tag{4.106}$$

by the Error Bounded Property in Def. 1. From the analysis above, we see this is applicable with a probability at least $(1-\frac{T}{A^2}-\delta)$.

For given $\eta > 0$, we choose the threshold factor $A = \sqrt{T/\eta}$, such that $\eta = \frac{T}{A^2}$. Therefore, we get our most general bound

$$|Q_{i,\mathrm{PEAL}}(T) - Q_{i,\mathrm{Exact}}(T)| \leq O(\sqrt{T\epsilon/\eta}) \tag{4.107}$$

with probability $\mathbb{P} \geq 1-\eta-\delta$.

This $(1-\eta-\delta)$ behavior in the probability is expected, because we have an adiabatic hybrid algorithm with both quantum and classical updates. The δ failure comes from approximating the quantum algorithm, and the η failure comes from the adiabatic quantum-classical dynamics.

This most general bound is showing a $\sqrt{T}$ behavior, which happens to be the same as a diffusion model.

We can improve this bound if we can acquire more knowledge on the distribution of the prediction error $\delta\langle\hat{O}\rangle$. For example, if $\delta\langle\hat{O}\rangle$ has a sub-Gaussian distribution with a

moment-generating function (MGF)

$$M_{\delta\langle\hat{O}\rangle}(s) = \mathbb{E}\left[e^{s\delta\langle\hat{O}\rangle}\right] \leq \exp\frac{\epsilon s^2}{2}, \tag{4.108}$$

then we can apply the Chernoff bound and get

$$\mathbb{P}\left[|\delta\langle\hat{O}\rangle| \geq B\sqrt{\epsilon}\right] \leq 2\exp\left(-\frac{(B\sqrt{\epsilon})^2}{2\epsilon}\right) = 2\exp\left(-B^2/2\right), \tag{4.109}$$

where B is also a threshold factor.

Repeat the union bound argument, we can get $|Q_{i,\mathrm{PEAL}}(T) - Q_{i,\mathrm{Exact}}(T)| \leq O(B\sqrt{\epsilon})$ with a probability at least $(1-2T\exp(-B^2/2)-\delta)$. For given $\eta > 0$, we choose $B = \sqrt{2\log(2T/\eta)}$, such that $\eta = 2T\exp(-B^2/2)$. Therefore, we get our bound with assuming sub-Gaussian prediction error

$$|Q_{i,\mathrm{PEAL}}(T) - Q_{i,\mathrm{Exact}}(T)| \leq O(\sqrt{2\epsilon\log(2T/\eta)}) \tag{4.110}$$

with probability $\mathbb{P} \geq 1 - \eta - \delta$.

This improves the general $\sqrt{T}$ behavior to a better $\sqrt{\log(T)}$ behavior.

We can improve this bound even further if we add even stronger assumption on the distribution of the prediction error $\delta\langle\hat{O}\rangle$. If we assume there exists a constant factor C such that $|\delta\langle\hat{O}\rangle| \leq C\sqrt{\epsilon}$ almost surely, then we can directly apply our Thm. 3 and get

$$|Q_{i,\mathrm{PEAL}}(T) - Q_{i,\mathrm{Exact}}(T)| \leq O(\sqrt{\epsilon}) \tag{4.111}$$

with probability $\mathbb{P} \geq 1 - \delta$.

This is a constant bound which is independent on T, i.e. the accumulated position error of the dynamical simulation is bounded by a constant.

Because we also have a controlled $|p(t)|$ in Thm. 3, all the arguments above are also true

if replacing Q by P.

With the proof of the following lemma, we complete the proof of Thm. 6. □

Lemma 1. *All k-local, bounded observables have the same provably efficient bound under PEAL, no matter whether they are involved in the dynamics or not. For such an observable $\hat{\Omega}$, given a training data set $\{(\vec{P},\vec{Q})_l, \langle\hat{\Omega}\rangle_l\}_{l=1}^N$ of size N same as in Thm. 6, under various assumptions in Thm. 6, the accumulated error $|\langle\hat{\Omega}\rangle_{PEAL}(\vec{P}_{PEAL}(T),\vec{Q}_{PEAL}(T)) - \langle\hat{\Omega}\rangle_{Exact}(\vec{P}_{Exact}(T),\vec{Q}_{Exact}(T))|$ holds similar bounds as in Eq. 4.100, 4.101, and 4.102.*

Proof. The accumulated error for an observable is defined as

$$|\langle\hat{\Omega}\rangle_{\mathrm{PEAL}}(\vec{P}_{\mathrm{PEAL}}(T),\vec{Q}_{\mathrm{PEAL}}(T)) - \langle\hat{\Omega}\rangle_{\mathrm{Exact}}(\vec{P}_{\mathrm{Exact}}(T),\vec{Q}_{\mathrm{Exact}}(T))|. \tag{4.112}$$

There are two source of error in this operator learning: one from the PEAL path $(\vec{P}_{\mathrm{PEAL}}(T),\vec{Q}_{\mathrm{PEAL}}(T))$ deviate from the exact simulation $(\vec{P}_{\mathrm{Exact}}(T),\vec{Q}_{\mathrm{Exact}}(T))$, the other from the single-step ML prediction error. In terms of formula, we have

$$\begin{aligned}
&|\langle\hat{\Omega}\rangle_{\mathrm{PEAL}}(\vec{P}_{\mathrm{PEAL}}(T),\vec{Q}_{\mathrm{PEAL}}(T)) - \langle\hat{\Omega}\rangle_{\mathrm{Exact}}(\vec{P}_{\mathrm{Exact}}(T),\vec{Q}_{\mathrm{Exact}}(T))| \\
\leq\ &|\langle\hat{\Omega}\rangle_{\mathrm{PEAL}}(\vec{P}_{\mathrm{PEAL}}(T),\vec{Q}_{\mathrm{PEAL}}(T)) - \langle\hat{\Omega}\rangle_{\mathrm{Exact}}(\vec{P}_{\mathrm{PEAL}}(T),\vec{Q}_{\mathrm{PEAL}}(T))| \\
&+ |\langle\hat{\Omega}\rangle_{\mathrm{Exact}}(\vec{P}_{\mathrm{PEAL}}(T),\vec{Q}_{\mathrm{PEAL}}(T)) - \langle\hat{\Omega}\rangle_{\mathrm{Exact}}(\vec{P}_{\mathrm{Exact}}(T),\vec{Q}_{\mathrm{Exact}}(T))|.
\end{aligned} \tag{4.113}$$

We first analyze the second term by the perturbation theory. We have

$$\langle\hat{\Omega}\rangle_{\mathrm{Exact}}(\vec{P}_{\mathrm{PEAL}}(T),\vec{Q}_{\mathrm{PEAL}}(T)) = \langle \mathrm{GS}_{\mathrm{PEAL}}|\hat{\Omega}|\mathrm{GS}_{\mathrm{PEAL}}\rangle, \tag{4.114}$$

$$\langle\hat{\Omega}\rangle_{\mathrm{Exact}}(\vec{P}_{\mathrm{Exact}}(T),\vec{Q}_{\mathrm{Exact}}(T)) = \langle \mathrm{GS}_{\mathrm{Exact}}|\hat{\Omega}|\mathrm{GS}_{\mathrm{Exact}}\rangle, \tag{4.115}$$

where $|\mathrm{GS}_{\mathrm{PEAL/Exact}}\rangle = |\mathrm{GS}(\vec{P}_{\mathrm{PEAL/Exact}}(T),\vec{Q}_{\mathrm{PEAL/Exact}}(T))\rangle$ is the ground state wavefunction for the Hamiltonian with classical parameters $(\vec{P}_{\mathrm{PEAL/Exact}}(T),\vec{Q}_{\mathrm{PEAL/Exact}}(T))$, respectively.

Note that $(\vec{P}, \vec{Q})$ are served as parameters of the Hamiltonian. For slightly different $(\vec{P}_{\text{PEAL}}(T), \vec{Q}_{\text{PEAL}}(T))$ and $(\vec{P}_{\text{Exact}}(T), \vec{Q}_{\text{Exact}}(T))$, the corresponding Hamiltonians are slightly different, and thus the difference between the ground states can be analyzed by first order perturbation

$$|\text{GS}_{\text{PEAL}}\rangle - |\text{GS}_{\text{Exact}}\rangle = \sum_{n\geq 1} \frac{\langle n_{\text{Exact}}|\hat{V}|\text{GS}_{\text{Exact}}\rangle}{E_{\text{GS,Exact}} - E_{n,\text{Exact}}} |n_{\text{Exact}}\rangle + o(\vec{p}, \vec{q}), \tag{4.116}$$

where $|n_{\text{Exact}}\rangle$ is the n-th excited state for the Hamiltonian with classical parameters $(\vec{P}_{\text{Exact}}(T), \vec{Q}_{\text{Exact}}(T))$. $E_{\text{GS,Exact}}$ and $E_{n,\text{Exact}}$ are energies of $|\text{GS}_{\text{PEAL}}\rangle$ and $|n_{\text{Exact}}\rangle$, respectively. We define the accumulated errors of classical parameters $\vec{p} = \vec{P}_{\text{PEAL}}(T) - \vec{P}_{\text{Exact}}(T)$, $\vec{q} = \vec{Q}_{\text{PEAL}}(T) - \vec{Q}_{\text{Exact}}(T)$. $\hat{V}$ is the first order Taylor expansion of the Hamiltonian

$$\hat{V} = \sum_i \left(\frac{\partial \hat{H}}{\partial Q_i} q_i + \frac{\partial \hat{H}}{\partial P_i} p_i \right). \tag{4.117}$$

Note the the dependence on $(\vec{p}, \vec{q})$ in Eq. 4.116 only appears in $\hat{V}$, which is linear in $(\vec{p}, \vec{q})$. Moreover, Eq. 4.116 is bounded by looking at its left hand side. Therefore, we see that overall $|\text{GS}_{\text{PEAL}}\rangle - |\text{GS}_{\text{Exact}}\rangle$ is of order $O(\vec{p}, \vec{q})$, and is controlled by the various bounds in Thm. 6.

Therefore, the second term can be controlled by

$$\begin{aligned}
&|\langle\hat{\Omega}\rangle_{\text{Exact}}(\vec{P}_{\text{PEAL}}(T), \vec{Q}_{\text{PEAL}}(T)) - \langle\hat{\Omega}\rangle_{\text{Exact}}(\vec{P}_{\text{Exact}}(T), \vec{Q}_{\text{Exact}}(T))| \\
&= |\langle \text{GS}_{\text{PEAL}}|\hat{\Omega}|\text{GS}_{\text{PEAL}}\rangle - \langle \text{GS}_{\text{Exact}}|\hat{\Omega}|\text{GS}_{\text{Exact}}\rangle| \\
&\leq |\langle \text{GS}_{\text{PEAL}}|\hat{\Omega}|\text{GS}_{\text{PEAL}}\rangle - \langle \text{GS}_{\text{PEAL}}|\hat{\Omega}|\text{GS}_{\text{Exact}}\rangle| + |\langle \text{GS}_{\text{PEAL}}|\hat{\Omega}|\text{GS}_{\text{Exact}}\rangle - \langle \text{GS}_{\text{Exact}}|\hat{\Omega}|\text{GS}_{\text{Exact}}\rangle| \\
&= |\langle \text{GS}_{\text{PEAL}}|\hat{\Omega}(|\text{GS}_{\text{PEAL}}\rangle - |\text{GS}_{\text{Exact}}\rangle)| + |(\langle \text{GS}_{\text{PEAL}}| - \langle \text{GS}_{\text{Exact}}|)\hat{\Omega}|\text{GS}_{\text{Exact}}\rangle|,
\end{aligned} \tag{4.118}$$

where $(|\text{GS}_{\text{PEAL}}\rangle - |\text{GS}_{\text{Exact}}\rangle)$ and $(\langle \text{GS}_{\text{PEAL}}| - \langle \text{GS}_{\text{Exact}}|)$ is of order $O(\vec{p}, \vec{q})$ and everything else is $O(1)$. Therefore the last line in Eq. 4.118 is of order $O(\vec{p}, \vec{q})$ because both terms are of

order $O(\vec{p}, \vec{q})$. Hence, the second error term satisfies the same bounds as Q does in Thm. 6, which in the proof we analyze the probability of all T steps' predictions having errors under a certain threshold.

The first term is the single-step prediction error $\delta\langle\hat{\Omega}\rangle$ at T-th step, which is analyzed in the proof of Thm. 6. Combining the first term and the second term is equivalent to requiring $(T+1)$ steps' prediction having errors under a certain threshold, which can be analyzed with the same technique we used in the proof of Thm. 6. More precisely, we have $(T+1)$ terms in the union bound in Eq. 4.105. This is equivalent to having results in Thm. 6 by changing T into $(T+1)$. However, such change does not affect the scaling behaviors of the bounds with T.

Therefore, the first and second terms combined also satisfy the same bounds as Q does in Thm. 6. This completes the proof of Lemma 1, that the accumulated error of any k-local observable satisfy the same bounds in Thm. 6. With this lemma proved, we complete the entire proof of Thm. 6. □

4.6.9 PEAL implementation

Here we provide more details about how we implement the PEAL algorithm in our numerical experiment on the Holstein model.

PEAL Step I: Collecting data. For each of the six training values of coupling constants $g \in \{1.3, 1.32, 1.34, 1.36, 1.38, 1.4\}$, we randomly sampled 18 independent initial conditions $\vec{Q}(t=0) \overset{\text{iid}}{\sim} \mathcal{N}(0, Q_v)^{\otimes L}$ with the standard deviation $Q_v = 0.2$. $L = 50$ is the system size. We set $\vec{P}(t=0) = 0$. For each initial condition, We iteratively perform quantum steps and classical steps, for 10,000 epochs, to generate a dynamical evolution path. We set the simulation time step $dt = 0.01$ and the total time is 100. In the quantum steps, we use exact diagonalization (ED) to obtain the quantum observables. In the classical steps, we use fourth order Runge-Kutta method. For each path, we randomly sampled 500 pairs of $(\vec{Q}_{\text{shift-}i}(t), n_i(t))$ data, where t is a random time step and i is a random site. $\vec{Q}_{\text{shift-}i}$ is the $\vec{Q}$

vector with elements rolled by a shift of i, so that the i-th element is put on the first place. Overall, we have $6 \times 18 \times 500 = 54,000$ data pairs, which effectively serve as 1,080 samples on the size $L = 50$ system.

The purpose to use this kind of site-shifting data pairs is to respect the translation symmetry of the system. With periodic boundary condition, the system has translation symmetry. Therefore, we can use the same model to predict n_i on any location in the system, as long as we also translate the $\vec{Q}$ vector accordingly.

PEAL Step II: ML training. We use the provably efficient ML algorithm introduced in [60]. For each length-50 vector $\vec{Q}$, we generate 50 local regions, each local region having radius 1 and consisting of 3 elements. We perform a random Fourier feature map on the local regions, generate R number of cosine features and R number of sine features for each local region. R is a hyperparameter chosen from $\{5, 10, 20, 40, 80, 160\}$. The frequency factor γ_ω for the random Fourier feature map is another hyperparameter chosen from $\{0.3, 0.6, 1, 2, 3, 6, 10, 20\}$. We trained an l_1-regularized regression (LASSO) on the non-linear features. The strength of regularization α is determined by LassoLars method with 4-fold cross validation [31]. For 1,024 samples, the grid-search best hyperparameters are $R = 20$, $\gamma_\omega = 6$, and $\alpha = 4.98 \times 10^{-6}$. The best model has 316 non-zero linear coefficients after the LASSO feature selection.

PEAL Step III: ML prediction. To speed up the dynamical simulation, we replace the ED steps by the prediction from the learning model. We take care of the $U(1)$ global symmetry of the system. After each ML boosted quantum step, we subtract the electron density n_i by the mean of their excess over 1/2. Therefore, we can make the total electron number conserved at half filling, and respect the $U(1)$ global symmetry of the system. See more details in the next section.

4.6.10 Details of symmetry-preserving PEAL

In the application of PEAL to specific systems with symmetries, we would like to preserve the symmetries during our numerical simulation. Here we present symmetry-preserving PEAL for two types of symmetries: The $U(1)$ global symmetry and the translation symmetry.

To preserve the $U(1)$ global symmetry, we would like to have the total charge conservation at each time step during the dynamics. When we sum up the model's prediction of the electron charge density at each site of the system, often case the result is not the same as the total charge in the previous time step. We can make a correction on the electron charge density at each site during each time step of the dynamics, in order to conserve the total charge.

There are two possible ways to do the correction. The first one is to uniformly add or subtract a constant on the electron charge density at each site. The second is to uniformly multiply a factor to the electron charge density at each site. However, the second way does not treat an electron (charge density equals to 1) and a hole (charge density equals to 0) equivalently. Therefore, we use the first way to do the correction.

Suppose the learning model $\mathcal{M}$ predicts the electron charge density $n_i = \langle c_i^\dagger c_i \rangle$ on each site i. In order to preserve the $U(1)$ global symmetry, we would like to have the corrected electron charge density $\tilde{n}_i$ such that $\sum_i \tilde{n}_i = L/2$, assuming at half filling for a system with L sites. It is straightforward to see that we can achieve this charge conservation by doing the correction $n_i \to \tilde{n}_i = n_i + \Delta n$ with $\Delta n = \frac{1}{L}\sum_i (\frac{1}{2} - n_i)$.

Now we prove the error bounds for our PEAL algorithm are still valid with this correction. Suppose each n_i has a prediction error $\delta n_i = n_i - n_i^*$, where n_i^* is the electron charge density computed with QSS, which satisfies $\sum_i n_i^* = L/2$. We can see $\Delta n = -\frac{1}{L}\sum_i \delta n_i$, and the error of the corrected electron charge density is $\delta\tilde{n}_i = \tilde{n}_i - n_i^* = \delta n_i + \Delta n = \delta n_i - \frac{1}{L}\sum_i \delta n_i$.

In the proof of PEAL error bounds, we analyzed all situations by turning the problem into the calculation of the probability of $|\delta\langle\hat{O}\rangle| \leq D\sqrt{\epsilon}$, where the constant D stands for A,

B, or C in the proof of Thm. 6. Note that when all $|\delta n_i| \leq D\sqrt{\epsilon}$, we have

$$|\delta \tilde{n}_i| = |\delta n_i - \frac{1}{L}\sum_i \delta n_i| \leq |\delta n_i| + \frac{1}{L}\sum_i |\delta n_i| \leq 2\, D\sqrt{\epsilon}, \tag{4.119}$$

which means that we are safe to apply every error bounds after we raise the corresponding constant D by a factor of 2. This completes the proof.

When the system has a translation symmetry, such as the one for the periodic chain we studied in the main text, every site i is on equal footing. Therefore, we will get the identical error distribution when we apply a model $\mathcal{M}_i$ trained for n_i to another site j to predict n_j. This means that we can save our cost by applying one model repeatedly on every site i instead of training an independent model for every n_i, and we have the error bounds unaffected. Moreover, by doing so, we preserve the translation symmetry in the PEAL prediction: If instead of the original initial condition $\vec{Q}(0) = (Q(0)_0, Q(0)_1, \ldots, Q(0)_{L-2}, Q(0)_{L-1})$ we input a shifted initial condition $(Q(0)_1, Q(0)_2, \ldots, Q(0)_{L-1}, Q(0)_0)$, then all outputs from the symmetry-preserving PEAL algorithm will be also shifted correspondingly comparing to the original outputs.

4.6.11 Details of numerical experiments

We are interested in the quantum dynamics of the Holstein model in Eq. 4.8 with a random initial distribution of $Q_i(0)$, and we set initial momentum $P_i(0) = 0$. Under the adiabatic approximation, the quantum dynamics can be further described by three equations:

$$Q_i'(t) = \frac{1}{M} P_i \tag{4.120}$$

$$P_i'(t) = -kQ_i + g(n_i - \frac{1}{2}) - \gamma P_i \tag{4.121}$$

$$H_e(\{Q_i(t)\}) = -t\sum_{i,j} c_i^\dagger c_j - g\sum_i (c_i^\dagger c_i - \frac{1}{2})Q_i \tag{4.122}$$

where $n_i = \langle c_i^\dagger c_i \rangle$ and γ is the damping coefficient.

In the experiment, we observed three regimes of g values. For a small g value, the final stable configuration of the system has no CDW. This is due to the finite size effect. For the system size $L = 50$ we used, the critical value to generate stable CDW is $g_{\text{crit}} = 1.152$. This critical value can be analytically solved and we present the calculation already in earlier Appendix 4.6.2. For a large g value, domain walls can be generated in the system. The characteristic length of the domain walls decreases when g increases. Therefore, when the system size is much larger than the domain wall characteristic length, domain walls can be relatively far from each other, which makes their interaction exponentially small and the equilibrium time exponentially large. For the system size $L = 50$ we used, the value to generate long-lasting domain walls is $g_{\text{DW}} \sim 1.6$. For the value $g_{\text{crit}} < g < g_{\text{DW}}$, we can see a clear CDW developing during the dynamics. Therefore, we collect a data set for $g \in \{1.3, 1.32, 1.34, 1.36, 1.38, 1.4\}$, mimicking a uniform distribution in $[1.3, 1.4]$.

For each g value, we generate 18 ED dynamical evolution paths with random initial conditions, serving as the training data. We also generate 10 more ED dynamical evolution paths with random unseen initial conditions for each $g \in \{1.3, 1.32, 1.34, 1.36, 1.38, 1.4\}$ and for each $g \in \{1.31, 1.33, 1.35, 1.37, 1.39\}$, serving as the standard learning test set and the transfer learning test set, respectively. In Figure 4.4 in the main text, we show how the test error scales with the number of samples used in model training. We trained models with number of samples from 1, 2, 4, ..., to 1,024. (Each sample contains 50 data pairs based on the system size we used.) We see an error scaling law agrees with the predicted logarithmic scaling. The transfer learning test error is only slightly higher than the standard learning test error. The scatter plots of the target values show the model has learned nicely for both the normal case and the transfer learning case.

Chapter 5

Hamiltonian Lattice Formulation of Compact Maxwell-Chern-Simons Theory

5.1 Introduction

The material of this Chapter is largely based on Ref. [11]. As discussed in the overview of this thesis in Sec. 1.1, as the first step to perform numerical methods on a theory, we need to construct a formulation of the theory which can be input into the simulation device. Sometimes it is difficult to even come up with such a construction. A known example with such difficulty is the Chern-Simons theory [91].

Chern-Simons theory is a topological quantum field theory with numerous applications in condensed matter and high-energy physics, including the study of anomalies, fermion/boson dualities, and the fractional quantum Hall effect [91]. Recently, a Lagrangian lattice formulation of pure Chern-Simons theory and its canonical quantization has been proposed [9], [10]. However, pure lattice Chern-Simons theory faces a doubling problem, similar to the fermion doubling problem. The presence of a Maxwell term with Chern-Simons theory solves the doubling problem, in a way similar to the Wilson term that eliminates the fermion doubling problem [92]. The resulting theory is lattice Maxwell-Chern-Simons theory, which we will

consider here. In the continuum, the Maxwell-Chern-Simons theory has been first introduced in Ref. [93], where it was shown that, in (2+1) dimensions, when a Chern-Simons term is added to the Maxwell Lagrangian, the photon becomes massive trough a topological mechanism, without spontaneous symmetry breaking via the Higgs mechanism. This mechanism of topological mass generation is relevant for topological phases of matter (for a review see Ref. [94]), which are gapped systems with a new type of quantum order that is not due to symmetry breaking [95]. These phases of matter can have various exotic quantum features, like excitations with non-trivial statistics, or ground-state degeneracy on manifolds with non-trivial topology.

The Lagrangian formulation of compact Maxwell-Chern-Simons theory for 2+1D Euclidean spacetime lattices has been first derived in Ref. [5] using the self-dual approximation introduced in Ref. [96], and later studied in other works (see, e.g., Refs. [6]–[8]). The Hamiltonian formulation has so far been derived only for non-compact gauge fields [4], but the corresponding formulation for compact gauge fields remains absent. Such a formulation would be particularly important for future Hamiltonian-based simulations of the theory on classical and quantum computers. The Hamiltonian formulation provides a promising approach to simulate sign-problem afflicted regimes in lattice field theory, including topological terms, chemical potentials, and out-of-equilibrium dynamics. Recently, there has been growing interest in the development of Hamiltonian-based simulation methods, including tensor network states [97], [98], non-Gaussian states [99]–[102], machine-learning-based approaches [103]–[105], and quantum computing [106], [107]. In particular, topological terms have been numerically investigated in 1+1D using tensor network states [108]–[112] and quantum algorithms [113], [114], as well as in 3+1D using exact diagonalization [115]. Topological terms in 2+1D have not yet been simulated, due to the lack of a suitable Hamiltonian lattice formulation.

In this chapter, we derive a Hamiltonian lattice formulation of compact Maxwell-Chern-Simons theory using the Villain approximation. We analytically solve this theory and show

that the mass gap in the continuum limit matches the well-known continuum formula. Moreover, topological features such as the quantization of the Chern-Simons level, the degeneracy of the energy eigenstates, and the non-trivial properties of Wilson loops are reproduced. When fermions are introduced into the theory, numerical methods become necessary. Thus, our Hamiltonian formulation of Maxwell-Chern-Simons theory lays the groundwork for future Hamiltonian-based simulations of the theory on classical and quantum computers.

The chapter is organized as follows. In Sec. 5.2, we review the Lagrangian lattice formulation of compact Abelian Chern-Simons theory as proposed in Ref. [9]. In Sec. 5.3, we review the compact Maxwell lattice Hamiltonian and emphasize there are two versions of Hamiltonian with instantons allowed or suppressed. In Sec. 5.4, we derive the Hamiltonian lattice formulation of compact Maxwell-Chern-Simons theory. Here, we discuss the quantization of the Chern-Simons level and the degeneracy of the states. We also discuss some physical properties of the lattice Maxwell-Chern-Simons theory, including the perimeter law of Wilson loops and their non-trivial linking, as well as the mutual and self statistics of anyons. In Sec. 5.5, we analytically solve the quadratic Hamiltonian that we derived in Sec. 5.4, and we plot the resulting band structure. In Sec. 5.6, we summarize and discuss our results. Throughout this chapter, we use the Euclidean spacetime formulation.

5.2 Review of compact Chern-Simons lattice action

In the following, we review the Lagrangian lattice formulation of compact Abelian Chern-Simons theory, based on Ref. [9]. In the continuum, the Abelian Chern-Simons action is defined as

$$S_{CS}(A) = -\frac{ik}{4\pi}\int d^3x\, \epsilon^{\mu\nu\rho} A_\mu \partial_\nu A_\rho, \tag{5.1}$$

where A is the U(1) gauge field configuration and k is the Chern-Simons level.

For the lattice discretization of this action, we consider a 2+1D cubic lattice with periodic

boundary conditions in all directions. The U(1) gauge field A lives on the links of the lattice. A naive lattice discretization of the continuous Chern-Simons action in Eq. 5.1 is

$$S_{CS}(A) = -\frac{ik}{4\pi} a^2 d\tau \sum_{x \in \text{sites}} \epsilon^{\mu\nu\rho} A_{x;\mu} \Delta_\nu A_{x+\hat{\mu};\rho}, \tag{5.2}$$

where a and $d\tau$ are the lattice spacings in the space and time directions, respectively. Here, the finite (forward) difference operator of the A field on the lattice is defined as

$$\Delta_0 A_{x;\mu} = \frac{A_{x+\hat{0};\mu} - A_{x;\mu}}{d\tau}, \tag{5.3}$$

$$\Delta_i A_{x;\mu} = \frac{A_{x+\hat{i};\mu} - A_{x;\mu}}{a}, \tag{5.4}$$

where Δ_0 represents the time difference and $\Delta_{i\in\{1,2\}}$ represents the spacial difference.

We note that after integration by parts, Eq. 5.2 can be equivalently written in terms of the backward lattice difference operator:

$$S_{CS}(A) = -\frac{ik}{4\pi} a^2 d\tau \sum_{x \in \text{sites}} \epsilon^{\mu\nu\rho} A_{x;\mu} \hat{\Delta}_\nu A_{x-\hat{\rho};\rho}, \tag{5.5}$$

where

$$\hat{\Delta}_0 A_{x;\mu} = \frac{A_{x;\mu} - A_{x-\hat{0};\mu}}{d\tau}, \tag{5.6}$$

$$\hat{\Delta}_i A_{x;\mu} = \frac{A_{x;\mu} - A_{x-\hat{i};\mu}}{a}, \tag{5.7}$$

Thus, we can try to write the action symmetrically with both the forward and backward difference operators:

$$S_{CS}(A) = -\frac{ik}{4\pi} a^2 d\tau \sum_{x \in \text{sites}} \epsilon^{\mu\nu\rho} \frac{A_{x;\mu} \Delta_\nu A_{x+\hat{\mu};\rho} + A_{x;\mu} \hat{\Delta}_\nu A_{x-\hat{\rho};\rho}}{2}. \tag{5.8}$$

As shown in Refs. [116], [117], this symmetric form of the action respects Osterwalder-

Schrader reflection positivity. Next, we introduce a pictorial illustration of the lattice action. For this, we first explicitly write out the epsilon tensor in Eq. 5.2, which results in

$$\begin{aligned} S_{CS}(A) = -\frac{ik}{4\pi} a^2 d\tau \sum_{x \in \text{sites}} \big[& A_{x;0} \left(\Delta_1 A_{x+\hat{0};2} - \Delta_2 A_{x+\hat{0};1} \right) \\ & - A_{x;1} \left(\Delta_0 A_{x+\hat{1};2} - \Delta_2 A_{x+\hat{1};0} \right) \\ & + A_{x;2} \left(\Delta_0 A_{x+\hat{2};1} - \Delta_1 A_{x+\hat{2};0} \right) \big] . \end{aligned} \tag{5.9}$$

This action can be visualized as

$$S_{CS}(A) = -\frac{ik}{4\pi} a^2 d\tau \sum_{\text{cubes}} \Bigg[$$

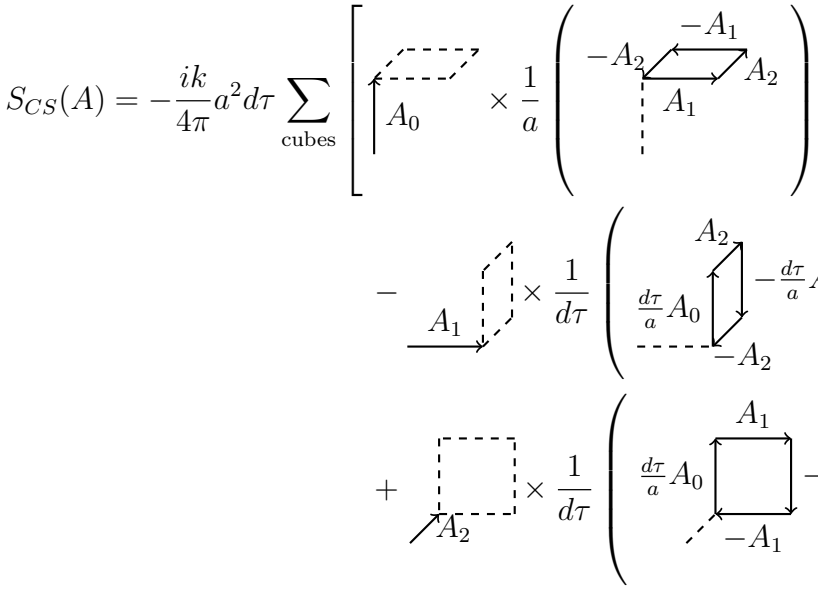

$$\Bigg] . \tag{5.10}$$

Here, the solid lines correspond to the actual terms in the action, while the dashed lines are for visual guidance only; the dashed lines denote the positions of the other gauge fields in the products. Moreover, A_0, A_1, and A_2 denote the gauge fields on the links in the 0, 1, and 2 directions, which correspond to the directions upwards, right, and into the plane, respectively. Each solid "plaquette" in Eq. 5.10 corresponds to the two terms in the round brackets of Eq. 5.9, which—according to the definition of the finite difference operators in Eqs. 5.3 and 5.4—can be expressed in terms of four gauge fields multiplied by a prefactor of $1/d\tau$ or $1/a$, respectively.

This naive definition of the lattice action in Eq. 5.10 is invariant under local gauge trans-

formations, $A \to A + d\lambda$. However, it is not invariant under the discrete shift of the compact gauge variable, $A_0 \to A_0 + \frac{2\pi}{d\tau}$ and $A_i \to A_i + \frac{2\pi}{a}$, $i = 1, 2$. This discrete shift invariance is necessary because we aim to formulate lattice Chern-Simons theory with a compact gauge group, i.e., U(1) rather than $\mathbb{R}$. The compactness of the gauge group implies the existence of quantized magnetic fluxes, $\int_\Sigma dA \in 2\pi\mathbb{Z}$, where Σ is a closed surface. This indicates the presence of a monopole configuration if the surface is contractible. Consequently, lattice discretizations of compact U(1) gauge theory generically comprise dynamical lattice-scale monopole configurations. However, monopoles are known to violate gauge invariance in the presence of a Chern-Simons term, as shown in the continuum limit [118], [119]. While this has been considered an obstacle for formulating a gauge-invariant Chern-Simons theory on the lattice, this issue can be circumvented using the modified Villain approach [120]–[123]. In the conventional Villain approach [120], the standard algebra-valued gauge fields $A \in \mathbb{R}$ are accompanied by discrete plaquette variables $n \in \mathbb{Z}$, which encode the quantized magnetic flux. These variables n can be interpreted as discrete gauge fields for the $\mathbb{Z}$ sub-symmetry of the non-compact $\mathbb{R}$ gauge symmetry, which is precisely the discrete shift symmetry mentioned above, $A_0 \to A_0 + \frac{2\pi}{d\tau}$ and $A_i \to A_i + \frac{2\pi}{a}$, $i = 1, 2$. Upon gauging these discrete shifts, one effectively studies compact $\mathrm{U}(1) = \mathbb{R}/2\pi\mathbb{Z}$ gauge theory instead of non-compact $\mathbb{R}$ gauge theory. This so-called Villain formulation of compact U(1) gauge theory contains instantons (i.e. monopoles in 2+1D), which can be elimated by a Lagrange multiplier φ that constrains the discrete gauge field to be flat, called the modified Villain approach [122].

Following the modified Villain approach, the authors of Ref. [9] have built a gauge-invariant Chern-Simons lattice action by introducing integer degrees of freedom on each plaquette, as well as angular variables on each lattice site. In the following, we will use a different sign convention of the Chern-Simons action and therefore obtain a slightly different Chern-Simons lattice action (for the original Chern-Simons lattice action introduced in Ref. [9], see their Eq. (17)):

$$S_{CS}(A,n,\varphi) = -\frac{ik}{4\pi}a^2 d\tau \sum_{\text{cubes}} \Bigg[$$

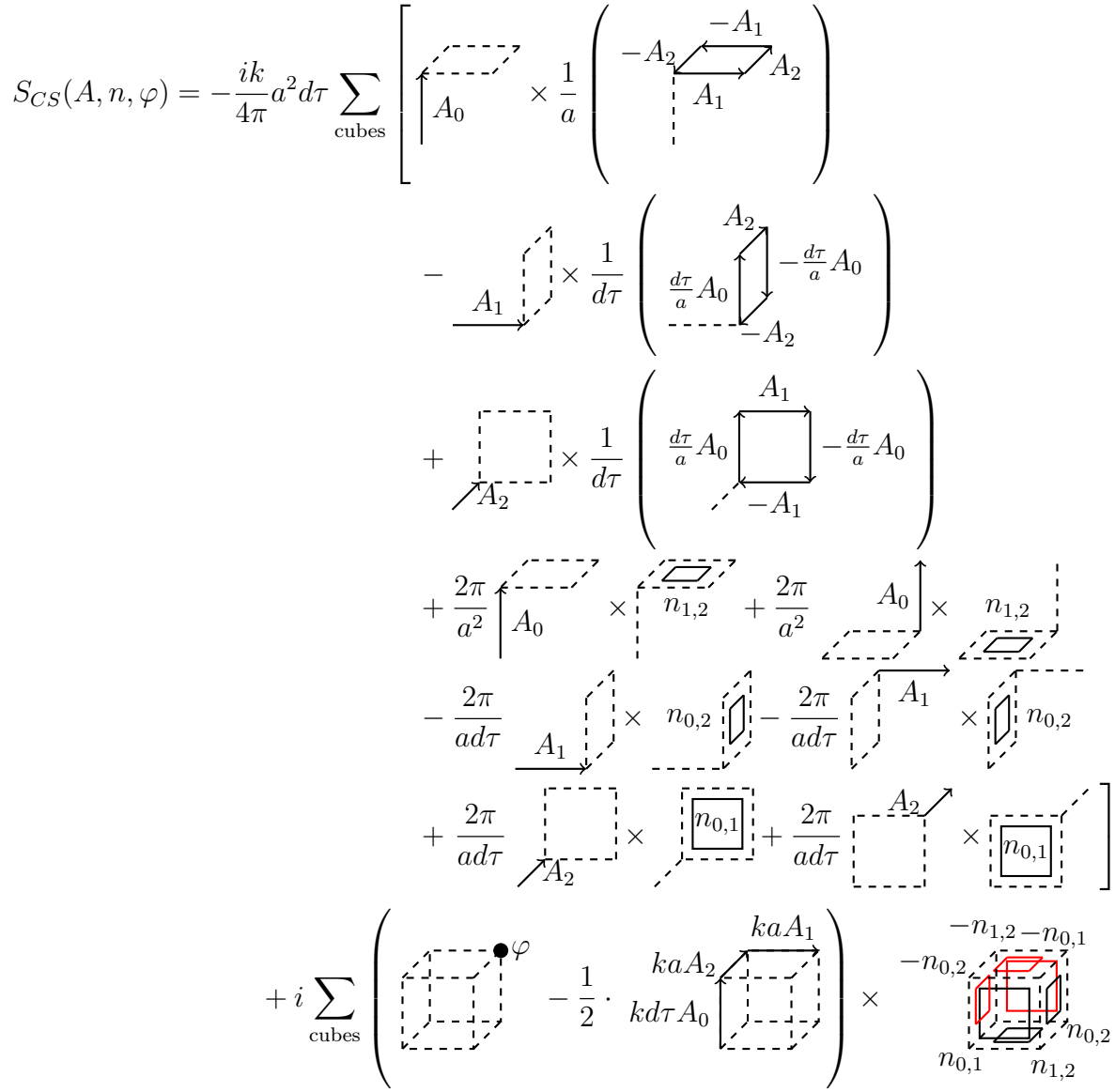

$$+ i \sum_{\text{cubes}} \Bigg(\varphi \; - \frac{1}{2} \cdot \; kaA_1 \; kaA_2 \; kd\tau A_0 \Bigg) \times$$

$$, \tag{5.11}$$

where $n_{0,1}$ and $n_{0,2}$ are integer variables living on time-like plaquettes, and $n_{1,2}$ are integer variables living on space-like plaquettes. These integer variables are drawn as smaller squares in each plaquette for visual clarity, and the negative n values are indicated by red squares. In the last term in Eq. 5.11, there is an angular variable $\varphi \in [0, 2\pi)$ on each lattice site as the Lagrangian multiplier to impose the zero-instanton constraint for each unit cell. For any configuration where a unit cell contains non-zero total flux (i.e. instanton number, shown

as the cube in Eq. 5.11), summing over the corresponding φ from 0 to 2π in the partition function makes the partition function vanish. Therefore, the φ variables impose hard constraints that eliminate all instantons. Later, we will show that φ is not necessary in our lattice Hamiltonian formulation in Eq. 5.23 because we impose those constraints directly by ignoring the instanton configurations in the counting of degrees of freedom (see the detailed derivation in Appendix 5.7.7).

There are two types of gauge transformations associated with the action $S_{CS}(A, n, \varphi)$ (see Eq. (22) in Ref. [9] for the corresponding mathematical formula). For $\forall \lambda \in \mathbb{R}$, $\forall k \in 2\mathbb{Z}$,

$$S_{CS}\left(\begin{array}{ccc} & A_0 + \frac{\lambda}{d\tau} & \\ \varphi - k\lambda & & A_2 + \frac{\lambda}{a} \\ A_1 - \frac{\lambda}{a} & & A_1 + \frac{\lambda}{a} \\ A_2 - \frac{\lambda}{a} & A_0 - \frac{\lambda}{d\tau} & \end{array} , * \right) = S_{CS}\left(\begin{array}{ccc} & A_0 & \\ \varphi & & A_2 \\ A_1 & & A_1 \\ A_2 & A_0 & \end{array} , * \right) \tag{5.12}$$

$$e^{-S_{CS}}\left(\begin{array}{ccc} & A_0 + \frac{2\pi}{d\tau} n_{0,2} - 1 & \\ n_{0,1} + 1 & & n_{0,1} - 1 \\ & n_{0,2} + 1 & \end{array} , * \right) = e^{-S_{CS}}\left(\begin{array}{ccc} & A_0 \; n_{0,2} & \\ n_{0,1} & & n_{0,1} \\ & n_{0,2} & \end{array} , * \right) \tag{5.13}$$

$$e^{-S_{CS}}\left(\begin{array}{ccc} & & n_{0,1} + 1 \\ & & n_{1,2} - 1 \\ n_{1,2} + 1 & & A_1 + \frac{2\pi}{a} \\ n_{0,1} - 1 & & \end{array} , * \right) = e^{-S_{CS}}\left(\begin{array}{ccc} & & n_{0,1} \\ & & n_{1,2} \\ n_{1,2} & & A_1 \\ n_{0,1} & & \end{array} , * \right) \tag{5.14}$$

$$e^{-S_{CS}}\left(\begin{array}{ccc} n_{0,2} + 1 & & A_2 + \frac{2\pi}{a} \\ n_{1,2} - 1 & & n_{1,2} + 1 \\ & n_{0,2} - 1 & \end{array} , * \right) = e^{-S_{CS}}\left(\begin{array}{ccc} n_{0,2} & & A_2 \\ n_{1,2} & & n_{1,2} \\ & n_{0,2} & \end{array} , * \right) \tag{5.15}$$

The $*$ in the parentheses represents all other variables, which are the same on the left and right hand sides in the equations. Equation 5.12 shows a local gauge transformation, under

which S_{CS} itself is invariant. Equations 5.13–5.15 are the discrete gauge transformations, under which the partition function $e^{-S_{CS}}$ is invariant. In fact, S_{CS} changes by $i\pi k\mathbb{Z}$ from the last term in the action Eq. 5.11 under discrete gauge transformations. When k is an odd integer, there can be an extra π phase in S_{CS}, and the partition function changes by an extra minus sign. This extra minus sign can be cancelled by the anomaly inflow from an auxiliary 4D bulk [9], or by introducing additional fermionic degrees of freedom [10]. More precisely, the odd-k theory is a theory of fermions, where the Chern-Simons action depends on the choice of the spin structure of the manifold [124]. Here, we only consider the pure gauge theory in 2+1D, so we assume that k is an even integer in the beginning. What may be surprising is that, in Sec. 5.4, after we add the Maxwell term and derive the compact Maxwell-Chern-Simons theory in Hamiltonian formaluation, the corresponding Hamiltonian works for any integer k. We will show that the fermionic nature for odd k is still present and can be probed with our formulation.

The authors of Ref. [9] have shown that the lattice action in Eq. 5.11 reproduces various aspects of the continuum Chern-Simons theory, including the level quantization and the discrete $\mathbb{Z}$ 1-form symmetry. In a more recent work by the same authors [10], they have tried to canonically quantize the lattice action in Eq. 5.11. However, without the Maxwell term, the quantization of the pure Chern-Simons action unavoidably has non-trivial commutators between gauge field variables on different links (see Eq. (23) in Ref. [10]). The non-commuting gauge field variables make it hard to find an orthonormal basis of the Hilbert space, and thus lose the capability of performing numerical simulations with their formulation.

5.3 Review of compact Maxwell lattice Hamiltonian

In 2+1D lattice QED, it is common to consider the following compact Maxwell action [125]:

$$S_{\text{Maxwell}}(A) = -\frac{\beta_0}{d\tau}\sum_{x\in\text{sites}}\left[\cos\left(ad\tau(\Delta_0 A_{x;1} - \Delta_1 A_{x;0})\right) + \cos\left(ad\tau(\Delta_0 A_{x;2} - \Delta_2 A_{x;0})\right)\right] - \frac{\beta d\tau}{a^2}\sum_{x\in\text{sites}}\left[\cos\left(a^2(\Delta_1 A_{x;2} - \Delta_2 A_{x;1})\right)\right], \tag{5.16}$$

where β_0 and β are the temporal and spatial gauge coupling coefficients, respectively, $d\tau$ and a are the temporal and spatial lattice spacings, respectively, and A_0 and A_i with $i = 1, 2$ are the gauge field in the temporal and spatial directions, respectively. This lattice action can be visualized as

$$S_{\text{Maxwell}}(A) = -\frac{\beta_0}{d\tau}\sum_{\substack{\text{time-like}\\\text{plaquettes}}}\left[\cos\left(a\cdot\ \tfrac{d\tau}{a}A_0 \square -\tfrac{d\tau}{a}A_0 \ \text{(}A_1\text{ top, }-A_1\text{ bottom)}\right) + \cos\left(a\cdot\ \tfrac{d\tau}{a}A_0 \square -\tfrac{d\tau}{a}A_0 \ \text{(}A_2\text{ top, }-A_2\text{ bottom)}\right)\right] - \frac{\beta d\tau}{a^2}\sum_{\substack{\text{space-like}\\\text{plaquettes}}}\left[\cos\left(a\cdot\ -A_2 \square A_2 \ \text{(}-A_1\text{ top, }A_1\text{ bottom)}\right)\right]. \tag{5.17}$$

In order to do the canonical quantization to obtain the Hamiltonian formulation, we need to use the Villain approximation to expand the cosine terms in the action into quadratic forms [126]. The Villain approximated action is

$$S_{\text{Maxwell}}(A, n) = \frac{\beta_0}{2d\tau}\sum_{\substack{x\in\text{sites}\\ i\in\{1,2\}}}\left(ad\tau(\Delta_0 A_{x;i} - \Delta_i A_{x;0}) + 2\pi n_{x;0,i}\right)^2 + \frac{\beta d\tau}{2a^2}\sum_{x\in\text{sites}}\left(a^2(\Delta_1 A_{x;2} - \Delta_2 A_{x;1}) + 2\pi n_{x;1,2}\right)^2, \tag{5.18}$$

where the integer degrees of freedom n live on every plaquettes. This Villain approximated

lattice action can be visualized as

$$S_{\text{Maxwell}}(A,n) = \frac{\beta_0}{2d\tau} \sum_{\substack{\text{time-like}\\ \text{plaquettes}}} \left[\left(a \cdot \frac{d\tau}{a} A_0 \square^{A_1}_{-A_1} - \frac{d\tau}{a} A_0 + 2\pi \boxed{n_{0,1}} \right)^2 + \left(a \cdot \frac{d\tau}{a} A_0 \square^{A_2}_{-A_2} - \frac{d\tau}{a} A_0 + 2\pi \square n_{0,2} \right)^2 \right] + \frac{\beta d\tau}{2a^2} \sum_{\substack{\text{space-like}\\ \text{plaquettes}}} \left[\left(a \cdot -A_2 \square^{-A_1}_{A_1} A_2 + 2\pi \overset{n_{1,2}}{\square} \right)^2 \right], \tag{5.19}$$

which converges to the non-approximated action in Eq. 5.17 in the $d\tau \to 0$ limit [126].

From the above Villain approximated lattice action, if we allow the presence of instantons, we can derive the familiar lattice QED Hamiltonian [127]. In the derivation, the presence of instantons allows an integer degree of freedom on every cubic unit cell in the lattice (i.e. the instanton number in every cube). Summing over these instanton degrees of freedom in the partition function provides an reversed Villain approximation and allows us to wrap the space-like plaquettes into the familiar cosine term in the Hamiltonian again, while the time-like plaquettes becomes the E_i^2 term.

$$H_{\text{Maxwell with instantons}} = \frac{e^2}{2a^2} \sum_{\text{links}} E_i^2 + \frac{1}{e^2 a^2} \sum_{\text{plaquettes}} \left(1 - \cos a^2 B\right) , \tag{5.20}$$

where E_i is the electric field in the i direction, and B is the magnetic field. The coefficients in Eq. 5.19 and the coupling constant are related by $\beta_0 = \beta = 1/e^2$. See Appendix 5.7.5 for a detailed derivation.

Meanwhile, if we totally suppress the instantons, from the same Villain approximated lattice action in Eq. 5.19, we can derive a different version of the lattice Hamiltonian. In our derivation, we enforce the zero-intanton constraint by taking out the integer degrees

of freedom which correspond to instanton numbers in cubes (this process is equivalent to adding the Lagrangian multipliers to the action and then integrate them out in the partition function). Without summing over instanton degrees of freedom, the space-like plaquette terms cannot be wrap into cosine terms and stay quadratic.

$$H_{\text{Maxwell without instantons}} = \frac{e^2}{2a^2} \sum_{\text{links}} E_i^2 + \frac{a^2}{2e^2} \sum_{\text{plaquettes}} B^2, \tag{5.21}$$

which comes together with two more constraints on its Hilbert space to guarantee the compactness of the theory. We introduce this Hamiltonian and the associated Hilbert space constraints in Appendix 5.7.6.

To summarize, there are two types of Maxwell theory: instanton-allowed or instanton-suppressed. Sometimes the instanton-suppressed Maxwell theory is referred to as the "non-compact QED". However, we would like to emphasize that the instanton-suppressed Maxwell theory is a compact theory due to the additional Hilbert space constraints. Later when we discuss the Maxwell-Chern-Simons theory, we will only talk about the the instanton-suppressed Maxwell theory. This is because accompanied with the Chern-Simons action, instantons carry charges, which is similar to the Witten effect in 3+1D Maxwell theory with the θ term [128]. Therefore, in order to study the pure gauge theory without matter fields, here we have to suppress the instantons. We refer to Appendix 5.7.1 for more discussions on the instanton effects.

5.4 Compact Maxwell-Chern-Simons lattice Hamiltonian

In the previous work of canonical quantization of lattice Chern-Simons theory [10], there is no proposal of adding the Maxwell term. In this section, we provide a formulation of the Maxwell-Chern-Simons Lattice Hamiltonian, which can be implemented in classical and

quantum simulations. We consider the sum of Eqs. 5.11 and 5.19 as the total action,

$$S(A, n, \varphi) = S_{\text{Maxwell}}(A, n) + S_{CS}(A, n, \varphi), \tag{5.22}$$

which will be our starting point to obtain the lattice Hamiltonian for the Maxwell-Chern-Simons theory.

The Chern-Simons term, being topological, does not contribute to the Hamiltonian. Therefore, we would expect to see a Maxwell-Chern-Simons lattice Hamiltonian that looks similar to the Hamiltonian of compact QED with instantons suppressed as shown in Eq. 5.21. We would also expect to obtain two additional Hilbert space constraints. However, the expression of the electric field E appearing in the Hamiltonian, the Gauss' law, and the Hilbert space constraints will be modified due to the Chern-Simons term.

We use the transfer matrix method [129], suppress the instantons by ignoring their configurations in the counting of degrees of freedom, and construct a lattice Hamiltonian based on the action in Eq. 5.22 (see Appendix 5.7.7 for more details):

$$\begin{aligned}
\hat{H} = &+ \frac{e^2}{2a^2} \sum_{\text{plaquettes}} \left[\left(\overrightarrow{\hat{p}_1} - \left(\frac{ka^2}{4\pi}\right) \uparrow \hat{A}_2 \right)^2 + \left(\hat{p}_2 \uparrow + \left(\frac{ka^2}{4\pi}\right) \hat{A}_1 \rightarrow \right)^2 \right] \\
&+ \frac{1}{2e^2} \sum_{\text{plaquettes}} \left(-\hat{A}_2 \square \hat{A}_2 \right)^2 \quad (-\hat{A}_1 \text{ above}, \hat{A}_1 \text{ below}) \\
= &\sum_{x \in \text{sites}} \frac{e^2}{2a^2} \left[\left(\hat{p}_{x;1} - \frac{ka^2}{4\pi} \hat{A}_{x-\hat{2};2} \right)^2 + \left(\hat{p}_{x;2} + \frac{ka^2}{4\pi} \hat{A}_{x-\hat{1};1} \right)^2 \right] + \frac{1}{2e^2} \left(\Box \hat{A}_{x;1,2} \right)^2,
\end{aligned} \tag{5.23}$$

where e^2 is the coupling constant, a is the lattice spacing, k is the Chern-Simons level, $\hat{A}_i$ is the gauge field operator in the direction $i = 1$ or 2, and $\hat{p}_i$ is the corresponding conjugate momentum operator. They have the standard commutation relation $\left[\hat{A}_{x;i}, \hat{p}_{y;j}\right] = i\delta_{x,y}\delta_{i,j}$. We also define $\Box \hat{A}_{x;1,2} \equiv \hat{A}_{x;1} + \hat{A}_{x+\hat{1};2} - \hat{A}_{x+\hat{2};1} - \hat{A}_{x;2}$. The action coefficients and the coupling constant are related by $\beta_0 = \beta = \frac{1}{e^2}$. This lattice Hamiltonian lives on a constraint

Hilbert space which we will detail below.

5.4.1 Hilbert space and constraints

We construct the Hilbert space on a 2D time slice, which is a 2D square lattice. The Hilbert space is constructed with a set of basis $\{|A\rangle : A \in \mathbb{R}^{2N_1N_2}\}$, where A denotes a configuration of the gauge fields, N_1 and N_2 are the lattice sizes in the two spacial directions, respectively, and $2N_1N_2$ is the total number of links. i.e., each basis vector is labeled by a configuration in which every link has a variable ranging in $(-\infty, +\infty)$. We note that our formulation provides a natural basis in terms of the gauge field configurations for classical and quantum simulations.

The compactness of the theory is reflected by several constraints on the Hilbert space. Any physical state $|\psi\rangle$ in the Hilbert space needs to satisfy the following constraints, where $\hat{A}$ is the gauge field operator, $\hat{p}$ is the conjugate momentum operator, k is the Chern-Simons level, and a is the lattice spacing:

1.

$$\hat{G}|\psi\rangle = 0, \tag{5.24}$$

where

$\hat{G} =$ 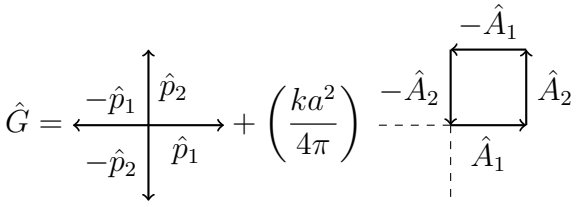

$$= \hat{p}_{x;1} + \hat{p}_{x;2} - \hat{p}_{x-\hat{1};1} - \hat{p}_{x-\hat{2};2} + \frac{ka^2}{4\pi}\left(\Box \hat{A}_{x;1,2}\right), \tag{5.25}$$

for any lattice site x.

Equivalently,

$$e^{i\lambda\hat{G}}|\psi\rangle = |\psi\rangle, \quad \forall\lambda \in \mathbb{R}, \tag{5.26}$$

which is the Gauss' law or the local gauge transformation.

2.

$$e^{2\pi i\hat{L}_1}|\psi\rangle = e^{i\theta_1}|\psi\rangle, \tag{5.27}$$

where θ_1 is a constant global phase, and

$\hat{L}_1 =$ 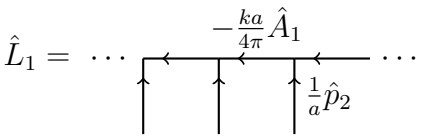

$$= \sum_{x_1=0}^{N_1-1} \left(\frac{1}{a}\hat{p}_{(x_1,x_2);2} - \frac{ka}{4\pi}\hat{A}_{(x_1,x_2+1);1} \right), \tag{5.28}$$

for any $x_2 \in \{0, 1, \ldots, N_2 - 1\}$. This loop operator generates one of the large gauge transformations. Note that such a loop can be locally deformed by adding or subtracting the Gauss' law (constraint 1). Therefore, more generally we can write $\hat{L}_1$ for any topologically non-trivial horizontal loop that wraps through the boundary, i.e., any curve with the winding number $(1, 0)$. This means $\hat{L}_1$ is a 1-form symmetry operator.

3.

$$e^{2\pi i\hat{L}_2}|\psi\rangle = e^{i\theta_2}|\psi\rangle, \tag{5.29}$$

where θ_2 is another constant global phase, and

$\hat{L}_2 =$ 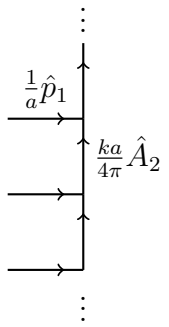

$$= \sum_{x_2=0}^{N_2-1} \left(\frac{1}{a}\hat{p}_{(x_1,x_2);1} + \frac{ka}{4\pi}\hat{A}_{(x_1+1,x_2);2} \right), \tag{5.30}$$

for any $x_1 \in \{0, 1, \ldots, N_1 - 1\}$. This loop operator generates the other large gauge transformations. Note that such a loop can also be locally deformed by adding or subtracting the Gauss' law (constraint 1). Therefore, more generally we can write $\hat{L}_2$ for any topologically non-trivial vertical loop that wraps through the boundary, i.e., any curve with the winding number $(0, 1)$. This means $\hat{L}_2$ is a 1-form symmetry operator.

The second and the third constraints compactify the theory. In fact, the two constraints $e^{2\pi i \hat{L}_i}|\psi\rangle = e^{i\theta_i}|\psi\rangle$ allows $\hat{L}_i|\psi\rangle = \left(\frac{\theta_i}{2\pi} + m_i\right)|\psi\rangle$, where $m_i \in \mathbb{Z}$, $i = 1, 2$. These two integers m_1 and m_2 encode the information of the fluxes through the non-contractible cycles in the two directions with winding numbers $(1, 0)$ and $(0, 1)$, respectively. Since the U(1) gauge group is compact, these two fluxes are defined up to module of 2π. Therefore, we need to sum over all possible values of m_i with equal weights in the partition function, regarding them as denoting different sectors of the theory. A large gauge transformation $|\psi\rangle \to e^{2\pi i \hat{L}_j}|\psi\rangle$ changes $m_i \to m_i + k\,\epsilon_{ij}$ and brings us to a different sector (see the commutator between $\hat{L}_i$ and $\hat{L}_j$ in Eq. 5.34). However, since all sectors are summed with equal weights in the partition function, the discrete gauge transformation does not change the partition function, i.e., we have a compact theory. This compactification is similar in spirit to the Villain

approximation, where multiple non-periodic functions are summed with equal weights to become a periodic function.

After having formulated these three constraints, we need to ensure that the lattice Hamiltonian operator in Eq. 5.23 is well defined on this constrained Hilbert space. This is true because of

$$[\hat{H}, \hat{G}] = 0, \tag{5.31}$$

$$[\hat{H}, \hat{L}_i] = 0, \quad i = 1, 2, \tag{5.32}$$

which can be checked straight-forwardly. Moreover, we need to check the mutual compatibility between the three constraints, as discussed in the next subsection.

5.4.2 Quantization of Chern-Simons level

To check the compatibility between the three constraints introduced in the previous subsection, we need to ensure that the operators $e^{i\lambda\hat{G}}$, $e^{2\pi i\hat{L}_1}$, and $e^{2\pi i\hat{L}_2}$ commute with each other. The first operator commutes with the latter two for any λ because

$$[\hat{G}, \hat{L}_i] = 0, \quad i = 1, 2\ . \tag{5.33}$$

The latter two, instead, do not commute with each other for arbitrary values of k, since

$$[\hat{L}_1, \hat{L}_2] = -\frac{k}{2\pi} i, \tag{5.34}$$

and therefore

$$e^{2\pi i\hat{L}_1} e^{2\pi i\hat{L}_2} = e^{2\pi ik} e^{2\pi i\hat{L}_2} e^{2\pi i\hat{L}_1}. \tag{5.35}$$

The compatibility of the constraints 2 and 3, which is necessary to obtain a non-trivial

Hilbert space that contains more than the zero vector, seems to enforce the quantization of the Chern-Simons coupling constant k in integers:

$$e^{2\pi ik} = 1 \tag{5.36}$$

$$\implies k \in \mathbb{Z}. \tag{5.37}$$

Note that in our starting lattice action in Eq. 5.22, we require $k \in 2\mathbb{Z}$ in order to make the action periodic in the gauge field variables and therefore gauge invariant. This requirement is relaxed to $k \in \mathbb{Z}$ in our Hamiltonian formulation. However, we can still probe the fermionic nature of the odd-k theory in our formulation. Note that $e^{2\pi i\hat{L}_1}e^{2\pi i\hat{L}_2} = e^{\pi ik}e^{2\pi i(\hat{L}_1+\hat{L}_2)}$. In an odd-$k$ theory, the three operators, $e^{2\pi i\hat{L}_1}$, $e^{2\pi i\hat{L}_2}$, and $e^{2\pi i(\hat{L}_1+\hat{L}_2)}$, cannot be all imposed to be the identity consistently. This reflects the fact that there is no standard choice of boundary conditions (spin structures) in a fermionic theory. The result of the theory could depend on the choice of spin structure for an odd k level [124].

5.4.3 Degeneracy of states

One of the most interesting aspects of the Chern-Simons theory is its topological nature: pure Chern-Simons theories are metric independent and therefore independent of the geometry of the manifold on which they are defined, i.e., they depend only on the topology of the manifold. The ground state is degenerate on a manifold with non-trivial topology. On a manifold of genus g, the degeneracy is k^g for integer k [130]. As we will show, the ground-state degeneracy is present also in the Maxwell-Chern-Simons theory. In fact, this degeneracy of the states can be directly seen from our construction of the constrained Hilbert space.

Let us consider the following two loop operators:

$$e^{2\pi i\hat{L}_1/k} \quad \text{and} \quad e^{2\pi i\hat{L}_2/k}. \tag{5.38}$$

These two operators are well defined on the constraint Hilbert space. They commute with the Gauss' law by Eq. 5.33. They also commute with the large gauge transformations. For example,

$$\begin{aligned} e^{2\pi i\hat{L}_1/k}e^{2\pi i\hat{L}_2} &= e^{2\pi ik/k}e^{2\pi i\hat{L}_2}e^{2\pi i\hat{L}_1/k} \\ &= e^{2\pi i\hat{L}_2}e^{2\pi i\hat{L}_1/k}. \end{aligned} \tag{5.39}$$

i.e. If $|\psi\rangle$ is a physical state in the constraint Hilbert space, then $e^{2\pi i\hat{L}_1/k}|\psi\rangle$ and $e^{2\pi i\hat{L}_2/k}|\psi\rangle$ are also physical states in the constraint Hilbert space.

Furthermore, the new physical states are different from $|\psi\rangle$ because the two operators do not commute with each other:

$$\begin{aligned} e^{2\pi i\hat{L}_1/k}e^{2\pi i\hat{L}_2/k} &= e^{2\pi ik/k^2}e^{2\pi i\hat{L}_2/k}e^{2\pi i\hat{L}_1/k} \\ &= e^{2\pi i/k}e^{2\pi i\hat{L}_2/k}e^{2\pi i\hat{L}_1/k}, \end{aligned} \tag{5.40}$$

unless $k = 1$.

Because $e^{i\theta_1}|\psi\rangle = e^{2\pi i\hat{L}_1}|\psi\rangle$, where θ_1 is a global phase defined in Eq. 5.27, by applying different powers of the $e^{2\pi i\hat{L}_1/k}$ operator we can obtain k different physical states

$$\{|\psi\rangle, e^{2\pi i\hat{L}_1/k}|\psi\rangle, \cdots, e^{(k-1)2\pi i\hat{L}_1/k}|\psi\rangle\}. \tag{5.41}$$

These states span a k-dimensional subspace of the Hilbert space and can be distinguished by the $e^{2\pi i\hat{L}_2/k}$ operator. This confirms the degeneracy of states first obtained on the lattice for pure Chern-Simons theories in [131].

Note that the two operators defined in Eq. 5.38 commute with the Hamiltonian by Eq. 5.32. Therefore, if $|\psi\rangle$ is an energy eigenstate of the Hamiltonian, all k distinguishable physical states in Eq. 5.41 have the same energy. Therefore, there is a k-fold degeneracy for each state in the spectrum.

We also note that $e^{2\pi i\hat{L}_1/k}$ and $e^{2\pi i\hat{L}_2/k}$ are loop operators that wrap around the periodic boundary condition in the 1 and 2 directions respectively. The distinguishability between the k physical states in Eq. 5.41 relies on such global operator, and thus they represent different topological sectors. This topological aspect can also be seen from that the operators generate the $\mathbb{Z}_k$ 1-form symmetry.

5.4.4 Wilson loop operator

In the earlier discussion of the degeneracy of states, we saw that the two loop operators in Eq. 5.38 span the finite-dimensional Hilbert space. As usual, we can construct a Wilson loop operator

$$\hat{W} = \exp\left(iQa\sum_{\text{loop}}\hat{A}\right), \tag{5.42}$$

where Q is the charge of the Wilson loop. The Wilson loop commutes with the gauge transformation operators $\hat{G}$, $\hat{L}_1$, and $\hat{L}_2$ if the charge Q is an integer. In particular, the loop can be chosen to be non-contractible. We define two non-contractible Wilson loops

$$\hat{W}_1 = \exp\left(iQa\sum_{x_1=0}^{N_1-1}\hat{A}_{(x_1,0);1}\right), \quad \hat{W}_2 = \exp\left(iQa\sum_{x_2=0}^{N_2-1}\hat{A}_{(0,x_2);2}\right). \tag{5.43}$$

However, the Wilson loop operator $\hat{W}$ does not commute with the Hamiltonian. When inserting $\hat{W}$, we shift the ground state to another topological sector. Let us evaluate the commutator between a non-contractible Wilson loop operator and the operators $e^{2\pi i\hat{L}_1/k}$, $e^{2\pi i\hat{L}_2/k}$ defined in Eq. 5.38,

$$\hat{W}_1 e^{2\pi i\hat{L}_1/k} = e^{2\pi i\hat{L}_1/k}\hat{W}_1, \quad \hat{W}_1 e^{2\pi i\hat{L}_2/k} = e^{-2\pi iQ/k}e^{2\pi i\hat{L}_2/k}\hat{W}_1, \tag{5.44}$$

$$\hat{W}_2 e^{2\pi i\hat{L}_1/k} = e^{-2\pi iQ/k}e^{2\pi i\hat{L}_1/k}\hat{W}_2, \quad \hat{W}_2 e^{2\pi i\hat{L}_2/k} = e^{2\pi i\hat{L}_2/k}\hat{W}_2. \tag{5.45}$$

We can see from these commutation relations that on the degenerate ground state subspace, a horizontal non-contractible Wilson loop $\hat{W}_1$ with charge Q is equivalent to $e^{-2\pi iQ\hat{L}_1/k}$, which

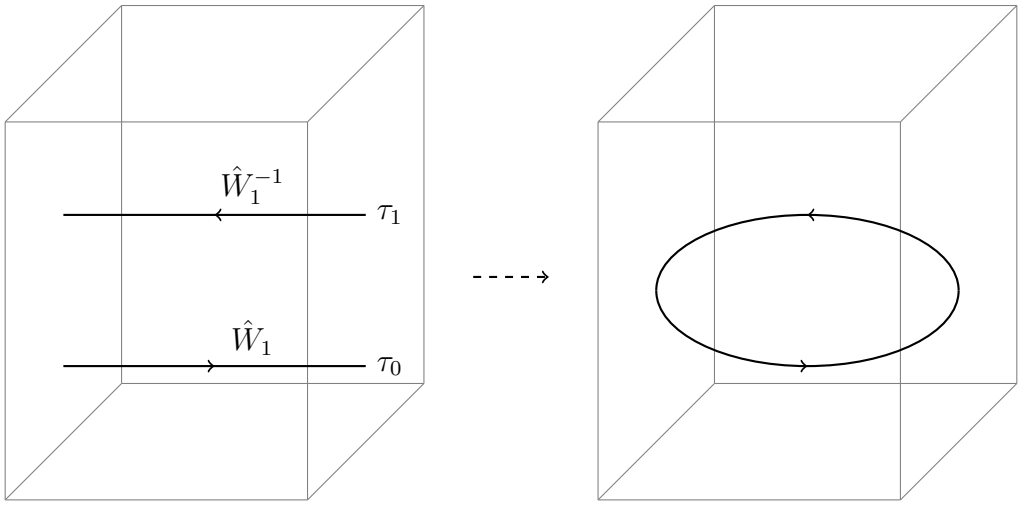

Figure 5.1: An example of a contractible Wilson loop displaying the perimeter law. Note that with periodic boundary conditions, the two straight lines in the left panel represent two non-contractible Wilson loops $\hat{W}_1$ and $\hat{W}_1^{-1}$. Thus, they form one contractible loop. This implies that the left panel can be smoothly deformed into the right panel, which helps to visualize the topology. The upward direction is the positive time direction. Evaluating $\langle \hat{W}_1^{-1}(\tau_1)\hat{W}_1(\tau_0)\rangle$ gives a constant value independent of $|\tau_1 - \tau_0|$ when $\tau_1 \gg \tau_0$, which implies the perimeter law.

has exactly same commutation relations as shown in Eq. 5.44. A vertical non-contractible Wilson loop $\hat{W}_2$ is equivalent to $e^{2\pi i Q\hat{L}_2/k}$, which has exactly same commutation relations as shown in Eq. 5.45. In other words, the projections of $\hat{W}_1$, $\hat{W}_2$ on the degenerate ground state subspace is $\hat{W}_1^{\mathrm{GS}} = e^{-2\pi i Q\hat{L}_1/k}$, $\hat{W}_2^{\mathrm{GS}} = e^{2\pi i Q\hat{L}_2/k}$, respectively. We note that the Wilson loop here is different from the framed Wilson loop introduced in Ref. [9], but we still capture the framing topological feature of the Wilson loop. This is because its projection on the degenerate ground state subspace, $\hat{W}_i^{\mathrm{GS}} = e^{\pm 2\pi i Q\hat{L}_i/k}$, has dangling links indicating the framing as shown in Eqs. 5.28 and 5.30. Furthermore, this ground state projection can be used to show the perimeter scaling law of the Wilson loop operator $\hat{W}$, as explained in the following.

As in the continuum Maxwell-Chern-Simons theory, the Wilson loop operator always exhibits a perimeter law. For example, in Fig. 5.1, we consider a contractible Wilson loop consisting of two non-contractible Wilson loops across the spatial boundary, $\hat{W}_1$ and $\hat{W}_1^{-1}$, with a temporal distance of $|\tau_1 - \tau_0|$ between each other. The area of the Wilson loop

is $|\tau_1 - \tau_0| \cdot L$, which is linearly dependent on $|\tau_1 - \tau_0|$. Here, L is the system size in the spatial direction. The perimeter of the Wilson loop is $2L$, which is independent of $|\tau_1 - \tau_0|$. We can distinguish the scaling law of the Wilson loop by looking at how its expectation value $\langle \hat{W}_1^{-1}(\tau_1)\hat{W}_1(\tau_0)\rangle$ scales with $|\tau_1 - \tau_0|$. If $\hat{W}_1(\tau_0)$ is applied to one of the ground states which is an eigenstate of $e^{2\pi i \hat{L}_2/k}$, it shifts the ground state to another topological sector (i.e. another eigenstate of $e^{2\pi i \hat{L}_2/k}$ but with a different eigenvalue) by Eq. 5.44 , and also excites the system to some higher energy state. For example, we start with one ground state and eigenstate of $e^{2\pi i \hat{L}_2/k}$, $|\mathrm{GS}_\alpha\rangle$. Suppose we get $\hat{W}_1(\tau_0)|\mathrm{GS}_\alpha\rangle = |\mathrm{GS}_\beta\rangle + \sum_i |E_i\rangle$, where $|\mathrm{GS}_\beta\rangle$ is another ground state and eigenstate of $e^{2\pi i \hat{L}_2/k}$, and $|E_i\rangle$ is the excited state with energy E_i (all states unnormalized). At time τ_1, the resulted state evolves into $|\mathrm{GS}_\beta\rangle + \sum_i e^{-E_i(\tau_1-\tau_0)}|E_i\rangle$. Contract the time-evolved state with $\langle \mathrm{GS}_\alpha|\hat{W}_1^{-1}(\tau_1)$ we get the expectation value $\langle \hat{W}_1^{-1}(\tau_1)\hat{W}_1(\tau_0)\rangle = \langle \mathrm{GS}_\beta|\mathrm{GS}_\beta\rangle + \sum_i e^{-E_i(\tau_1-\tau_0)}\langle E_i|E_i\rangle$. Because the system is gapped, the excited state components decay upon time evolution. When $|\tau_1 - \tau_0| \to \infty$, the Wilson loop expectation value $\langle \hat{W}_1^{-1}(\tau_1)\hat{W}_1(\tau_0)\rangle$ converges to a constant value $\langle \mathrm{GS}_\beta|\mathrm{GS}_\beta\rangle$ which is independent of $|\tau_1 - \tau_0|$. Therefore, the Wilson loop expectation value agrees with the perimeter law.

In addition to the perimeter scaling law, the Wilson loop operators also display non-trivial topological features. For example, we can consider two linked Wilson loops, as shown in Fig. 5.2. The pair of non-contractible loops $\hat{W}_1$ and $\hat{W}_1^{-1}$ form one contractible Wilson loop, and the other pair of non-contractible loops $\hat{W}_2$ and $\hat{W}_2^{-1}$ form a second contractible Wilson loop. The two contractible Wilson loops are linked with each other. To unlink the two loops, we can exchange $\hat{W}_2$ and $\hat{W}_1^{-1}$, which are perpendicular to each other. If $\hat{W}_1$ has charge Q_1 and $\hat{W}_2$ has charge Q_2, this exchange generates a commutator with a topological phase factor $e^{2\pi i Q_1 Q_2/k}$, as shown in the following:

$$\begin{aligned}\hat{W}_2^{-1}(\tau_3)\hat{W}_1^{-1}(\tau_2)\hat{W}_2(\tau_1)\hat{W}_1(\tau_0) &\sim e^{2\pi i Q_1 Q_2/k}\,\hat{W}_2^{-1}(\tau_3)\hat{W}_2(\tau_2)\hat{W}_1^{-1}(\tau_1)\hat{W}_1(\tau_0) \\ &\sim e^{2\pi i Q_1 Q_2/k},\end{aligned} \tag{5.46}$$

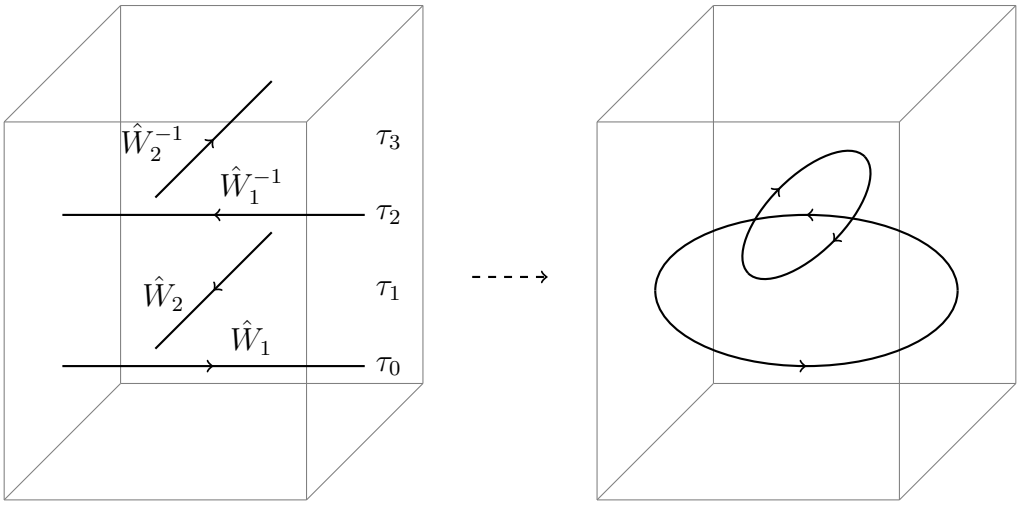

Figure 5.2: Illustration of linked Wilson loops. The upward direction is the positive time direction. The pair of non-contractible Wilson loops $\hat{W}_1$ and $\hat{W}_1^{-1}$ together form a contractible loop. The pair of non-contractible Wilson loops $\hat{W}_2$ and $\hat{W}_2^{-1}$ together form another contractible loop. These two contractible loops are linked with each other and have a non-zero linking number between them. The left panel can be smoothly deformed into the right panel, which helps to visualize the topology. Evaluating $\hat{W}_2^{-1}(\tau_3)\hat{W}_1^{-1}(\tau_2)\hat{W}_2(\tau_1)\hat{W}_1(\tau_0)$ on the ground state Hilbert space will give a non-trivial topological phase factor of $e^{2\pi i Q_1 Q_2/k}$, where k is the Chern-Simons level, Q_1 is the charge of $\hat{W}_1$, and Q_2 is the charge of $\hat{W}_2$. This non-trivial topological phase is due to the non-zero linking number between the two loops.

where the times $\tau_0 < \tau_1 < \tau_2 < \tau_3$ are well separated, k is the Chern-Simons level, and in the last step $\hat{W}_2^{-1}(\tau_3)$ almost cancels with $\hat{W}_2(\tau_2)$, $\hat{W}_1^{-1}(\tau_1)$ almost cancels with $\hat{W}_1(\tau_0)$, by a similar argument as above when we discussed the perimeter law. Therefore, this example demonstrates that two linked Wilson loops with linking number 1 have a non-trivial ground state expectation value with a topological phase factor of $e^{2\pi i Q_1 Q_2/k}$.

5.4.5 Anyon statistics

In the earlier subsections, we have seen that our formulation supports Wilson loops and they display topological features. Here we extend the discussion to open Wilson lines, which means that in Eq. 5.42 we integrate the gauge field on an open line instead of a loop, i.e. $\hat{W}_{\text{open}} = \exp(iQa\sum_{\text{line}}\hat{A})$. We know that in order to have $\hat{W}_{\text{open}}$ commute with the large gauge transformations $e^{2\pi i\hat{L}_1}$ and $e^{2\pi i\hat{L}_2}$, we need Q to be an integer, which is called

the charge of the open Wilson line. Although a single open Wilson line is not local gauge invariant (the Gauss' law in Eq. 5.25 does not commute with the open Wilson line at its two ends), the combination of an open Wilson line $\hat{W}_{\text{open}}$ with its inverse $\hat{W}^{-1}_{\text{open}}$ is gauge invariant, because the gauge non-invariant parts at their ends cancel with each other. For example, the combined operator $\hat{W}_{\text{open},1}\hat{W}_{\text{open},2}\hat{W}^{-1}_{\text{open},1}\hat{W}^{-1}_{\text{open},2}$ is gauge invariant: After a gauge transformation, the four open Wilson line operators generate c-number phases, and those phases generated by the operators and by their inverse operators cancel respectively.

We are interested in open Wilson lines because they can be viewed as the world lines of anyons, which are excitations with fractional statistics [132], [133]. Although our formulation does not involve any matter fields, we can still probe the mutual statistics and self statistics of the anyons through the open Wilson lines. We briefly demonstrate the ideas below. The operators $\hat{W}$ in this subsection all refer to open Wilson lines unless otherwise stated.

First, we look at the mutual statistics between two types of anyons, one with charge Q_1 and the other with charge Q_2. To probe their mutual statistics, we want to move one anyon around the other and compare the phases between the initial and final states. We can move the charge-Q_1 anyon by a Wilson line $\hat{W}_1$ with charge Q_1, and the charge-Q_2 anyon by a Wilson line $\hat{W}_2$ with charge Q_2. To make the movements, we apply $\hat{W}_2^{-1}(\tau_4)\hat{W}_1^{-1}(\tau_3)\hat{W}_2(\tau_2)\hat{W}_1(\tau_1)$ to a state with a charge-Q_2 anyon present [134] (see Fig. 5.3), where time $\tau_1 < \tau_2 < \tau_3 < \tau_4$ and the spacing between them are large enough so that we only need to consider the ground-state properties. (The system is gapped and correlation from the the excited states are exponentially suppressed in long time.) The presence of the initial charge-Q_2 anyon can be created by some Wilson line on the ground state at $\tau \to -\infty$, and we can annihilate it by the inverse Wilson line at $\tau \to \infty$ to go back to the degenerate ground-state Hilbert space. The creation and annihilation of this initial charge-Q_2 anyon are not important to our discussion later.

As shown in Fig. 5.3, we apply $\hat{W}_2^{-1}(\tau_4)\hat{W}_1^{-1}(\tau_3)\hat{W}_2(\tau_2)\hat{W}_1(\tau_1)$ and operate the anyons as follows: We first create a pair of anyon and anti-anyon of charge Q_1 with the open Wilson

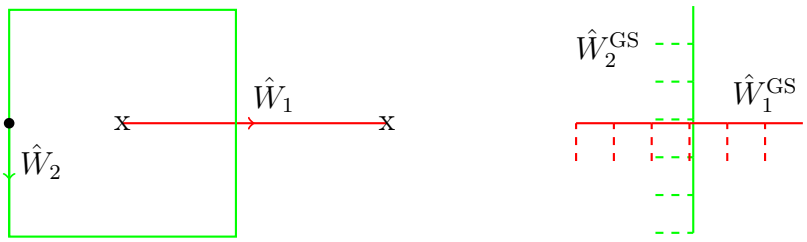

Figure 5.3: Illustration of mutual statistics between anyons. On the left panel, $\hat{W}_1$ is an open Wilson line with charge Q_1, and $\hat{W}_2$ is a Wilson loop with charge Q_2. When we compute the ground state expectation value of the gauge invariant operator $\hat{W}_2^{-1}(\tau_4)\hat{W}_1^{-1}(\tau_3)\hat{W}_2(\tau_2)\hat{W}_1(\tau_1)$, $\tau_1 < \tau_2 < \tau_3 < \tau_4$, we measure the mutual statistics between a charge-Q_1 anyon and a charge-Q_2 anyon as follows [134]. Suppose initially there is a charge-Q_2 anyon at the dot. We first create a charge-Q_1 anyon-anti-anyon pair by $\hat{W}_1(\tau_1)$ at its two ends (the x's), second we move the charge-Q_2 anyon around the charge-Q_1 anyon by $\hat{W}_2(\tau_2)$, then we annihilate the charge-Q_1 anyon-anti-anyon pair by $\hat{W}_1^{-1}(\tau_3)$, finally we move back the charge-Q_2 anyon by $\hat{W}_2^{-1}(\tau_4)$ to cancel the dynamical phase created by its movement. Therefore, $\langle\hat{W}_2^{-1}(\tau_4)\hat{W}_1^{-1}(\tau_3)\hat{W}_2(\tau_2)\hat{W}_1(\tau_1)\rangle$ shows the topological phase of a charge-Q_2 anyon circling around a charge-Q_1 anyon, i.e. their mutual statistics [134]. On the right panel, we zoom in to look at the intersection of the red and green lines. $\hat{W}_1^{\rm GS}$ and $\hat{W}_2^{\rm GS}$ are the projections of the operators $\hat{W}_1$ and $\hat{W}_2$ on the degenerate ground-state Hilbert space, respectively. From the microscopic details of $\hat{W}_1^{\rm GS}$ and $\hat{W}_2^{\rm GS}$ on the lattice (solid links are proportional to the gauge field $\hat{A}$, dashed links are proportional to the canonical conjugate momentum $\hat{p}$, similar to $\hat{L}_i$ in Eqs. 5.28 and 5.30), we can see that $\hat{W}_1^{\rm GS}$ and $\hat{W}_2^{\rm GS}$ do not commute with each other by sharing common links.

line $\hat{W}_1(\tau_1)$. Second we circle the exiting charge-Q_2 anyon around the charge-Q_1 anyon with $\hat{W}_2(\tau_2)$. Then we annihilate the charge-Q_1 anyon-anti-anyon pair with $\hat{W}_1^{-1}(\tau_3)$. Finally we cancel the dynamical phase of the charge-Q_2 anyon with $\hat{W}_2^{-1}(\tau_4)$. The net effect of these operations results in a charge-Q_2 anyon circling around a charge-Q_1 anyon. Therefore, the ground state expectation value $\langle\hat{W}_2^{-1}(\tau_4)\hat{W}_1^{-1}(\tau_3)\hat{W}_2(\tau_2)\hat{W}_1(\tau_1)\rangle$ has a topological phase showing the mutual statistics between charge-Q_1 and charge-Q_2 anyons. (More precisely, we compare the phase between $\langle\hat{W}_0^{-1}(+\infty)\hat{W}_2^{-1}(\tau_4)\hat{W}_1^{-1}(\tau_3)\hat{W}_2(\tau_2)\hat{W}_1(\tau_1)\hat{W}_0(-\infty)\rangle$ and $\langle\hat{W}_0^{-1}(+\infty)\hat{W}_2^{-1}(\tau_4)\hat{W}_2(\tau_3)\hat{W}_1^{-1}(\tau_2)\hat{W}_1(\tau_1)\hat{W}_0(-\infty)\rangle$, where $\hat{W}_0(-\infty)$ prepares the initial charge-Q_2 anyon and $\hat{W}_0^{-1}(+\infty)$ annihilate it back to the ground state. Note that the latter process is trivial. Therefore, this relative phase showing the mutual statistics is equivalent to the phase of the $\langle\hat{W}_2^{-1}(\tau_4)\hat{W}_1^{-1}(\tau_3)\hat{W}_2(\tau_2)\hat{W}_1(\tau_1)\rangle$.)

Now we see how the ground state expectation value $\langle\hat{W}_2^{-1}(\tau_4)\hat{W}_1^{-1}(\tau_3)\hat{W}_2(\tau_2)\hat{W}_1(\tau_1)\rangle$ can

be computed. We consider a charge-Q open Wilson line

$$\hat{W} = \exp(iQa \sum_{(x,i)} \hat{A}_{x;i}), \tag{5.47}$$

and a "dangling Wilson line" (which is a truncated line segment of the loop operator $e^{\pm 2\pi i Q \hat{L}_i/k}$, where $\hat{L}_i$ are the large gauge transformation operators in Eqs. 5.28 and 5.30)

$$\begin{aligned} \hat{W}^{\mathrm{GS}} &= \exp\left[\frac{2\pi i Q}{k} \sum_{(x,i)} (\frac{ka}{4\pi} \hat{A}_{x;i} - \epsilon_{ij} \frac{1}{a} \hat{p}_{x-\hat{j};j})\right] \\ &= \exp\left[iQ \sum_{(x,i)} (\frac{a}{2} \hat{A}_{x;i} - \epsilon_{ij} \frac{2\pi}{ka} \hat{p}_{x-\hat{j};j})\right], \end{aligned} \tag{5.48}$$

where $(x,i) \in \{\text{(site,direction) in line}\}$ represent the sites in a line and the corresponding directions along the line. For visualization, see the correspondence between left and right panels in Fig. 5.3 and 5.4, where solid links contain the gauge field $\hat{A}$ and the dashed links contain the canonical conjugate momentum $\hat{p}$. The relative signs between $\hat{A}$ and $\hat{p}$ in $\hat{W}^{\mathrm{GS}}$ follows the ones in $\hat{L}_i$ in Eqs. 5.28 and 5.30.

When the temporal spacings are large, we can compute $\langle \hat{W}_2^{-1}(\tau_4) \hat{W}_1^{-1}(\tau_3) \hat{W}_2(\tau_2) \hat{W}_1(\tau_1) \rangle$ by projecting everything onto the degenerate ground state subspace. We note that by a similar argument we used in the discussion before on the perimeter law in Sec. 5.4.4, $\hat{W}$ is equivalent to its projection $\hat{W}^{\mathrm{GS}}$ on the degenerate ground state subspace when its temporal spacings between other operators are large enough, which ensures the excited-state components exponentially decay out. Although we have only proved this with Wilson loops, but not with open Wilson lines, we assume the equivalence also holds for open Wilson lines, i.e.

$$\langle \hat{W}_2^{-1}(\tau_4) \hat{W}_1^{-1}(\tau_3) \hat{W}_2(\tau_2) \hat{W}_1(\tau_1) \rangle \sim \langle \hat{W}_2^{\mathrm{GS}^{-1}} \hat{W}_1^{\mathrm{GS}^{-1}} \hat{W}_2^{\mathrm{GS}} \hat{W}_1^{\mathrm{GS}} \rangle. \tag{5.49}$$

We note that the operators in both sides of Eq. 5.49 are gauge invariant due to the gauge

phase cancellation between the open Wilson lines and their corresponding inverse operators.

The right hand side of Eq. 5.49 can be directly computed:

$$\begin{aligned}\langle \hat{W}_2^{\mathrm{GS}^{-1}} \hat{W}_1^{\mathrm{GS}^{-1}} \hat{W}_2^{\mathrm{GS}} \hat{W}_1^{\mathrm{GS}} \rangle &= e^{\frac{2\pi i}{k} Q_1 Q_2} \langle \hat{W}_2^{\mathrm{GS}^{-1}} \hat{W}_2^{\mathrm{GS}} \hat{W}_1^{\mathrm{GS}^{-1}} \hat{W}_1^{\mathrm{GS}} \rangle \\ &= e^{\frac{2\pi i}{k} Q_1 Q_2},\end{aligned} \tag{5.50}$$

where we used the commutation relation

$$\hat{W}_1^{\mathrm{GS}^{-1}} \hat{W}_2^{\mathrm{GS}} = e^{\frac{2\pi i}{k} Q_1 Q_2} \hat{W}_2^{\mathrm{GS}} \hat{W}_1^{\mathrm{GS}^{-1}}, \tag{5.51}$$

which can be seen by the overlapping red solid link ($\hat{A}_{x-\hat{1};1}$) and green dashed link ($\hat{p}_{x-\hat{1};1}$) with commutator $[\hat{A}_{x-\hat{1};1}, \hat{p}_{x-\hat{1};1}] = i$, and green solid link ($\hat{A}_{x-\hat{2};2}$) and red dashed link ($\hat{p}_{x-\hat{2};2}$) with commutator $[\hat{A}_{x-\hat{2};2}, \hat{p}_{x-\hat{2};2}] = i$, where red variables are in $\hat{W}_1^{\mathrm{GS}^{-1}}$ and green variables are in $\hat{W}_2^{\mathrm{GS}}$, x is the intersection site of the red and green solid lines, shown in the right panel in Fig. 5.3. In particular, the phase comes from

$$\begin{aligned}&\exp\left[-iQ_1(\frac{a}{2}\hat{A}_{x-\hat{1};1} - \frac{2\pi}{ka}\hat{p}_{x-\hat{2};2})\right] \exp\left[iQ_2(\frac{a}{2}\hat{A}_{x-\hat{2};2} + \frac{2\pi}{ka}\hat{p}_{x-\hat{1};1})\right] \\ &= e^{\frac{2\pi i}{k} Q_1 Q_2} \exp\left[iQ_2(\frac{a}{2}\hat{A}_{x-\hat{2};2} + \frac{2\pi}{ka}\hat{p}_{x-\hat{1};1})\right] \exp\left[-iQ_1(\frac{a}{2}\hat{A}_{x-\hat{1};1} - \frac{2\pi}{ka}\hat{p}_{x-\hat{2};2})\right],\end{aligned} \tag{5.52}$$

due to the commutator

$$[-iQ_1(\frac{a}{2}\hat{A}_{x-\hat{1};1} - \frac{2\pi}{ka}\hat{p}_{x-\hat{2};2}),\ iQ_2(\frac{a}{2}\hat{A}_{x-\hat{2};2} + \frac{2\pi}{ka}\hat{p}_{x-\hat{1};1})] = \frac{2\pi i}{k} Q_1 Q_2, \tag{5.53}$$

where the minus sign in the first term comes from the inverse (-1) in $\hat{W}_1^{\mathrm{GS}^{-1}}$.

In summary, we have computed that $\langle \hat{W}_2^{-1}(\tau_4) \hat{W}_1^{-1}(\tau_3) \hat{W}_2(\tau_2) \hat{W}_1(\tau_1) \rangle$ has a non-trivial topological phase $e^{\frac{2\pi i}{k} Q_1 Q_2}$, which demonstrates the mutual statistics between charge-Q_1 and charge-Q_2 anyons.

We can also study the anyon self statistics using open Wilson lines. To probe the self

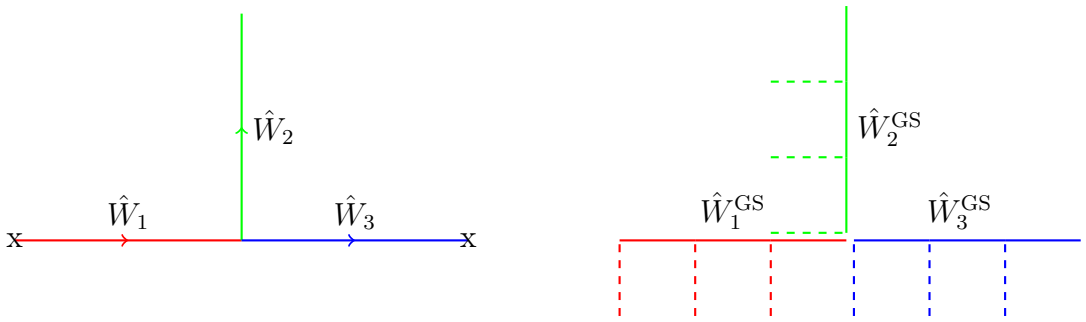

Figure 5.4: Illustration of self statistics of one type of anyon. On the left panel, $\hat{W}_1$, $\hat{W}_2$, and $\hat{W}_3$ are three open Wilson lines all with charge Q. When we compute the ground state expectation value of the gauge invariant operator $\hat{W}_3(\tau_6)\hat{W}_2^{-1}(\tau_5)\hat{W}_1^{-1}(\tau_4)\hat{W}_3^{-1}(\tau_3)\hat{W}_2(\tau_2)\hat{W}_1(\tau_1)$, $\tau_1 < \tau_2 < \tau_3 < \tau_4 < \tau_5 < \tau_6$, we measure the self statistics of exchanging a pair of charge-Q anyons as follows [135]. Suppose initially there are two identical anyons located at the x's. We first move the left anyon to the middle by $\hat{W}_1(\tau_1)$, second we move it upward by $\hat{W}_2(\tau_2)$, third we move the right anyon to the middle by $\hat{W}_3^{-1}(\tau_3)$, fourth we move it leftward by $\hat{W}_1^{-1}(\tau_4)$, fifth we move the original left anyon back to middle by $\hat{W}_2^{-1}(\tau_5)$, and finally we move it rightward by $\hat{W}_3(\tau_6)$. We have exchanged the position of the two anyons without them getting close to each other, and all dynamical phases created by anyon movements are cancelled. Therefore, $\langle\hat{W}_3(\tau_6)\hat{W}_2^{-1}(\tau_5)\hat{W}_1^{-1}(\tau_4)\hat{W}_3^{-1}(\tau_3)\hat{W}_2(\tau_2)\hat{W}_1(\tau_1)\rangle$ shows the topological phase of two anyons exchanging their positions, i.e. the self statistics [135]. On the right panel, we zoom in to look at the intersection of the red, green, and blue lines. $\hat{W}_1^{\mathrm{GS}}$, $\hat{W}_2^{\mathrm{GS}}$, and $\hat{W}_3^{\mathrm{GS}}$ are the projections of the operators $\hat{W}_1$, $\hat{W}_2$, and $\hat{W}_3$ on the degenerate ground-state Hilbert space, respectively. From the microscopic details of $\hat{W}_1^{\mathrm{GS}}$, $\hat{W}_2^{\mathrm{GS}}$, and $\hat{W}_3^{\mathrm{GS}}$ on the lattice (solid links are proportional to the gauge field $\hat{A}$, dashed links are proportional to the canonical conjugate momentum $\hat{p}$, similar to $\hat{L}_i$ in Eqs. 5.28 and 5.30), we can see that $\hat{W}_1^{\mathrm{GS}}$ and $\hat{W}_2^{\mathrm{GS}}$ do not commute with each other by sharing a common link.

statistics, we want to exchange the position of two anyons with the same charge Q and compare the phase between the initial and final states. To make the movements, we apply the gauge invariant composite operator $\hat{W}_3(\tau_6)\hat{W}_2^{-1}(\tau_5)\hat{W}_1^{-1}(\tau_4)\hat{W}_3^{-1}(\tau_3)\hat{W}_2(\tau_2)\hat{W}_1(\tau_1)$ to a state with two charge-Q anyons present at the end of $\hat{W}_1$ and $\hat{W}_3$ [135] (see Fig. 5.4), where time $\tau_1 < \tau_2 < \tau_3 < \tau_4 < \tau_5 < \tau_6$ and the spacing between them are large enough so that we only need to consider the ground-state properties. Similar to the earlier discussion on the mutual statistics, the creation and annihilation of the anyons are performed at $\tau \to -\infty$ and $\tau \to \infty$, respectively, and they are not important to our discussion.

As shown in Fig. 5.4, we apply $\hat{W}_3(\tau_6)\hat{W}_2^{-1}(\tau_5)\hat{W}_1^{-1}(\tau_4)\hat{W}_3^{-1}(\tau_3)\hat{W}_2(\tau_2)\hat{W}_1(\tau_1)$ to operate the anyons as follows: Initially, we have two anyons locating at the two crosses respectively,

and we want to exchange their location without having them close to each other. First, we move the anyon on the left to the middle with the open Wilson line $\hat{W}_1(\tau_1)$. Second, we move it upward with $\hat{W}_2(\tau_2)$, in order to make space for the other anyon. Third, we move the other anyon on the right to the middle with $\hat{W}_3^{-1}(\tau_3)$. Forth, we move it to the left cross with $\hat{W}_1^{-1}(\tau_4)$. Fifth, we move the original left anyon downward back to the middle with $\hat{W}_2^{-1}(\tau_5)$. Finally, we move it to the right cross with $\hat{W}_3(\tau_6)$. With these six steps, we exchange the locations of the two anyons.

Therefore, the expectation value $\langle \hat{W}_3(\tau_6)\hat{W}_2^{-1}(\tau_5)\hat{W}_1^{-1}(\tau_4)\hat{W}_3^{-1}(\tau_3)\hat{W}_2(\tau_2)\hat{W}_1(\tau_1)\rangle$ comparing to the trivial process $\langle \hat{W}_1^{-1}(\tau_6)\hat{W}_2^{-1}(\tau_5)\hat{W}_3(\tau_4)\hat{W}_3^{-1}(\tau_3)\hat{W}_2(\tau_2)\hat{W}_1(\tau_1)\rangle$ has a topological phase showing the self statistics between two charge-Q anyons. The former anyon-exchanged ground state expectation value can be computed similarly with the projections of the open Wilson lines on the degenerate ground state subspace. On the right pannel in Fig. 5.4, we show the corresponding projections $\hat{W}_i^{\mathrm{GS}}$ at the junction point of the three open Wilson lines. The formula of the open Wilson lines and their projections are written in Eqs. 5.47 and 5.48, respectively.

When the temporal spacings are large, we can compute the ground state expectation value $\langle \hat{W}_3(\tau_6)\hat{W}_2^{-1}(\tau_5)\hat{W}_1^{-1}(\tau_4)\hat{W}_3^{-1}(\tau_3)\hat{W}_2(\tau_2)\hat{W}_1(\tau_1)\rangle$ by projecting everything onto the degenerate ground state subspace, similar to what we did above in the discussion on the mutual statistics in Eqs. 5.49 and 5.50. We have

$$\begin{aligned}\langle \hat{W}_3(\tau_6)\hat{W}_2^{-1}(\tau_5)\hat{W}_1^{-1}(\tau_4)\hat{W}_3^{-1}(\tau_3)\hat{W}_2(\tau_2)\hat{W}_1(\tau_1)\rangle &\sim \langle \hat{W}_3^{\mathrm{GS}}\hat{W}_2^{\mathrm{GS}^{-1}}\hat{W}_1^{\mathrm{GS}^{-1}}\hat{W}_3^{\mathrm{GS}^{-1}}\hat{W}_2^{\mathrm{GS}}\hat{W}_1^{\mathrm{GS}}\rangle \\ &\sim e^{\frac{\pi i}{k}Q^2}\langle \hat{W}_1^{\mathrm{GS}^{-1}}\hat{W}_2^{\mathrm{GS}^{-1}}\hat{W}_3^{\mathrm{GS}}\hat{W}_3^{\mathrm{GS}^{-1}}\hat{W}_2^{\mathrm{GS}}\hat{W}_1^{\mathrm{GS}}\rangle \\ &\sim e^{\frac{\pi i}{k}Q^2}, \end{aligned} \tag{5.54}$$

where we use the fact that $\hat{W}_3^{\mathrm{GS}}$ commutes with the other open Wilson lines' projections because of no overlapping links (see the right pannel in Fig. 5.4), and we use the commutation

relation

$$\hat{W}_2^{\mathrm{GS}^{-1}}\hat{W}_1^{\mathrm{GS}^{-1}} = e^{\frac{\pi i}{k}Q^2}\hat{W}_1^{\mathrm{GS}^{-1}}\hat{W}_2^{\mathrm{GS}^{-1}}, \tag{5.55}$$

which can be seen by the overlapping red solid link ($\hat{A}_{x-\hat{1};1}$) and green dashed link ($\hat{p}_{x-\hat{1};1}$) with commutator $[\hat{A}_{x-\hat{1};1}, \hat{p}_{x-\hat{1};1}] = i$, where red variables are in $\hat{W}_1^{\mathrm{GS}^{-1}}$ and green variables are in $\hat{W}_2^{\mathrm{GS}^{-1}}$, x is the junction site of the three solid lines, shown in the right panel in Fig. 5.4. In particular, the phase comes from

$$\exp\left[-iQ\frac{2\pi}{ka}\hat{p}_{x-\hat{1};1}\right]\exp\left[-iQ\frac{a}{2}\hat{A}_{x-\hat{1};1}\right] = e^{\frac{\pi i}{k}Q^2}\exp\left[-iQ\frac{a}{2}\hat{A}_{x-\hat{1};1}\right]\exp\left[-iQ\frac{2\pi}{ka}\hat{p}_{x-\hat{1};1}\right], \tag{5.56}$$

due to the commutator

$$[-iQ\frac{2\pi}{ka}\hat{p}_{x-\hat{1};1},\ -iQ\frac{a}{2}\hat{A}_{x-\hat{1};1}] = \frac{\pi i}{k}Q^2, \tag{5.57}$$

where the minus sign in both terms come from the inverse (-1) in $\hat{W}_i^{\mathrm{GS}^{-1}}$.

In summary, we have computed that $\langle\hat{W}_3(\tau_6)\hat{W}_2^{-1}(\tau_5)\hat{W}_1^{-1}(\tau_4)\hat{W}_3^{-1}(\tau_3)\hat{W}_2(\tau_2)\hat{W}_1(\tau_1)\rangle$ has a non-trivial topological phase $e^{\frac{\pi i}{k}Q^2}$, which demonstrates the self statistics between two charge-Q anyons.

Note that for the minimally charged anyons with $Q = 1$, the self statistics has the exchange phase $e^{\frac{\pi i}{k}}$. We know the bosonic statistics has the phase $(+1)$ and the fermionic statistics has the phase (-1). Therefore, for $k \geq 2$, this phase $e^{\frac{\pi i}{k}}$ demonstrates a fractional statistics (i.e. neither bosonic nor fermionic statistics) of anyons.

We discussed earlier in Sec. 5.4.2 that an odd-k Chern-Simons level implies the fermionic nature of the theory. Now from the self statstics, we can directly see that the theory contains fermions when k is odd. Consider the anyons with charge $Q = k$. Their self statistics has the exchange phase $e^{\frac{\pi i}{k}Q^2} = e^{i\pi k}$. When k is even, the charge-k anyons are bosons. When k

is odd, the charge-k anyons are fermions.

From the calculation of the anyon statistics above, we demonstrate that our lattice Hamiltonian formulation captures the non-trivial braiding of Wilson lines, and therefore realizes the framing anomaly [9], [10], [136]–[138]. In our formulation, the projections of the Wilson lines on the degenerate ground state subspace, as shown in Eq. 5.48, explicitly include a well-defined point-splitting regularization. The dangling dashed links shown in Figs. 5.3 and 5.4, on which the canonical conjugate momentum operators $\hat{p}$ are sitting, define the framing of the Wilson loops. This agrees with the observation in Ref. [9], [10] that the physical operators are ribbons, or framed Wilson loops. There the authors construct the framed Wilson loops by two displaced Wilson loops [9], [10]. Here with the Maxwell term introduced, we can define independent canonical conjugate momentum operators $\hat{p}$, and we construct the framed Wilson loops by the "dangling Wilson loops" as shown in Figs. 5.3 and 5.4.

5.5 Analytical solution

In this section, we present the solution of all lattice momentum modes to the Hamiltonian in Eq. 5.23. Since the Hamiltonian is quadratic, we can use the Fourier transform to decompose it into independent momentum sectors. We rewrite the Hamiltonian as

$$\hat{H} = \sum_{\substack{x=(x_1,x_2) \\ x_1\in\{0,1,\ldots,N_1-1\} \\ x_2\in\{0,1,\ldots,N_2-1\}}} \frac{e^2}{2a^2} \sum_{\mu,\nu\in\{1,2\}} \left(\hat{p}_{x;\mu} - \epsilon_{\mu\nu}\frac{ka^2}{4\pi}\hat{A}_{x-\hat{\nu};\nu}\right)^2 + \frac{1}{2e^2}\left(\Box\hat{A}_{x;1,2}\right)^2. \tag{5.58}$$

We apply the following Fourier transform

$$\hat{A}_{q;\mu} = \frac{1}{\sqrt{N_1 N_2}} \sum_{\substack{x=(x_1,x_2) \\ x_1\in\{0,1,\ldots,N_1-1\} \\ x_2\in\{0,1,\ldots,N_2-1\}}} e^{i\vec{q}\cdot\vec{x}} \hat{A}_{x;\mu}, \tag{5.59}$$

$$\hat{p}_{q;\mu} = \frac{1}{\sqrt{N_1 N_2}} \sum_{\substack{x=(x_1,x_2) \\ x_1\in\{0,1,\ldots,N_1-1\} \\ x_2\in\{0,1,\ldots,N_2-1\}}} e^{i\vec{q}\cdot\vec{x}} \hat{p}_{x;\mu}, \tag{5.60}$$

with inverse Fourier transform

$$\hat{A}_{x;\mu} = \frac{1}{\sqrt{N_1 N_2}} \sum_{\substack{q=(q_1,q_2) \\ q_1\in\{0,\frac{2\pi}{N_1},\ldots,\frac{2\pi}{N_1}(N_1-1)\} \\ q_2\in\{0,\frac{2\pi}{N_2},\ldots,\frac{2\pi}{N_2}(N_2-1)\}}} e^{-i\vec{q}\cdot\vec{x}} \hat{A}_{q;\mu}, \tag{5.61}$$

$$\hat{p}_{x;\mu} = \frac{1}{\sqrt{N_1 N_2}} \sum_{\substack{q=(q_1,q_2) \\ q_1\in\{0,\frac{2\pi}{N_1},\ldots,\frac{2\pi}{N_1}(N_1-1)\} \\ q_2\in\{0,\frac{2\pi}{N_2},\ldots,\frac{2\pi}{N_2}(N_2-1)\}}} e^{-i\vec{q}\cdot\vec{x}} \hat{p}_{q;\mu}. \tag{5.62}$$

The commutation relation between the operators is

$$[\hat{A}_{x;\mu}, \hat{p}_{y;\nu}] = i\delta_{x,y}\delta_{\mu,\nu} \tag{5.63}$$

$$[\hat{A}_{q;\mu}, \hat{p}_{r;\nu}] = i\delta_{q+r,2\pi\mathbb{Z}}\delta_{\mu,\nu} \tag{5.64}$$

The Fourier transformed Hamiltonian looks like

$$\begin{aligned}\hat{H} = \sum_{\substack{q=(q_1,q_2) \\ q_1\in\{0,\frac{2\pi}{N_1},\ldots,\frac{2\pi}{N_1}(N_1-1)\} \\ q_2\in\{0,\frac{2\pi}{N_2},\ldots,\frac{2\pi}{N_2}(N_2-1)\}}} &+\frac{e^2}{2a^2}\left[\left(\hat{p}_{q;1} - \frac{ka^2}{4\pi}e^{iq_2}\hat{A}_{q;2}\right)\left(\hat{p}_{-q;1} - \frac{ka^2}{4\pi}e^{-iq_2}\hat{A}_{-q;2}\right)\right. \\ &\left. + \left(\hat{p}_{q;2} + \frac{ka^2}{4\pi}e^{iq_1}\hat{A}_{q;1}\right)\left(\hat{p}_{-q;2} + \frac{ka^2}{4\pi}e^{-iq_1}\hat{A}_{-q;1}\right)\right] \\ +\frac{1}{2e^2}&\left[\left(1-e^{-iq_2}\right)\hat{A}_{q;1} - \left(1-e^{-iq_1}\right)\hat{A}_{q;2}\right]\left[\left(1-e^{iq_2}\right)\hat{A}_{-q;1} - \left(1-e^{iq_1}\right)\hat{A}_{-q;2}\right].\end{aligned} \tag{5.65}$$

After some change of variables and applying the Gauss' law Eq. 5.25 (see more details in the Appendix 5.7.8), the Hamiltonian in the lattice momentum $q = (q_1, q_2)$ sector corresponds to a simple harmonic oscillator with angular frequency

$$\omega^2 = \frac{1}{a^2}\left[2(1-\cos q_1) + 2(1-\cos q_2)\right] + \left(\frac{ke^2}{4\pi}\right)^2 \left[2 + 2\cos(q_1+q_2)\right]. \tag{5.66}$$

The energy of the corresponding first excited state above the ground state is

$$\Delta E = \omega = \sqrt{\frac{1}{a^2}\left[2(1-\cos q_1) + 2(1-\cos q_2)\right] + \left(\frac{ke^2}{4\pi}\right)^2 \left[2 + 2\cos(q_1+q_2)\right]}, \tag{5.67}$$

which is plotted in Fig. 5.5. The different subplots in Fig. 5.5 correspond to different values of a combined parameter $(ke^2a/4\pi)^2$. Each state in the band is k-fold degenerate.

There are two interesting limits of this energy spectrum. First we note that the dimensionless lattice momentum $q = a\tilde{q}$, where $\tilde{q}$ is the dimensionful momentum. Then by taking the continuum limit $a \to 0$, we get

$$\omega^2 \to |\tilde{q}|^2 + \left(\frac{ke^2}{2\pi}\right)^2, \tag{5.68}$$

which describes a massive particle with mass equals to $ke^2/2\pi$. i.e., the photon becomes massive, and the theory opens a gap. The $|\tilde{q}|^2$ part comes from the first term $\frac{2}{a^2}(1-\cos a\tilde{q}_i)$ in Eq. 5.66. This energy dispersion agrees with the one in the continuous Maxwell-Chern-Simons theory [93].

Another limit is when $k \to \infty$. The Chern-Simons term dominates. The band structure looks similar to the one of the pure continuous Chern-Simons theory, with the band bottom located at two lines specified by $q_1 + q_2 = \pi + 2\pi\mathbb{Z}$. These two lines correspond to the "staggered momentum modes" mentioned in Ref. [10].

One interesting observation is that the band bottom changes location, although this does not mean a phase transition because the band is showing the first excited state but not the

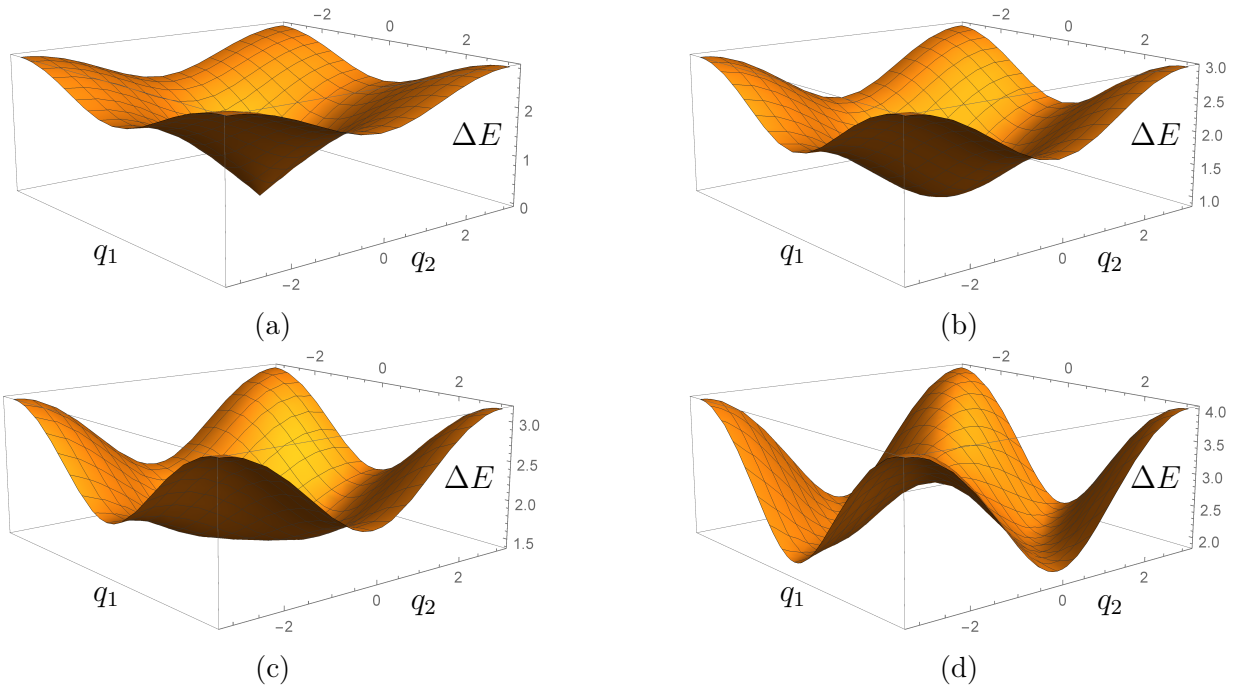

Figure 5.5: 3D plot of the band structure of the analytical solution to the Maxwell-Chern-Simons Hamiltonian. The vertical axis is the energy of the first excited state ΔE above the ground state. Two horizontal axes are the two components of the lattice momentum $q = (q_1, q_2)$. Each subfigure corresponds to a different coupling strength $\lambda = (ke^2a/4\pi)^2$. (a) $\lambda = 0$, this corresponds to the pure Maxwell theory, in which we can see a linear-dispersion gapless photon. (b) $\lambda = 0.2$, the Chern-Simons term gaps out the theory and gives the photon a mass. (c) $\lambda = 0.5$, this is the special λ value beyond which the band bottom is no longer at $q = (0, 0)$. (d) $\lambda = 2.0$, for large λ value the band looks like the one for a pure Chern-Simons theory, in which the band bottom are two lines specified by $q_1 + q_2 = \pi + 2\pi\mathbb{Z}$. These two lines correspond to the "staggered momentum modes" mentioned in Ref. [10].

ground state.

There is also a distinction between the $q = (0, 0)$ zero mode and the other modes. The Gauss' law (constraint 1) acts trivially on the zero mode, and therefore leaves a free degree of freedom. The Constraint 2 and 3 requires both the momentum and the coordinate of this free degree of freedom to be quantized, which is equivalent to a single particle on a circle with finite sites. As shown in the Appendix 5.7.8, there are exactly k sites on the circle. Therefore, the Hilbert space for the zero mode is k dimensional, and results in the k-fold degeneracy of every states. This is consistent with our earlier discussion in Sec. 5.4.3.

5.6 Summary and discussion

In this chapter, we derive the Hamiltonian formulation of Maxwell-Chern-Simons theory on a lattice in (2+1) dimensions. Comparing to the well-known 2+1D compact lattice QED Hamiltonian, the modification in our Hamiltonian formulation is as follows. First, the instantons in the theory are suppressed as a hard constraint. Similar to the Witten effect in 3+1D [128], an instanton (i.e. a magnetic monopole in 2+1D) must have an electric charge under the Chern-Simons action, our pure gauge theory cannot allow instantons. We further show the instanton suppression can turn the 2+1D compact lattice QED Hamiltonian into an unusual form (see Appendix 5.7.6). This instanton-suppressed compact lattice QED Hamiltonian will have quadratic terms in the gauge field $\hat{A}$, and it is indeed a compact theory by the Villain approximation with two 1-form constraints. The two 1-form constraints make sure that the theory is invariant under the large gauge transformations in two spacial directions. Furthermore, this instanton-suppressed quadratic Hamiltonian is analytically solvable, showing a gapless theory with massless photons. Unlike the instanton-allowed compact lattice QED, which is gapped in 2+1D, the instanton-suppressed version is the Maxwell theory in the continuum, which is gapless.

The second modification is to introduce the Chern-Simons term to this instanton-suppressed Hamiltonian. The effect of this step is that a gauge field operator $\hat{A}$ on a shifted site and in the perpendicular direction is attached to the conjugate momentum operator $\hat{p}$ wherever $\hat{p}$ appears. Therefore, we see the modification in the quadratic $\hat{p}$ terms in the Hamiltonian in Eq. 5.23, the Gauss' law constraint in Eq. 5.28, and the two 1-form constraints in Eqs. 5.28 and 5.30.

We demonstrate the topological features of our Hamiltonian formulation. The compatibility between the constraints requires the quantization of the Chern-Simons level k. The existence of two 1-form operators generates the k-fold degeneracy of the spectrum. The Wilson loop expectation values in the theory always show a perimeter law. Linked Wilson loops

have non-trivial topological phases evaluated on the degenerate Hilbert subspace. Anyons as the excitations at the ends of open Wilson lines display fractional mutual statistics and self statistics. These topological features agree with the ones in a continuum Maxwell-Chern-Simons theory, showing our Hamiltonian formulation is the correct lattice theory for the continuum theory.

The continuum limit of our lattice Hamiltonian formulation can also be directly seen from the analytical solution of the theory. Since the Hamiltonian in Eq. 5.23 is quadratic, we perform the Fourier transform and solve its band structure in the Brillouin zone. We can see the correct band gap $ke^2/2\pi$ and the massive photon dispersion that agree with the continuum Maxwell-Chern-Simons theory.

In our work, we add the Maxwell term to the Chern-Simon theory, which allows us to construct the independent canonical conjugate momentum operator $\hat{p}$. Our formulation accepts the gauge field configurations as the natural basis for the Hilbert space. This is in contract to the recent work that presents a canonical quantization of lattice Chern-Simons theory [10], which does not have Maxwell action and the canonical quantization unavoidably has non-trivial commutation between operators on different spacial locations. This "fuzzy" space makes it difficult to construct a good orthonormal basis for the Hilbert space and apply numerical methods. Therefore, our lattice Hamiltonian formulation opens the door to many possible numerical methods to study this interesting topological theory. For future study, it is possible to design quantum algorithms for simulating with our lattice Hamiltonian formulation. Numerical simulations with tensor network ansatz or machine-learning approach are also applicable with our formulation. It will also be an important direction to further extend the simulations for our model coupled to matter fields.

5.7 Appendix

5.7.1 Review of instantons in compact Maxwell theory

In this section we briefly review the effect of instantons on a 2+1D compact U(1) gauge theory (i.e. Maxwell theory) [139], [140]. The theory contains instantons if it has a finite cut-off scale, which is our lattice spacing here. Instantons are discontinuities in the gauge field configuration where the total flux through a plane suddenly changes by 2π. In 2+1D, an instanton configuration has a finite action. Therefore, when computing the contribution to the partition function $e^{-S(A)}$, instanton configurations have non-zero weight. Because we need to take into account the instanton configurations, the theory is no longer Gaussian quadratic around the $A = 0$ minimum, i.e. no longer a free theory. Moreover, because an instanton changes the flux permanently after its appearance, its long-range feature has significant influence on the correlation functions. In particular, it makes the Wilson loops scale as the Area law, and confines charged particles [139].

The effect of instantons can be seen clearly using the duality between the U(1) gauge theory and the XY model [141]. In the duality, the flux in the U(1) gauge theory maps to the charge in the XY model. Therefore, the instanton operator, as creation/annihilation operator of the flux, maps to $e^{\pm i\theta}$ in the XY model. Summing over instanton configurations in the partition function maps to the following Lagrangian in the XY model:

$$\mathcal{L} = \frac{\chi}{2}(\partial_\mu \theta)^2 - K\cos\theta, \tag{5.69}$$

where χ and K are coefficients related to the coupling strength and instanton fugacity, respectively.

Because the $\cos\theta$ term is always relevant in 2+1D [142], the instanton operator gaps out the theory. The $\cos\theta$ term also breaks the $\mathrm{U}(1)_{XY}$ symmetry, leaving the theory with a unique ground state and massive excitations. The linear potential between charges in the

U(1) gauge theory maps to the linear potential between vortices in the XY model, which is due to the $\cos\theta$ energy cost at the $\theta = \pi$ or $-\pi$ branch-cut line between the vortices [141].

When the Chern-Simons action is present, an instanton will carry charge, which is similar to the Witten effect in 3+1D [128]. Moreover, when the Chern-Simons level k is an odd integer, the instanton operator will be fermionic. We do not consider the matter field in this work, and therefore we would like to suppress the instantons.

When instantons are suppressed, it is equivalent to set $K = 0$ in Eq. 5.69. The $\mathrm{U}(1)_{XY}$ symmetry is spontaneously broken and we have massless Goldstone modes, which are the massless photons in the U(1) gauge theory. However, we can no longer view the gauge field $A \in [0, 2\pi/a)$ on each link for the instanton-suppressed compact U(1) gauge theory. The equivalence between $A = 0$ and $A = 2\pi/a$ makes the flux only well defined by mod 2π, which naturally allows the existence of instantons. We have to use the Villain approximation to formulate an instanton-suppressed theory.

5.7.2 Villain approximation

A theory with compact variables means that the partition function Z is periodic in these compact variables θ_i. For such a theory, it is natural to include in the action terms like $\cos(\sum_i c_i\theta_i)$, where c_i are the coefficients that match the periodicity of the compact variable θ_i. However, these cosine terms are nonlinear and are difficult to handle analytically. The Villain approximation simplifies the analysis by replacing the cosine terms with a periodic Gaussian potential [126].

$$e^{\beta\cos(\theta)} \approx \sum_{n=-\infty}^{\infty} e^{-\frac{\tilde{\beta}}{2}(\theta+2\pi n)^2}, \tag{5.70}$$

where $\tilde{\beta}$ is a function of β, and without loss of generality we write here θ as 2π periodic.

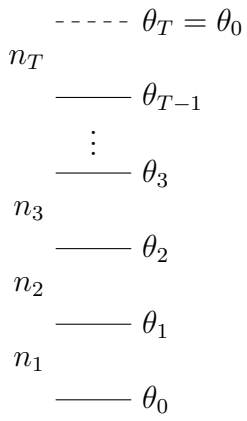

Figure 5.6: Illustration of the variables in a single quantum rotor model, i.e. a $0+1$-D compact quantum field. The vertical direction is time. There are T number of discrete time slices, and have periodic boundary condition.

5.7.3 Single quantum rotor

We will go step by step to see how to construct a Hamiltonian formulation for a compact lattice field theory. We start with the action of a single quantum rotor, i.e. a $0+1$-D compact quantum field. A careful construction of its Hamiltonian formulation will show the spirit of the later steps.

We use Euclidean time formulation, discretize the time, and set up periodic boundary condition. The action of the rotor is

$$S(\theta) = -\frac{\beta}{d\tau} \sum_{i=0}^{T-1} \cos(\theta_{i+1} - \theta_i), \tag{5.71}$$

where β is a coefficient, $d\tau$ is the time spacing, $\theta_i \in [0, 2\pi)$ is the rotor angle at the i-th time slice, $\theta_T = \theta_0$, T is the total number of time slices.

The partition function of the rotor is

$$Z = \sum_{\theta_0, \theta_1, \ldots, \theta_{T-1} \in [0, 2\pi)} e^{-S(\theta)}, \tag{5.72}$$

where we have use the summation symbol to represent the integral over continuous variables

θ's.

We can apply the Villain approximation to the cosine terms in the action. By doing this, we introduce T number of integer degrees of freedom, $n_1, n_2, \ldots, n_T$, each between a pair of θ's, as illustrated in Fig. 5.6. The approximated action with these extra degrees of freedom looks like

$$S(n,\theta) = \frac{\tilde{\beta}}{2d\tau}\sum_{i=0}^{T-1}(\theta_{i+1} - \theta_i + 2\pi n_{i+1})^2, \tag{5.73}$$

where $\tilde{\beta}$ is a function of β. When $d\tau \to 0$, $\beta/d\tau \to \infty$, the asymptotic behavior of the Villain approximation says $\tilde{\beta} \to \beta$ [143].

The approximated partition function with the extra degrees of freedom looks like

$$Z = \sum_{\substack{\theta_0,\theta_1,\ldots,\theta_{T-1}\in[0,2\pi) \\ n_1,n_2,\ldots,n_T\in\mathbb{Z}}} e^{-S(n,\theta)}. \tag{5.74}$$

The approximated action $S(n,\theta)$ holds discrete transformations that keeps it invariant. For every $i \in 0, 1, \ldots, T-1$, the following transformation

$$\theta_i \to \theta_i + 2\pi$$

$$n_i \to n_i - 1$$

$$n_{i+1} \to n_{i+1} + 1$$

keeps the approximated action, and thus the approximated partition function, invariant.

Writing down the transformation invariance of the approximated action explicitly, and taking $i = 1$, we have

$$S(n_1 - 1, n_2 + 1, \theta_1 + 2\pi, *) = S(n_1, n_2, \theta_1, *), \tag{5.75}$$

where $*$ represents all the other variables in $S(n,\theta)$, which are fixed.

We can apply this transformation multiple times, until we make $n_1 = 0$. That is to say,

$$S(0, n_2 + n_1, \theta_1 + 2\pi n_1, *) = S(n_1, n_2, \theta_1, *). \tag{5.76}$$

Note that $\theta_1 + 2\pi n_1$ takes value in $[2\pi n_1, 2\pi(n_1 + 1))$. When we sum over $n_1 \in \mathbb{Z}$, it is equivalent to sum over $\theta_1 \in (-\infty, +\infty)$. In other words, by absorbing n_1, θ_1 is lifted from $[0, 2\pi)$ to $(-\infty, +\infty)$. More rigorously, we define new variables

$$\tilde{\theta}_1 = \theta_1 + 2\pi n_1, \quad \tilde{\theta}_1 \in (-\infty, +\infty), \tag{5.77}$$

$$\tilde{n}_2 = n_2 + n_1, \quad \tilde{n}_2 \in \mathbb{Z}, \tag{5.78}$$

with the inverse

$$n_1 = \left\lfloor \frac{\tilde{\theta}_1}{2\pi} \right\rfloor, \tag{5.79}$$

$$\theta_1 = \tilde{\theta}_1 - 2\pi \left\lfloor \frac{\tilde{\theta}_1}{2\pi} \right\rfloor, \quad \theta_1 \in [0, 2\pi), \tag{5.80}$$

$$n_2 = \tilde{n}_2 - \left\lfloor \frac{\tilde{\theta}_1}{2\pi} \right\rfloor, \tag{5.81}$$

where $\lfloor \cdot \rfloor$ is the largest integer less than or equal to a given number.

The approximate partition function now looks like

$$\begin{aligned} Z &= \sum_{\substack{\theta_0,\theta_1,\ldots,\theta_{T-1}\in[0,2\pi)\\ n_1,n_2,\ldots,n_T\in\mathbb{Z}}} e^{-S(n_1,n_2,\theta_1,*)} \\ &= \sum_{\substack{\theta_0,\theta_1,\ldots,\theta_{T-1}\in[0,2\pi)\\ n_1,n_2,\ldots,n_T\in\mathbb{Z}}} e^{-S(0,n_2+n_1,\theta_1+2\pi n_1,*)} \\ &= \sum_{\substack{\theta_0,\theta_2,\ldots,\theta_{T-1}\in[0,2\pi)\\ \tilde{\theta}_1\in(-\infty,+\infty),\tilde{n}_2\in\mathbb{Z}\\ n_3,n_4,\ldots,n_T\in\mathbb{Z}}} e^{-S(0,\tilde{n}_2,\tilde{\theta}_1,*)} \\ &= \sum_{\substack{\theta_0,\theta_2,\ldots,\theta_{T-1}\in[0,2\pi)\\ \tilde{\theta}_1\in(-\infty,+\infty),\tilde{n}_2\in\mathbb{Z}\\ n_3,n_4,\ldots,n_T\in\mathbb{Z}}} e^{-\tilde{S}(\tilde{n}_2,\tilde{\theta}_1,*)}, \end{aligned} \tag{5.82}$$

where $\tilde{S}(\tilde{n}_2,\tilde{\theta}_1,*) = S(0,\tilde{n}_2,\tilde{\theta}_1,*)$, i.e. n_1 is dropped from the dependencies.

We can repeat this process to absorb $\tilde{n}_2$ by

$$\tilde{\theta}_2 = \theta_2 + 2\pi\tilde{n}_2, \quad \tilde{\theta}_2 \in (-\infty,+\infty), \tag{5.83}$$

$$\tilde{n}_3 = n_3 + \tilde{n}_2, \quad \tilde{n}_3 \in \mathbb{Z}, \tag{5.84}$$

$$\ldots$$

Until

$$\tilde{\theta}_{T-1} = \theta_{T-1} + 2\pi\tilde{n}_{T-1}, \quad \tilde{\theta}_{T-1} \in (-\infty,+\infty), \tag{5.85}$$

$$\tilde{n}_T = n_T + \tilde{n}_{T-1} = \sum_{i=1}^{T} n_i, \quad \tilde{n}_T \in \mathbb{Z}, \tag{5.86}$$

which makes the approximate partition function into

$$Z = \sum_{\substack{\theta_0\in[0,2\pi)\\ \tilde{\theta}_1,\tilde{\theta}_2,\ldots,\tilde{\theta}_{T-1}\in(-\infty,+\infty),\\ \tilde{n}_T\in\mathbb{Z}}} e^{-\frac{\tilde{\beta}}{2d\tau}\left[(\tilde{\theta}_1-\theta_0)^2+(\tilde{\theta}_2-\tilde{\theta}_1)^2+\cdots+(\tilde{\theta}_{T-1}-\tilde{\theta}_{T-2})^2+(\theta_0-\tilde{\theta}_{T-1}+2\pi\tilde{n}_T)^2\right]}. \tag{5.87}$$

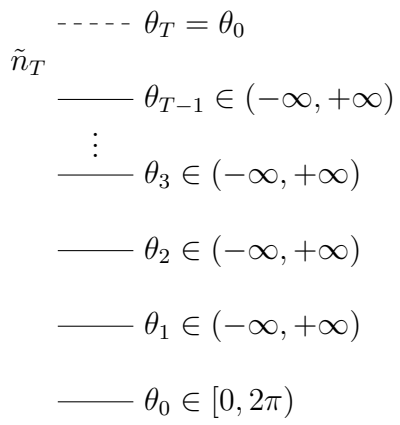

Figure 5.7: Illustration of the variables in a single quantum rotor model, i.e. a $0+1$-D compact quantum field. The vertical direction is time. There are T number of discrete time slices, and have periodic boundary condition. After absorbing most of the extra integer degrees of freedom introduced by the Villain approximation, most of the compact variables are lifted to $(-\infty, +\infty)$. However, the variable in the bottom layer, θ_0, is not lifted. Also, the integer in the last layer, $\tilde{n}_T$, cannot be absorbed.

Note that the θ_0 is not lifted, and the extra integer degree of freedom on the last layer, $\tilde{n}_T$, cannot be absorbed. It cannot be absorbed because $\tilde{n}_T = \sum_{i=1}^{T} n_i$ has a physical meaning of the total flux in the Polyakov loop, and thus is gauge invariant.

Now with this quadratic formulation of the partition function, we can apply the standard method to get the Hamiltonian formulation. More explicitly, we set up the Hilbert space, write down the transfer matrix, construct the Hamiltonian operator, and recognize the non-absorb-able degree of freedom as constraint on the Hilbert space.

When setting up the Hilbert space, we choose the set of basis to be the configurations of a middle time layer. In our example here, the set of basis is $\{|\tilde{\theta}\rangle : \tilde{\theta} \in (-\infty, +\infty)\}$. Note that even if we start from a compact model, after the Villain approximation and absorption of degrees of freedom, we end up with a seemingly non-compact set of basis. We do not need to worry at this moment, as later the constraint on the Hilbert space will bring us back to a compact model.

We also note that the first time layer (i.e. the bottom layer in Fig. 5.7) has fewer configurations. Because of the periodicity of the variable θ_0, we can duplicate the partition function

to extend its configuration space to match the one of the middle layers. In a non-rigorous way, we can do

$$\sum_{\theta_0\in[0,2\pi)} = \frac{1}{|\mathbb{Z}|}\sum_{\tilde{\theta}_0\in(-\infty,+\infty)} . \tag{5.88}$$

This $|\mathbb{Z}|$ factor will later be cancelled out when we set the constraint on the Hilbert space. We will return the degree of freedom we borrowed here.

Given the Hilbert space, we want to write down the transfer matrix $\hat{T}$. For two neighboring middle time layers, we have the matrix elements of the transfer matrix as

$$\langle\tilde{\theta}_{i+1}|\hat{T}|\tilde{\theta}_i\rangle = e^{-\frac{\tilde{\beta}}{2d\tau}(\tilde{\theta}_{i+1}-\tilde{\theta}_i)^2}, \tag{5.89}$$

where $\tilde{\theta}_{i+1}, \tilde{\theta}_i \in (-\infty, +\infty)$ are configurations on the two neighboring middle time layers.

For the last time layer (i.e. the top layer in Fig. 5.7), we have a different transfer matrix $\hat{T}_{top}$ with matrix elements as

$$\langle\tilde{\theta}_0|\hat{T}_{top}|\tilde{\theta}_{T-1}\rangle = e^{-\frac{\tilde{\beta}}{2d\tau}(\tilde{\theta}_0-\tilde{\theta}_{T-1}+2\pi\tilde{n}_T)^2}. \tag{5.90}$$

In terms of the transfer matrices, the partition function looks like

$$Z = \frac{1}{|\mathbb{Z}|}\sum_{\tilde{n}_T\in\mathbb{Z}} Tr(\hat{T}_{top}\hat{T}^{T-1}), \tag{5.91}$$

where the $|\mathbb{Z}|$ factor was borrowed earlier to match the configuration spaces.

Now we construct the Hamiltonian operator. For a general function $f(\hat{p})$ of the momentum operator $\hat{p}$, its matrix elements can be calculated by inserting the complete momentum basis $\mathbb{I} = \int_{-\infty}^{\infty}\frac{dp}{2\pi}|p\rangle\langle p|$. Therefore, for any $\tilde{\theta}', \tilde{\theta} \in (-\infty, +\infty)$,

$$\langle\tilde{\theta}'|f(\hat{p})|\tilde{\theta}\rangle = \int_{-\infty}^{\infty}\frac{dp}{2\pi}e^{ip(\theta'-\theta)}f(p), \tag{5.92}$$

from which we can do the Fourier transform to get back the function $f(\cdot)$,

$$f(p) = \int_{-\infty}^{\infty} d\tilde{\theta} e^{-ip\tilde{\theta}} \langle \tilde{\theta} | f(\hat{p}) | 0 \rangle. \tag{5.93}$$

Do Fourier transform on the transfer matrix elements:

$$\begin{aligned} \int_{-\infty}^{\infty} d\tilde{\theta} e^{-ip\tilde{\theta}} \langle \tilde{\theta} | \hat{T} | 0 \rangle &= \int_{-\infty}^{\infty} d\tilde{\theta} e^{-ip\tilde{\theta}} e^{-\frac{\tilde{\beta}}{2d\tau}\tilde{\theta}^2} \\ &\propto e^{-\frac{d\tau}{2\tilde{\beta}}p^2}, \end{aligned} \tag{5.94}$$

and

$$\begin{aligned} \int_{-\infty}^{\infty} d\tilde{\theta} e^{-ip\tilde{\theta}} \langle \tilde{\theta} | \hat{T}_{top} | 0 \rangle &= \int_{-\infty}^{\infty} d\tilde{\theta} e^{-ip\tilde{\theta}} e^{-\frac{\tilde{\beta}}{2d\tau}(\tilde{\theta}+2\pi\tilde{n}_T)^2} \\ &\propto e^{ip2\pi\tilde{n}_T} e^{-\frac{d\tau}{2\tilde{\beta}}p^2}. \end{aligned} \tag{5.95}$$

The partition function now becomes

$$\begin{aligned} Z &= \frac{1}{|\mathbb{Z}|} \sum_{\tilde{n}_T \in \mathbb{Z}} Tr(e^{i\hat{p}2\pi\tilde{n}_T} e^{-\frac{d\tau}{2\tilde{\beta}}\hat{p}^2 T}) \\ &= Tr(\hat{C} e^{-\hat{H}\tau}), \end{aligned} \tag{5.96}$$

where $\hat{H} = \frac{1}{2\tilde{\beta}}\hat{p}^2$ is the Hamiltonian operator, $\tau = d\tau T$ is the total Euclidean time, and

$$\begin{aligned} \hat{C} &= \frac{1}{|\mathbb{Z}|} \sum_{\tilde{n}_T \in \mathbb{Z}} e^{i\hat{p}2\pi\tilde{n}_T} \\ &= \frac{1}{|\mathbb{Z}|} \sum_{\tilde{n}_T \in \mathbb{Z}} (e^{2\pi i\hat{p}})^{\tilde{n}_T} \\ &= \begin{cases} \mathbb{I} & \text{if } e^{2\pi i\hat{p}} = \mathbb{I}, \\ 0 & \text{if } e^{2\pi i\hat{p}} \neq \mathbb{I}. \end{cases} \end{aligned} \tag{5.97}$$

Note that the $|\mathbb{Z}|$ factor is cancelled. This sum over non-absorb-able degree of freedom $\tilde{n}_T$ sets up a constraint on the physical Hilbert space. In order to have a non-zero partition function, the allowed physical states $|\psi\rangle$ in the Hilbert space need to satisfy

$$e^{2\pi i\hat{p}}|\psi\rangle = |\psi\rangle, \tag{5.98}$$

which tells us that the momentum $\hat{p}$ is quantized, which is expected for a single quantum rotor. This constraint also tells us that the physical wave functions are periodic $\psi(\theta+2\pi) = \psi(\theta)$. We are back to a compact variable θ.

In conclusion, for a single quantum rotor, this road map of constructing lattice Hamiltonian finally leads to the following result:

- Hilbert space basis: $\{|\tilde{\theta}\rangle : \tilde{\theta} \in (-\infty, +\infty)\}$,
- Hamiltonian operator: $\hat{H} = \frac{1}{2\tilde{\beta}}\hat{p}^2$,
- Constraint on physical states: $e^{2\pi i\hat{p}}|\psi\rangle = |\psi\rangle$.

5.7.4 General road map from lattice action to lattice Hamiltonian

From the example of deriving the Hamiltonian for a single quantum rotor, we can summarize the procedure to go from a time-discrete action to the Hamiltonian, involving the Villain approximation. In the following sections, we will apply similar procedures to the pure compact lattice Maxwell theory with instantons allowed, to the one with instantons suppressed, and finally to the compact lattice Maxwell-Chern-Simons theory we are interested in. The following steps are conceptual summary of the procedures in the following sections.

- Start from a compact lattice action.
- Apply Villain approximation: add an integer degree of freedom for every cosine term in the action. Turn the cosine terms into quadratic.

- Gauge fixing the variables to get rid of all gauge degrees of freedom. Absorb some integer degrees of freedom introduced earlier, to lift some compact variables into $(-\infty, +\infty)$.

- Set up the Hilbert space with the set of basis to be the configurations in a middle time layer.

- Usually the first time layer (bottom layer) has fewer configurations. Duplicate the partition function to match the configuration space with the one in a middle layer. The degrees of freedoms borrowed here will be returned later.

- Usually the last time layer (top layer) has extra degrees of freedom. Summing over these degrees of freedom becomes constraints on the Hilbert space. Check that the number of extra degrees of freedom in the top layer equals to the borrowed degrees of freedom by the bottom layer.

- Write down the transfer matrix elements for a pair of neighboring middle layers, and for the top layer.

- Fourier transform the transfer matrix elements for middle layers to see the Hamiltonian operator.

- Fourier transform the transfer matrix elements for the top layer to see the constraints on the physical Hilbert space.

5.7.5 Pure Maxwell lattice theory with instantons

The second example we will show here is the 2+1D U(1) lattice gauge theory. One could allow the existence of instantons in the theory. One could also completely suppress the instantons. In this subsection, we show how to derive the lattice Hamiltonian for the former theory. In next subsection, we will show the instanton-suppressed version.

We have a cubic lattice with periodic boundary condition on all three directions. We set the up direction to be the positive time direction. The U(1) gauge field A lives on the links of the cubic lattice. The lattice action is

$$S(A) = -\frac{\beta_0}{d\tau} \sum_{\substack{\text{time-like} \\ \text{plaquettes}}} \left[\cos\left(a \cdot \ \tfrac{d\tau}{a} A_0 \ \square^{A_1}_{-A_1} \ -\tfrac{d\tau}{a} A_0 \right) + \cos\left(a \cdot \ \tfrac{d\tau}{a} A_0 \ \square^{A_2}_{-A_2} \ -\tfrac{d\tau}{a} A_0 \right) \right]$$
$$- \frac{\beta d\tau}{a^2} \sum_{\substack{\text{space-like} \\ \text{plaquettes}}} \left[\cos\left(a \cdot \ -A_2 \ \square^{-A_1}_{A_1} \ A_2 \right) \right], \tag{5.99}$$

where β_0 and β are the coefficients in the time and space direction respectively, $d\tau$ and a are the lattice spacing in the time and space direction respectively, A_0 is the gauge field in the time direction, and A_1, A_2 are the gauge fields in the two spacial direction.

We can also define the lattice difference of a field

$$\Delta_0 A_{x;\mu} = \frac{A_{x+\hat{0};\mu} - A_{x;\mu}}{d\tau}, \tag{5.100}$$
$$\Delta_i A_{x;\mu} = \frac{A_{x+\hat{i};\mu} - A_{x;\mu}}{a}, \tag{5.101}$$

where Δ_0 represents the time difference, $\Delta_{i\in\{1,2\}}$ represents the spacial difference, $d\tau$ and a are the lattice spacing in the time and space direction, respectively.

Using the lattice difference notation, the action is

$$S(A) = -\frac{\beta_0}{d\tau} \sum_{\substack{x\in\text{sites} \\ i\in\{1,2\}}} \cos(ad\tau(\Delta_0 A_{x;i} - \Delta_i A_{x;0})) - \frac{\beta d\tau}{a^2} \sum_{x\in\text{sites}} \cos(a^2(\Delta_1 A_{x;2} - \Delta_2 A_{x;1})). \tag{5.102}$$

The partition function is

$$Z = \sum_A e^{-S(A)}, \tag{5.103}$$

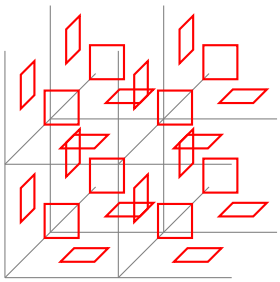

Figure 5.8: Illustration of the integer degrees of freedom in the cubic lattice. On every plaquette, the Villain approximation introduces an integer variable, shown as the red squares in the figure.

where the summation is over the gauge equivalent classes, i.e. all possible configurations of A quotient by the gauge transformations. In particular, $A_0 \in [0, 2\pi/d\tau)$, $A_{1,2} \in [0, 2\pi/a)$, and the configurations related by local gauge transformations are viewed as equivalent and are not duplicated in the sum.

We follow our road map and apply the Villain approximation, replace the cosine terms by quadratic terms, and introduce integer degrees of freedom on every plaquettes. The approximated partition function is

$$Z = \sum_{A,n} e^{-S(A,n)}, \tag{5.104}$$

where

$$\begin{aligned} S(A,n) = \frac{\beta_0}{2d\tau} \sum_{\substack{x\in\text{sites} \\ i\in\{1,2\}}} (ad\tau(\Delta_0 A_{x;i} - \Delta_i A_{x;0}) + 2\pi n_{x;0,i})^2 \\ + \frac{\beta d\tau}{2a^2} \sum_{x\in\text{sites}} (a^2(\Delta_1 A_{x;2} - \Delta_2 A_{x;1}) + 2\pi n_{x;1,2})^2, \end{aligned} \tag{5.105}$$

where $n_{x;\mu,\nu} \in \mathbb{Z}$ is the integer degree of freedom on the plaquette at location x extended in μ, ν directions. The sum over A has the same meaning as before.

Written in the graphic representation, it is

$$S(A,n) = \frac{\beta_0}{2d\tau} \sum_{\substack{\text{time-like}\\ \text{plaquettes}}} \left[\left(a \cdot \ \tfrac{d\tau}{a} A_0 \ \square^{A_1}_{-A_1} \ -\tfrac{d\tau}{a} A_0 \ + 2\pi \ \boxed{n_{0,1}} \right)^2 + \left(a \cdot \ \tfrac{d\tau}{a} A_0 \ \square^{A_2}_{-A_2} \ -\tfrac{d\tau}{a} A_0 \ + 2\pi \ n_{0,2} \right)^2 \right] + \frac{\beta d\tau}{2a^2} \sum_{\substack{\text{space-like}\\ \text{plaquettes}}} \left[\left(a \cdot \ -A_2 \ \square^{-A_1}_{A_1} \ A_2 \ + 2\pi \ n_{1,2} \right)^2 \right], \tag{5.106}$$

which has the following gauge redundancies:

$$S\left(\begin{matrix} & A_0 + \frac{\lambda}{d\tau} & \\ & A_2 + \frac{\lambda}{a} & \\ A_1 - \frac{\lambda}{a} & & A_1 + \frac{\lambda}{a} \\ A_2 - \frac{\lambda}{a} & & A_0 - \frac{\lambda}{d\tau} \end{matrix} , * \right) = S\left(\begin{matrix} & A_0 & \\ & A_2 & \\ A_1 & & A_1 \\ A_2 & & A_0 \end{matrix} , * \right) \tag{5.107}$$

$$S\left(\begin{matrix} & A_0 + \frac{2\pi}{d\tau} n_{0,2} - 1 & \\ n_{0,1} + 1 & & n_{0,1} - 1 \\ & n_{0,2} + 1 & \end{matrix} , * \right) = S\left(\begin{matrix} & A_0 \ n_{0,2} & \\ n_{0,1} & & n_{0,1} \\ & n_{0,2} & \end{matrix} , * \right) \tag{5.108}$$

$$S\left(\begin{matrix} & n_{0,1} + 1 & \\ & n_{1,2} - 1 & \\ n_{1,2} + 1 & A_1 + \frac{2\pi}{a} & \\ n_{0,1} - 1 & & \end{matrix} , * \right) = S\left(\begin{matrix} & n_{0,1} & \\ & n_{1,2} & \\ n_{1,2} & A_1 & \\ n_{0,1} & & \end{matrix} , * \right) \tag{5.109}$$

$$S\left(\begin{array}{ccc} & n_{0,2}+1 & \\ n_{1,2}-1 & & n_{1,2}+1 \\ & n_{0,2}-1 & \end{array}\begin{array}{l} A_2+\frac{2\pi}{a} \\ \\ ,* \end{array}\right) = S\left(\begin{array}{ccc} & n_{0,2} & \\ n_{1,2} & & n_{1,2} \\ & n_{0,2} & \end{array}\begin{array}{l} A_2 \\ \\ ,* \end{array}\right) \tag{5.110}$$

for $\forall\lambda \in \mathbb{R}$. The $*$ in the parentheses represents all other variables, which are the same on the left and right hand sides in the equations. Note that comparing to the Eq. 5.13, 5.14, and 5.15 in the main text, here the S itself is invariant.

Next, we do gauge fixing by applying the invariant transformations above. We want to get rid of all gauge degrees of freedom, and to fix the gauge field and integer field configurations into a canonical form, where we can explicitly read out the true physical degrees of freedom.

The gauge fixing is done step by step. First we use Eq. 5.107 to fix some gauge fields into zero. We show this process in Fig. 5.9. (i) We apply Eq. 5.107 on the site $(x_0, x_1, x_2) = (0, 0, 1)$ to fix $A_{(0,0,0);2} = 0$. (ii) Then we go to the site $(0, 0, 2)$, $(0, 0, 3)$, ..., $(0, 0, N_2 - 1)$ to fix $A_{(0,0,1);2} = 0$, $A_{(0,0,2);2} = 0$, ..., $A_{(0,0,N_2-2);2} = 0$, respectively. Note that $A_{(0,0,N_2-1);2}$ cannot be fixed to zero, because it will finally carry the information of $\sum_{x_2=0}^{N_2-1} A_{(0,0,x_2);2}$, which is a gauge invariant quantity. (iii) We then apply Eq. 5.107 on the sites $(0, 1, x_2)$, $\forall x_2 \in \{0, 1, \ldots, N_2 - 1\}$, to fix $A_{(0,0,x_2);1} = 0$. (iv) We go to the sites $(0, 2, x_2)$, $(0, 3, x_2)$, ..., $(0, N_1 - 1, x_2)$ to fix $A_{(0,1,x_2);1} = 0$, $A_{(0,2,x_2);1} = 0$, ..., $A_{(0,N_1-2,x_2);1} = 0$, respectively. Similarly, note that $A_{(0,N_1-1,x_2);1}$ cannot be fixed to zero. (v) Apply on $(1, x_1, x_2)$, $\forall x_1 \in \{0, 1, \ldots, N_1-1\}$, $\forall x_2 \in \{0, 1, \ldots, N_2-1\}$, to fix $A_{(0,x_1,x_2);0} = 0$. (vi) Finally, go to $(2, x_1, x_2)$, $(3, x_1, x_2)$, ..., $(N_0 - 1, x_1, x_2)$ to fix $A_{(1,x_1,x_2);0} = 0$, $A_{(2,x_1,x_2);0} = 0$, ..., $A_{(N_0-2,x_1,x_2);0} = 0$, respectively. We also illustrate the gauge fields in each layer after the gauge fixing process in Fig. 5.10. Note that the top layer $A_{(N_0-1,x_1,x_2);0}$ cannot be fixed to zero.

The second step of gauge fixing is to absorb some integer degrees of freedom and lift some gauge fields to $\mathbb{R}$. We apply Eq. 5.109 and 5.110 to the links on the bottom layer, then on middle layers, and finally on the top layer. Figure 5.11 shows on the bottom layer how the integer degrees of freedom are absorbed and the gauge fields are lifted to $\mathbb{R}$. Some integer degrees of freedom on the bottom layer are then absorbed by the gauge fields on the

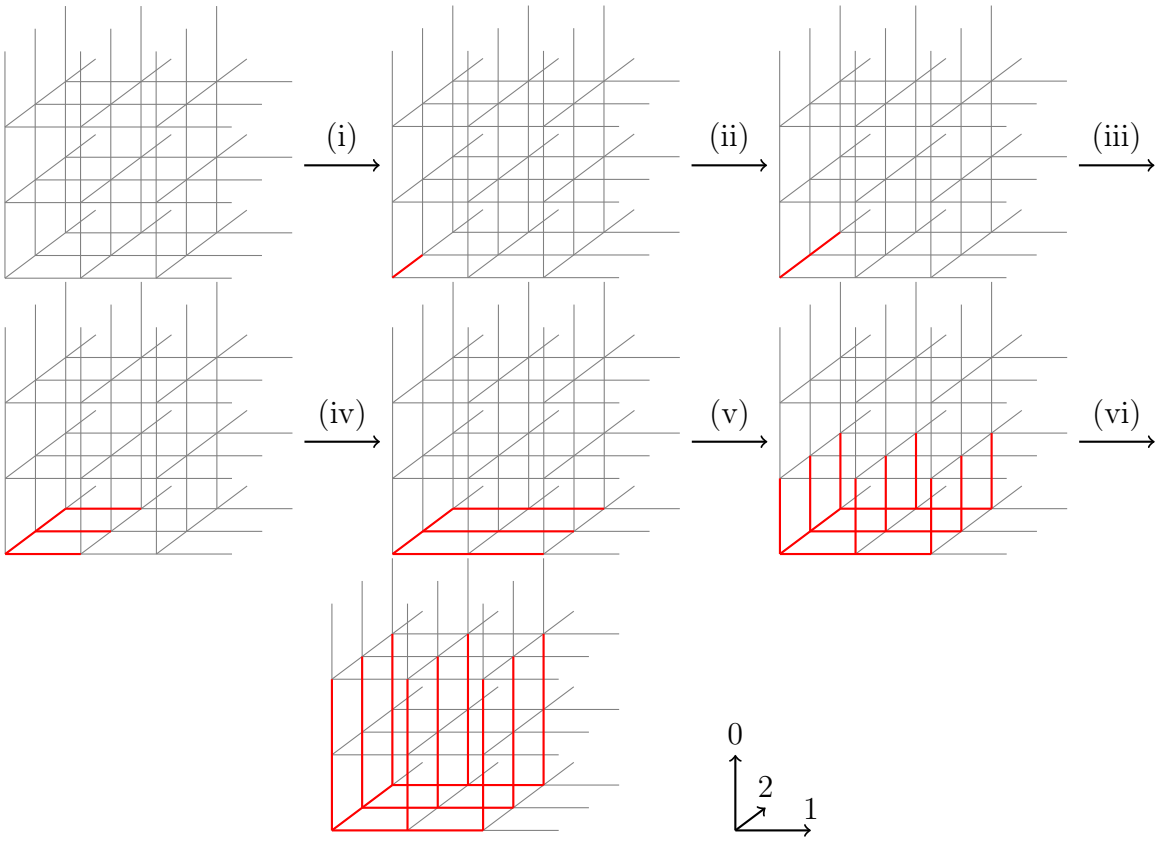

Figure 5.9: Illustration of the gauge fixing steps. The gauge fields on the red links are fixed to zero.

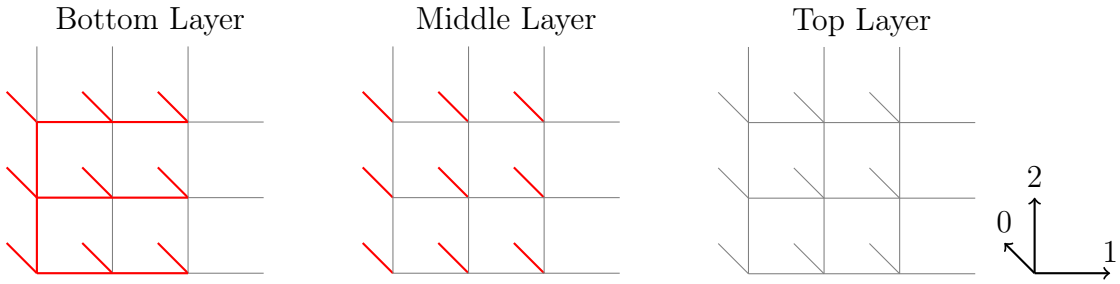

Figure 5.10: View of the bottom layer, middle layers, and the top layer after first-step gauge fixing. The gauge fields on the red links are fixed to zero.

upper middle layer, see (iv) in Fig. 5.11 and (i) in Fig. 5.12. Figure 5.12 shows the process of second-step gauge fixing on the middle layer, and Figure 5.13 shows the top layer.

Figure 5.14 summarize the results after fixing all gauge degrees of freedom. Each surviving gauge field variable or integer plaquette actually encodes some true physical information that is gauge invariant. The bottom layer has $N_1N_2 - 1$ number of $\mathbb{R}$-ranged gauge fields (green),

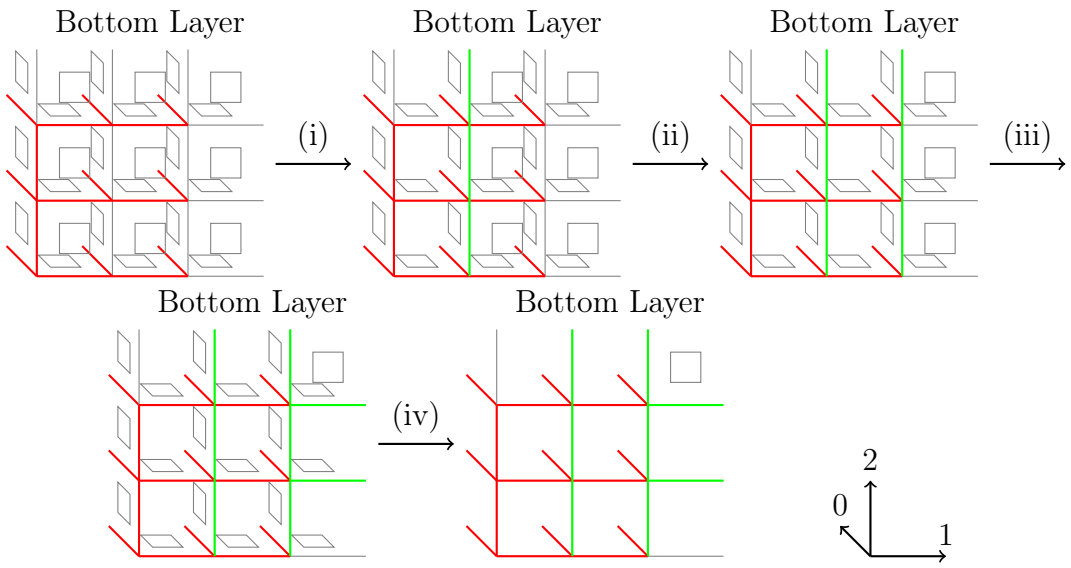

Figure 5.11: Illustration of the gauge fixing steps on the bottom layer. The gauge fields on the green links absorb the integer degrees of freedom on nearby plaquettes and are lifted to $\mathbb{R}$. In the last step (iv), plaquettes are absorbed by the links on the upper middle layer.

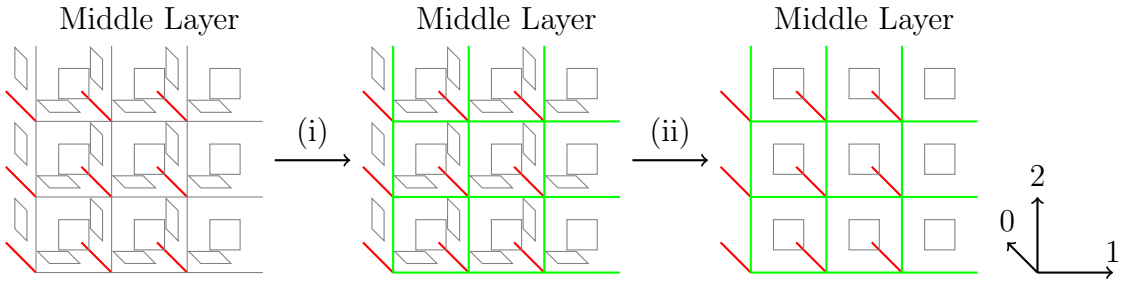

Figure 5.12: Illustration of the gauge fixing steps on the middle layer. The gauge fields on the green links absorb the integer degrees of freedom on nearby plaquettes and are lifted to $\mathbb{R}$. (i) Links absorb the plaquettes from the lower layer. (ii) Plaquettes are absorbed by the links from the upper layer.

each including the information of the flux in a space-like plaquette. It also has two ($\frac{2\pi}{a}$)-ranged gauge fields (grey), each including the information of the flux through a space-like non-contractible cycle. Moreover, it has one remaining integer degree of freedom (plaquette), including the information of the total flux through the bottom plane, which is a torus in the space. By the Dirac quantization condition we know that this total flux is (integer)$\times 2\pi$ [144], which agrees with the remaining integer degree of freedom.

The middle layers each has $2N_1N_2$ number of $\mathbb{R}$-ranged gauge fields, which include the information of the fluxes in time-like plaquettes. It also has N_1N_2 number of integer degrees

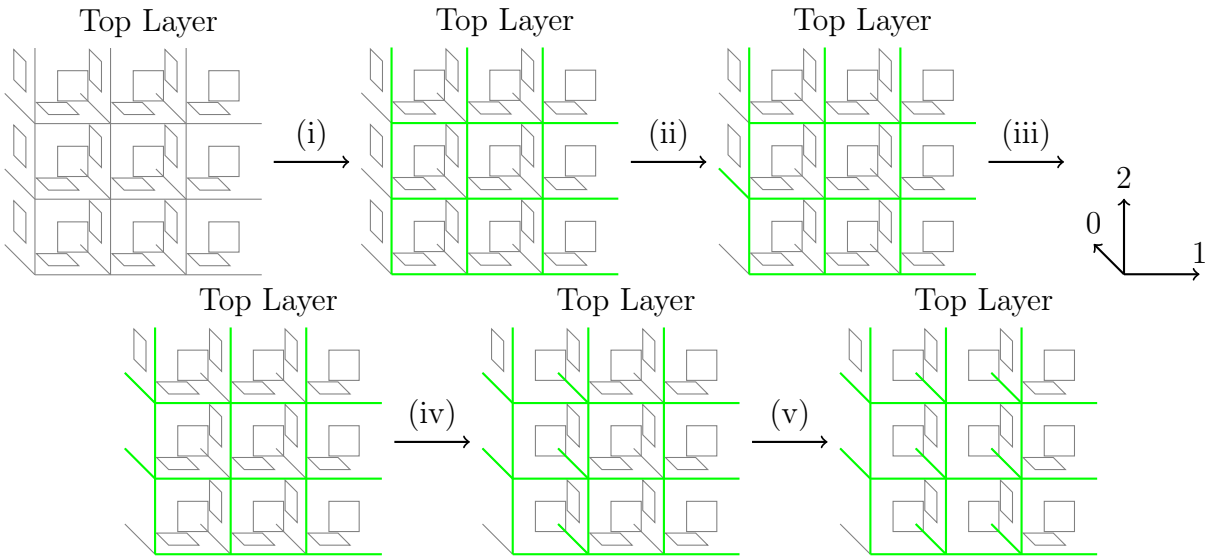

Figure 5.13: Illustration of the gauge fixing steps on the top layer. The gauge fields on the green links absorb the integer degrees of freedom on nearby plaquettes and are lifted to $\mathbb{R}$. (i) Links absorb the plaquettes from the lower layer. (ii-v) Links absorb the plaquettes nearby.

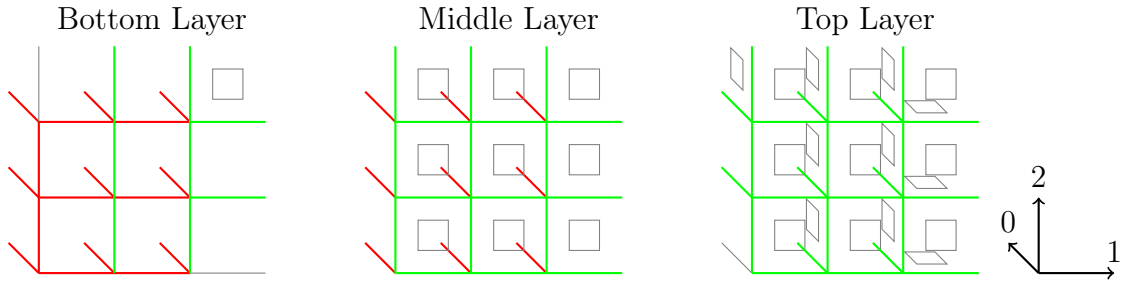

Figure 5.14: View of the bottom layer, middle layers, and the top layer after second-step gauge fixing. The gauge fields on the red links are fixed to zero, on the green links are lifted to $\mathbb{R}$.

of freedom, each including the information of the total flux through a unit cell, i.e. the number of instantons in a unit cell. As we will see later, in an instanton-suppressed theory, these integer degrees of freedom in the middle layers will disappear.

In the top layer, there are $3N_1N_2-1$ number of $\mathbb{R}$-ranged gauge fields including the information of the fluxes in time-like plaquettes. There is one $(\frac{2\pi}{d\tau})$-ranged gauge field including the information of the flux through a time-like non-contractible cycle. There are $2N_1N_2+1$ number of integer degrees of freedom, two of them including the information of the total flux through time-like planes, and the other $2N_1N_2-1$ of them including information of

instantons in unit cells. Note that similar to the fact that monopoles have to come in pairs, the total number of instantons will sum to zero.

After identifying all the physical degrees of freedoms, we are ready to build up the Hilbert space with the set of basis which are the gauge field configurations in a middle layer. The integer degrees of freedom are regarded as sectors that need to be sum over in the partition function, not entering the trace over the Hilbert space. From the analysis above of middle-layer degrees of freedom, a basis vector is labeled by $\mathbb{R}$-ranged gauge fields on every links. The bottom layer needs to borrow $|\mathbb{Z}|^2 \times |\mathbb{R}|^{N_1N_2-1} \times |\mathbb{Z}|^{N_1N_2-1}$ to match the dimension of variables on the middle layer. The $|\mathbb{Z}|^2$ comes from lifting the two $(\frac{2\pi}{a})$-ranged gauge fields (grey), the $|\mathbb{R}|^{N_1N_2-1}$ comes from the gauge fields fixed to be zero (red), and the $|\mathbb{Z}|^{N_1N_2-1}$ comes from the missing plaquettes. The top layer has extra degrees of freedom which will become operator constraints on the Hilbert space. There are N_1N_2+1 extra $\mathbb{Z}$ plaquettes, N_1N_2-1 extra $\mathbb{R}$ gauge fields, and one extra $(\frac{2\pi}{a})$-ranged gauge field. By summing or integrating out those extra degrees of freedom, $|\mathbb{Z}|^{N_1N_2+1} \times |\mathbb{R}|^{N_1N_2-1}$ will be returned, which cancels with the borrowed dimensions and just leaves us an unimportant finite volume factor in the partition function.

Now with the Hilbert space ready, we can define the transfer matrix between a pair of neighboring middle layers. Assuming the lower layer has configuration $|A\rangle$ and the upper layer has configuration $|A'\rangle$, we can read out the transfer matrix element from the action in Eq. 5.106:

$$\langle A'|\hat{T}|A\rangle = \sum_n \exp\left[-\frac{\beta_0 a^2}{2d\tau}\sum_{\text{links}}(A'-A)^2 - \frac{\beta d\tau}{2a^2}\sum_{\text{plaq.}}(a\,\square A + 2\pi n)^2\right], \tag{5.111}$$

where $(\square A)_{x;1,2} \equiv A_{x;1} + A_{x+\hat{1};2} - A_{x+\hat{2};1} - A_{x;2}$.

We do a Fourier transform to get the formulation of $\hat{T} \equiv e^{-\hat{H}d\tau}$, where $\hat{H}$ is the Hamil-

tonian we want to derive. Assume

$$\hat{T}(\hat{p},\hat{A}) = f(\hat{p})\sum_n \exp\left[-\frac{\beta d\tau}{2a^2}\sum_{\text{plaq.}}(a\,\Box\hat{A}+2\pi n)^2\right], \tag{5.112}$$

where $\hat{p}$ is the canonical conjugate momentum operator of $\hat{A}$. f is a function we want to solve. Inserting the complete momentum basis $\mathbb{I} = \int_{-\infty}^{\infty}\frac{dp}{2\pi}|p\rangle\langle p|$, we have

$$\langle A'|f(\hat{p})|A\rangle = \int_{-\infty}^{\infty}\frac{dp}{2\pi}e^{ip(A'-A)}f(p) = \exp\left[-\frac{\beta_0 a^2}{2d\tau}\sum_{\text{links}}(A'-A)^2\right]. \tag{5.113}$$

We can solve the function $f(p)$ by the Fourier transform.

$$f(p) \propto \exp\left[-\frac{d\tau}{2\beta_0 a^2}\sum_{\text{links}}p^2\right] \tag{5.114}$$

The other term in Eq. 5.112 can be approximated by the reversed Villain approximation, which is good when $d\tau \to 0$:

$$\sum_n \exp\left[-\frac{\beta d\tau}{2a^2}\sum_{\text{plaq.}}(a\,\Box\hat{A}+2\pi n)^2\right] \approx \exp\left[\frac{\beta d\tau}{a^2}\sum_{\text{plaq.}}\cos(a\,\Box\hat{A})\right]. \tag{5.115}$$

Therefore, up to $O(d\tau^2)$,

$$\hat{T}(\hat{p},\hat{A}) \propto \exp\left[-\frac{d\tau}{2\beta_0 a^2}\sum_{\text{links}}\hat{p}^2 + \frac{\beta d\tau}{a^2}\sum_{\text{plaq.}}\cos(a\,\Box\hat{A})\right], \tag{5.116}$$

and we get the familiar compact lattice Maxwell Hamiltonian (with instantons allowed):

$$\hat{H} = \frac{1}{2\beta_0 a^2}\sum_{\text{links}}\hat{p}^2 - \frac{\beta}{a^2}\sum_{\text{plaq.}}\cos(a\,\Box\hat{A}). \tag{5.117}$$

However, this is not the end of the derivation. So far we allow $\mathbb{R}$-ranged gauge fields, and we do not have Gauss' law yet. We need to look at the top layer to figure out the constraints

on the Hilbert space. In Figure 5.14, we see that the top layer has N_1N_2+1 extra time-like plaquettes, N_1N_2-1 non-zero $\mathbb{R}$-ranged A_0, and one non-zero $(\frac{2\pi}{d\tau})$-ranged A_0. With these non-zero variables, the transfer matrix element in Eq. 5.111 becomes

$$\langle A'|\hat{T}|A\rangle = \sum_{n,m,A_0} \exp\left[-\frac{\beta_0 a^2}{2d\tau}\sum_{\substack{x\in\text{sites}\\ i\in\{1,2\}}}(A'_{x;i}-A_{x;i}+\frac{d\tau}{a}(A_{x;0}-A_{x+\hat{i};0})+\frac{2\pi}{a}m_{x;0,i})^2 \right.$$
$$\left. -\frac{\beta d\tau}{2a^2}\sum_{\text{plaq.}}(a\,\Box A+2\pi n)^2\right], \tag{5.118}$$

where we rename the integer degrees of freedom on time-like plaquettes as m, not to confuse with space-like n. This modification affects the Fourier transform in Eq. 5.114:

$$f(p)\propto\sum_{m,A_0}\exp\left[\sum_{\substack{x\in\text{sites}\\ i\in\{1,2\}}}-\frac{d\tau}{2\beta_0 a^2}p_{x;i}^2+ip_{x;i}\left(\frac{d\tau}{a}(A_{x;0}-A_{x+\hat{i};0})+\frac{2\pi}{a}m_{x;0,i}\right)\right], \tag{5.119}$$

and also Eq. 5.116:

$$\hat{T}(\hat{p},\hat{A})\propto\exp\left[-\frac{d\tau}{2\beta_0 a^2}\sum_{\text{links}}\hat{p}^2+\frac{\beta d\tau}{a^2}\sum_{\text{plaq.}}\cos(a\,\Box\hat{A})\right]$$
$$\times\sum_{m,A_0}\exp\left[\sum_{\substack{x\in\text{sites}\\ i\in\{1,2\}}}i\hat{p}_{x;i}\left(\frac{d\tau}{a}(A_{x;0}-A_{x+\hat{i};0})+\frac{2\pi}{a}m_{x;0,i}\right)\right]. \tag{5.120}$$

Here A_0's and m's are not operators. They are variables to be summed over in the partition function.

Note that the extra term is equivalent to:

$$\exp\left[\sum_{\substack{x\in\text{sites}\\ i\in\{1,2\}}} i\hat{p}_{x;i}\left(\frac{d\tau}{a}(A_{x;0}-A_{x+\hat{i};0})+\frac{2\pi}{a}m_{x;0,i}\right)\right]$$
$$=\prod_{x\in\text{sites}}\exp\left[i\frac{d\tau}{a}A_{x;0}(\hat{p}_{x;1}+\hat{p}_{x;2}-\hat{p}_{x-\hat{1};1}-\hat{p}_{x-\hat{2};2})\right]\prod_{\text{links}}\exp\left[i\frac{2\pi}{a}m\hat{p}\right]. \tag{5.121}$$

The sum over $(m,\, A_0)$ can be explicitly written as

$$\sum_{m,A_0}\equiv\int_0^{\frac{2\pi}{d\tau}}dA_{x=(0,0);0}\prod_{x\neq(0,0)}\int_{-\infty}^{\infty}dA_{x;0}\prod_{l\in\left\{\substack{\text{links where time-like}\\ \text{plaquettes are present}}\right\}}\sum_{m_l=-\infty}^{\infty}. \tag{5.122}$$

Applying the sum to the extra term, we can see that it does not vanish if and only if

$$\int_0^{\frac{2\pi}{d\tau}}dA_{x;0}\exp\left[i\frac{d\tau}{a}A_{x;0}(\hat{p}_{x;1}+\hat{p}_{x;2}-\hat{p}_{x-\hat{1};1}-\hat{p}_{x-\hat{2};2})\right]\neq 0,\quad \text{for } x=(0,0), \tag{5.123}$$
$$\int_{-\infty}^{\infty}dA_{x;0}\exp\left[i\frac{d\tau}{a}A_{x;0}(\hat{p}_{x;1}+\hat{p}_{x;2}-\hat{p}_{x-\hat{1};1}-\hat{p}_{x-\hat{2};2})\right]\neq 0,\quad \forall x\neq(0,0), \tag{5.124}$$
$$\sum_{m_l=-\infty}^{\infty}\exp\left[i\frac{2\pi}{a}m_l\,\hat{p}_l\right]\neq 0,\quad \forall l\in\left\{\substack{\text{links where time-like}\\ \text{plaquettes are present}}\right\}. \tag{5.125}$$

Equation 5.124 implies

$$\hat{p}_{x;1}+\hat{p}_{x;2}-\hat{p}_{x-\hat{1};1}-\hat{p}_{x-\hat{2};2}=0,\quad \forall x\neq(0,0), \tag{5.126}$$

which is the Gauss' law. Because $\sum_{x\in\text{sites}}(\hat{p}_{x;1}+\hat{p}_{x;2}-\hat{p}_{x-\hat{1};1}-\hat{p}_{x-\hat{2};2})=0$, the Gauss' law in Eq. 5.126 holds for $x=(0,0)$ as well. This also means Eq. 5.123 is automatically satisfied.

Equation 5.125 implies

$$\exp\left[i\frac{2\pi}{a}\hat{p}_l\right]=1,\quad \hat{p}_l\in a\mathbb{Z},\quad \forall l\in\left\{\substack{\text{links where time-like}\\ \text{plaquettes are present}}\right\}. \tag{5.127}$$

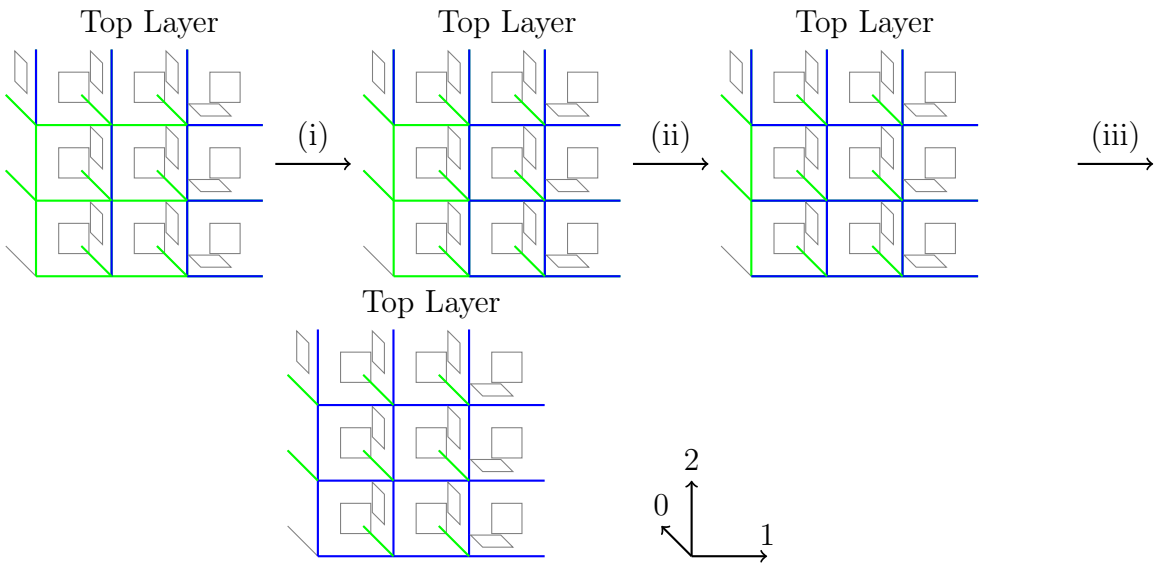

Figure 5.15: Illustration of the Hilbert space constraints on the top layer. The $\hat{p}$ operator, canonical conjugate momentum to the gauge field, on the blue links are constrained to take value in $a\mathbb{Z}$. Initially the blue links are under the time-like plaquettes. Equipped with the Gauss' law constraints, i.e. the sum of four $\hat{p}$'s sharing a common site is zero, all space-like links are colored blue step by step, which means all $\hat{p} \in a\mathbb{Z}$.

The links l are under the extra time-like plaquettes in the top layer, which are shown as the blue links in the first pannel in Fig. 5.15.

Combining Eq. 5.127 with Eq. 5.126, we can propagate the set of links where $\hat{p} \in a\mathbb{Z}$. For a given site, when three of the four links that share this site have $\hat{p} \in a\mathbb{Z}$ on them, then the last one should also have $\hat{p} \in a\mathbb{Z}$ by Eq. 5.126. In Figure. 5.15, we demonstrate this process and show that the constraints imply that all $\hat{p} \in a\mathbb{Z}$, i.e. all the gauge fields are defined with a period $\frac{2\pi}{a}$.

With the Gauss' law constraints and the momentum constraints derived, we complete the whole story for the pure lattice Maxwell theory with instantons allowed.

5.7.6 Pure Maxwell lattice theory without instantons

As reviewed in Sec. 5.7.1, the instantons in the 2+1D U(1) lattice gauge theory create a gap of the theory. We can completely suppress the instantons to get back to a gapless theroy, with behaves more like the pure Maxwell theory in the continuum.

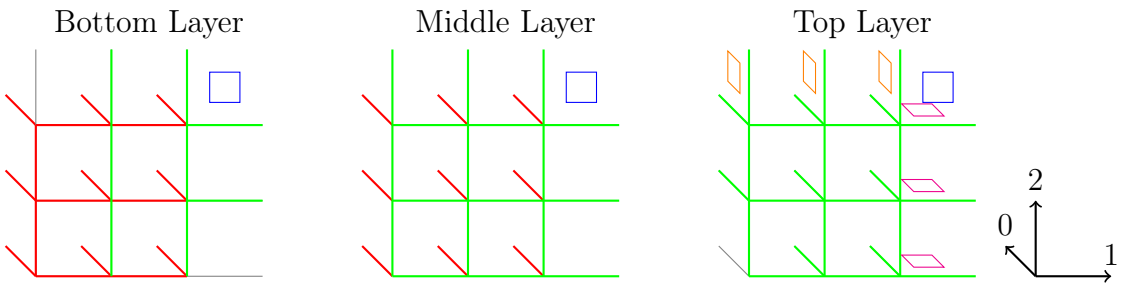

Figure 5.16: View of the bottom layer, middle layers, and the top layer after gauge fixing. Instantons are suppressed. The gauge fields on the red links are fixed to zero, on the green links are lifted to $\mathbb{R}$. The plaquettes with three different colors, blue, orange, and magenta, represent the three independent integer degrees of freedom. The plaquettes with the same color are not free degrees of freedom: they are enforced to have the same integer value.

We can repeat most of the derivations shown in the previous section, where we study the instanton-allowed version of the theory. The route differs after we fix all gauge degrees of freedom. Recall that in Fig. 5.14, most of the plaquettes are the integer degrees of freedom including information about the instantons in unit cells. For an instanton-suppressed theory, these integer degrees of freedom are eliminated. Therefore, we have a modified version for the physical degrees of freedom in each layers, as shown in Fig. 5.16. The gauge field degrees of freedom are in the same situation as the instanton-allowed case. However, there are only three remaining independent integer degrees of freedom, each includes the information of the total flux through a plane. Because there is no instanton, all planes with the same orientation have the same total flux. Therefore, to demonstrate the dependence on their values, we use three colors, blue, orange, and magenta, to color the plaquettes in Fig. 5.16. The plaquettes with the same color have the same integer value and represent one integer degree of freedom.

Because the gauge field degrees of freedom are the same, the Hilbert space basis vectors are also the same as in the previous section: We label each basis vector with a configuration of $\mathbb{R}$-ranged gauge fields on every links. We can define the transfer matrix between a pair of neighboring middle layers. Assuming the lower layer has configuration $|A\rangle$ and the upper layer has configuration $|A'\rangle$, we can read out the transfer matrix element from the action in

Eq. 5.106:

$$\langle A'|\hat{T}|A\rangle = \exp\left[-\frac{\beta_0 a^2}{2d\tau}\sum_{\text{links}}(A'-A)^2 - \frac{\beta d\tau}{2a^2}\left(\sum_{x\neq(N_1-1,N_2-1)}(a\,\square A_{x;1,2})^2 + (a\,\square A_{(N_1-1,N_2-1);1,2}+2\pi n)^2\right)\right], \tag{5.128}$$

where $(\square A)_{x;1,2} \equiv A_{x;1} + A_{x+\hat{1};2} - A_{x+\hat{2};1} - A_{x;2}$. n is the integer degree of freedom on space-like plaquettes (blue in Fig. 5.16), which is fixed for the transfer matrix, and should be summed over in the partition function as denoting different total-flux sectors.

Performing a similar Fourier transform as in the previous section, we obtain the Hamiltonian for the total-flux-n sector:

$$\hat{H}_n = \frac{1}{2\beta_0 a^2}\sum_{\text{links}}\hat{p}^2 + \frac{\beta}{2a^2}\left(\sum_{x\neq(N_1-1,N_2-1)}(a\,\square A_{x;1,2})^2 + (a\,\square A_{(N_1-1,N_2-1);1,2}+2\pi n)^2\right). \tag{5.129}$$

The $n = 0$ sector looks like a non-compact Maxwell theory. However, this theory is indeed compact after including all n sectors and the constraints we will discuss soon. It is the compact Maxwell theory with instantons suppressed. As we reviewed in Sec. 5.7.1, this theory is gappless with massless photons. The $n \neq 0$ sector can be considered as fluctuations around a classical configuration with a background magnetic field, which generates a total flux $2\pi n$.

For the constraints on the Hilbert space, we look at the top layer in Fig. 5.16. Similar to

the previous section, we get an extra phase factor to the transfer matrix in the top layer:

$$\begin{aligned}
&\exp\left[\sum_{\substack{x\in\text{sites}\\ i\in\{1,2\}}} i\hat{p}_{x;i}\left(\frac{d\tau}{a}(A_{x;0}-A_{x+\hat{i};0})+\frac{2\pi}{a}m_{x;0,i}\right)\right]\\
&=\prod_{x\in\text{sites}}\exp\left[i\frac{d\tau}{a}A_{x;0}(\hat{p}_{x;1}+\hat{p}_{x;2}-\hat{p}_{x-\hat{1};1}-\hat{p}_{x-\hat{2};2})\right]\\
&\quad\times\exp\left[i\frac{2\pi}{a}m_1\sum_{x_1=0}^{N_1-1}\hat{p}_{(x_1,N_2-1);2}\right]\times\exp\left[i\frac{2\pi}{a}m_2\sum_{x_2=0}^{N_2-1}\hat{p}_{(N_1-1,x_2);1}\right],
\end{aligned}\tag{5.130}$$

where we denote the integer degree of freedom on the 1-oriented plaquettes (orange in Fig. 5.16) as m_1, and the integer degree of freedom on the 2-oriented plaquettes (magenta in Fig. 5.16) as m_2. In the partition function, we sum over the extra degrees of freedom by

$$\sum_{m,A_0}\equiv\int_0^{\frac{2\pi}{d\tau}}dA_{x=(0,0);0}\prod_{x\neq(0,0)}\int_{-\infty}^{\infty}dA_{x;0}\sum_{m_1=-\infty}^{\infty}\sum_{m_2=-\infty}^{\infty}.\tag{5.131}$$

The gauge field part implies the Gauss' law $(\hat{p}_{x;1}+\hat{p}_{x;2}-\hat{p}_{x-\hat{1};1}-\hat{p}_{x-\hat{2};2})=0$ for all sites x using the same argument as in the previous section.

The sum over m_1 sets a constraint on the loop operator $e^{2\pi i\hat{L}_1}=1$, where

$$\hat{L}_1=\quad\cdots\quad\uparrow\qquad\uparrow\qquad\uparrow\ \tfrac{1}{a}\hat{p}_2\quad\cdots\quad=\frac{1}{a}\sum_{x_1=0}^{N_1-1}\hat{p}_{(x_1,N_2-1);2},\tag{5.132}$$

and the sum over m_2 sets a constraint on the loop operator $e^{2\pi i\hat{L}_2}=1$, where

$$\hat{L}_2=\begin{array}{c}\vdots\\ \xrightarrow{\ \frac{1}{a}\hat{p}_1\ }\\ \longrightarrow\\ \\ \longrightarrow\\ \vdots\end{array}=\frac{1}{a}\sum_{x_2=0}^{N_2-1}\hat{p}_{(N_1-1,x_2);1}.\tag{5.133}$$

We see the structure that is similar to the loop operators in Eq. 5.28 and 5.30 in the main text. These loop operators here can also be deformed by adding or subtracting the Gauss' law, showing their properties as 1-form symmetry operators.

We complete the story for the pure compact lattice Maxwell theory with instantons suppressed. The Hamiltonian is shown in Eq. 5.129. The Hilbert space has $\mathbb{R}$-ranged gauge fields on every links, but is subject to the Gauss' law constraints and two 1-form constraints shown above.

5.7.7 Maxwell-Chern-Simons lattice theory without instantons

With the preparations from the earlier sections, we can now start our derivation for the lattice Maxwell-Chern-Simons Hamiltonian. As reviewed in Sec. 5.7.1, we need to suppress the instantons in this theory, which makes its Hilbert space structure very similar to the pure lattice Maxwell theory with instantons suppressed. We have seen that in the previous section.

The starting point of the lattice Maxwell-Chern-Simons theory is the lattice action in Eq. 5.22, which has gauge transformations written in Eq. 5.12 - 5.15. The φ degrees of freedom are introduced to impose the instanton-suppression condition: Summing over φ in the partition function enforces the total flux through any unit cell is zero. Their existence is equivalent to our earlier elimination of instanton-related integer degrees of freedom in the previous section, and thus does not affect our discussion here.

Therefore, we can perform the exact same gauge fixing process as in the previous section. After gauge fixing, we are left with the physical degrees of freedom shown in Fig. 5.16. We also have the same Hilbert space basis vectors, labeled by configurations of $\mathbb{R}$-ranged gauge fields on every links.

To get the transfer matrix elements, we evaluate the lattice action in Eq. 5.22 on two neighboring middle layers in Fig. 5.16. The upper layer has a gauge field configuration $|A'\rangle$ and the lower layer has $|A\rangle$. Because the time-like gauge fields and the time-like integer

plaquettes are gauge fixed to zero, the result is largely simplified:

$$\begin{aligned}\langle A'|\hat{T}|A\rangle = \exp\Bigg[&-\frac{\beta_0 a^2}{2d\tau}\sum_{\text{links}}(A'-A)^2 \\ &-\frac{\beta d\tau}{2a^2}\left(\sum_{x\neq(N_1-1,N_2-1)}(a\,\square A_{x;1,2})^2+(a\,\square A_{(N_1-1,N_2-1);1,2}+2\pi n)^2\right) \\ &+\frac{ika^2}{4\pi}\sum_{x\in\text{sites}}\left(-A_{x-\hat{1};1}(A'_{x;2}-A_{x;2})+A_{x-\hat{2};2}(A'_{x;1}-A_{x;1})\right)\Bigg],\end{aligned} \tag{5.134}$$

where $(\square A)_{x;1,2}\equiv A_{x;1}+A_{x+\hat{1};2}-A_{x+\hat{2};1}-A_{x;2}$. n is the integer degree of freedom on space-like plaquettes (blue in Fig. 5.16), which denotes the flux sector and is fixed for the transfer matrix.

We apply the following general Fourier transform result:

$$\int_{-\infty}^{\infty} d(A'-A)e^{-ip(A'-A)}e^{-\frac{c}{2}(A'-A+d)^2+ib(A'-A)}\propto e^{-\frac{1}{2c}(p-b)^2}e^{i(p-b)d}. \tag{5.135}$$

We repeat the process in the earlier sections and derive the Hamiltonian for the total-flux-n sector:

$$\begin{aligned}\hat{H}_n=&\frac{1}{2\beta_0 a^2}\sum_{x\in\text{sites}}\left[(\hat{p}_{x;1}-\frac{ka^2}{4\pi}\hat{A}_{x-\hat{2};2})^2+(\hat{p}_{x;2}+\frac{ka^2}{4\pi}\hat{A}_{x-\hat{1};1})^2\right] \\ &+\frac{\beta}{2a^2}\left(\sum_{x\neq(N_1-1,N_2-1)}(a\,\square\hat{A}_{x;1,2})^2+(a\,\square\hat{A}_{(N_1-1,N_2-1);1,2}+2\pi n)^2\right).\end{aligned} \tag{5.136}$$

For the constraints on the Hilbert space, we look at the top layer in Fig. 5.16. Due to the Chern-Simons action in Eq. 5.11, the extra phase factor to the transfer matrix in the top

layer is much more complicated:

$$\exp\left\{\sum_{\substack{x\in\text{sites}\\ i\in\{1,2\}}} i\left(\hat{p}_{x;i}-\epsilon_{ij}\frac{ka^2}{4\pi}\hat{A}_{x-\hat{j};j}\right)\left(\frac{d\tau}{a}(A_{x;0}-A_{x+\hat{i};0})+\frac{2\pi}{a}m_{x;0,i}\right)\right.$$
$$+\frac{ika^2}{4\pi}\sum_{x\in\text{sites}}\left[\frac{d\tau}{a}\left(A_{x;0}\,\Box\hat{A}'_{x;1,2}-\hat{A}_{x-\hat{1};1}(A_{x;0}-A_{x+\hat{2};0})+\hat{A}_{x-\hat{2};2}(A_{x;0}-A_{x+\hat{1};0})\right)\right.$$
$$+\frac{2\pi d\tau}{a^2}(A_{x=(N_1-1,N_2-1);0}+A_{x=(0,0);0})\,n$$
$$\left.\left.+\frac{2\pi}{a}\left(-\hat{A}_{x-\hat{1};1}m_{x;0,2}-\hat{A}'_{x+\hat{2};1}m_{x;0,2}+\hat{A}_{x-\hat{2};2}m_{x;0,1}+\hat{A}'_{x+\hat{1};2}m_{x;0,1}\right)\right]\right\}, \tag{5.137}$$

where we denote the integer degree of freedom on the time-like plaquettes as m. Here A_0's and m's are not operators. They are variables to be summed over in the partition function. $\hat{A}'$ means this operator is placed between $\langle A'|$ and $\hat{T}$. Note that some terms in Eq. 5.137 can cancel with each other. We simplify it into

$$\exp\left\{\sum_{\substack{x\in\text{sites}\\ i\in\{1,2\}}} i\hat{p}_{x;i}\left(\frac{d\tau}{a}(A_{x;0}-A_{x+\hat{i};0})+\frac{2\pi}{a}m_{x;0,i}\right)\right.$$
$$+\frac{ika^2}{4\pi}\sum_{x\in\text{sites}}\left[\frac{d\tau}{a}A_{x;0}\,\Box\hat{A}'_{x;1,2}+\frac{2\pi d\tau}{a^2}(A_{x=(N_1-1,N_2-1);0}+A_{x=(0,0);0})\,n\right.$$
$$\left.\left.+\frac{2\pi}{a}\left(-\hat{A}'_{x+\hat{2};1}m_{x;0,2}+\hat{A}'_{x+\hat{1};2}m_{x;0,1}\right)\right]\right\}. \tag{5.138}$$

Further organizing the terms, we get

$$\prod_{x\in\text{sites}}\exp\left[i\frac{d\tau}{a}A_{x;0}\left(\hat{p}_{x;1}+\hat{p}_{x;2}-\hat{p}_{x-\hat{1};1}-\hat{p}_{x-\hat{2};2}+\frac{ka^2}{4\pi}\Box\hat{A}'_{x;1,2}+\frac{ka}{2}(\delta_{x=(N_1-1,N_2-1)}+\delta_{x=(0,0)})n\right)\right]$$
$$\times\exp\left[i\frac{2\pi}{a}m_1\left(\sum_{x_1=0}^{N_1-1}\hat{p}_{(x_1,N_2-1);2}-\frac{ka^2}{4\pi}\hat{A}'_{(x_1,N_2);1}\right)\right]$$
$$\times\exp\left[i\frac{2\pi}{a}m_2\left(\sum_{x_2=0}^{N_2-1}\hat{p}_{(N_1-1,x_2);1}+\frac{ka^2}{4\pi}\hat{A}'_{(N_1,x_2);2}\right)\right], \tag{5.139}$$

where we denote the integer degree of freedom on the 1-oriented plaquettes (orange in Fig. 5.16) as m_1, and the integer degree of freedom on the 2-oriented plaquettes (magenta in Fig. 5.16) as m_2.

In the partition function, we sum over the extra degrees of freedom by

$$\sum_{m,A_0} \equiv \int_0^{\frac{2\pi}{d\tau}} dA_{x=(0,0);0} \prod_{x\neq(0,0)} \int_{-\infty}^{\infty} dA_{x;0} \sum_{m_1=-\infty}^{\infty} \sum_{m_2=-\infty}^{\infty} . \tag{5.140}$$

The gauge field part implies

$$\hat{p}_{x;1} + \hat{p}_{x;2} - \hat{p}_{x-\hat{1};1} - \hat{p}_{x-\hat{2};2} + \frac{ka^2}{4\pi}\Box\hat{A}'_{x;1,2} + \frac{ka}{2}n = 0, \quad \text{for } x = (N_1-1, N_2-1), \tag{5.141}$$

$$\hat{p}_{x;1} + \hat{p}_{x;2} - \hat{p}_{x-\hat{1};1} - \hat{p}_{x-\hat{2};2} + \frac{ka^2}{4\pi}\Box\hat{A}'_{x;1,2} = 0, \quad \text{for } x \neq (N_1-1, N_2-1) \text{ or } (0,0), \tag{5.142}$$

and for $x = (0,0)$

$$\int_0^{\frac{2\pi}{d\tau}} dA_{x;0} \exp\left[i\frac{d\tau}{a}A_{x;0}\left(\hat{p}_{x;1} + \hat{p}_{x;2} - \hat{p}_{x-\hat{1};1} - \hat{p}_{x-\hat{2};2} + \frac{ka^2}{4\pi}\Box\hat{A}'_{x;1,2} + \frac{ka}{2}n\right)\right] \neq 0. \tag{5.143}$$

Note that $\sum_{x\in\text{sites}}(\hat{p}_{x;1}+\hat{p}_{x;2}-\hat{p}_{x-\hat{1};1}-\hat{p}_{x-\hat{2};2}+\frac{ka^2}{4\pi}\Box\hat{A}'_{x;1,2}) = 0$. Therefore, Eq. 5.141 and 5.142 implies that $(\hat{p}_{x;1} + \hat{p}_{x;2} - \hat{p}_{x-\hat{1};1} - \hat{p}_{x-\hat{2};2} + \frac{ka^2}{4\pi}\Box\hat{A}'_{x;1,2}) = \frac{ka}{2}n$ for $x = (0,0)$. Inserting it into Eq. 5.143, we get a constraint

$$\int_0^{\frac{2\pi}{d\tau}} dA_{x;0} \exp\left[i\frac{d\tau}{a}A_{x;0}\left(\frac{ka}{2}n + \frac{ka}{2}n\right)\right] = \int_0^{\frac{2\pi}{d\tau}} dA_{x;0} \exp\left(id\tau A_{x;0}\, k\, n\right) \neq 0. \tag{5.144}$$

Because we assume an even integer $k \neq 0$, this constraint implies that the integer n has to be zero, i.e. the Maxwell-Chern-Simons theory only allows the zero-total-flux sector.

With knowing $n = 0$, Eq. 5.141 and 5.142 can be summarized into

$$\hat{p}_{x;1} + \hat{p}_{x;2} - \hat{p}_{x-\hat{1};1} - \hat{p}_{x-\hat{2};2} + \frac{ka^2}{4\pi}\Box\hat{A}'_{x;1,2} = 0, \quad \text{for all sites } x, \tag{5.145}$$

as constraints on physical states $\langle A'|$. We can equally derive the hermitian conjugate version with $\hat{A}' \to \hat{A}$, which is exactly the Gauss' law in Eq. 5.25 in the main text.

We can also just keep the zero-total-flux sector in Eq. 5.136. The resulting Hamiltonian is

$$\hat{H} = \frac{1}{2\beta_0 a^2} \sum_{x\in\text{sites}} \left[(\hat{p}_{x;1} - \frac{ka^2}{4\pi} \hat{A}_{x-\hat{2};2})^2 + (\hat{p}_{x;2} + \frac{ka^2}{4\pi} \hat{A}_{x-\hat{1};1})^2 \right] + \frac{\beta}{2a^2} \sum_{x\in\text{sites}} (a \,\square \hat{A}_{x;1,2})^2. \tag{5.146}$$

Setting $\beta_0 = \beta = \frac{1}{e^2}$, we derive exactly the Hamiltonian in Eq. 5.23 in the main text.

Now we look at the m_1 part in Eq. 5.139. For the part to be non vanishing under the sum $\sum_{m_1=-\infty}^{\infty}$, we have the constraint $e^{2\pi i \hat{L}_1} = 1$, where

$\hat{L}_1 =$ 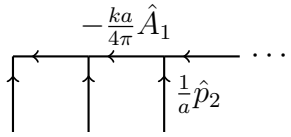

$$= \sum_{x_1=0}^{N_1-1} \left(\frac{1}{a} \hat{p}_{(x_1,N_2-1);2} - \frac{ka}{4\pi} \hat{A}'_{(x_1,N_2);1} \right). \tag{5.147}$$

For the m_2 part in Eq. 5.139, similarly, we have the constraint $e^{2\pi i \hat{L}_2} = 1$, where

$\hat{L}_2 =$ 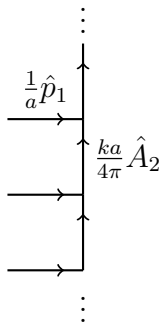

$$= \sum_{x_2=0}^{N_2-1} \left(\frac{1}{a} \hat{p}_{(N_1-1,x_2);1} + \frac{ka}{4\pi} \hat{A}'_{(N_1,x_2);2} \right). \tag{5.148}$$

Note that the Gauss' law allows us to shift $\hat{L}_1$ and $\hat{L}_2$ to arbitrary locations. Moreover, they

can be arbitrarily deformed as long as being topologically equivalent, i.e. they are 1-form symmetry operators. We can equally derive their hermitian conjugate versions with $\hat{A}' \to \hat{A}$, which are exactly the loop operator constraints in Eq. 5.28 and 5.30 in the main text. (We are allowed to add two global phases to the constraints by twisting the boundary conditions of the gauge bundle.)

5.7.8 Details of analytical solution

In this subsection, we add some details about the analytical solution mentioned in Sec. 5.5. In Eq. 5.65, we saw that in the momentum sector $q = (q_1, q_2)$, the Fourier transformed Hamiltonian was

$$\begin{aligned}\hat{H}_q = \; & \frac{e^2}{2a^2}\left[\left(\hat{p}_{q;1} - \frac{ka^2}{4\pi}e^{iq_2}\hat{A}_{q;2}\right)\left(\hat{p}_{-q;1} - \frac{ka^2}{4\pi}e^{-iq_2}\hat{A}_{-q;2}\right)\right. \\ & \left. + \left(\hat{p}_{q;2} + \frac{ka^2}{4\pi}e^{iq_1}\hat{A}_{q;1}\right)\left(\hat{p}_{-q;2} + \frac{ka^2}{4\pi}e^{-iq_1}\hat{A}_{-q;1}\right)\right] \\ & + \frac{1}{2e^2}\left[\left(1 - e^{-iq_2}\right)\hat{A}_{q;1} - \left(1 - e^{-iq_1}\right)\hat{A}_{q;2}\right] \times \\ & \left[\left(1 - e^{iq_2}\right)\hat{A}_{-q;1} - \left(1 - e^{iq_1}\right)\hat{A}_{-q;2}\right]. \end{aligned} \tag{5.149}$$

We define the following change of variables (the operator notation $\hat{\cdot}$ is omitted for sim-

plicity):

$$X = \frac{(1-e^{-iq_2})\hat{A}_{q;1} + (1-e^{iq_2})\hat{A}_{-q;1} - (1-e^{-iq_1})\hat{A}_{q;2} - (1-e^{iq_1})\hat{A}_{-q;2}}{2\sqrt{(1-\cos q_1)+(1-\cos q_2)}} \tag{5.150}$$

$$\tilde{X} = \frac{(1-e^{iq_1})\hat{A}_{q;1} + (1-e^{-iq_1})\hat{A}_{-q;1} + (1-e^{iq_2})\hat{A}_{q;2} + (1-e^{-iq_2})\hat{A}_{-q;2}}{2\sqrt{(1-\cos q_1)+(1-\cos q_2)}} \tag{5.151}$$

$$Y = \frac{(1-e^{-iq_2})\hat{A}_{q;1} - (1-e^{iq_2})\hat{A}_{-q;1} - (1-e^{-iq_1})\hat{A}_{q;2} + (1-e^{iq_1})\hat{A}_{-q;2}}{2i\sqrt{(1-\cos q_1)+(1-\cos q_2)}} \tag{5.152}$$

$$\tilde{Y} = \frac{(1-e^{iq_1})\hat{A}_{q;1} - (1-e^{-iq_1})\hat{A}_{-q;1} + (1-e^{iq_2})\hat{A}_{q;2} - (1-e^{-iq_2})\hat{A}_{-q;2}}{2i\sqrt{(1-\cos q_1)+(1-\cos q_2)}} \tag{5.153}$$

$$P_X = \frac{(1-e^{-iq_2})\hat{p}_{q;1} + (1-e^{iq_2})\hat{p}_{-q;1} - (1-e^{-iq_1})\hat{p}_{q;2} - (1-e^{iq_1})\hat{p}_{-q;2}}{2\sqrt{(1-\cos q_1)+(1-\cos q_2)}} \tag{5.154}$$

$$\tilde{P}_X = \frac{(1-e^{iq_1})\hat{p}_{q;1} + (1-e^{-iq_1})\hat{p}_{-q;1} + (1-e^{iq_2})\hat{p}_{q;2} + (1-e^{-iq_2})\hat{p}_{-q;2}}{2\sqrt{(1-\cos q_1)+(1-\cos q_2)}} \tag{5.155}$$

$$P_Y = \frac{(1-e^{-iq_2})\hat{p}_{q;1} - (1-e^{iq_2})\hat{p}_{-q;1} - (1-e^{-iq_1})\hat{p}_{q;2} + (1-e^{iq_1})\hat{p}_{-q;2}}{2i\sqrt{(1-\cos q_1)+(1-\cos q_2)}} \tag{5.156}$$

$$\tilde{P}_Y = \frac{(1-e^{iq_1})\hat{p}_{q;1} - (1-e^{-iq_1})\hat{p}_{-q;1} + (1-e^{iq_2})\hat{p}_{q;2} - (1-e^{-iq_2})\hat{p}_{-q;2}}{2i\sqrt{(1-\cos q_1)+(1-\cos q_2)}}. \tag{5.157}$$

Given the commutation relation in Eq. 5.64, one can check that $[X, P_X] = [\tilde{X}, \tilde{P}_X] = [Y, P_Y] = [\tilde{Y}, \tilde{P}_Y] = i$, and all other commutators are zero.

The Gauss' law Eq. 5.25 after the Fourier transform becomes

$$\left\{(1-e^{iq_1})\hat{p}_{q;1} + (1-e^{iq_2})\hat{p}_{q;2} + \frac{ka^2}{4\pi}\left[(1-e^{-iq_2})\hat{A}_{q;1} - (1-e^{-iq_1})\hat{A}_{q;2}\right]\right\}|\psi\rangle = 0 \tag{5.158}$$

for any physical state $|\psi\rangle$ in the Hilbert space, and any $q \in \{0, \frac{2\pi}{N_1}, \ldots, \frac{2\pi}{N_1}(N_1-1)\} \times \{0, \frac{2\pi}{N_2}, \ldots, \frac{2\pi}{N_2}(N_2-1)\}$. Note that Eq. 5.158 is trivially satisfied for the zero mode $q = (0,0)$. The zero mode is restricted by the two 1-form constraints Eq. 5.28 and Eq. 5.30. We will analyze the zero mode separately later. For non-zero modes, the two 1-form constraints do not introduce further restrictions.

Note that Eq. 5.158 also works for $-q$, which says

$$\left\{(1-e^{-iq_1})\hat{p}_{-q;1}+(1-e^{-iq_2})\hat{p}_{-q;2}+\frac{ka^2}{4\pi}\left[(1-e^{iq_2})\hat{A}_{-q;1}-(1-e^{iq_1})\hat{A}_{-q;2}\right]\right\}|\psi\rangle=0. \tag{5.159}$$

Linearly combining the Gauss' law constraints for q and $-q$,

(Eq. 5.158 + Eq. 5.159) $\implies$

$$\left(\tilde{P}_X+\frac{ka^2}{4\pi}X\right)|\psi\rangle=0, \tag{5.160}$$

and (Eq. 5.158 − Eq. 5.159) $\implies$

$$\left(\tilde{P}_Y+\frac{ka^2}{4\pi}Y\right)|\psi\rangle=0, \tag{5.161}$$

We then do another change of variables:

$$Q_X=P_X+\frac{ka^2}{4\pi}\tilde{X} \tag{5.162}$$

$$\tilde{Q}_X=\tilde{P}_X+\frac{ka^2}{4\pi}X \tag{5.163}$$

$$Q_Y=P_Y+\frac{ka^2}{4\pi}\tilde{Y} \tag{5.164}$$

$$\tilde{Q}_Y=\tilde{P}_Y+\frac{ka^2}{4\pi}Y. \tag{5.165}$$

One can check that $[X,Q_X]=[\tilde{X},\tilde{Q}_X]=[Y,Q_Y]=[\tilde{Y},\tilde{Q}_Y]=i$, and all other commutators are zero. With the new variables, the Gauss' law constraints Eq. 5.160 and Eq. 5.161 is further simplified:

$$\tilde{Q}_X|\psi\rangle=0, \tag{5.166}$$

$$\tilde{Q}_Y|\psi\rangle=0. \tag{5.167}$$

The inverse change of variables is:

$$\hat{A}_{q;1} = \frac{(1-e^{iq_2})(X+iY)+(1-e^{-iq_1})(\tilde{X}+i\tilde{Y})}{2\sqrt{(1-\cos q_1)+(1-\cos q_2)}} \tag{5.168}$$

$$\hat{A}_{-q;1} = \frac{(1-e^{-iq_2})(X-iY)+(1-e^{iq_1})(\tilde{X}-i\tilde{Y})}{2\sqrt{(1-\cos q_1)+(1-\cos q_2)}} \tag{5.169}$$

$$\hat{A}_{q;2} = \frac{-(1-e^{iq_1})(X+iY)+(1-e^{-iq_2})(\tilde{X}+i\tilde{Y})}{2\sqrt{(1-\cos q_1)+(1-\cos q_2)}} \tag{5.170}$$

$$\hat{A}_{-q;2} = \frac{-(1-e^{-iq_1})(X-iY)+(1-e^{iq_2})(\tilde{X}-i\tilde{Y})}{2\sqrt{(1-\cos q_1)+(1-\cos q_2)}} \tag{5.171}$$

$$\hat{p}_{q;1} = \frac{(1-e^{iq_2})(P_X+iP_Y)+(1-e^{-iq_1})(\tilde{P}_X+i\tilde{P}_Y)}{2\sqrt{(1-\cos q_1)+(1-\cos q_2)}} \tag{5.172}$$

$$\hat{p}_{-q;1} = \frac{(1-e^{-iq_2})(P_X-iP_Y)+(1-e^{iq_1})(\tilde{P}_X-i\tilde{P}_Y)}{2\sqrt{(1-\cos q_1)+(1-\cos q_2)}} \tag{5.173}$$

$$\hat{p}_{q;2} = \frac{-(1-e^{iq_1})(P_X+iP_Y)+(1-e^{-iq_2})(\tilde{P}_X+i\tilde{P}_Y)}{2\sqrt{(1-\cos q_1)+(1-\cos q_2)}} \tag{5.174}$$

$$\hat{p}_{-q;2} = \frac{-(1-e^{-iq_1})(P_X-iP_Y)+(1-e^{iq_2})(\tilde{P}_X-i\tilde{P}_Y)}{2\sqrt{(1-\cos q_1)+(1-\cos q_2)}} \tag{5.175}$$

$$P_X = Q_X - \frac{ka^2}{4\pi}\tilde{X} \tag{5.176}$$

$$\tilde{P}_X = \tilde{Q}_X - \frac{ka^2}{4\pi}X \tag{5.177}$$

$$P_Y = Q_Y - \frac{ka^2}{4\pi}\tilde{Y} \tag{5.178}$$

$$\tilde{P}_Y = \tilde{Q}_Y - \frac{ka^2}{4\pi}Y. \tag{5.179}$$

Inserting everything into the Fourier transformed Hamiltonian in Eq. 5.149, after some algebra we get

$$\begin{aligned}\hat{H}_q = \frac{a^2}{4e^2}&\left\{\frac{1}{a^2}\left[2(1-\cos q_1)+2(1-\cos q_2)\right]+\left(\frac{ke^2}{4\pi}\right)^2\left[2+2\cos(q_1+q_2)\right]\right\}(X^2+Y^2)\\ &+\frac{e^2}{4a^2}\left\{Q_X^2+Q_Y^2+\tilde{Q}_X^2+\tilde{Q}_Y^2-\frac{ka^2}{4\pi}\left[2(1-\cos q_1)+2(1-\cos q_2)\right](X\tilde{Q}_X+Y\tilde{Q}_Y)\right.\\ &\left.+\frac{ka^2}{4\pi}2\sin(q_1+q_2)(Y\tilde{Q}_X-X\tilde{Q}_Y)\right\}.\end{aligned} \tag{5.180}$$

Applying the Gauss' law constraints Eq. 5.166 and Eq. 5.167, we can set $\tilde{Q}_X = \tilde{Q}_Y = 0$. We define an angular frequency, which also appeared in Eq. 5.66 in the main text:

$$\omega^2 = \frac{1}{a^2}\left[2(1-\cos q_1) + 2(1-\cos q_2)\right] + (\frac{ke^2}{4\pi})^2\left[2 + 2\cos(q_1+q_2)\right]. \tag{5.181}$$

The Hamiltonian in sector q finally looks simple and familiar:

$$\hat{H}_q = \frac{e^2}{4a^2}(Q_X^2 + Q_Y^2) + \frac{a^2}{4e^2}\omega^2(X^2+Y^2). \tag{5.182}$$

Note that we actually have combined the q and $-q$ sectors together in the analysis above. On both sectors, the total Hamiltonian is

$$\hat{H}_q + \hat{H}_{-q} = \frac{e^2}{2a^2}(Q_X^2 + Q_Y^2) + \frac{a^2}{2e^2}\omega^2(X^2+Y^2). \tag{5.183}$$

Simply rescaling the momentum and coordinate, we see that the q and $-q$ sectors become two decoupled simple harmonic oscillators, both having the same angular frequency ω described in Eq. 5.181.

In the special case when $q = (0,\pi)$, $(\pi,0)$, or (π,π), i.e. when q and $-q$ are identical, one can proceed a similar analysis with half of the degrees of freedom (note that all Y-related variables become zero). The result is that the sector is equivalent to one simple harmonic oscillator with an angular frequency given by Eq. 5.181 as well. Therefore, the band structure is smooth and has no singularity on these special momentum values.

The zero mode $q = (0,0)$, however, need to be treated separately.

First, for $q = (0,0)$, the Hamiltonian in Eq. 5.149 does not have the magnetic potential term, and the electric kinetic terms are quadratic:

$$\hat{H}_{q=(0,0)} = \frac{e^2}{2a^2}\left[\left(\hat{p}_{q=(0,0);1} - \frac{ka^2}{4\pi}\hat{A}_{q=(0,0);2}\right)^2 + \left(\hat{p}_{q=(0,0);2} + \frac{ka^2}{4\pi}\hat{A}_{q=(0,0);1}\right)^2\right]. \tag{5.184}$$

Second, the Gauss' law constraint acts trivially on the zero mode. However, the two 1-form constraints Eq. 5.28 and Eq. 5.30 act non-trivially on the zero mode:

$$\exp\left[i2\pi\sqrt{\frac{N_1}{N_2}}\left(\frac{1}{a}\hat{p}_{q=(0,0);2}-\frac{ka}{4\pi}\hat{A}_{q=(0,0);1}\right)\right]|\psi\rangle = e^{i\theta_1}|\psi\rangle, \tag{5.185}$$

$$\exp\left[i2\pi\sqrt{\frac{N_2}{N_1}}\left(\frac{1}{a}\hat{p}_{q=(0,0);1}+\frac{ka}{4\pi}\hat{A}_{q=(0,0);2}\right)\right]|\psi\rangle = e^{i\theta_2}|\psi\rangle, \tag{5.186}$$

for any physical state $|\psi\rangle$ in the Hilbert space. Here N_1, N_2 are the number of lattice sites in the 1 and 2 directions, respectively. θ_1 and θ_2 are two constant global phases.

Third, the change of variables defined earlier does not work for the zero mode. We need to define a separate change of variables for the zero mode purpose (again, the operator notation $\hat{\cdot}$ is omitted for simplicity):

$$X_0 = \frac{\hat{A}_{q=(0,0);1}+\frac{4\pi}{ka^2}\hat{p}_{q=(0,0);2}}{\sqrt{2}} \tag{5.187}$$

$$Y_0 = \frac{\hat{A}_{q=(0,0);1}-\frac{4\pi}{ka^2}\hat{p}_{q=(0,0);2}}{\sqrt{2}} \tag{5.188}$$

$$P_{X_0} = \frac{\hat{p}_{q=(0,0);1}-\frac{ka^2}{4\pi}\hat{A}_{q=(0,0);2}}{\sqrt{2}} \tag{5.189}$$

$$P_{Y_0} = \frac{\hat{p}_{q=(0,0);1}+\frac{ka^2}{4\pi}\hat{A}_{q=(0,0);2}}{\sqrt{2}}. \tag{5.190}$$

One can check that $[X_0, P_{X_0}] = [Y_0, P_{Y_0}] = i$ and all other commutators are zero.

Inserting the change of variables, the zero mode Hamiltonian in Eq. 5.184 becomes

$$\begin{aligned}\hat{H}_{q=(0,0)} &= \frac{e^2}{2a^2}\cdot 2\left[P_{X_0}^2+\left(\frac{ka^2}{4\pi}\right)^2 X_0^2\right] \\ &= \frac{1}{2}\left(\frac{2e^2}{a^2}\right)P_{X_0}^2+\frac{1}{2}\left(\frac{a^2}{2e^2}\right)\left(\frac{ke^2}{2\pi}\right)^2 X_0^2,\end{aligned} \tag{5.191}$$

which can be recognized as a simple harmonic oscillator with effective mass $\frac{a^2}{2e^2}$ and the

angular frequency

$$\omega_0 = \frac{ke^2}{2\pi}. \tag{5.192}$$

This is the same result as inserting $q_1 = q_2 = 0$ into the band dispersion Eq. 5.181. Therefore, the band is smooth and has no singularity at $q = (0, 0)$ as well.

What makes the zero mode special, is that the constraints do not kill the degrees of freedom like in Eq. 5.166 and Eq. 5.167 for the non-zero modes. Instead, the constraints for the zero mode, Eq. 5.185 and Eq. 5.186, after change of variables, say

$$\exp\left(i2\pi\sqrt{\frac{N_1}{N_2}}\frac{ka}{4\pi}\sqrt{2}Y_0\right)|\psi\rangle = e^{i\theta_1}|\psi\rangle, \tag{5.193}$$

$$\exp\left(i2\pi\sqrt{\frac{N_2}{N_1}}\frac{1}{a}\sqrt{2}P_{Y_0}\right)|\psi\rangle = e^{i\theta_2}|\psi\rangle, \tag{5.194}$$

for any physical state $|\psi\rangle$ in the Hilbert space.

To make things cleaner, define a constant $b = \sqrt{\frac{N_2}{N_1}}\frac{4\pi}{ka}\frac{1}{\sqrt{2}}$. We rewrite the constraints above and get

$$e^{i2\pi Y_0/b}|\psi\rangle = e^{i\theta_1}|\psi\rangle, \tag{5.195}$$

$$e^{ikbP_{Y_0}}|\psi\rangle = e^{i\theta_2}|\psi\rangle, \tag{5.196}$$

which implies

$$Y_0 \in b\mathbb{Z} + \frac{b\theta_1}{2\pi}, \tag{5.197}$$

$$P_{Y_0} \in \frac{2\pi}{kb}\mathbb{Z} + \frac{\theta_2}{kb}, \tag{5.198}$$

the latter further implies that, in the Y_0 basis, the wave function has to be periodic with the period kb, i.e. $\psi(Y_0 + kb) = e^{i\theta_2}\psi(Y_0)$.

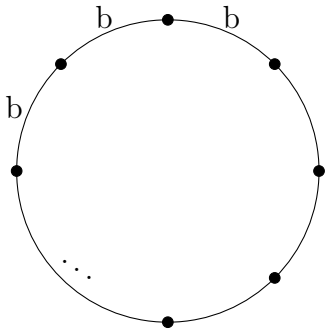

Figure 5.17: Illustration of the zero mode degree of freedom which generates the degenerate Hilbert space. It is equivalent to a particle on a ring of perimeter kb. There are k equally spacing sites on the ring, having distance b between the neighboring sites.

These constraints are very familiar to us. It is equivalent to a particle on a ring of perimeter kb, and the location of the particle can be chosen on k different sites, with the neighboring sites having distance b between them. See Fig. 5.17 for an illustration.

Because Y_0 does not appear in the Hamiltonian in Eq. 5.191, it is a decoupled degree of freedom with zero Hamiltonian. Therefore, its Hilbert space is a degenerate subspace, and is direct product to the other Hilbert spaces of the modes on the band structure.

Because the number of sites on the ring has to be an integer, we naturally get the quantization of k (otherwise the discreteness $Y_0 \in b\mathbb{Z} + \frac{b\theta_1}{2\pi}$ and the periodicity $\psi(Y_0 + kb) = e^{i\theta_2}\psi(Y_0)$ are incompatible). The number of independent states in the degenerate Hilbert subspace equals to the number of sites on the ring. Therefore, we also see the k-fold degeneracy of states from this analysis.

Chapter 6

Conclusions and Outlook

This thesis has investigated various numerical and analytical methods in the study of several low-dimensional strongly correlated quantum systems. By focusing on both lattice models and field theories, we have contributed to a deeper understanding of phase transitions, critical points, dynamic processes, and learning algorithms in these systems.

In Chapter 2 we introduced a simple 1+1D quantum field theory which demonstrated the complex phase transition phenomenon of multiversality, i.e. how different regions of the phase boundary can exhibit distinct universality classes. This multiversality phenomenon was first discovered in a more complicated 3+1D gauge theory [1], [2]. Our simpler model provided a more accessible starting point for exploring this intriguing phase transition phenomenon. We demonstrated the comprehensive phase diagram using analytical RG calculations, as well as numerical DMRG simulations of a concrete microscopic lattice model. Although we had difficulty nailing down the small multiversality segment in the numerical phase diagram due to the limited precision by the lattice size, we validated the existence of the conjectured $\tilde{K} = 1/2$ KT transition in the strong-coupling regime. Moreover, the absence of any first-order transition in our numerical experiments supported the evidence of multiversality.

In Chapter 3 we applied systematic statistical tools to refine the critical point analysis. By leveraging the smoothing spline method, we developed two approaches to accurately

pinpoint the critical point of the Ising phase transition, demonstrating the utility of statistical techniques in actual physics tasks. The consistency of the results with baseline estimates by human observation validated the effectiveness of these statistical tools. We analyzed the strengths and limitations of each approach, paving the way for more automated and reliable processes in future research.

In Chapter 4 we established a comprehensive framework for analyzing quantum-classical adiabatic dynamics using numerical learning algorithms, supported by rigorous analytical proofs of error bounds. We further developed a provably efficient adiabatic learning (PEAL) algorithm. By benchmarking our PEAL algorithm on the 1D Holstein model, we showcased its precise predictions of dynamics, scalability, and potential for transfer learning. Our framework and PEAL algorithm open new avenues for provably efficient learning in quantum-classical dynamics, suggesting promising future directions in enhancing the accuracy and efficiency of dynamics predictions.

In Chapter 5 we introduced a Hamiltonian lattice formulation for the 2+1D compact Maxwell-Chern-Simons theory, providing a crucial bridge between continuum theories and numerical applications. The derivation and analytical solution of this Hamiltonian formulation, along with its consistency with continuum Maxwell-Chern-Simons theory, established a solid foundation for future numerical simulations. This work highlighted the potential for quantum algorithms, learning algorithms, and other numerical methods to explore topological theories.

This thesis has studied select examples of numerical and analytical methods in quantum systems, yet numerous possibilities remain unexplored. Here, we highlight several promising directions for future research.

1. For the numerical evidence of multiversality, we had difficulty nailing down the small Ising segment in the phase diagram due to limited lattice sizes we could simulate. Possible improvements include using larger system sizes or more advanced algorithms to enhance resolution.

For the numerical phase diagram, we presented the plane in the parameter space by fixing coupling constant $\lambda = 1$. The phase diagram can be extended to other values of λ. We expect to see very rich structures in this extended phase diagram in the 3D parameter space. For example, the multiversality segment shrinks when λ increases. Then a natural question to ask is: What is the fate of multiversality when λ becomes very large, i.e. very strong coupling between the XXZ chain and the Ising chain? Does it eventually disappear? If yes, what is the universality class of the multicritical point into which the multiversality segment shrinks? If no, what does the phase diagram look like then?

Here, we offer a preliminary idea to serve as a starting point. We can think about the limit of $\lambda = 2J = -2\Delta \gg 1$ in the lattice Hamiltonian Eq. 2.6, and thus ignore the $(XX + YY)$ and σ^x terms. The effective Hamiltonian becomes

$$H \propto \sum_n (-Z_n Z_{n+1} + \sigma_n^z \sigma_{n+1}^z + Z_n \sigma_n^z), \tag{6.1}$$

which shows a frustrated spin ladder. This frustration model is dual to the dimer covering problem on the fish-bone-shaped dual lattice of the ladder. More interestingly, it can also link to the boundary lattice model of the $n = 1$ $Z_2 \times Z_2^f$ SPT introduced in Ref. [145]. The number of configurations (i.e. frustration degeneracy) for an open chain of length L is $[(1+\sqrt{2})^L + (1-\sqrt{2})^L]/2$. Adding the terms we ignored back to the Hamiltonian as perturbations, we could possibly figure out the phase diagram in the large λ limit.

2. We applied the smoothing spline method on the Ising transition, where the critical exponent $\nu = 1$ is known. It is a straightforward extension to apply the method on critical points with other values of ν. Moreover, it is also possible to employ the method to measure an unknown critical exponent ν. It will be interesting to think about whether we could use the method to systematically detect the existence of a

critical point as a data-driven approach, without any prior knowledge from the field theory.

3. We demonstrated our PEAL algorithm in 1D Holstein model, which had strongly localized groundstate wavefunction at every timestep. However, the wavefunctions are only weakly localized in 2D. In 3D, there is a conducting band with mobility edges [88]. Because the algorithm requests a gapped phase or localized wavefunctions, the application to 2D or 3D Holstein model is limited. However, this challenge can be overcome by searching for more general provably efficient learning algorithms of quantum systems which could apply on gapless phases. Nevertheless, it is possible to apply our PEAL algorithm on higher-dimensional systems, as long as they are gapped or localized. Moreover, it is also possible to apply PEAL on interacting systems. For example, it would be interesting to see the performance of PEAL on the Hubbard model.

4. We studied the Maxwell-Chern-Simons gauge theory without any matter fields. In our derivation of the Hamiltonian lattice formulation, we suppressed all instantons. However, charged matter fields and instantons come together in a theory with Chern-Simons action. A potential future research direction is to incorporate matter fields and instantons into our Hamiltonian lattice formulation.

References

[1] Z. Bi and T. Senthil, "Adventure in topological phase transitions in 3 + 1-d: Non-abelian deconfined quantum criticalities and a possible duality," *Phys. Rev. X*, vol. 9, p. 021 034, 2 May 2019. DOI: 10.1103/PhysRevX.9.021034. URL: https://link.aps.org/doi/10.1103/PhysRevX.9.021034.

[2] Z. Bi, E. Lake, and T. Senthil, "Landau ordering phase transitions beyond the landau paradigm," *Phys. Rev. Res.*, vol. 2, p. 023 031, 2 Apr. 2020. DOI: 10.1103/PhysRevResearch.2.023031. URL: https://link.aps.org/doi/10.1103/PhysRevResearch.2.023031.

[3] C. Peng, G.-W. Chern, J.-P. Liu, and D. Luo, "Provably efficient adiabatic learning for quantum-classical dynamics," *arXiv preprint arXiv:2408.00276*, 2024. URL: https://arxiv.org/abs/2408.00276.

[4] M. Lüscher, "Bosonization in (2+1)-Dimensions," *Nucl. Phys. B*, vol. 326, pp. 557–582, 1989. DOI: 10.1016/0550-3213(89)90544-0.

[5] M. C. Diamantini, P. Sodano, and C. A. Trugenberger, "Topological excitations in compact maxwell-chern-simons theory," *Phys. Rev. Lett.*, vol. 71, pp. 1969–1972, 1993. DOI: 10.1103/PhysRevLett.71.1969. arXiv: hep-th/9306073.

[6] G. Dunne, A. Kovner, and B. Tekin, "Magnetic symmetries and vortices in chern-simons theories," *Phys. Rev. D*, vol. 63, p. 025 009, 2 Dec. 2000. DOI: 10.1103/PhysRevD.63.025009. URL: https://link.aps.org/doi/10.1103/PhysRevD.63.025009.

[7] L. P. Colatto, J. A. Helayel-Neto, M. Hott, and W. A. Moura-Melo, "Remarks on charged vortices in the Maxwell-Chern-Simons model," *Phys. Lett. A*, vol. 314, pp. 184–190, 2003. DOI: 10.1016/S0375-9601(03)00903-4. arXiv: hep-th/0212305.

[8] L. E. Oxman and S. P. Sorella, "Vortex correlation functions in Maxwell-Chern-Simons models," *Phys. Lett. B*, vol. 531, pp. 305–310, 2002. DOI: 10.1016/S0370-2693(02)01474-0. arXiv: hep-th/0201005.

[9] T. Jacobson and T. Sulejmanpasic, "Modified villain formulation of abelian chern-simons theory," *Phys. Rev. D*, vol. 107, p. 125 017, 12 Jun. 2023. DOI: 10.1103/PhysRevD.107.125017. URL: https://link.aps.org/doi/10.1103/PhysRevD.107.125017.

[10] T. Jacobson and T. Sulejmanpasic, "Canonical quantization of lattice Chern-Simons theory," Jan. 2024. arXiv: 2401.09597 [hep-th].

[11] C. Peng, M. C. Diamantini, L. Funcke, S. M. A. Hassan, K. Jansen, S. Kühn, D. Luo, and P. Naredi, "Hamiltonian lattice formulation of compact maxwell-chern-simons theory," *arXiv preprint arXiv:2407.20225*, 2024. URL: https://arxiv.org/abs/2407.20225.

[12] K. Nomura and K. Okamoto, "Critical properties of s= 1/2 antiferromagnetic XXZ chain with next-nearest-neighbour interactions," *Journal of Physics A: Mathematical and General*, vol. 27, no. 17, pp. 5773–5788, Sep. 1994. DOI: 10.1088/0305-4470/27/17/012. URL: https://doi.org/10.1088/0305-4470/27/17/012.

[13] A. Ueda and M. Oshikawa, "Resolving the berezinskii-kosterlitz-thouless transition in the 2d xy model with tensor-network based level spectroscopy," 2021. arXiv: 2105.11460 [cond-mat.stat-mech].

[14] F. D. M. Haldane, "'luttinger liquid theory' of one-dimensional quantum fluids. i. properties of the luttinger model and their extension to the general 1d interacting spinless fermi gas," *Journal of Physics C: Solid State Physics*, vol. 14, no. 19, p. 2585,

Jul. 1981. DOI: 10.1088/0022-3719/14/19/010. URL: https://dx.doi.org/10.1088/0022-3719/14/19/010.

[15] P. Ginsparg, *Applied conformal field theory*, 1988. arXiv: hep-th/9108028 [hep-th]. URL: https://arxiv.org/abs/hep-th/9108028.

[16] D. Sénéchal, *An introduction to bosonization*, 1999. arXiv: cond-mat/9908262. URL: https://arxiv.org/abs/cond-mat/9908262.

[17] S. Sachdev, "Universal, finite-temperature, crossover functions of the quantum transition in the ising chain in a transverse field," *Nuclear Physics B*, vol. 464, no. 3, pp. 576–595, Apr. 1996, ISSN: 0550-3213. DOI: 10.1016/0550-3213(95)00657-5. URL: http://dx.doi.org/10.1016/0550-3213(95)00657-5.

[18] S. Lukyanov and V. Terras, "Long-distance asymptotics of spin–spin correlation functions for the xxz spin chain," *Nuclear Physics B*, vol. 654, no. 3, pp. 323–356, Mar. 2003, ISSN: 0550-3213. DOI: 10.1016/s0550-3213(02)01141-0. URL: http://dx.doi.org/10.1016/S0550-3213(02)01141-0.

[19] S. R. White, "Density matrix formulation for quantum renormalization groups," *Phys. Rev. Lett.*, vol. 69, pp. 2863–2866, 19 Nov. 1992. DOI: 10.1103/PhysRevLett.69.2863. URL: https://link.aps.org/doi/10.1103/PhysRevLett.69.2863.

[20] J. Hauschild and F. Pollmann, "Efficient numerical simulations with Tensor Networks: Tensor Network Python (TeNPy)," *SciPost Phys. Lect. Notes*, p. 5, 2018. DOI: 10.21468/SciPostPhysLectNotes.5. URL: https://scipost.org/10.21468/SciPostPhysLectNotes.5.

[21] U. Schollwöck, "The density-matrix renormalization group in the age of matrix product states," *Annals of Physics*, vol. 326, no. 1, pp. 96–192, 2011, January 2011 Special Issue, ISSN: 0003-4916. DOI: https://doi.org/10.1016/j.aop.2010.09.012. URL: https://www.sciencedirect.com/science/article/pii/S0003491610001752.

[22] R. Orús, "A practical introduction to tensor networks: Matrix product states and projected entangled pair states," *Annals of Physics*, vol. 349, pp. 117–158, 2014, ISSN: 0003-4916. DOI: https://doi.org/10.1016/j.aop.2014.06.013. URL: https://www.sciencedirect.com/science/article/pii/S0003491614001596.

[23] J. L. Cardy, "Conformal invariance and universality in finite-size scaling," *Journal of Physics A: Mathematical and General*, vol. 17, no. 7, p. L385, 1984.

[24] J. L. Cardy, "Operator content of two-dimensional conformally invariant theories," *Nuclear Physics B*, vol. 270, pp. 186–204, 1986.

[25] P. Calabrese and J. Cardy, "Entanglement entropy and quantum field theory," *Journal of Statistical Mechanics: Theory and Experiment*, vol. 2004, no. 06, P06002, Jun. 2004. DOI: 10.1088/1742-5468/2004/06/P06002. URL: https://dx.doi.org/10.1088/1742-5468/2004/06/P06002.

[26] P. Serna, J. T. Chalker, and P. Fendley, "Deconfinement transitions in a generalised xy model," *Journal of Physics A: Mathematical and Theoretical*, vol. 50, no. 42, p. 424 003, Sep. 2017. DOI: 10.1088/1751-8121/aa89a1. URL: https://dx.doi.org/10.1088/1751-8121/aa89a1.

[27] D. V. Schroeder, *Ising model*, 2013. URL: https://physics.weber.edu/schroeder/software/demos/isingmodel.html.

[28] G. Wahba, *Spline Models for Observational Data*. Society for Industrial and Applied Mathematics, 1990. DOI: 10.1137/1.9781611970128. eprint: https://epubs.siam.org/doi/pdf/10.1137/1.9781611970128. URL: https://epubs.siam.org/doi/abs/10.1137/1.9781611970128.

[29] N. E. Helwig, *Smoothing spline regression in r*, 2021. URL: http://users.stat.umn.edu/~helwig/notes/smooth-spline-notes.html.

[30] C. E. Rasmussen and C. K. I. Williams, *Gaussian Processes for Machine Learning*. The MIT Press, Nov. 2005, ISBN: 9780262256834. DOI: 10.7551/mitpress/3206.001.0001. URL: https://doi.org/10.7551/mitpress/3206.001.0001.

[31] F. Pedregosa, G. Varoquaux, A. Gramfort, *et al.*, "Scikit-learn: Machine learning in python," *Journal of Machine Learning Research*, vol. 12, no. 85, pp. 2825–2830, 2011. URL: http://jmlr.org/papers/v12/pedregosa11a.html.

[32] J. Shawe-Taylor, N. Cristianini, *et al.*, *Kernel methods for pattern analysis*. Cambridge university press, 2004.

[33] C. M. Bishop and N. M. Nasrabadi, *Pattern recognition and machine learning*. Springer, 2006, vol. 4.

[34] R. Kapral and G. Ciccotti, "Mixed quantum-classical dynamics," *The Journal of chemical physics*, vol. 110, no. 18, pp. 8919–8929, 1999.

[35] R. Kapral, "Progress in the theory of mixed quantum-classical dynamics," *Annu. Rev. Phys. Chem.*, vol. 57, no. 1, pp. 129–157, 2006.

[36] H. Lin and D. G. Truhlar, "Qm/mm: What have we learned, where are we, and where do we go from here?" *Theoretical Chemistry Accounts*, vol. 117, pp. 185–199, 2007.

[37] M. W. van der Kamp and A. J. Mulholland, "Combined quantum mechanics/molecular mechanics (qm/mm) methods in computational enzymology," *Biochemistry*, vol. 52, no. 16, pp. 2708–2728, 2013.

[38] B. Bauer, D. Wecker, A. J. Millis, M. B. Hastings, and M. Troyer, "Hybrid quantum-classical approach to correlated materials," *Phys. Rev. X*, vol. 6, p. 031 045, 3 Sep. 2016. DOI: 10.1103/PhysRevX.6.031045. URL: https://link.aps.org/doi/10.1103/PhysRevX.6.031045.

[39] M. C. Melo, R. C. Bernardi, T. Rudack, M. Scheurer, C. Riplinger, J. C. Phillips, J. D. Maia, G. B. Rocha, J. V. Ribeiro, J. E. Stone, *et al.*, "Namd goes quantum: An integrative suite for hybrid simulations," *Nature methods*, vol. 15, no. 5, pp. 351–354, 2018.

[40] O. T. Unke, M. Stöhr, S. Ganscha, T. Unterthiner, H. Maennel, S. Kashubin, D. Ahlin, M. Gastegger, L. Medrano Sandonas, J. T. Berryman, *et al.*, "Biomolecular dynamics with machine-learned quantum-mechanical force fields trained on diverse chemical fragments," *Science Advances*, vol. 10, no. 14, eadn4397, 2024.

[41] D. Marx and J. Hutter, *Ab initio molecular dynamics: basic theory and advanced methods*. Cambridge University Press, 2009.

[42] J. Behler and M. Parrinello, "Generalized neural-network representation of high-dimensional potential-energy surfaces," *Phys. Rev. Lett.*, vol. 98, p. 146 401, 14 Apr. 2007. DOI: 10.1103/PhysRevLett.98.146401. URL: https://link.aps.org/doi/10.1103/PhysRevLett.98.146401.

[43] A. P. Bartók, M. C. Payne, R. Kondor, and G. Csányi, "Gaussian approximation potentials: The accuracy of quantum mechanics, without the electrons," *Phys. Rev. Lett.*, vol. 104, p. 136 403, 13 Apr. 2010. DOI: 10.1103/PhysRevLett.104.136403. URL: https://link.aps.org/doi/10.1103/PhysRevLett.104.136403.

[44] Z. Li, J. R. Kermode, and A. De Vita, "Molecular dynamics with on-the-fly machine learning of quantum-mechanical forces," *Phys. Rev. Lett.*, vol. 114, p. 096 405, 9 Mar. 2015. DOI: 10.1103/PhysRevLett.114.096405. URL: https://link.aps.org/doi/10.1103/PhysRevLett.114.096405.

[45] A. V. Shapeev, "Moment tensor potentials: A class of systematically improvable interatomic potentials," *Multiscale Modeling & Simulation*, vol. 14, no. 3, pp. 1153–1173, 2016. DOI: 10.1137/15M1054183. URL: https://doi.org/10.1137/15M1054183.

[46] J. Behler, "Perspective: Machine learning potentials for atomistic simulations," *The Journal of Chemical Physics*, vol. 145, no. 17, p. 170 901, Nov. 2016, ISSN: 0021-9606. DOI: 10.1063/1.4966192. URL: https://doi.org/10.1063/1.4966192.

[47] V. Botu, R. Batra, J. Chapman, and R. Ramprasad, "Machine learning force fields: Construction, validation, and outlook," *The Journal of Physical Chemistry C*, vol. 121, no. 1, pp. 511–522, Jan. 2017, ISSN: 1932-7447. DOI: 10.1021/acs.jpcc.6b10908. URL: https://doi.org/10.1021/acs.jpcc.6b10908.

[48] L. Zhang, J. Han, H. Wang, R. Car, and W. E, "Deep potential molecular dynamics: A scalable model with the accuracy of quantum mechanics," *Phys. Rev. Lett.*, vol. 120, p. 143 001, 14 Apr. 2018. DOI: 10.1103/PhysRevLett.120.143001. URL: https://link.aps.org/doi/10.1103/PhysRevLett.120.143001.

[49] R. T. McGibbon, A. G. Taube, A. G. Donchev, K. Siva, F. Hernandez, C. Hargus, K.-H. Law, J. L. Klepeis, and D. E. Shaw, "Improving the accuracy of möller-plesset perturbation theory with neural networks," *The Journal of Chemical Physics*, vol. 147, no. 16, p. 161 725, Sep. 2017, ISSN: 0021-9606. DOI: 10.1063/1.4986081. URL: https://doi.org/10.1063/1.4986081.

[50] H. Suwa, J. S. Smith, N. Lubbers, C. D. Batista, G.-W. Chern, and K. Barros, "Machine learning for molecular dynamics with strongly correlated electrons," *Phys. Rev. B*, vol. 99, p. 161 107, 16 Apr. 2019. DOI: 10.1103/PhysRevB.99.161107. URL: https://link.aps.org/doi/10.1103/PhysRevB.99.161107.

[51] S. Chmiela, A. Tkatchenko, H. E. Sauceda, I. Poltavsky, K. T. Schütt, and K.-R. Müller, "Machine learning of accurate energy-conserving molecular force fields," *Science Advances*, vol. 3, no. 5, e1603015, 2017. DOI: 10.1126/sciadv.1603015. URL: https://www.science.org/doi/abs/10.1126/sciadv.1603015.

[52] S. Chmiela, H. E. Sauceda, K.-R. Müller, and A. Tkatchenko, "Towards exact molecular dynamics simulations with machine-learned force fields," *Nature Communications*,

vol. 9, no. 1, p. 3887, Sep. 2018, ISSN: 2041-1723. DOI: 10.1038/s41467-018-06169-2. URL: https://doi.org/10.1038/s41467-018-06169-2.

[53] H. E. Sauceda, M. Gastegger, S. Chmiela, K.-R. Müller, and A. Tkatchenko, "Molecular force fields with gradient-domain machine learning (GDML): Comparison and synergies with classical force fields," *The Journal of Chemical Physics*, vol. 153, no. 12, p. 124 109, Sep. 2020, ISSN: 0021-9606. DOI: 10.1063/5.0023005. URL: https://doi.org/10.1063/5.0023005.

[54] P. Zhang and G.-W. Chern, "Arrested phase separation in double-exchange models: Large-scale simulation enabled by machine learning," *Phys. Rev. Lett.*, vol. 127, p. 146 401, 14 Sep. 2021. DOI: 10.1103/PhysRevLett.127.146401. URL: https://link.aps.org/doi/10.1103/PhysRevLett.127.146401.

[55] S. Zhang, P. Zhang, and G.-W. Chern, "Anomalous phase separation in a correlated electron system: Machine-learning enabled large-scale kinetic monte carlo simulations," *Proceedings of the National Academy of Sciences*, vol. 119, no. 18, e2119957119, 2022. DOI: 10.1073/pnas.2119957119. URL: https://www.pnas.org/doi/abs/10.1073/pnas.2119957119.

[56] P. Zhang and G.-W. Chern, "Machine learning nonequilibrium electron forces for spin dynamics of itinerant magnets," *npj Computational Materials*, vol. 9, no. 1, p. 32, Mar. 2023, ISSN: 2057-3960. DOI: 10.1038/s41524-023-00990-0. URL: https://doi.org/10.1038/s41524-023-00990-0.

[57] C. Cheng, S. Zhang, and G.-W. Chern, "Machine learning for phase ordering dynamics of charge density waves," *Phys. Rev. B*, vol. 108, p. 014 301, 1 Jul. 2023. DOI: 10.1103/PhysRevB.108.014301. URL: https://link.aps.org/doi/10.1103/PhysRevB.108.014301.

[58] X. Cheng, S. Zhang, P. C. H. Nguyen, S. Azarfar, G.-W. Chern, and S. S. Baek, "Convolutional neural networks for large-scale dynamical modeling of itinerant magnets,"

Phys. Rev. Research, vol. 5, p. 033 188, 3 Sep. 2023. DOI: 10.1103/PhysRevResearch.5.033188. URL: https://link.aps.org/doi/10.1103/PhysRevResearch.5.033188.

[59] H.-Y. Huang, R. Kueng, G. Torlai, V. V. Albert, and J. Preskill, "Provably efficient machine learning for quantum many-body problems," *Science*, vol. 377, no. 6613, eabk3333, 2022. DOI: 10.1126/science.abk3333. eprint: https://www.science.org/doi/pdf/10.1126/science.abk3333. URL: https://www.science.org/doi/abs/10.1126/science.abk3333.

[60] L. Lewis, H.-Y. Huang, V. T. Tran, S. Lehner, R. Kueng, and J. Preskill, "Improved machine learning algorithm for predicting ground state properties," *Nature Communications*, vol. 15, no. 1, p. 895, Jan. 2024.

[61] H.-Y. Huang, R. Kueng, and J. Preskill, "Predicting many properties of a quantum system from very few measurements," *Nature Physics*, vol. 16, no. 10, pp. 1050–1057, 2020.

[62] E. Onorati, C. Rouzé, D. S. França, and J. D. Watson, "Efficient learning of ground & thermal states within phases of matter," *arXiv preprint arXiv:2301.12946*, 2023.

[63] J. Haah, R. Kothari, and E. Tang, "Learning quantum hamiltonians from high-temperature gibbs states and real-time evolutions," *Nature Physics*, pp. 1–5, 2024.

[64] H.-Y. Huang, S. Chen, and J. Preskill, "Learning to predict arbitrary quantum processes," *PRX Quantum*, vol. 4, no. 4, p. 040 337, 2023.

[65] M. C. Caro, H.-Y. Huang, M. Cerezo, K. Sharma, A. Sornborger, L. Cincio, and P. J. Coles, "Generalization in quantum machine learning from few training data," *Nature communications*, vol. 13, no. 1, p. 4919, 2022.

[66] J. Gibbs, Z. Holmes, M. C. Caro, N. Ezzell, H.-Y. Huang, L. Cincio, A. T. Sornborger, and P. J. Coles, "Dynamical simulation via quantum machine learning with provable generalization," *Physical Review Research*, vol. 6, no. 1, p. 013 241, 2024.

[67] M. Fanizza, Y. Quek, and M. Rosati, "Learning quantum processes without input control," *PRX Quantum*, vol. 5, no. 2, p. 020 367, 2024.

[68] R. Levy, D. Luo, and B. K. Clark, "Classical shadows for quantum process tomography on near-term quantum computers," *Physical Review Research*, vol. 6, no. 1, p. 013 029, 2024.

[69] M. C. Caro, H.-Y. Huang, N. Ezzell, J. Gibbs, A. T. Sornborger, L. Cincio, P. J. Coles, and Z. Holmes, "Out-of-distribution generalization for learning quantum dynamics," *Nature Communications*, vol. 14, no. 1, p. 3751, 2023.

[70] A. Bakshi, A. Liu, A. Moitra, and E. Tang, "Structure learning of hamiltonians from real-time evolution," *arXiv preprint arXiv:2405.00082*, 2024.

[71] E. Onorati, C. Rouzé, D. S. França, and J. D. Watson, "Provably efficient learning of phases of matter via dissipative evolutions," *arXiv preprint arXiv:2311.07506*, 2023.

[72] H.-Y. Huang, Y. Tong, D. Fang, and Y. Su, "Learning many-body hamiltonians with heisenberg-limited scaling," *Physical Review Letters*, vol. 130, no. 20, p. 200 403, 2023.

[73] A. Weiße and H. Fehske, "Exact diagonalization techniques," in *Computational Many-Particle Physics*, H. Fehske, R. Schneider, and A. Weiße, Eds. Berlin, Heidelberg: Springer Berlin Heidelberg, 2008, pp. 529–544, ISBN: 978-3-540-74686-7. DOI: 10.1007/978-3-540-74686-7_18. URL: https://doi.org/10.1007/978-3-540-74686-7_18.

[74] P. Hohenberg and W. Kohn, "Inhomogeneous electron gas," *Physical review*, vol. 136, no. 3B, B864, 1964.

[75] S. R. White, "Density-matrix algorithms for quantum renormalization groups," *Physical review b*, vol. 48, no. 14, p. 10 345, 1993.

[76] D. Luo and B. K. Clark, "Backflow transformations via neural networks for quantum many-body wave functions," *Physical review letters*, vol. 122, no. 22, p. 226 401, 2019.

[77] G. Carleo and M. Troyer, "Solving the quantum many-body problem with artificial neural networks," *Science*, vol. 355, no. 6325, pp. 602–606, 2017.

[78] D. Luo, G. Carleo, B. K. Clark, and J. Stokes, "Gauge equivariant neural networks for quantum lattice gauge theories," *Physical review letters*, vol. 127, no. 27, p. 276 402, 2021.

[79] D. Luo, Z. Chen, K. Hu, Z. Zhao, V. M. Hur, and B. K. Clark, "Gauge-invariant and anyonic-symmetric autoregressive neural network for quantum lattice models," *Physical Review Research*, vol. 5, no. 1, p. 013 216, 2023.

[80] D. Luo, Z. Chen, J. Carrasquilla, and B. K. Clark, "Autoregressive neural network for simulating open quantum systems via a probabilistic formulation," *Physical review letters*, vol. 128, no. 9, p. 090 501, 2022.

[81] D. Wecker, M. B. Hastings, and M. Troyer, "Progress towards practical quantum variational algorithms," *Physical Review A*, vol. 92, no. 4, p. 042 303, 2015.

[82] J. R. McClean, J. Romero, R. Babbush, and A. Aspuru-Guzik, "The theory of variational hybrid quantum-classical algorithms," *New Journal of Physics*, vol. 18, no. 2, p. 023 023, 2016.

[83] A. Peruzzo, J. McClean, P. Shadbolt, M.-H. Yung, X.-Q. Zhou, P. J. Love, A. Aspuru-Guzik, and J. L. O'brien, "A variational eigenvalue solver on a photonic quantum processor," *Nature communications*, vol. 5, no. 1, p. 4213, 2014.

[84] U. Dorner, R. Demkowicz-Dobrzanski, B. J. Smith, J. S. Lundeen, W. Wasilewski, K. Banaszek, and I. A. Walmsley, "Optimal quantum phase estimation," *Physical review letters*, vol. 102, no. 4, p. 040 403, 2009.

[85] T. Holstein, "Studies of polaron motion: Part i. the molecular-crystal model," *Annals of Physics*, vol. 8, no. 3, pp. 325–342, 1959, ISSN: 0003-4916. DOI: https://doi.org/10.1016/0003-4916(59)90002-8. URL: https://www.sciencedirect.com/science/article/pii/0003491659900028.

[86] R. M. Noack, D. J. Scalapino, and R. T. Scalettar, "Charge-density-wave and pairing susceptibilities in a two-dimensional electron-phonon model," *Phys. Rev. Lett.*, vol. 66, pp. 778–781, 6 Feb. 1991. DOI: 10.1103/PhysRevLett.66.778. URL: https://link.aps.org/doi/10.1103/PhysRevLett.66.778.

[87] J. Bon ča, S. A. Trugman, and I. Batisti ć, "Holstein polaron," *Phys. Rev. B*, vol. 60, pp. 1633–1642, 3 Jul. 1999. DOI: 10.1103/PhysRevB.60.1633. URL: https://link.aps.org/doi/10.1103/PhysRevB.60.1633.

[88] P. W. Anderson, "Absence of diffusion in certain random lattices," *Phys. Rev.*, vol. 109, pp. 1492–1505, 5 Mar. 1958. DOI: 10.1103/PhysRev.109.1492.

[89] P. L. DeVries and J. E. Hasbun, *A first course in computational physics*. Jones & Bartlett Publishers, 2011.

[90] E. W. Weisstein, *Complete elliptic integral of the first kind*, 2024. URL: https://mathworld.wolfram.com/CompleteEllipticIntegraloftheFirstKind.html.

[91] S.-S. Chern and J. Simons, "Characteristic forms and geometric invariants," *Annals of Mathematics*, vol. 99, no. 1, pp. 48–69, 1974, ISSN: 0003486X, 19398980. URL: http://www.jstor.org/stable/1971013 (visited on 07/18/2024).

[92] F. Berruto, M. C. Diamantini, and P. Sodano, "On the doubling phenomenon in lattice Chern-Simons theories," *Nucl. Phys. B Proc. Suppl.*, vol. 94, T. Bhattacharya, R. Gupta, and A. Patel, Eds., pp. 657–660, 2001. DOI: 10.1016/S0920-5632(01)01004-0. arXiv: hep-lat/0011052.

[93] S. Deser, R. Jackiw, and S. Templeton, "Topologically Massive Gauge Theories," *Annals Phys.*, vol. 140, p. 372, 1982, [Erratum: Annals Phys. 185, 406 (1988)]. DOI: 10.1016/0003-4916(82)90164-6.

[94] X. Wen, "Zoo of quantum-topological phases of matter," *Rev. Mod. Phys.*, vol. 89, p. 041 004, 2017. DOI: 10.1103/RevModPhys.89.041004.

[95] X. Wen, "Topological orders in rigid states," *International Journal of Modern Physics B*, vol. 04, pp. 239–271, 1990. DOI: 10.1142/S0217979290000139.

[96] S. Deser and R. Jackiw, "Self duality of topologically massive gauge theories," *Phys.Lett. B*, vol. 139, pp. 371–373, 1984. DOI: 10.1016/0370-2693(84)91833-1.

[97] M.-C. Bañuls, K. Cichy, J. I. Cirac, K. Jansen, and S. Kühn, "Tensor Networks and their use for Lattice Gauge Theories," *PoS*, vol. LATTICE2018, p. 022, 2018. DOI: 10.22323/1.334.0022.

[98] M.-C. Bañuls and K. Cichy, "Review on novel methods for lattice gauge theories," *Rep. Prog. Phys.*, vol. 83, no. 2, p. 024 401, Jan. 2020. DOI: 10.1088/1361-6633/ab6311. URL: https://doi.org/10.1088%2F1361-6633%2Fab6311.

[99] T. Shi, E. Demler, and J. Ignacio Cirac, "Variational study of fermionic and bosonic systems with non-gaussian states: Theory and applications," *Annals of Physics*, vol. 390, pp. 245–302, 2018, ISSN: 0003-4916. DOI: https://doi.org/10.1016/j.aop.2017.11.014. URL: https://www.sciencedirect.com/science/article/pii/S0003491617303251.

[100] P. Sala, T. Shi, S. Kühn, M. C. Bañuls, E. Demler, and J. I. Cirac, "Variational study of u(1) and su(2) lattice gauge theories with gaussian states in $1+1$ dimensions," *Phys. Rev. D*, vol. 98, p. 034 505, 3 Aug. 2018. DOI: 10.1103/PhysRevD.98.034505. URL: https://link.aps.org/doi/10.1103/PhysRevD.98.034505.

[101] J. Bender, P. Emonts, E. Zohar, and J. I. Cirac, "Real-time dynamics in $2+1D$ compact qed using complex periodic gaussian states," *Phys. Rev. Res.*, vol. 2, p. 043 145, 4 Oct. 2020. DOI: 10.1103/PhysRevResearch.2.043145. URL: https://link.aps.org/doi/10.1103/PhysRevResearch.2.043145.

[102] J. Bender, P. Emonts, and J. I. Cirac, "Variational monte carlo algorithm for lattice gauge theories with continuous gauge groups: A study of $(2+1)$-dimensional compact qed with dynamical fermions at finite density," *Phys. Rev. Res.*, vol. 5, p. 043 128, 4

Nov. 2023. DOI: 10.1103/PhysRevResearch.5.043128. URL: https://link.aps.org/doi/10.1103/PhysRevResearch.5.043128.

[103] D. Luo, G. Carleo, B. K. Clark, and J. Stokes, "Gauge equivariant neural networks for quantum lattice gauge theories," *Physical review letters*, vol. 127, no. 27, p. 276 402, 2021.

[104] D. Luo, Z. Chen, K. Hu, Z. Zhao, V. M. Hur, and B. K. Clark, "Gauge invariant and anyonic symmetric autoregressive neural networks for quantum lattice models," *arXiv preprint arXiv:2101.07243*, 2021.

[105] Z. Chen, D. Luo, K. Hu, and B. K. Clark, "Simulating 2+ 1d lattice quantum electrodynamics at finite density with neural flow wavefunctions," *arXiv preprint arXiv:2212.06835*, 2022.

[106] L. Funcke, T. Hartung, K. Jansen, and S. Kühn, "Review on Quantum Computing for Lattice Field Theory," *PoS*, vol. LATTICE2022, p. 228, 2023. DOI: 10.22323/1.430.0228. arXiv: 2302.00467 [hep-lat].

[107] A. Di Meglio *et al.*, "Quantum Computing for High-Energy Physics: State of the Art and Challenges. Summary of the QC4HEP Working Group," Jul. 2023. arXiv: 2307.03236 [quant-ph].

[108] T. Byrnes, P. Sriganesh, R. J. Bursill, and C. J. Hamer, "Density matrix renormalization group approach to the massive Schwinger model," *Nucl. Phys. B Proc. Suppl.*, vol. 109, A. C. Kalloniatis, D. B. Leinweber, W. Melnitchouk, and A. G. Williams, Eds., p. 202, 2002. DOI: 10.1016/S0920-5632(02)01416-0.

[109] B. Buyens, S. Montangero, J. Haegeman, F. Verstraete, and K. Van Acoleyen, "Finite-representation approximation of lattice gauge theories at the continuum limit with tensor networks," *Phys. Rev. D*, vol. 95, no. 9, p. 094 509, 2017. DOI: 10.1103/PhysRevD.95.094509.

[110] L. Funcke, K. Jansen, and S. Kühn, "Topological vacuum structure of the Schwinger model with matrix product states," *Phys. Rev. D*, vol. 101, no. 5, p. 054 507, 2020. DOI: 10.1103/PhysRevD.101.054507. arXiv: 1908.00551 [hep-lat].

[111] K. Nakayama, L. Funcke, K. Jansen, Y.-J. Kao, and S. Kühn, "Phase structure of the CP(1) model in the presence of a topological θ-term," *Phys. Rev. D*, vol. 105, no. 5, p. 054 507, 2022. DOI: 10.1103/PhysRevD.105.054507. arXiv: 2107.14220 [hep-lat].

[112] L. Funcke, K. Jansen, and S. Kühn, "Exploring the CP-violating Dashen phase in the Schwinger model with tensor networks," *Phys. Rev. D*, vol. 108, no. 1, p. 014 504, 2023. DOI: 10.1103/PhysRevD.108.014504. arXiv: 2303.03799 [hep-lat].

[113] S. Thompson and G. Siopsis, "Quantum computation of phase transition in the massive schwinger model," *Quantum Science and Technology*, vol. 7, no. 3, p. 035 001, Apr. 2022. DOI: 10.1088/2058-9565/ac5f5a. URL: https://dx.doi.org/10.1088/2058-9565/ac5f5a.

[114] T. Angelides, P. Naredi, A. Crippa, K. Jansen, S. Kühn, I. Tavernelli, and D. S. Wang, "First-Order Phase Transition of the Schwinger Model with a Quantum Computer," Dec. 2023. arXiv: 2312.12831 [hep-lat].

[115] A. Kan, L. Funcke, S. Kühn, L. Dellantonio, J. Zhang, J. F. Haase, C. A. Muschik, and K. Jansen, "Investigating a (3+1)D topological θ-term in the Hamiltonian formulation of lattice gauge theories for quantum and classical simulations," *Phys. Rev. D*, vol. 104, no. 3, p. 034 504, 2021. DOI: 10.1103/PhysRevD.104.034504. arXiv: 2105.06019 [hep-lat].

[116] S. Froehlich and P. Marchetti, "Quantum field theories of vortices and anyons," *Commun. Math. Phys*, vol. 121, pp. 177–223, 1989. DOI: 10.1007/BF01217803.

[117] V. Mueller, "On the connection between euclidean and hamiltonian lattice field theories of vortices and anyons," *Z. Phys. C - Particles and Fields*, vol. 51, p. 665 674, 1991. DOI: 10.1007/BF01565594.

[118] R. D. Pisarski, "Magnetic Monopoles in Topologically Massive Gauge Theories," *Phys. Rev. D*, vol. 34, p. 3851, 1986. DOI: 10.1103/PhysRevD.34.3851.

[119] I. Affleck, J. A. Harvey, L. Palla, and G. W. Semenoff, "The Chern-Simons Term Versus the Monopole," *Nucl. Phys. B*, vol. 328, pp. 575–584, 1989. DOI: 10.1016/0550-3213(89)90220-4.

[120] J. Villain, "Theory of one-dimensional and two-dimensional magnets with an easy magnetization plane. 2. The Planar, classical, two-dimensional magnet," *J. Phys. (France)*, vol. 36, pp. 581–590, 1975. DOI: 10.1051/jphys:01975003606058100.

[121] D. J. Gross and I. R. Klebanov, "One-dimensional string theory on a circle," *Nucl. Phys. B*, vol. 344, E. Brezin and S. R. Wadia, Eds., pp. 475–498, 1990. DOI: 10.1016/0550-3213(90)90667-3.

[122] T. Sulejmanpasic and C. Gattringer, "Abelian gauge theories on the lattice: θ-Terms and compact gauge theory with(out) monopoles," *Nucl. Phys. B*, vol. 943, p. 114 616, 2019. DOI: 10.1016/j.nuclphysb.2019.114616.

[123] P. Gorantla, H. T. Lam, N. Seiberg, and S.-H. Shao, "A modified Villain formulation of fractons and other exotic theories," *J. Math. Phys.*, vol. 62, no. 10, p. 102 301, 2021. DOI: 10.1063/5.0060808. arXiv: 2103.01257 [cond-mat.str-el].

[124] N. Seiberg and E. Witten, "Gapped boundary phases of topological insulators via weak coupling," *Progress of Theoretical and Experimental Physics*, vol. 2016, no. 12, p. 12C101, Nov. 2016, ISSN: 2050-3911. DOI: 10.1093/ptep/ptw083. eprint: https://academic.oup.com/ptep/article-pdf/2016/12/12C101/9620064/ptw083.pdf. URL: https://doi.org/10.1093/ptep/ptw083.

[125] K. G. Wilson, "Confinement of quarks," *Phys. Rev. D*, vol. 10, no. 8, p. 2445, 1974. DOI: 10.1103/PhysRevD.10.2445. URL: https://journals.aps.org/prd/abstract/10.1103/PhysRevD.10.2445.

[126] Villain, J., "Theory of one- and two-dimensional magnets with an easy magnetization plane. ii. the planar, classical, two-dimensional magnet," *J. Phys. France*, vol. 36, no. 6, pp. 581–590, 1975. DOI: 10.1051/jphys:01975003606058100. URL: https://doi.org/10.1051/jphys:01975003606058100.

[127] S. D. Drell, H. R. Quinn, B. Svetitsky, and M. Weinstein, "Quantum electrodynamics on a lattice: A hamiltonian variational approach to the physics of the weak-coupling region," *Phys. Rev. D*, vol. 19, pp. 619–638, 2 Jan. 1979. DOI: 10.1103/PhysRevD.19.619. URL: https://link.aps.org/doi/10.1103/PhysRevD.19.619.

[128] E. Witten, "Dyons of charge $e\theta/2\pi$," *Physics Letters B*, vol. 86, no. 3, pp. 283–287, 1979, ISSN: 0370-2693. DOI: https://doi.org/10.1016/0370-2693(79)90838-4. URL: https://www.sciencedirect.com/science/article/pii/0370269379908384.

[129] A. M. Polyakov, *Gauge fields and strings*. Taylor & Francis, 1987.

[130] D. Tong, *Lectures on gauge theory*, 2018. URL: https://www.damtp.cam.ac.uk/user/tong/gaugetheory.html.

[131] D. Eliezer and G. W. Semenoff, "Intersection forms and the geometry of lattice Chern-Simons theory," *Phys. Lett. B*, vol. 286, pp. 118–124, 1992. DOI: 10.1016/0370-2693(92)90168-4. arXiv: hep-th/9204048.

[132] J. Leinaas and J. Myrheim, "On the theory of identical particles," *Il nuovo cimento*, vol. 37, p. 132, 1977.

[133] F. Wilczek, "Quantum mechanics of fractional-spin particles," *Physical review letters*, vol. 49, no. 14, p. 957, 1982.

[134] M. Levin and X.-G. Wen, "Fermions, strings, and gauge fields in lattice spin models," *Physical Review B*, vol. 67, no. 24, p. 245 316, 2003.

[135] K. Kawagoe and M. Levin, "Microscopic definitions of anyon data," *Physical Review B*, vol. 101, no. 11, p. 115 113, 2020.

[136] A. M. Polyakov, "Fermi-bose transmutations induced by gauge fields," *Modern Physics Letters A*, vol. 3, no. 03, pp. 325–328, 1988.

[137] E. Witten, "Quantum field theory and the jones polynomial," *Communications in Mathematical Physics*, vol. 121, no. 3, pp. 351–399, 1989.

[138] A. Kitaev, "Anyons in an exactly solved model and beyond," *Annals of Physics*, vol. 321, no. 1, pp. 2–111, Jan. 2006, ISSN: 0003-4916. arXiv: cond-mat/0506438.

[139] A. Polyakov, "Compact gauge fields and the infrared catastrophe," *Physics Letters B*, vol. 59, no. 1, pp. 82–84, 1975, ISSN: 0370-2693. DOI: https://doi.org/10.1016/0370-2693(75)90162-8. URL: https://www.sciencedirect.com/science/article/pii/0370269375901628.

[140] A. Polyakov, "Quark confinement and topology of gauge theories," *Nuclear Physics B*, vol. 120, no. 3, pp. 429–458, 1977, ISSN: 0550-3213. DOI: https://doi.org/10.1016/0550-3213(77)90086-4. URL: https://www.sciencedirect.com/science/article/pii/0550321377900864.

[141] X.-G. Wen, *Quantum Field Theory of Many-body Systems*. New York, NY: Oxford University Press, 2004, ISBN: 9780198530947.

[142] G. Busiello, L. De Cesare, and I. Rabuffo, "Wilson's renormalization-group approach to a d-dimensional quantum sine-gordon model," *Phys. Rev. B*, vol. 32, pp. 5918–5924, 9 Nov. 1985. DOI: 10.1103/PhysRevB.32.5918. URL: https://link.aps.org/doi/10.1103/PhysRevB.32.5918.

[143] H. Kleinert, *Gauge Fields in Condensed Matter*. Singapore; Teaneck, NJ: World Scientific, 1989, ISBN: 9789971502102.

[144] P. A. M. Dirac, "Quantised singularities in the electromagnetic field," en, *Proc. R. Soc. Lond. A Math. Phys. Sci.*, vol. 133, no. 821, pp. 60–72, Sep. 1931.

[145] R. A. Jones and M. A. Metlitski, "One-dimensional lattice models for the boundary of two-dimensional majorana fermion symmetry-protected topological phases: Kramers-wannier duality as an exact Z_2 symmetry," *Phys. Rev. B*, vol. 104, p. 245 130, 24 Dec. 2021. DOI: 10.1103/PhysRevB.104.245130. URL: https://link.aps.org/doi/10.1103/PhysRevB.104.245130.